FROM MICRO TO MACRO: MULTI-SCALE BRAIN CONNECTOME ANALYSIS

by

HANBO CHEN

(Under the Direction of Tianming Liu)

ABSTRACT

A connectome is a comprehensive map of neural connections in the brain. It plays a critical role in implementing brain functions such as memory, decision making, emotion, and language, and is believed to correlate with mental disorders such as autism and schizophrenia. To study brain connectome, researchers need to investigate from different views such as structural connectivity, functional connectivity, molecular regulators, development progress, and plasticity property. Since brain connectome is a multi-scale concept and a finest neuron wiring map of the human brain is not feasible due to the technique limits, current studies usually focus on single view in a specific resolution scale using certain imaging modalities and animal models. Despite many novel findings achieved in these studies, a comprehensive map of brain network is still missing. To achieve such map, in my study, I propose to jointly analysis brain in different scales and fuse brain connectome derived from different image modalities, different animal models, and different resolution scales. In micro-scale, I developed a set of software to automatically reconstruct neuron morphologies. In meso-scale, I computed whole brain connectome derived from neuron tracing experiments and employed it to evaluate the result of diffusion tensor image which is in macro-scale. And in macro-scale, I developed a set of brain landmarks to study group-wise inter-regional connectivity. Then I jointly analyzed brain wiring pattern and folding

pattern across primate species and adopted machine learning algorithms to fuse brain functional connectome and structural connectome. Those studies involve different imaging modalities such as confocal microscopy imaging, neuron tracers, and structural/functional/diffusion magnetic resonance imaging. A wide range of study subjects has also been included to enable analysis in different resolution scales. In these studies, I have identified interesting brain connectome patterns that preserved or altered across species, modalities, populations, and between healthy and diseased human brains. Moreover, the newly developed computational frameworks will be further applied in other studies and shed light on the understanding of brain architectures and development mechanisms.

INDEX WORDS: brain connectome, multi-scale analysis, multi-modality analysis, medical image analysis, computational neuroscience, neuron reconstruction, brain structural network, brain functional network, magnetic resonance imaging

FROM MICRO TO MACRO: MULTI-SCALE BRAIN CONNECTOME ANALYSIS

by

HANBO CHEN

B.E., Northwestern Polytechnical University, Xi'an, China, 2010

A Dissertation Submitted to the Graduate Faculty of The University of Georgia in Partial Fulfillment of the Requirements for the Degree

DOCTOR OF PHILOSOPHY

ATHENS, GEORGIA

2016

FROM MICRO TO MACRO: MULTI-SCALE BRAIN CONNECTOME ANALYSIS

by

HANBO CHEN

Major Professor:	Tianming Liu
Committee:	Hanchuan Peng
	Dinggang Shen
	Suchendra M. Bhandarkar
	Qun Zhao

Electronic Version Approved:

Suzanne Barbour
Dean of the Graduate School
The University of Georgia
December 2016

DEDICATION

This thesis is dedicated to my parents Qinglin Chen and Yuling Li. Without their education, encouragement, and support, I cannot make today's achievement. This thesis is also dedicated to my wife Yujie Li who accompanied me, helped me, and married me during my Ph.D. studies.

ACKNOWLEDGEMENTS

First, I would like to thank my advisor, Prof. Tianming Liu. He offered me this opportunity to study in his team at the University of Georgia, introduced me to the field of computational neuroscience, and inspired, supervised, supported my Ph.D. research projects. Most of the works introduced in this thesis are accomplished under his supervision. Second, I would like to thank all my graduate committee members and all the professors that supervised me in my studies. Specifically, I want to thank Prof. Hanchuan Peng, who offered me a valuable opportunity to contribute to the exciting research projects at Allen Institute for Brain Science and supervised me in developing computational tools for neuron reconstructions. I want to thank Prof. Dinggang Shen, who invited me to visit his lab at Chapel Hill, University of Carolina and supervised me in polishing algorithms to fuse brain functional and structural networks. I want to thank Prof. Xiaoping Hu at Emory University who shared macaque and chimpanzee brain data with us and supervised me in conducting across species brain analysis. I want to thank Prof. Joe Z. Tsien at Augusta University who guided me in studying mouse brain connectome. I want to thank Prof. Zhifeng Kou and his students for collaborating with us on studying brain network alternations in mTBI patients. I want to thank Prof. Ping Shen from the department of cellular biology and Dr. Albert Cardona at Janelia Research Campus, who directed me in investing drosophila larvae nerve system. I want to thank Prof. Xianqiao Wang from college of engineering, who collaborated with us in investigating brain development mechanism. Last, but the most, I would like to offer my sincere thanks to all my colleagues, without your collaboration, I cannot finish the research projects in this thesis.

TABLE OF CONTENTS

Page

LIST OF TABLES

Page

LIST OF FIGURES

Page

CHAPTER 1

INTRODUCTION

"I am my connectome." - Sebastian Seung, in 2010 Ted Conference speech.

A connectome is a comprehensive map of neural connections in the brain (Sporns et al. 2005). It is believed that the wiring circuitry made up of billions of neurons defines the infrastructure for the mind and brain functions such as emotion, decision, creativity, and memory. To fully understand brain functions and architectures, a comprehensive investigation of connectome is of essential importance. The term "connectome" is inspired by the term "genome" (Lichtman and Sanes 2008; DeFelipe 2010) which aims for a comprehensive map of gene sequence, and when defining the value and the aims for brain connectome projects, the success experiences of human genome projects are usually borrowed and compared (Lichtman and Sanes 2008; Van Essen et al. 2012; Assaf et al. 2013; Jiang 2013). However, considering the differences between genome and connectome, such comparison may not be applicable. The gene sequence is more static – it is heritable, consistent within species, comparable between species, and stable within the life span of an individual subject. While elasticity is one of the key feature of neuron wiring – the environment, experience, and injury will alternate brain network. In addition, it is not clear to which degree connectome can heritate (even cortical shape may vary between siblings, not to mention neuron connections) and thus comparing and correlating connectome between individuals is challenging. As a result, 10 years after defining the term "connectome", there are still debates on the goal of connectome studies. Considering the cost of establishing comprehensive wiring diagram in large animal's brain (which is technically

implacable up to date), whether establishing such a map is necessary and whether a coarser map is sufficient to investigate brain functions are still open questions for the whole field.

In my opinion, instead of reconstructing a comprehensive map of neuron wiring diagram in the brain, it is more reasonable to define and study connectome in a hierarchical manner – multi-scale brain connectome. Similar concepts have also been suggested to define and analysis connectome in different scales in previous literature (Kötter 2007; Sporns 2011; Jiang 2013; Petersen and Sporns 2015) and different levels of the scale corresponding to levels of spatial resolution in brain imaging. Specifically, these scales are usually categorized as micro-scale, meso-scale and macro-scale. Different scales usually correspond to different imaging techniques and infer different aspects of connectome. In this thesis, according to the imaging resolution and objects, I further separate the definition of multi-scale brain connectome into five scales: molecular scale, cellular scale, circuitry scale, systems scale, and populations scale (Figure 1. 1). And this thesis is organized by the scales of each study such that I will introduce my studies of brain connectome from micro-scale to macro-scale (Figure 1. 1).

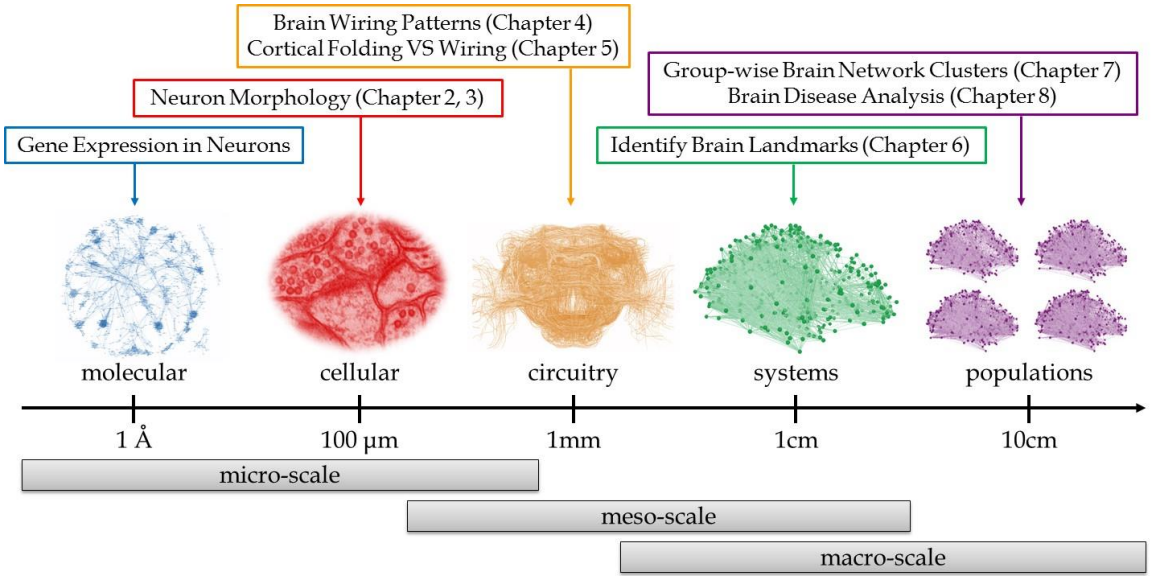

Figure 1. 1. Illustration of the multi-scale concept of brain connectome analysis and the corresponding organization of the whole thesis.

It should be mentioned that though the major focus of this study is brain connectome, the major contribution and novelty of my studies are in the computational scales. Notably, neuroscience is an interdisciplinary area. To study brain connectome demands integration of domain knowledge from different areas and thus requires the collaboration of experts with a different specialty. For instance, neuroscientists conduct experiments to classify neuron types and correlate different types of neurons with different brain functions. Biologists use genetic tools to develop animal models of different neuron developmental disorders. Engineers design cutting-edge equipment to capture high resolution images of neuron or brain with solid quality. Chemists find and synthesize ideal substance such as fluorescent protein to label neurons of interest for visual inspections. Psychologists design questionnaire tests to quantitatively examine the behavior of normal and abnormal subjects. Physicists and mathematicians define mathematical models to simulate the activity of single neuron as well as brain functional networks.

Computer scientists also play a critical role in the field of neuroscience. Today, for most research fields and commercial applications, data collection, processing, analysis and visualization using computers are inevitable. As for neuroscience, following the advances in imaging techniques, the computer infrastructure is first needed to store and share the exponentially growing amount of digital images. Then image pre-processing such as noise reduction, artifact removal, foreground/background segmentation, image alignment and registration are usually conducted automatically using image processing toolboxes. Following that, further analysis is conducted for different purposes. For instance, some researchers are designing different metric to quantify brain development and degeneration process and are searching for brain regions and biomarkers related to mental disorders. Some researchers are

developing advanced algorithms to automatically and accurately reconstruction neuron morphologies. For more examples, Table 1. 1 lists a set of state-of-art computational tools for brain connectome analysis.

Table 1. 1. List of state-of-art software widely used for studying brain connectome.

Software	Scale	Command	Modality	Vis	Computation
Vaa3D (Peng, Ruan, Long, et al. 2010; Peng et al. 2014)	micro	Yes	volumetric image, mesh surface, lines	2D 3D 3D+	image processing, neuron reconstruction
Paraview (Henderson 2007)	-	Python Shell	volumetric image, mesh surface, lines, points	2D 3D 3D+	simple 3D object analysis
ImageJ/FIJI	micro	Yes	Volumetric image, EM slices	2D 3D	image processing, neuron reconstruction
FSL (Jenkinson et al. 2012)	macro	Yes	MRI, fMRI, DTI	2D	MRI/fMRI/DTI image processing and analysis
MedInria (Toussaint et al. 2007)	macro	No	MRI, DTI	2D 3D 4D	Registration, DTI tractography
TrackVis (Wedeen et al. 2008)	macro	Yes	DTI	3D	DTI tractography

As for multi-scale brain connectome study, there are 3 major computational problems need to be solved. (1) Reconstruct brain/neuron network. (2) Visualize network. (3) Analysis and fuse networks from different image modalities and resolution scales. In the rest of this chapter, I will discuss these 3 major problems in detail and survey current solutions and the associated state-of-art computational tools.

BRAIN CONNECTOME COMPUTATION

For most brain network studies, the raw data did not give a direct measurement of brain connectivity. Further computation is needed to quantify brain networks. For instance, segmentation and labeling are required to reconstruct neurons and identify inter-neuron connections in electron microscopy images. Tractography is needed to reconstruct axonal fiber

bundles in diffusion tensor imaging data. For brain functional data, signal processing is needed to correlate signal with events or between regions. Table 1. 2 listed the majority of image modalities, the major computation steps required to analysis brain network, and the computational tools that are readily available to process the raw data.

Table 1. 2. List of imaging modalities used for studying brain networks

Modality	Scale	Key Computation Step	Representative tools
Confocal Microscopy	micro	Stitch image tiles, neuron reconstruction	Vaa3D, Neurolucida
Electron Microscopy	micro	Stitch and align slices, segmentation, neuron labeling	TrakEM2, CATMAID
Calcium Imaging (Microscopy)	micro	Segmentation, signal extraction, signal processing	FluoroSNNAP, OpenFluo
Neuron Tracer	meso	Slice alignment, connectivity calculation	N/A
Diffusion Tensor Imaging	macro	Registration, tractography, connectivity calculation	DTI Studio, MedInria, TrackVis, mritrix, FSL
Functional Magnetic Resonance Imaging	macro	Registration, signal processing, activation detection	FSL, SPM, HELPNI
Electroencephalography (EEG)	macro	Signal processing	R/Python/Matlab libraries

Despite the great success of the existing tools in inferring brain network information, there are still limitations that can be further improved. First, some tools still require human intervention and label works (e.g. CATMAID is designed for fast manual annotation). Second, some tools still require further computation for a final quantification (e.g. most tractography software requires further computation with in-house tools to quantify brain structural network). Third, the reliability of some results is largely unknown (e.g. DTI tractography) and some findings are criticized by the poor reproducibility. How to design efficient algorithms or take the advantage of the state-of-art machine learning algorithms to automate these process and increase the accuracy and throughput is still an open question that the whole field of medical image analysis is working on.

BRAIN CONNECTOME VISUALIZATION

Seeing is believing. Visual inspection is always necessary to make sure the results are correct and reasonable. For instance, it is always a good habit to visually inspect the input data and make sure the data are loaded correctly by the program. Also, it is desired to save and visualize the temporary results calculated by each step to make sure there is no bug in the program and the parameters selected are reasonable. Moreover, when the final results are surprisingly good (e.g. p-value << 0.01, accuracy > 99%), it is always a good practice to visualize the connections/features in brain and check if such result is reasonable before making the conclusion and reporting the result.

In addition, a good visualization will lead to a better interpretation of the result and even novel findings. So far, the representations of brain connectome can be classified into 2 major types. (1) Graph representation defines the regions of interests or neurons as nodes and the structural connectivity or functional interaction between them as edges. (2) Spatial map representation is usually applied in studying brain functional networks and defines a brain area with strong concurrent signals as a network.

For graph representation, it can be visualized by adjacency matrix (Figure 1. 2 (a)) or an edge-node visualization (Figure 1. 2 (b)-(c)). The adjacency matrix offers a complete view of the graph with each row/column corresponding to a node and the intensity of each matrix entry representing the edge between the corresponding nodes. The columns/rows can be rearranged by anatomical/functional roles for a better biological interpretation. Such matrix can be easily generated using matlab or other program libraries. However, it is relatively difficult to examine and explain when there are hundreds of nodes in the graph. For edge-node visualization, nodes can be arranged by circle layout (Krzywinski et al. 2009) (Figure 1. 2 (b)), cluster layout, or

brain layout (Figure 1. 2 (c)). And the edges can be visualized by a straight or curved line with/without arrows to represent directional/none-directional connections. The size/thickness and the color of nodes and edges can be adjusted to reflect different parameters. The circle layout can be generated using software circus (http://circos.ca/), the cluster layout can be generated using software gephi (https://gephi.org), and the brain layout can be generated using software paraview (http://www.paraview.org). However, though all these software are well designed and can be used interactively, the researchers need to first convert their findings to the correct formats before they can get the desired visualization and a certain level of programming skills are required to master these tools. Nevertheless, edge-node visualization will be less informative when the connection is relatively dense.

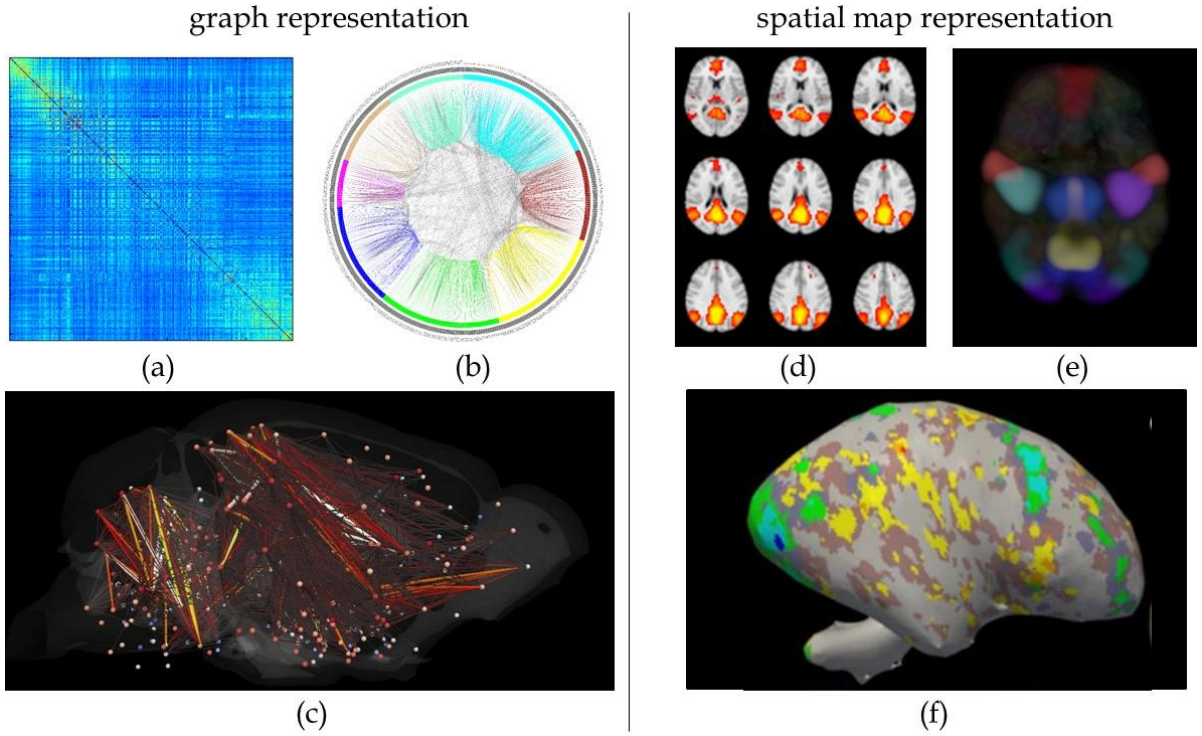

Figure 1. 2. Examples of two types of brain network visualization. (a)-(c) Examples of visualizing graph representations. (d)-(f) Examples of visualizing a spatial map of functional brain networks.

A spatial map representation can either be in 3D (e.g. fMRI data) or in 2D space (e.g. EEG data). It is relatively intuitive to visualize 2D images on a monitor. As for 3D spatial map, one simple option is to show by slices (Figure 1. 2 (d)). However, slice view may overlook 3D pattern of the network. Alternatively, we can render spatial map volumes in 3D space based on maximum projection (Figure 1. 2 (e)) or surface representation. Also, the 3D volume can be projected onto smoothed cortical surface (Figure 1. 2 (f)) such that both the spatial pattern and the anatomical pattern can be visualized. Software FSL (http://fsl.fmrib.ox.ac.uk/fsl/fslwiki/) features a slice visualization of brain functional network. Software Vaa3D (http://vaa3d.org) and Paraview (http://www.paraview.org) can jointly visualize 3D volumes and Surfaces.

MULTI-MODALITY, MULTI-SCALE DATA FUSION

Features from different imaging modalities offer complementary views. Multimodal fusion provides a more comprehensive description of altered brain patterns and connectivity than a single modality (Arbabshirani et al. 2016). In addition, the combination of function and structure may provide more informative insights into both altered brain patterns and connectivity in brain disorders (Arbabshirani et al. 2016). The goal of mapping multi-view information can be explained in two-folds: (1) more accurate diagnose than single modality; (2) more insights to the cause of diseases for a better treatment (e.g. functional and structural causes of brain disease and their inner correlations). As recently reviewed by Arbabshirani et al. (Arbabshirani et al. 2016), it is surprising that among recent studies on brain disease diagnose, there are more multi-modality studies than single modality studies.

Feature Selection

One intuitive way of data fusion is to equally treat features from different views and use feature selection method to select the features that are informative for classification and

diagnosis. When selecting features for prediction, the major criteria is that the selected features need to fit the label to predict. To measure the fitness, measurement such as correlation coefficient, mutual information (Ding and Peng 2005; Peng et al. 2005), or graph matching (Liu et al. 2013) are mostly used. In addition to data fitting criteria, other constraints will be added to further optimize the selection: (1) feature sparseness is widely applied to allow the most important features "pop-up" and lead to a better interpretation of the result (Lv, Jiang, Li, Zhu, Chen, et al. 2015), (2) information independence is usually enforced to eliminate redundant features (Peng et al. 2005).

Nevertheless, since each modality carries different information, specific feature selection scheme can be designed considering the inner correlation between and within modalities. For instance, in Sparse Multimodal Learning (SMML) method proposed by Wang et al. (Wang et al. 2013; Zhang, Huang, et al. 2014), in addition to loss function which tries to fit data, two extra cost functions are defined to add sparse constraint between modalities and sparse constraint between features (high weight to features contribute to more labels):

$$\min_{\boldsymbol{W}} \sum_{i=1}^{c} f_i(\boldsymbol{w_i}, b_i) + 2\gamma_1 \|\boldsymbol{W}\|_{G_1} + 2\gamma_2 \|\boldsymbol{W}\|_{2,1} \tag{1.1}$$

where **W** indicates the weights of all features from all modalities in classifying c classes. The first part of the equation is the loss function. The second part captures the global relationships between modalities such that low (zero) weight will be assigned to modalities with little contribution to a certain label. The last part imposed sparsity to feature selection such that the weights of most features are close to zeroes and only the features important to classification tasks have large weights.

Another trend in applying multimodal data for classification is to use the information from other modalities to guide a better selection of features in a single modality. That is, in

feature selection phase, multiple modality data will be used, and in training and testing phase, only a single modality will be used. Such technique will be helpful when some modalities are absent in the testing data or when some modalities are more expensive to acquire than other ones. For instance, it is more time consuming to acquire functional MRI and diffusion MRI image than structural MRI image. And in some clinical cases, only structural MRI image will be available. On the other hand, spatial and anatomical information will be preserved across these modalities. Thus, based on such correspondence, if the features of one ROI derived from different modalities are shown to be a good fit of predefined labels, then more weight should be given to the corresponding features from structural MRI image, based on which classifier will be trained and tested. Then for the individual subject, only structural MRI image is needed for prediction and diagnose.

Feature Fusion

Another approach is to fuse the features before further analysis. For instance, to perform image segmentation / graph clustering based on features from different views, we can first compute similarity matrix based on each view and then fuse these similarity matrices together for final clustering. To fuse, the most intuitive approach is to average the similarities between modalities. Also, given that similarity value distributes between 1 and 0, we can also multiply the values, use maximum similarity value, or use minimum similarity value across modalities as final fused similarity value for different purposes.

However, since the features from different views may have different scales and the similarity matrix may have different distributions, such intuitive and empirical approach will not be applicable in those scenarios. In my previous work (Chen, Li, Zhu, Jiang, et al. 2013), I

proposed to fuse brain structural and functional connectivity in the Eigenspace across modalities and individuals to cluster group-wise and modality-wise consistent brain networks:

$$proj(W_i, U_j) = (U_j {U_j}^T W_i + (U_j {U_j}^T W_i)^T)/2 \quad (1.2)$$

where W_i is the connectivity matrix of view i and U_j is the top k eigenvectors of connectivity matrix from view j.

This approach is ideal for identifying common clusters since it will smooth the connectivity of view i within the clusters of view j and weaken and erase the connectivity between the clusters of view j. In this way, the common clusters can be obtained for further analysis. For instance, to study brain network alternations in the diseased brain, such method can be applied to identify common brain networks across individuals based on which within or between network changes can be studied (Chen, Iraji, et al. 2015). Or it can be used on different populations to identify population-specific brain sub-networks. However, such fusion approach is only proposed for group-wise analysis and may not be applicable for individual predictions.

Multiple Kernel Learning

Instead of selecting or fusing features which will be used for training classifiers, another set of approaches is to train the classification kernel for each modality and then select or fuse these kernels, namely multiple kernel learning (MKL) (Gönen and Alpaydın 2011). For instance, give a set of data X with labels Y, n additive kernels K can be trained and linearly combined into a new kernel:

$$K' = \sum_{i=1}^{n} \beta_i K_i \quad (1.3)$$

In the fruitful review paper composed by Gonen and Alpaydın (Gönen and Alpaydın 2011), 6 dimensions of MKL methods have been proposed including: (1) the learning method, (2) the functional form, (3) the target function, (4) the training method, (5) the base learner, and

(6) the computational complexity. For each dimension, multiple options have been proposed in the previous literature. And based on different combinations of options, different methods can be designed to solve the classification problem. It has been shown that using multiple kernels outperforms using a single one. However, trained linear combination is not always better than an untrained, unweighted combination and nonlinear or data-dependent combination seem more promising.

One example of using MKL in disease prediction is the work by Zhang *et al*. (Zhang et al. 2011). In this paper, the authors proposed a kernel combination method to combine three modalities of biomarkers (MRI, FDG-PET, and CSF) to discriminate between AD (or MCI) and healthy controls. In this framework, a linear combination of SVM kernels is proposed with a single and separate step in searching optimal weights for kernels. The results showed higher accuracy when including multiple modalities than a single modality.

Multimodal Deep Learning

Deep learning algorithms are shown to be efficient for unsupervised or semi-supervised feature learning and hierarchical feature extraction. The methods are inspired by advances in neuroscience such that multiple hidden layers are placed between the input layer and output layer. The connection parameters between layers will be trained for feature representation. Deep learning has shown to be successful in producing state-of-the-art results on various tasks in different fields such as computer vision, automatic speech recognition, natural language processing, audio recognition and bioinformatics. The method is initially proposed for single modality while it can be extended for multimodal representation (Ngiam et al. 2011; Srivastava and Salakhutdinov 2012; Wu et al. 2013; Sohn et al. 2014).

One identical architecture of deep learning algorithm is its layered structure. The combination of different modalities can be conducted in either shadow layer (input layer) or deep layer (hidden layer). In (Ngiam et al. 2011; Srivastava and Salakhutdinov 2012), the authors proposed to use deep Boltzmann machine to fuse features from different views. Specifically, a deep hidden layer is proposed to connect the hidden layers learnt from different modalities. This approach can (1) fuse features from different modalities into a joint representation (hidden layer features) for classification, and (2) reconstruct features of a missing modality from other modalities. In a study by Suk, Lee, and Shen (Suk et al. 2014), a similar framework has been applied and was shown to be effective in fusing features from MRI and PET image to predict Alzheimer's disease patients. Multimodal learning approach can also be employed in other deep learning architectures. For instance, convolutional neural network (CNN) (Ma et al. 2015) has been successfully adjusted for multimodal learning in recent works by Ma and his colleagues. Mao et al. have deployed a deep layer in recurrent neural network to include image features trained based on CNN to perform text prediction (Mao et al. 2014). Deep learning is a fast-growing field, and new architectures, variants, or algorithms appear every few weeks. Apply deep learning technique in treating multimodal data is a brand new field with many potentials. I believe it will advance current solutions of aligning multi-view features and distinguishing group difference.

CHAPTER 2

SMART TRACING: SELF-LEAENING BASED NEURON RECONSTRUCTION [1]

[1] Hanbo Chen, Hang Xiao, Tianming Liu, Hanchuan Peng. 2015, SmartTracing: self-learning-based Neuron reconstruction. *Brain Informatics*. 2:135–144.

ABSTRACT

In this chapter, we propose SmartTracing, an automatic tracing framework that does not require substantial human intervention. There are two major novelties in SmartTracing. First, given an input image, SmartTracing invokes a user-provided existing neuron tracing method to produce an initial neuron reconstruction, from which the likelihood of every neuron reconstruction unit is estimated. This likelihood serves as a confidence score to identify reliable regions in a neuron reconstruction. With this score, SmartTracing automatically identifies reliable portions of a neuron reconstruction generated by some existing neuron-tracing algorithms, without human intervention. These reliable regions are used as training exemplars. Second, from the training exemplars the most characteristic wavelet features are automatically selected and used in a machine-learning framework to predict all image areas that most probably contain neuron signal. Since the training samples and their most characterizing features are selected from each individual image, the whole process is automatically adaptive to different images. Notably, SmartTracing can improve the performance of an existing automatic tracing method. In our experiment, with SmartTracing we have successfully reconstructed complete neuron morphology of 120 *Drosophila* neurons. In the future, it may lead to more advanced tracing algorithms and increase the throughput of neuron morphology related studies.

INTRODUCTION

The manual reconstruction of a neuron's morphology has been in practice for one century now since the time of Ramón y Cajal. Today, the technique has evolved such that researchers can quantitatively trace neuron morphologies in 3D with the help of computers. As a quantitative description of neuron morphology, the digital representation has been widely applied in the tasks of modern neuroscience studies (Meijering 2010; Donohue and Ascoli 2011; Parekh and Ascoli

2013) such as characterizing and classifying neuron phenotype, or modeling and simulating electrophysiology behavior of neurons. However, many popular neuron reconstruction tools such as Neurolucida (http://www.mbfbioscience.com/neurolucida) still relies on manual tracing to reconstruct neuron morphology, which limits the throughput of analyzing neuron morphology.

In the past decade, many efforts have been given to eliminate such a bottleneck by developing automatic or semi-automatic neuron reconstruction algorithms (Meijering 2010; Donohue and Ascoli 2011). In these algorithms, different strategies and models were applied, such as pruning of over-complete neuron-trees (Peng et al. 2011; Xiao and Peng 2013), shortest path graph (Lee et al. 2012), distance transforms (Yang et al. 2013), snake curve (Wang et al. 2011) and deformable curve (Peng, Ruan, Atasoy, et al. 2010). However, the completeness and the attribute of resulted neuron morphology vary tremendously between different algorithms. Recently, to quantitatively access such variability between algorithms and advance the state-of-art of automatic neuron reconstruction method, a project named BigNeuron (Peng, Hawrylycz, et al. 2015; Peng, Meijering, et al. 2015) has been launched to bench-test existing algorithms on big dataset. One reason causing such variability is that image quality and attributes vary between different data sets – partially due to the differences in imaging modality, imaging parameter, animal model, neuron type, tissue processing protocol, and the proficiency of microscopic operator. And some of the algorithms were developed based on specific data or were developed to solve specific problems in the data which may not be applicable for other types of data. Another reason is that most of the tracing algorithms required user input of parameters. As a consequence, the optimal parameters vary between images and thus requires manual tune by the user with sufficient knowledge to the algorithm.

It should be noted that most of the current automatic neuron reconstruction algorithms are not "smart" enough. Indeed many times they require human intervention to obtain a reasonable result. To conquer this limitation, one can adapt learning based methods so the algorithm can be trained for different data. In (Gala et al. 2014), the authors proposed a machine learning approach to estimate the optimal solution of linking neuron fragments. However, the fragments to link were still generated by model-driven approaches and it requires manual work in generating training samples.

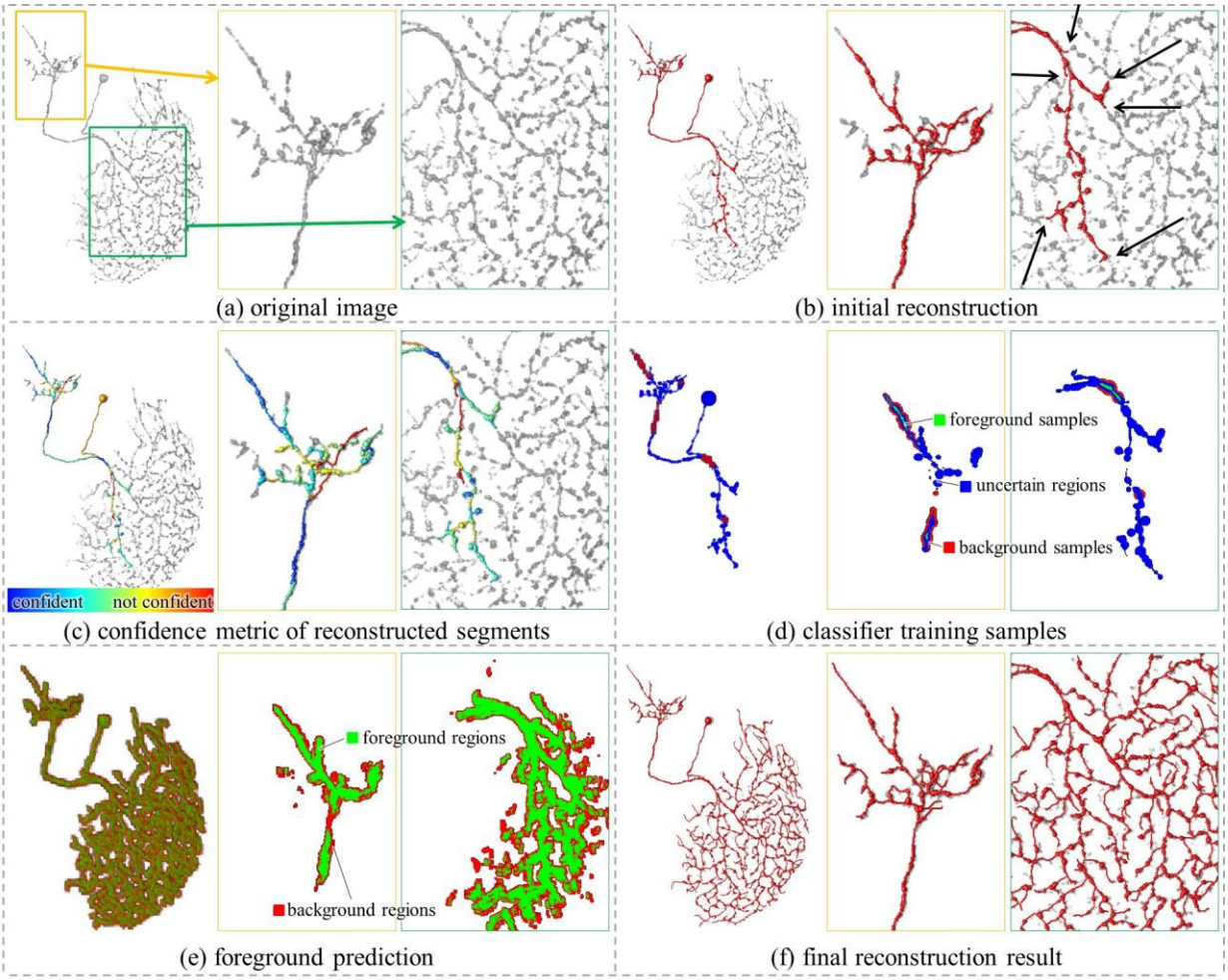

Figure 2. 1. Overview of SmartTracing method and the result for a single image. In each subfigure, the global 3D view of images and the overlapped reconstructions are shown on the left. The zoomed in 3D view ((a)-(c) and (f)) or slice view ((d)-(e)) are shown on the right. The locations of the zoomed in view are highlighted in (a).

In this chapter, based on machine learning algorithms, we proposed SmartTracing, an automatic tracing framework that does not require human intervention. The procedure of the SmartTracing algorithm was outlined in Figure 2. 1. First, the initial reconstruction was obtained based on existing automatic tracing algorithms (Figure 2. 1(b)). Second, a confidence metric proposed in this chapter was computed for each reconstruction segment to identify reliable tracing (Figure 2. 1(c)). Third, a training sample (Figure 2. 1(d)) and the most characteristic features were obtained. Fourth, a classifier was then trained and the foreground containing neuron morphology was predicted (Figure 2. 1(e)). Finally, after adjusting the image based on prediction result, the final reconstruction was traced (Figure 2. 1(f)).

This chapter is organized as follows. we first discuss the key steps of SmartTracing. Then we describe the implementation and the availability of the algorithm. Finally, we present experimental results on real neuron image data, followed by some brief discussion of the pros and cons and the future extension of SmartTracing.

METHOD

Confidence score of reconstruction

In SmartTracing, we first identify the reliable neuron reconstructions as training exemplars. A neuron reconstruction can be decomposed into multiple segments by breaking the reconstruction at the branch point. Whether or not a segment is trustworthy can be tested by checking if there is an alternative path connecting the two ends of the segment compared to this segment. Our premise is that a segment with no better alternative pathway (e.g. Figure 2. 2(c)) is more reliable in comparison with a segment with alternative pathway (e.g. Figure 2. 2(d)). Specifically, for a segment L_{ij} between points i and j, the image intensity alone L_{ij} will be

masked to 0 first. Then, the shortest path $L_{ij}{}^{*}$ weighted by intensity between points i and j will be identified. In the original image, the average intensity alone L_{ij} and $L_{ij}{}^{*}$ will be measured:

$$\bar{I_{ij}} = \frac{\int_{L_{ij}} I(x)dx}{\|L_{ij}\|} \tag{2.1}$$

where $I(x)$ is the intensity of x, and $\|L_{ij}\|$ is the length of L_{ij}.

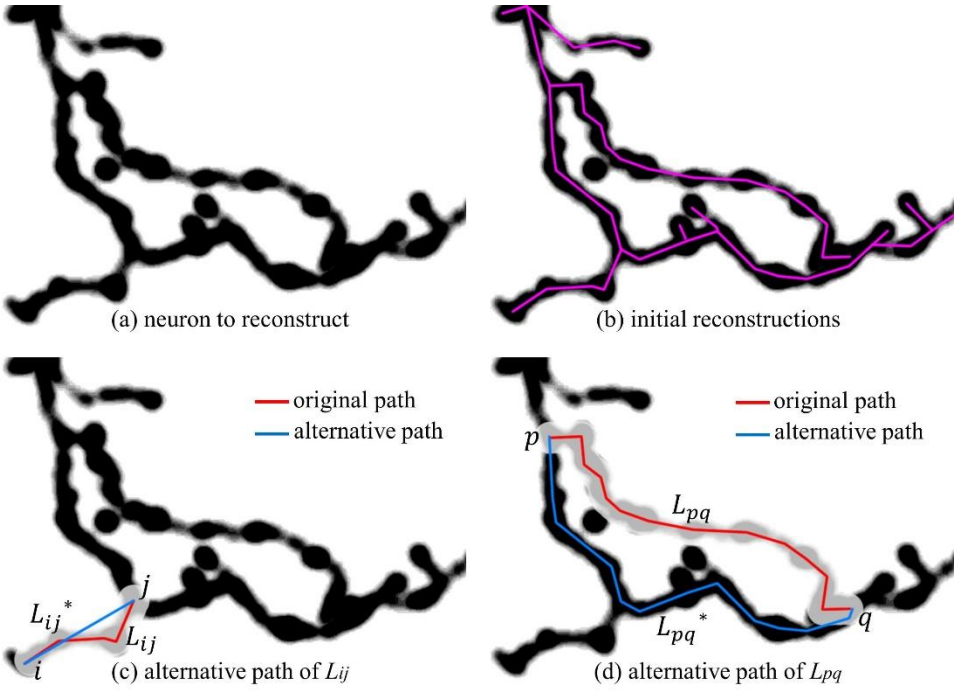

Figure 2. 2. Illustration of an alternative path. For each segment in the reconstructions, after masking the image alone the segment, the alternative path will be searched by fast marching from one end to the other end of the segment based on intensity.

Then the confidence metric can be obtained by dividing $\bar{I_{ij}}{}^{*}$ with $\bar{I_{ij}}$:

$$C_{ij} = \bar{I_{ij}}{}^{*} / \bar{I_{ij}} \tag{2.2}$$

Our method is that if an alternative path exists, $\bar{I_{ij}}{}^{*}$ will be closer or even larger to $\bar{I_{ij}}$ and C_{ij} will be close to 1. Otherwise, $L_{ij}{}^{*}$ will be a relatively straight line passing through background with low intensity connecting i and j, and thus $C_{ij} \ll 1$. This measurement is based

on the assumption that background intensity is lower than foreground intensity. When the background intensity is greater than foreground (e.g. for brightfield images), we can simply invert C_{ij} in Eq. (2.2).

Obtain training exemplars

Based on the confidence score obtained, the original image can be classified into 4 groups of regions – foreground samples (labeled neurons), background samples (none-neuron area), uncertain regions, and the irrelevant area (Figure 2. 1(d)). Foreground samples are defined as the skeleton regions of confident reconstruction segments. Background samples are defined as the non-skeleton regions surrounding the confident reconstruction segments. The intermediate zones between these two regions are taken as uncertain regions. And the zones surrounding less confident reconstructions are taken as uncertain regions as well. These 3 types of regions compose 3 layers surrounding the confident reconstructions - core layer: foreground samples; middle layer: uncertain regions; outer layer: background samples.

Extract features for classification

Image intensity based features are extracted by adopting the method proposed in (Zhou and Peng 2007). The whole procedure is outlined in Figure 2. 3. For each sample voxel, features are extracted in a 3D cube surrounding this voxel (Figure 2. 3 (a)). Multi-resolution wavelet representation (MWR) is applied to project the sub-volume of the local 3D cube into a feature space (Figure 2. 3(b)-(c)). Then, a subset of features is selected based on the minimal-redundancy-maximal-relevance (mRMR) method (Peng et al. 2005) for classification (Figure 2. 3(d)).

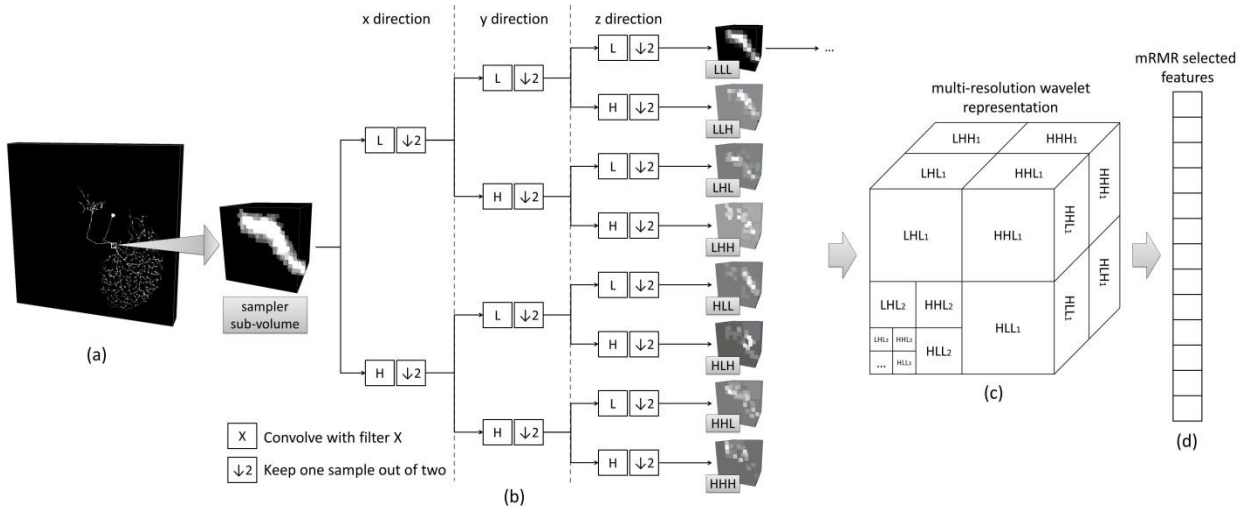

Figure 2. 3. Illustration of feature selection procedure. (a) Extract sub-volume in 3D cube surrounding the sample voxel. (b) Wavelet decomposition for volume data. (c) Multi-resolution wavelet representation. (d) Select a characterizing subset of features based on mRMR for classification.

MWR codes the information in both frequency domain and spatial domain. It is effective for identifying local and multi-scale features from signals or images and has been widely used in pattern recognition tasks. The MWR framework was firstly introduced on 1-dimensional (1D) signals and then extended to 2-dimensional (2D) images by Mallat (Mallat 1989). In brief, a pair of functions was defined to conduct wavelet transform – the mother wavelet $\psi(x)$ representing the detail and high-frequency parts of a signal, and the scaling function $\varphi(x)$ representing the smooth and low-frequency parts of the signal. To decompose a signal into multiple resolutions, the calculation is performed iteratively on the smoothed signal calculated based on $\varphi(x)$. In practice, for discrete signal, instead of calculating wavelet $\psi(x)$ and scaling function $\varphi(x)$, a high pass filter H and a low pass filter L will be applied to calculate MWR. Mallat has shown that, MWR can be extended from 1D signal to 2D image by convolving the image with the filters in one dimension first and then convolving the output image with the filters in the other dimension (Mallat 1989). Such operation can be further extended to 3D volume (Muraki 1993). As

illustrated in Figure 2. 3(b), in one level of decomposition, 8 groups of wavelet coefficients are obtained by convolving volume with different permutations of two filters in three directions successively. The smoothed volume LLL is further decomposed in the next level to achieve multiresolution representations.

After MWR decomposition, the dimension of feature space is relatively high – the number of features $\{f_i\}$ equals to the number of voxels in the sub-volume (Figure 2. 3(c)). Since some of these features may carry redundant information or none-discriminative information, using the full set of MWR coefficients directly may lead to inaccurate result. To better discriminate patterns and improve the robustness and accuracy of training framework, we select the most characterizing subset of features S. We consider the mRMR feature selection method to solve the problem. The algorithm has been widely applied in selecting features in high dimensional data such as microarray gene expression data to solve classification problems (Ding and Peng 2005). In the algorithm, the statistical dependency between the exemplar type and the joint distribution of the selected features will be maximized. To meet this criterion, mRMR method search for the features that are mutually far away from each other (minimum redundancy) but also individually most similar to the distribution of sampler types (maximum relevance). In practice, these two conditions were optimized simultaneously:

$$\max_{S \in W} \left\{ \frac{1}{|S|} \sum_{i \in S} I(c, f_i) - \frac{1}{|S|^2} \sum_{i,j \in S} I(f_i, f_j) \right\} \tag{2.3}$$

where W denotes the full set of MWR coefficients, c denotes the vector of sampler type, $|S|$ is the number of features, and $I(x, y)$ is the mutual information between x and y. The first term in the equation is the maximum relevance condition and the second term is the minimum redundancy condition. It has been shown in (Peng et al. 2005), the solution can be computed efficiently in $O(|S| * |W|)$.

Training classifier and tracing neuron reconstruction

Based on the extracted features of training samples, supervised training can be performed to train a classifier for foreground/background predictions. In our proposed framework, we use Support Vector Machine (SVM) implemented in LIBSVM toolkit (Chang and Lin 2011). The default parameter setting of LIBSVM is used. A subset of foreground and background training samples are randomly chosen from the pool to make sure the numbers of training samples from each class are the same.

With the trained classifier, we then examine the voxels in the image and label them as foreground or background (Figure 2. 1(e)). Since in neuron tracing problem, foreground signals are often sparse and relatively continuous in the image, we use a fast marching algorithm to search for the foreground signals. Initially, the voxels of foreground samples are pre-labeled as foreground and the rest voxels are marked "unknown". The algorithm would then march from foreground voxels to their adjacent unknown voxels. For each of such "unknown" voxels, its feature will be extracted and it will be classified as foreground or background based on the classifier trained. If the voxel is classified as foreground, it will be taken as a new starting point for the next round of marching. The marching will stop until no more foreground voxel can be reached and all of the unknown voxels left will be labeled as background.

Based on the labeled image, the original image is adjusted to obtain the final tracing result. The intensity of background voxels is set to 0. For foreground voxel, if its intensity is lower than the threshold set for tracing algorithm, the intensity of the voxel will be set as the threshold value. Otherwise, its intensity will be kept unchanged. Then the tracing algorithm will be re-run on the adjusted image to trace the final corrected neuron reconstruction.

IMPLEMENTATION

Intuitively, the proposed sampling, training, and prediction framework can be applied on any existing neuron tracing algorithms to test and improve its performance. In our implementation, we used the APP2 tracing algorithm (Xiao and Peng 2013) to generate the initial tracing from the original image as well as the final tracing from the image after prediction. To our best knowledge, APP2 tracing algorithm is the fastest tracing algorithm among existing methods and is reliable in generating tree shape morphology for neuron reconstructions, which makes it an ideal algorithm to implement proposed framework. On the other hand, the APP2 algorithm has its own limitations. It will stop tracing when there is a gap between signals such as the ones highlighted by arrows in Figure 2. 1(b). Also, like many other tracing algorithms, it needs to fine tune the background threshold and other parameters to avoid over-tracing. Thus, our proposed framework can further improve the performance of APP2.

We implemented the SmartTracing algorithm as a plugin of Vaa3D (Peng, Ruan, Long, et al. 2010; Peng et al. 2014) which is the common platform to implement algorithms for the BigNeuron project (bigneuron.org) bench-testing. Since the APP2 algorithm has already been implemented in Vaa3D, the algorithm was directly invoked via the Vaa3D plugin interface. The default parameters of APP2 were taken to generate initial neuron reconstruction. To generate the final reconstruction, the background threshold was set to 1 since the intensity of all the background voxels were set to 0 as introduced in the previous section. The neighborhood 3D window size was 16×16×16 voxels. The cube of each such 3D small window was decomposed into 3 levels MWR. The mRMR feature selection was implemented based on the code downloaded from http://penglab.janelia.org/proj/mRMR/ and the top 20 characteristic features

were selected. Classifier training and prediction were implemented based on the code downloaded from LIBSVM toolkit (http://www.csie.ntu.edu.tw/~cjlin/libsvm/).

EXPERIMENTAL RESULTS

The whole framework was tested on 120 confocal images of single neurons in the *Drosophila* brain downloaded from the flycircuit.tw database. The dimension of each image is 1024*1024*120 voxels. For some of the images, APP2 works reasonably well in reconstructing neuron morphologies. However, due to the loss of signals during the image preprocessing, there could be gap between neuron segments which resulted in incomplete reconstructions by APP2. 10 examples of incomplete reconstructions were shown and highlighted by arrows in Figure 2. 4. Those gaps were classified as foreground with proposed SmartTracing framework and filled for complete tracing (red skeletons in Figure 2. 4). The quantitative measurements of the morphology and the computational running time (using single CPU) of these 10 examples were listed in Table 2. 1.

For the 120 confocal images tested, the proposed SmartTracing algorithm successfully improved the overall completeness of reconstructions. In comparison with initial reconstructions, the total length, bifurcation number, branch number, and tip number all increased after the optimization of SmartTracing (Figure 2. 5). Among those, the completeness of 30 reconstructions were significantly improved (the total length of final reconstruction is 1.2 times larger than initial reconstruction). By visual inspection, the SmartTracing algorithm only failed to trace the complete neuron morphology on 1 image out of the 120 images. In this failure case, there is a gap that is too big to be filled (Figure 2. 6(b)).

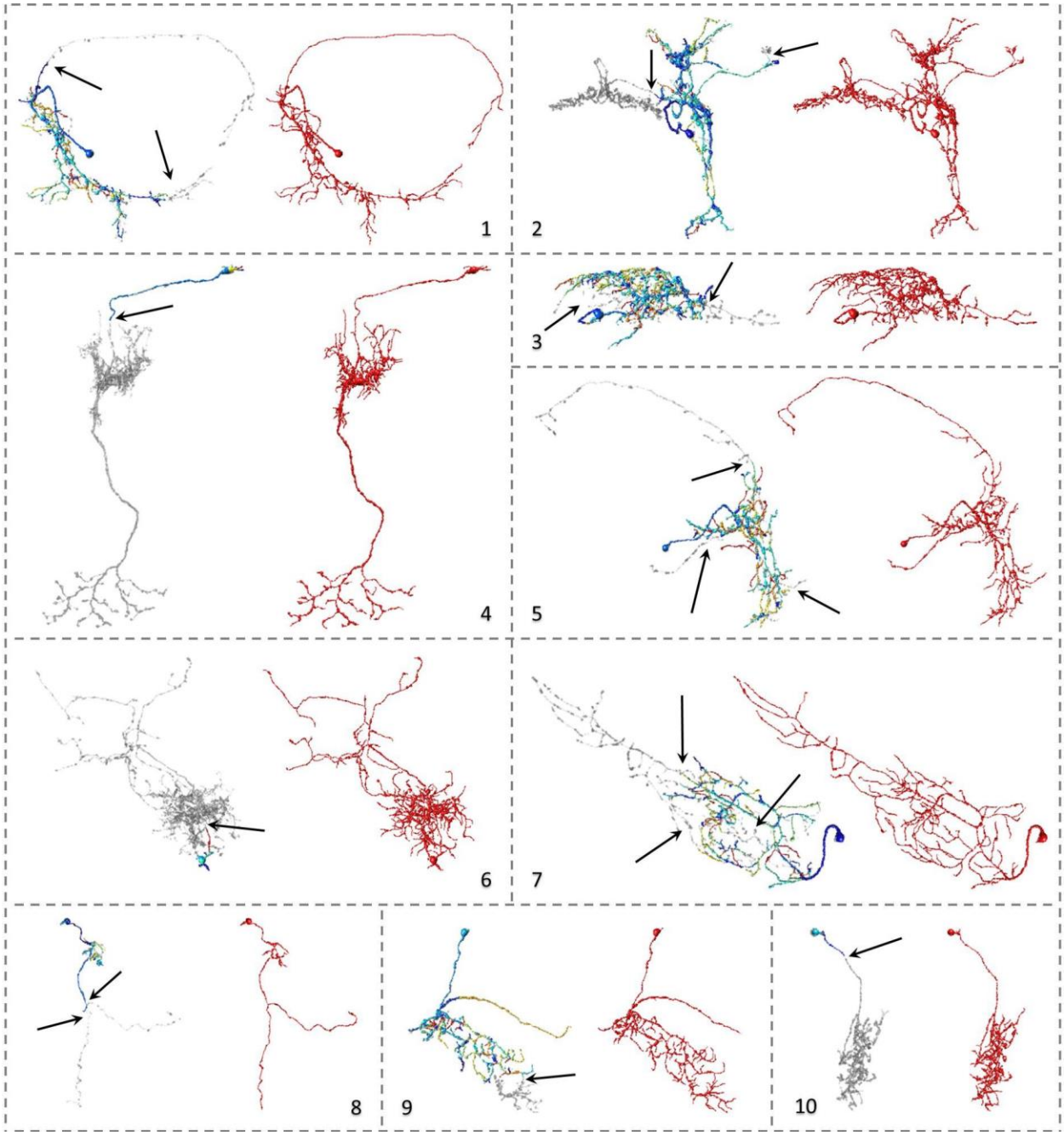

Figure 2. 4. Visualization of reconstructed neuron morphology of 10 selected examples. In each sub-figure, initial reconstruction generated by APP2 (colored skeletons) was overlapped on the original image (grey skeletons). The corresponding final reconstruction obtained by SmartTracing was shown in red skeletons on the right. The initial reconstructions were color coded by confidence scores (blue: more confident, red: less confident). The incomplete part of the reconstruction and the gap that caused the problem were highlighted by black arrows. The detailed measurements of these reconstructions were listed in Table 2. 1.

Table 2. 1. The running time of each procedure and the quantitative neuron morphology measurement of 10 selected example datasets. Visualization of the morphology of reconstructions and the original image of these examples were shown in Figure 2. 4.

ID	Running time (seconds)						Length		Bifurcation		Branch		Tip	
	T_{in}	T_s	T_m	T_t	T_p	T_{st}	R_{in}	R_{st}	R_{in}	R_{st}	R_{in}	R_{st}	R_{in}	R_{st}
1	10.4	254	0.19	12.7	110	12.7	3027	4686	69	74	141	153	72	79
2	10.6	456	0.22	17.9	185	15.1	4469	7557	112	180	228	367	116	187
3	11.1	474	0.23	12.1	89	14.6	4611	6163	145	159	293	325	149	167
4	9.2	310	0.17	7.4	58	15.9	483	5823	5	117	11	240	7	124
5	10.9	310	0.19	8.5	119	16.7	3992	5635	84	92	175	188	91	96
6	9.2	29	0.17	7.5	133	22.2	176	8298	4	174	9	359	6	186
7	9.3	249	0.16	7.9	120	19.2	4408	7016	74	98	151	198	77	101
8	9.3	61	0.17	11.6	69	9.9	545	1174	7	8	14	16	8	9
9	10.1	307	0.17	9.2	53	13.4	3021	4024	75	93	155	190	81	98
10	9.0	37	0.16	7.3	78	15.3	125	3494	2	76	5	159	3	83

T_{in}: generate initial reconstruction by APP2; T_s: compute confidence score; T_m: mRMR feature selection; T_t: SVM classifier training; T_p: searching foreground; T_{st}: generate final reconstruction; R_{in}: initial reconstruction; R_{st}: final reconstruction; Length unit: voxel.

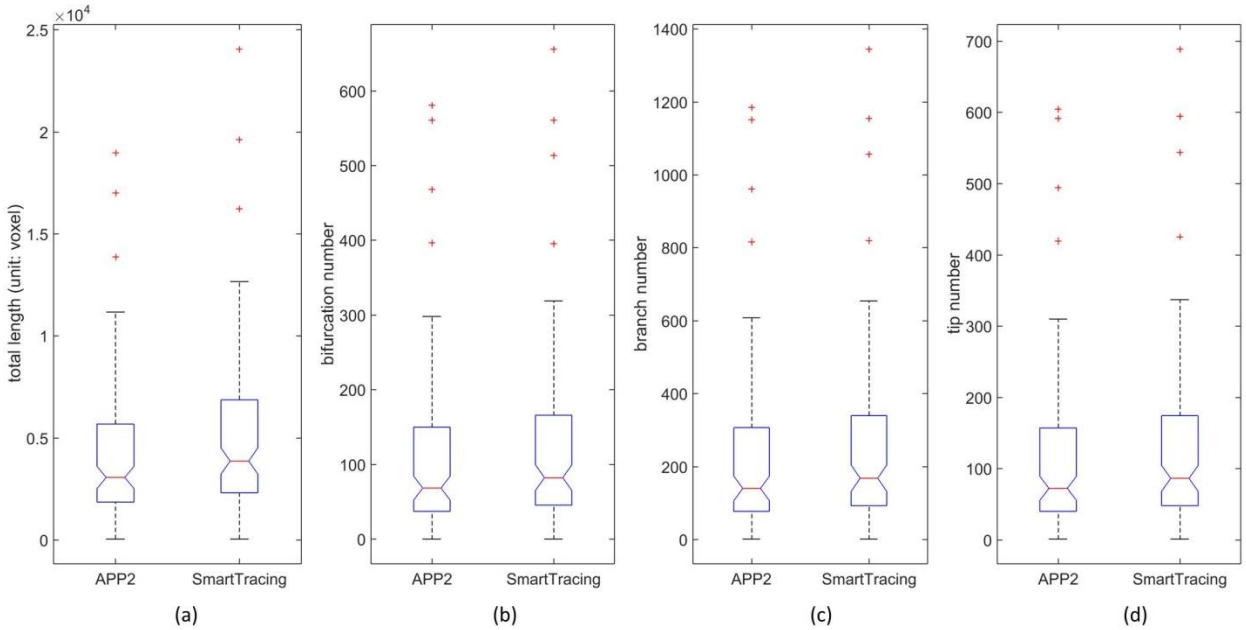

Figure 2. 5. Box plots of neuron morphology measurements of the 120 neuron reconstructions obtained.

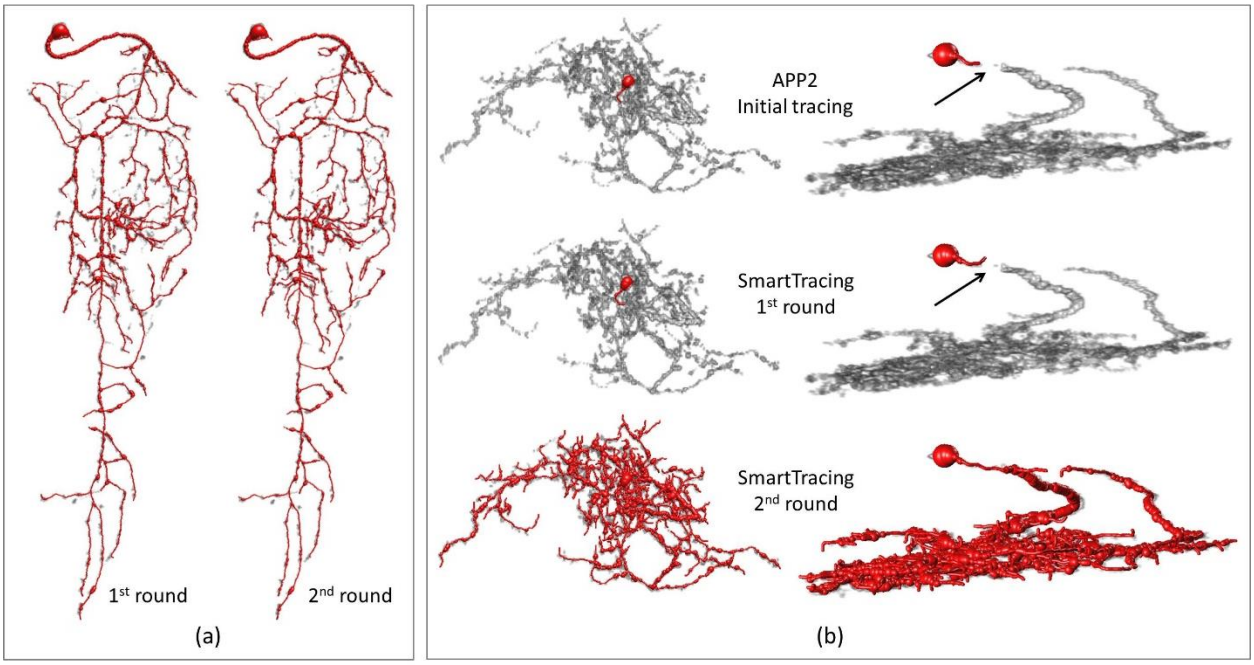

Figure 2. 6. Examples of performing SmartTracing iteratively. Reconstruction shown in red tube is overlapped on the original image shown in gray. (a) Reconstruction of the first and second round SmartTracing of case #7 shown in Figure 2. 4. (b) Reconstruction of the case that failed in the first round of SmartTracing but succeeds after two rounds shown in different angles. The gap that caused the failure in the first round is highlighted by arrows.

Notably, SmartTracing is able to run iteratively. The reconstruction generated from the previous round is used as the initial reconstruction for the next round. However, for the reconstruction that is relatively complete, further iteration will not change the result significantly (Figure 2. 6(a)) and is time-consuming. On the other hand, for the incorrect reconstruction, better training samples could be obtained based on the reconstruction from the previous iteration which may successively remedy the reconstruction. Thus we tried performing SmartTracing iteratively on the previously failed case. Intriguingly, it only took two rounds of SmartTracing to successfully filled the gap and obtain complete reconstruction (Figure 2. 6(b)). This is mainly because with the result from the first round, more training samples from the gap area were obtained to train the classifier so the gap can be filled in the second round.

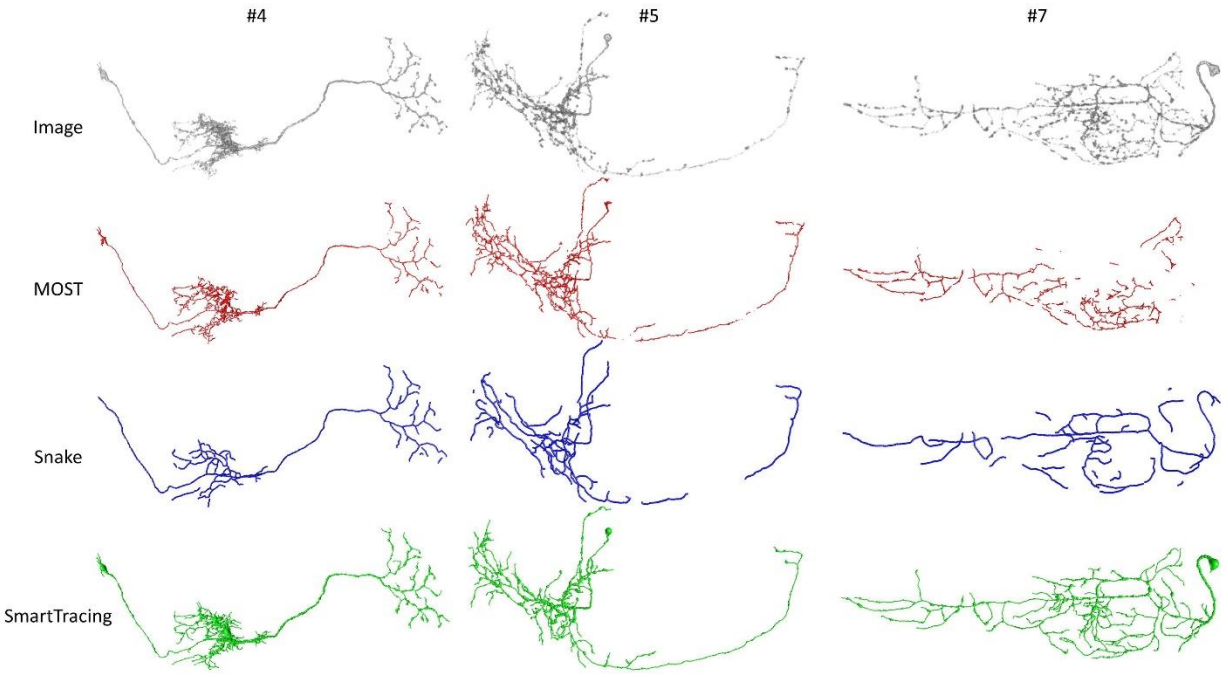

Figure 2. 7. Comparisons of the reconstructions generated by 3 different tracing algorithms using 3 testing images. Image ID is the same as Table 2. 1. The original images were shown in the top row followed by the reconstructions generated by MOST (red), Snake (blue), and SmartTracing (green).

We then compared the result generated by SmartTracing with other methods (Figure 2. 7). Specifically, the results generated by Micro-Optical Sectioning Tomography (MOST) ray-shooting tracing (Wu et al. 2014) and open-curve snake (Snake) tracing (Narayanaswamy et al. 2011; Wang et al. 2011) were compared. By visual inspection, the results generated by our proposed SmartTracing were more complete, more topologically correct, and better at reflecting the morphology of the neurons in original images than other tracing methods.

DISCUSSION

In our experiments, the proposed SmartTracing method improved the APP2 tracing and successfully reconstructed 120 *Drosophila* neurons from confocal images. In addition to filling the gaps between neuron segments, SmartTracing can also reduce over-traces due to image noise, inhomogeneous distribution of image intensity, and inappropriate tracing parameters. Essentially, SmartTracing is an adaptive and self-training image preprocessing procedure that segments the image into the foreground area containing neuron signals and the background voxels. The major novelty of SmartTracing lies in two aspects.

First, we proposed a likelihood measurement that serves as a confidence score to identify reliable regions in a neuron reconstruction. With this score, reliable portions of a neuron reconstruction generated by some existing neuron-tracing algorithms are identified, without human intervention, as training exemplars for learning based tracing method. On the other hand, the human proofreader can also benefit from the metric. By ranking the reconstructions by the confidence score, the human annotators are able to prioritize on the less reliable reconstructions, which increase the overall accuracy and saves time.

Second, from the training exemplars, the most characteristic wavelet features are automatically selected and used in a machine-learning framework to predict all image areas that

most probably contain neuron signal. Since the training samples and their most characterizing features are selected from each individual image, the whole process is automatically adaptive to different images and does not require prior knowledge of the object to identify. Potentially, the proposed machine learning and prediction framework can be extended to other image segmentation tasks and 3D object recognition systems such as neuron spine detection, cell segmentation, etc.

SmartTracing is applicable to most of the existing tracing algorithms. However, the performance and the outcome of SmartTracing are largely relied on the tracing algorithm applied. For instance, the cause of the only failed case among 120 tested images is that APP2 did not generate sufficient initial reconstruction due to the gap which results in a lack of training exemplars. One solution to this limitation is to run SmartTracing iteratively so better training samples can be acquired from the previous iteration. Also, we can take the merit of different tracing algorithms and use different algorithms in different steps to further improve the performance of the framework – e.g. use MOST algorithm to generate initial tracing for scoring and thus training since it is not sensitive to gaps and can capture more signals; then use APP2 to generate final tracing since it is robust, efficient, and optimal to generate tree shape topology of neurons.

Another limitation of SmartTracing is the relatively high computational complexity. At present, the top two time consuming procedures are the computation of confidence metric, which is proportional to the initial neuron reconstruction complexity, and the predictions of foreground voxels, which is proportional to the size of the neuron. The previously reported computation time is calculated based on a single CPU. With parallel computation framework, both steps can be speed up.

In recent years, a growing number of model-driven approaches have been proposed for automatic neuron reconstructions. To our best knowledge, SmartTracing is one of the earliest machine learning based methods for automatic neuron reconstruction. Different from the traditional learning based method, SmartTracing does not require the human input of training exemplars and can self-adapt to different types of neuroimage data. Additionally, the method can be applied to improve the performance of other existing tracing methods. As part of future work, the performance of SmartTracing will be further examined and improved by BigNeuron project. In the near future, we hope SmartTracing can significantly facilitate manual tracing and contribute to the neuron morphology reconstructions in large.

CHAPTER 3

NEURON STITCHER: FAST ASSEMBLING OF NEURON FRAGMENTS IN SERIAL 3D SECTIONS [2]

[2] Hanbo Chen, Daniel M. Iascone, Nuno Macarico da Costa, Ed S. Lein, Tianming Liu, Hanchuan Peng. 2016. NeuronStitcher: Fast Assembling of Neuron Fragments in Serial 3D Sections. *In submission*

ABSTRACT

Reconstructing neurons from 3D image-stacks of serial sections of thick brain tissue is a time-consuming step in high-throughput brain mapping projects. We developed NeuronStitcher, a software suite for stitching non-overlapping neuron fragments reconstructed in serial 3D image sections. This tool features an efficient automatic matching algorithm, severed neurite filters, and a user-friendly interface for result-proofreading. Intensive evaluations have quantitatively and qualitatively shown that NeuronStitcher is accurate, efficient, and robust toolkit for stitching fragments of neurons over multiple tissue sections. Here we use this tool to reconstruct large and complex human and mouse neurons.

INTRODUCTION

Digital reconstruction of neurons from very large three-dimensional (3D) brain images is crucial for modern neuroscience (Meijering 2010; Helmstaedter and Mitra 2012; Parekh and Ascoli 2013). Despite recent advances in neuron labeling, brain clearing, and high-resolution 3D tissue-imaging (Hama et al. 2011; Chung et al. 2013) to study mammalian brains, many neuroscientists still rely on physical sectioning of brains followed by imaging with confocal or two-photon microscopy. The resulting image data over many serial sections are then stacked and aligned individually to generate a complete image volume, from which neurons are reconstructed and quantified. Dendrites and axons that cross an imaged volume and were severed at the section boundaries then need to be stitched. This is a crucial step and a bottleneck for the proper reconstruction of the topology of the dendritic and axonal trees, which is particularly difficult given the density of local axonal arborization. It is extremely labor-intensive to stitch neuron segments manually over multiple sections (Oberlaender et al. 2007; Luzzati et al. 2011).

Automated methods can therefore provide a significant increase in the throughput of neuron reconstruction.

However, this is a non-trivial task for automatic algorithms as there could be missing tissue as well as distortions during sectioning, making stitching of neuronal segments across multiple sections much more challenging than stitching overlapping tiles within single sections (Preibisch et al. 2009; Bria and Iannello 2012). Moreover, unlike stitching serial 2D images from serial electron microscopy (EM) (Helmstaedter et al. 2011; Cardona et al. 2012), neurons imaged with confocal and two-photon microscopes are often sparsely distributed throughout the 3D image stacks, making it difficult to use other stitching tools such as TrakEM2 (Helmstaedter et al. 2011).

To address these challenges, we developed NeuronStitcher, a software package that automatically assembles complicated neuron fragments reconstructed from adjacent serial sections in real time. The merits of computing based on the neuron reconstruction rather than the raw image are in three-fold. (1) It requires less memory. Neuron reconstruction that is composed of sparsely connected vertices (tree graphs) is much smaller than raw images. (2) It is fast to compute. Intuitively, sections can be matched based on severed neurites. Severed neurites can be identified by searching for terminal vertices in reconstruction. (3) It is flexible and adaptable to different studies. Instead of working directly with images that are known to vary enormously due to different modalities or neuron labelling techniques, our stitching algorithm deals with the extracted reconstructions, which could be produced using different neuron reconstruction methods. In this way our method is more generalizable than image stitching methods.
In comparison with previous work (Hogrebe et al. 2011; Luzzati et al. 2011; Dercksen et al. 2014; Weber et al. 2014), NeuronStitcher used similar methods such as a triangle match

algorithm to match severed neurites on the sectioning plane based on their relative location and orientation. However, NeuronStitcher has four advantages over other methods. (1) NeuronStitcher includes a filter to eliminate noise resulting from terminal branches based on three criteria when selecting severed neurite candidates. Notably, the accuracy of reconstruction matching largely relies on the identification of severed neurites. Filtering noisy objects before analysis improves the matching accuracy and computational speed. (2) The performance of NeuronStitcher has been intensively and quantitatively evaluated with different types of data. In most previous works, the performance of automatic matching algorithm is usually evaluated by a few simple cases without quantification. In this chapter, our proposed algorithm has been quantitatively evaluated by more complicated cases. (3) Our method has an interactive interface which does not only allow visual evaluation of stitching results and live adjustments of matching parameters, but also enable manual correction of matching results. (4) Our method is readily available to other researchers. The software was implemented in C/C++ as a plugin of Vaa3D (Peng, Ruan, Long, et al. 2010; Peng et al. 2014), which is a publicly available open source platform with user-friendly interface for 3D+ image analysis and visualization (http://www.vaa3d.org).

MATCH, ALIGN, AND STITCH RECONSTRUCTION

The goal of NeuronStitcher is to first align and connect neuron fragments across sections and then infer a complete neuron reconstruction. In practice, the order of sections is usually known. The sections can be matched and aligned by shifting and rotating reconstructions in parallel to the sectioning plane. For a set of input neuron fragments, the task can be defined by three major steps: (1) identify severed neurites candidates which will be matched and connected later on; (2) match severed neurites and align reconstructions from different sections; (3) connect

matched neurites. The whole pipeline is outlined in blue in Figure 3. 1. Each step is elaborated in this section.

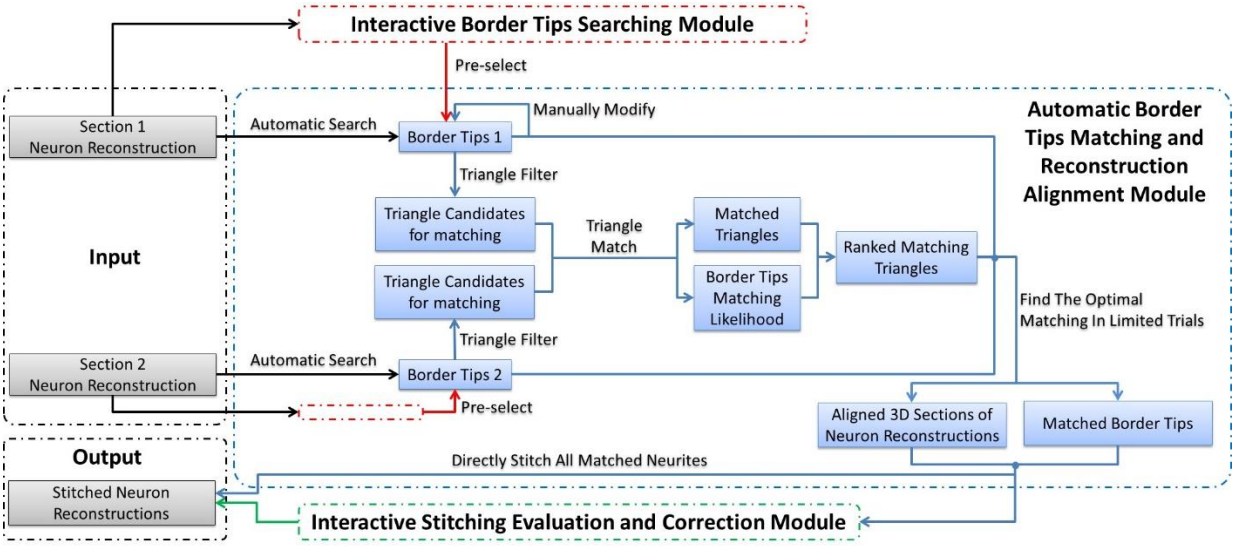

Figure 3. 1. Software architecture of NeuronStitcher. The software takes a set of neuron-reconstruction fragments as input and outputs the stitched neuron reconstruction. It includes an automatic module to match, align, and stitch neuron reconstructions, as well as two interactive operation modules which allow users to visually inspect and manually correct results. The computational pipeline of automatically stitching module is outlined in blue.

Neuron Reconstruction

Neuron reconstruction typically encodes the morphology of the neuron using a tree structure. Usually, connected vertices are taken as basic units in a reconstruction file. For each vertex, its coordinate, parent vertex, and radius are recorded. In previous studies, many automatic and semiautomatic tools have been proposed to reconstruct neuron morphology from microscopy images. One may refer to the review paper by Duncan and Ascoli (Donohue and Ascoli 2011) for a survey of neuron reconstruction methods. In this chapter, the initial reconstructions are obtained based on the built-in tools of publicly available Vaa3D software (Peng, Ruan, Long, et al. 2010; Peng et al. 2014). Nevertheless, our NeuronStitcher tool is generally applicable to neuron reconstructions produced by other tools.

Notably, since the image-resolution in the depth direction (z-axis) is usually lower than those of plane directions (x-axis and y-axis), we rescale the reconstructed neurite-fragments to isotropic "resolution" before analysis.

Identify Border Tips

We defined the severed neurites at the section plane as border tips. Intuitively, the terminal branches identified near the section plane can be taken as border tips. However, there are also other sources of terminal branches near the section plane and some of them can be excluded by a simple method to increase accuracy and efficiency of the matching algorithm. Based on our observation, 3 types of tips that should be excluded were identified (Figure 3. 2) – (1) reconstruction gaps, (2) spine, and (3) fragments of background noise. We explained those tips with details and introduced our strategy to automatically exclude them below. This border tips searching framework was embedded in the automatic matching and alignment module.

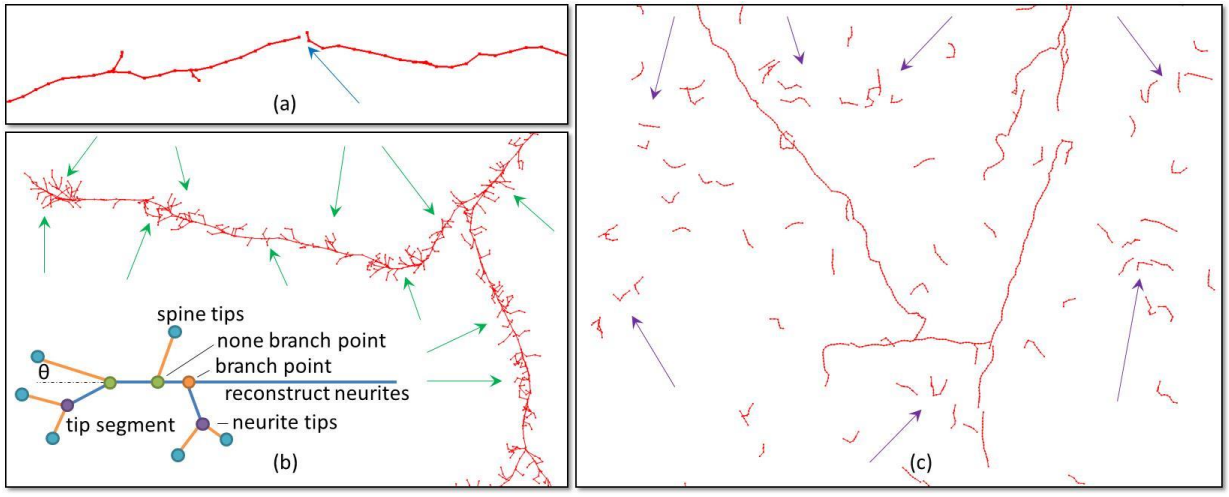

Figure 3. 2. Examples of 3 types of tips that should not be considered as border tips. (a) Gap in the reconstruction, highlighted by the blue arrow. (b) Spine tips, highlighted by green arrows. (c) Fragments of background noise, highlighted by purple arrows.

Reconstruction gaps

Some reconstruction algorithms generate a gap between segments as shown in (Figure 3. 2(a)). Usually, the gap can be erased and the segments are connected after post-processing to build complete neuron tree structure. However, if the gap was close to the section plane, the introduced neurite tips can be identified as border tips and be taken as candidates to be matched and connected with the border tips from adjacent sections.

The tips introduced by reconstruction gaps are usually generated in pairs, where they are close but not connected to each other. Thus, to filter them, a gap size threshold is defined such that, if a set of border tips are 1) close to each other (distance < gap threshold), and 2) not connected (no path exists between them) in current reconstruction, they will be identified as a reconstruction gap and excluded from further analysis.

Spine tips

Some of the neuron reconstruction algorithms also trace spine structures during reconstruction (Figure 3. 2(b)). If we take the spine structures close to section plane as border tips, they will result in a lot of noise. We therefore need an efficient solution to eliminate the tips from spine structures and find the tips of the severed neurites for matching. To better explain our solution, some terminology is defined below.

Spine tip: Tip on reconstructed spine structure (blue dots in Figure 3. 2(b)).

Tip segment: The section of the reconstruction from the tip to its nearest fork (orange lines in Figure 3. 2(b)).

Tip segment turning angle: The angle between a tip segment and its parent segment (θ in Figure 3. 2 (b)).

Neurite tip: The tips of the neurite that could be taken as border tips for matching (purple dots in Figure 3. 2 (b)).

Reconstructed spines are a relatively thin, short segments that are perpendicular to neurites. A tip is defined as a *spine tip* if it meets three criteria: (1) tip segment is short, (2) turning angle is relatively large, and (3) radius is small. For each tip point, its identity as a *neurite tip* or *spine tip* is determined based on a decision tree shown in Figure 3. 3. In addition to the remaining *neurite tips*, the tips that are newly generated by removing the spine segment are defined as neurite tips (purple dots in Figure 3. 2 (b)).

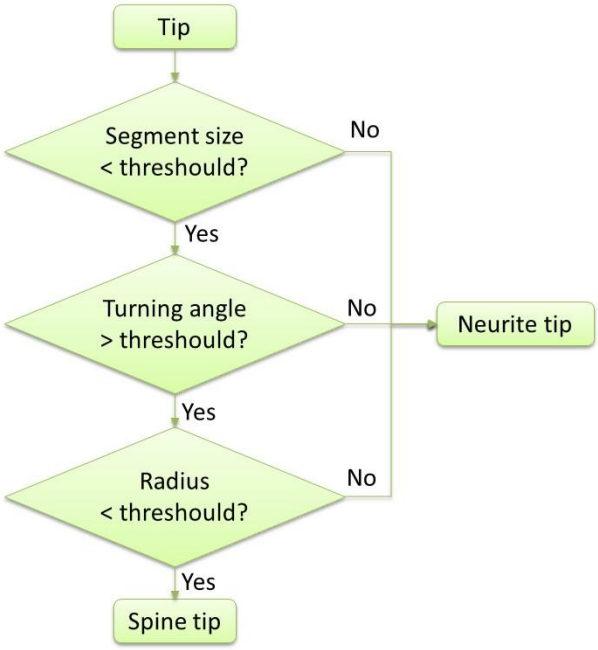

Figure 3. 3. Decision tree to determine whether a tip is *spine tip* or *neurite tip*.

Fragments of background noise

Some reconstruction algorithms do not eliminate background noise and thus generate small noise fragments (highlighted by arrows in Figure 3. 2 (c)). Intuitively, such fragments can be eliminated by looking at the size of each reconstruction fragment and ignoring the tips of small fragments that should not be considered to be border tips.

Nevertheless, because reconstruction quality and character vary between datasets, image modality, and reconstruction method, it is hard to guarantee that all the border tips that are automatically identified are true border tips. Further, the algorithm can result in a false positive connection when falsely detected border tip gets matched. With this in mind, we included an interactive border tips searching module to take advantage of user knowledge in the identification of border tips. In this module, the automatically identified border tips are shown together with the raw image and reconstructions. The user can then visually screen through the results and accept, reject, or manually add border tips.

Match Border Tips and Estimate Alignment

It is intuitive to match adjacent sections by matching border tips such that a correct match will allow most severed neurites to be reasonably connected. To achieve this, two factors can be taken into consideration: 1) Geodesic location of border tips – the neighborhood relation of the paired border tips should match, and 2) The orientation of the branch connected to border tips – two branches should not be connected when there is a sharp angle between them. In the study of computer vision, affine-invariant features based on triangle shapes have been widely applied to match objects in images and graphs (Shen et al. 1999; Duchenne et al. 2011). Because our matching object requires rotation and shifting to be matched and the orientation of the branch connected to border tips changes during rotation, we adopted ideas from previous work and proposed a set of rotation invariant features to describe neighborhood and branch orientation based on triangles. Based on a matched triangle, the matching probability between border tips is then defined. By taking matched border tip pairs with the highest probability as an initial match, alignment and matching can be estimated and refined iteratively for an optimal alignment. In this section, we will introduce our algorithm to solve the match and alignment problem in two

adjacent sections. A and B represent the set of border tips between these two sections accordingly. Without loss of generality, we assume that A will be fixed and B will be moved and aligned to A.

Triangle Match

For any combination of 3 border tips, a triangle can be constructed (for illustration and symbols notation, see Figure 3. 4). For each triangle, its edges and vertices are sorted by the length of edges such that $\|e_{1,2}\| \leq \|e_{2,3}\| \leq \|e_{1,3}\|$ where e is the edge of the triangle. The sorted length of its edges is then applied to describe the geodesic shape of a triangle: $D=(d_{1,2}, d_{2,3}, d_{1,3})$, $d_{i,j}=\|e_{i,j}\|$. To quantify the orientation of branches, a local coordinate system is defined for each vertex such that the axis from triangle center to the vertex is the x-axis and the norm direction of the triangle plane is the z-axis (Figure 3. 4). The orientation vector of the branch connected to the border tip is then transformed into this local coordinate system. Two triangles Δ_I, Δ_J and the corresponding vertices could be matched when the L_1 distance between their geodesic shape vector D and the angle between branch orientation vectors of corresponding vertices are smaller than threshold defined:

$$\Delta_I \cong \Delta_J, v_{I1} = v_{J1}, v_{I2} = v_{J2}, v_{I3} = v_{J3} \tag{3.1}$$

if and only if:

$$|D_I - D_J| < distance\ threshold \tag{3.2}$$

$$angle(\overrightarrow{T_{Ik}}, \overrightarrow{T_{Jk}}) < angular\ threshould\ (k = 1,2,3) \tag{3.3}$$

Notably, since the angle is defined in the local coordinate of each vertex, these proposed features are rotation invariant. Thus, triangles can be matched directly based on these features without alignment.

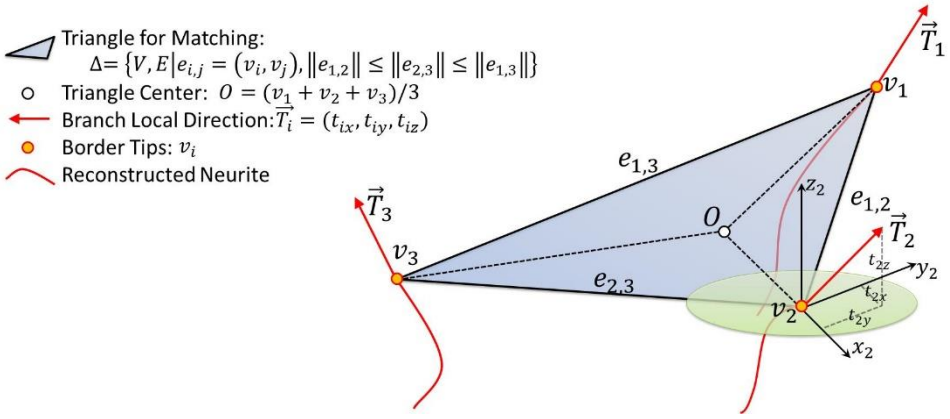

Figure 3. 4. Illustration of the rotation invariant features of the triangle to match.

Border Tips Matching Probability

Based on the triangle matching previously proposed, a global search can be performed to pair-wisely match all triangles formed by border tips. Then, for each pair of border tips (v_a, v_b), the number of times they get matched is accumulated and their matching probability is defined as:

$$P_{a,b} = 2N_{a,b} \Big/ \left(\sum_{k\in A} N_{k,b} + \sum_{k\in B} N_{a,k} \right) \tag{3.4}$$

For each pair of matched triangles $(\Delta_a, \Delta_b), a \subset A, b \subset B$, the matching likelihood between them is computed by summing the matching probability between corresponding vertices. The pair of matched triangles with the highest matching likelihood can be taken as the initial match to estimate alignment.

However, the number of triangles grows cubically with the number of border tips. If the number of border tips identified on the section plane of two adjacent sections is $|A|$ and $|B|$, the computational complexity for matching is $O(|A|^3 \times |B|^3)$. This can be extremely time consuming when A and B are large. To increase computational efficiency, we found that it is unnecessary to compare all triangles. Specifically, for the purpose of matching corresponding vertices, the

matching based on the triangles with anisotropic shape was more reliable than equilateral triangles. Moreover, large triangles offer more global view than small triangles. Based on these observations, we propose a triangle priority score in which only the top triangles with the highest scores are applied to estimating border tips matching probability. Given a triangle with geodesic shape feature: $D=(d_{1,2}, d_{2,3}, d_{1,3})$, its priority score is simply defined as the difference between the lengths of its longest edge and the shortest edge:

$$Score = d_{1,3} - d_{1,2} \tag{3.5}$$

We show in the result section that only matching a few hundred triangles with the highest scores is sufficient to infer accurate results while the computational time required is reduced from minutes to seconds.

Estimate Alignment

Because adjacent sections are usually imaged separately from mounted sections, each section can be aligned by shifting it in all three directions and rotating it in parallel to the section plane (4 degrees of freedom (4DOF). While there could be other types of movement and distortions between sections, our results on existing data suggested that the 4DOF alignment is sufficiently accurate to generate reasonable results. Such alignment can be easily estimated based on the matched border tips between sections in the following two steps. 1st) Shifting movement will be estimated such that the center of matched border tips will be the same. 2nd) Rotation around the center will be estimated to minimize the distance between matched border tips.

The pair of matched triangles with the highest matching likelihood is taken as the initial match. After transformation, the border tips that are close to each other and have similar branch directions are matched. Based on updated matching border tips, a new transformation can be estimated, and this match-transform procedure is iteratively performed until no more border tips

can be matched. Notably, selecting the correct pair of matched triangles to start is critical to acquire the correct matching and alignment. To make the framework robust, different initial combinations are examined and the alignment that has the most matching border tips is taken as the final result.

Stitch Border Tips

After affine transformation, the matched border tips are connected to construct a complete neuron. Because slicing causes distortion which leads to systematic errors in imaging and reconstruction procedures, a gap between matching border tips after transformation might be created that results in sharp angles between connections. To reduce the presence of these angles, we propose a stitching framework to adaptively adjust border tip segments to smooth out the gap when separated neurites are connected. The border tip segments are defined as the segment from border tips to the nearest branch point (shortest path from purple dot to orange dot in Figure 3. 5(b)). Denote $\boldsymbol{a}_1$ as the i^{th} point on the tip segment of a border tip of section A (i=1…N), $\boldsymbol{a}_1$ is the border tip, and $\boldsymbol{a}_N$ is the branch point. To stitch border tips $\boldsymbol{a}_1$ and $\boldsymbol{b}_1$, the shifting vector of $\boldsymbol{a}_i$ denoted by $\boldsymbol{va}_i$ is calculated as following:

$$\boldsymbol{Va} = \frac{N_A(\boldsymbol{a}_1 - \boldsymbol{b}_1)}{N_A + N_B} \tag{3.6}$$

$$\boldsymbol{va}_i = \frac{(N_A - i)}{N_A}\boldsymbol{Va} \tag{3.7}$$

The shifting vector of b_i is calculated in a similar way. As illustrated in Figure 3. 5, the matched border tips are moved to a new location where they are relatively close to each other while the successive points are moved by distances reduced successively until the branch point is reached. The distance to move is scaled based on the size of the tip segment such that more shifting is taken for larger segment. Notably, if there is a spine tip segment connected to a border tip

segment to stitch, the spine tip segment is moved by the shifting vector of its root (green dots in Figure 3. 5).

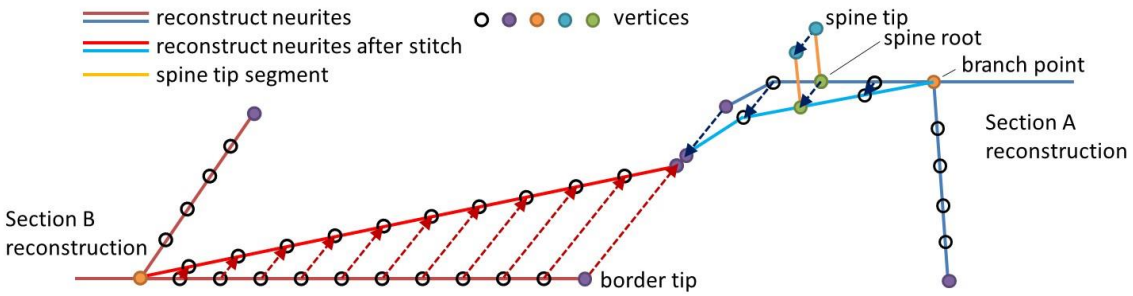

Figure 3. 5. Illustration of adjusting branches to stitch matched border tips.

INTERACTIVE USER INTERFACE

Neuron reconstruction quality will affect the performance of NeuronStitcher and the parameter selection may vary between different data. To broaden the utility of NeuronStitcher to work with a variety of different data acquisition processes, we designed an interactive interface to (1) allow visual evaluation of stitching results and live adjustments of matching parameters; and (2) enable manual correction of incorrect matching results. The software was implemented in C/C++ as a plugin of Vaa3D (Peng, Ruan, Long, et al. 2010; Peng et al. 2014), which is a publicly available open source platform with a user-friendly interface for 3D+ image analysis and visualization (http://www.vaa3d.org). In the following sections, we will introduce how to use the tool based on 5 scenarios. Each operation is indexed by the scenario's ID and the step number such that A-2 means step 2 of scenario A.

Stitch Reconstructions

In this section, we show the interactive user interface of NeuronStitcher and illustrate how to use NeuronStitcher to stitch adjacent sections. This section covers stitching neuron traces in three steps: A. Automatically match and align reconstructions, B. Visually check and stitch

matched reconstructions, and C. Manually correct matching result. We then use the protocol to stitch adjacent sections.

A. Automatically match and align reconstructions (Figure 3. 6)

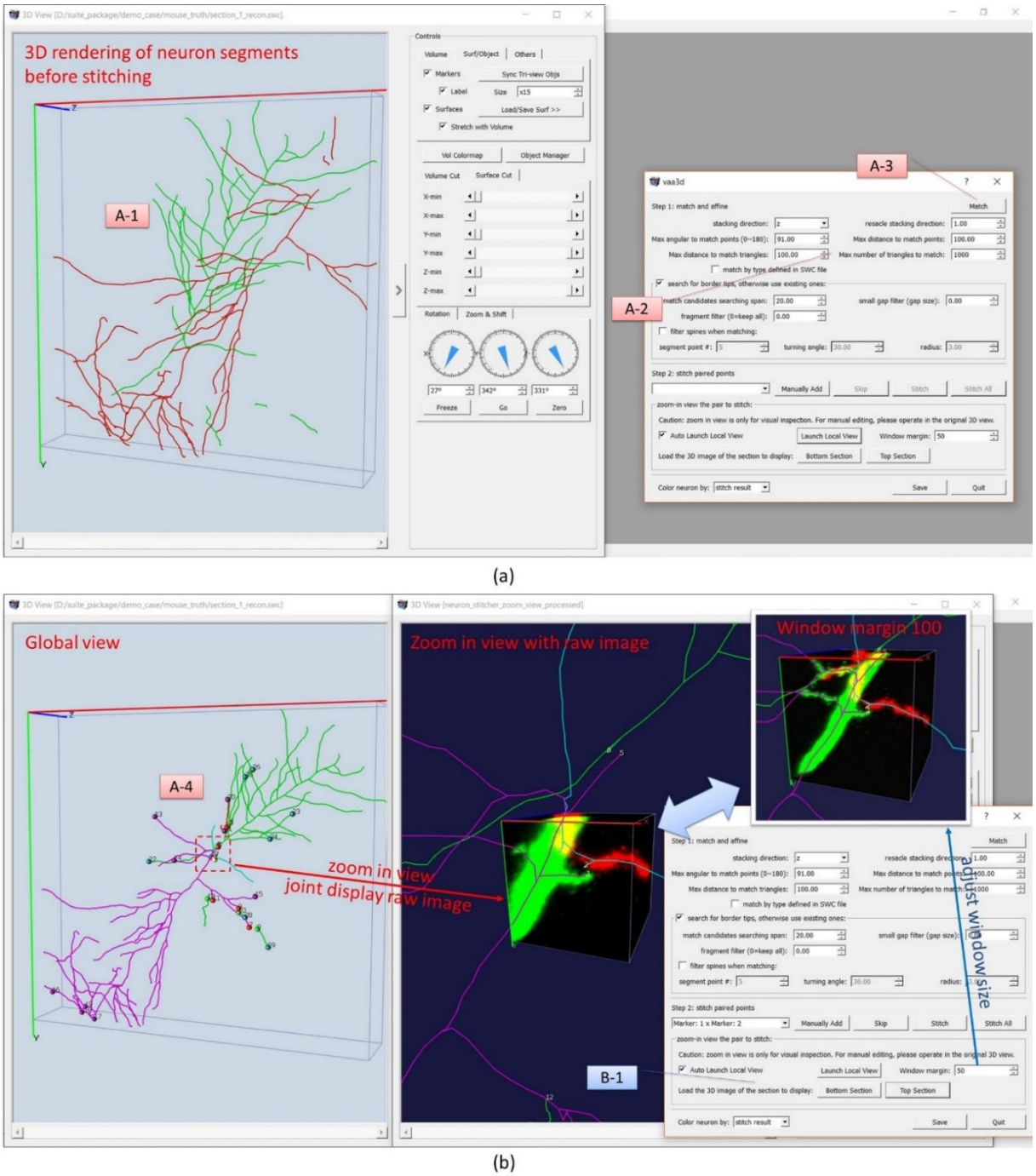

Figure 3. 6. Illustration of automatically matched and aligned reconstructions.

A-1: Load the reconstructions to be stitched in the same 3D view in Vaa3D. Make sure the section on the bottom was loaded first. Then launch the NeuronStitcher: Plug-in->neuron_stitch->live_stitch_neuron_SWC

A-2: Adjust the parameters in the pop-up window accordingly.

A-3: Click "Match" button. Then the program will search for border tips, align reconstructions, and match border tips automatically.

A-4: Check the alignment and matching result. The border tips identified will be shown in bubbles. Matched border tips will be in green/red colors while unmatched ones will be in dark green/magenta color. If the results are not good, adjust the parameters and repeat A-2 and A-3.

B. Visually check and stitch matched reconstructions (Figure 3. 7)

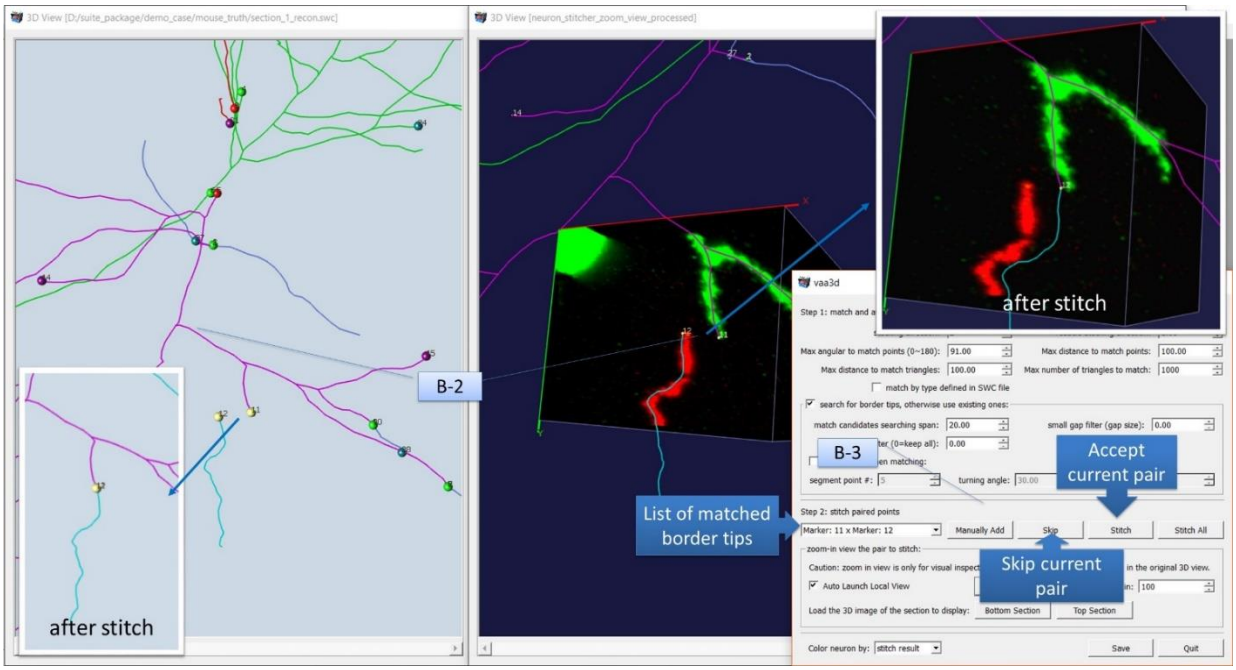

Figure 3. 7. Illustration of visual check and stitch matched reconstructions.

B-1: A zoom in window that focuses on the pair of matched border tips selected will pop up by default. Clicking the "Bottom Section" or "Top Section" buttons loads the raw images of each neuron fragment for joint display in the zoom in window (volumes are aligned into the same

space and colored in red/green for the bottom/top section accordingly). Change "window margin" to adjust the size of zoom in view window. The zoom in window updates after clicking "Launch Local View" button or after changing the selected matched border tips (when "Auto Launch Local View" is checked).

B-2: Visually check the pair of matched border tips selected. The selected border tips are shown in yellow color and the branch connected to it is highlighted in azure/magenta colors accordingly.

B-3: Click the "Stitch" button if the match is reasonable, the "Skip" button if not sure, or follow the steps in C-4 to reject and break the match if it is a mismatch. After stitching, the program jumps to the next pair of matched border tips automatically.

C. Manually correct matching result (Figure 3. 8)

C-1: Identify the pair of border tips that needs to be corrected. If there are no border tips identified on the neurite you would like to stitch, right click on the neurite and select "create marker from the nearest neuron node" to define one.

C-2: Click the "Manually Add" button. Then a "Match Markers" dialog will pop up. On the left of the pop-up dialog is a list of matched pairs of border tips.

C-3: To manually match two border tips, first select the ID of the border tips we are going to match. Then click "Match this pair of neurons" button and the matched pair will then be added to the list on the left.

C-4: To manually break a matched pair, first select the pair from the list on left. Then click "Free selected matching pair" button. The pair will then be removed from the list and the markers will be added to "Available Markers".

C-5: Click the “Done” button after the finish. The list of matched border tips will then be updated.

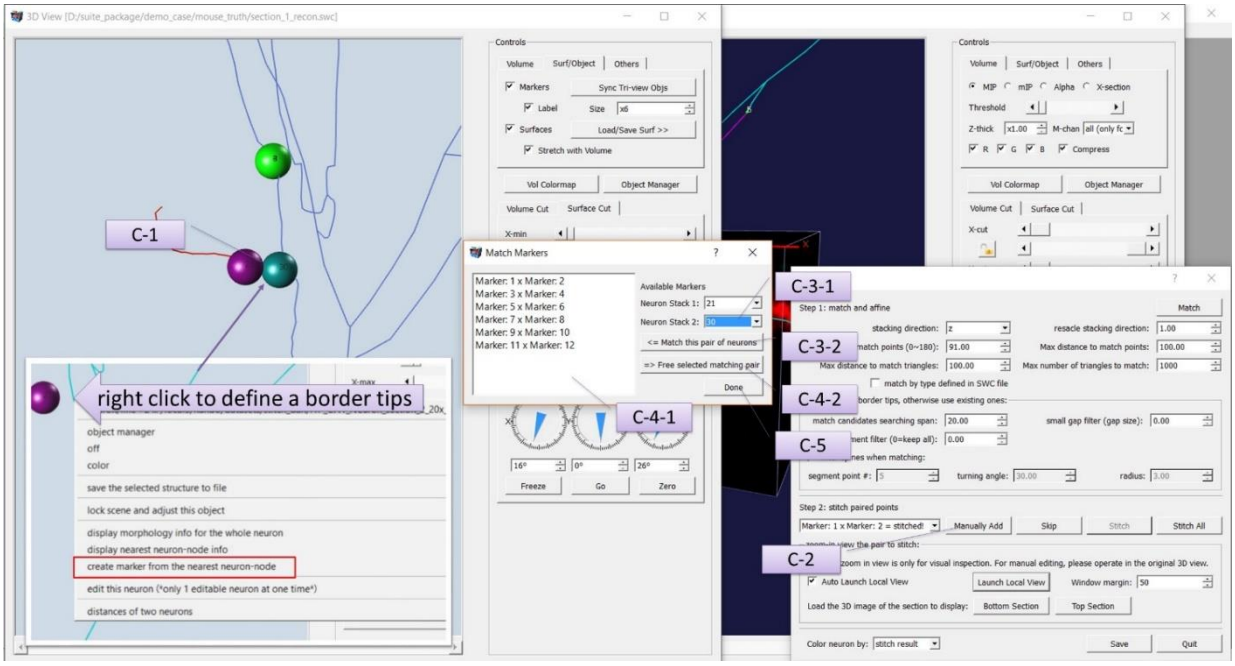

Figure 3. 8. Illustration of manually corrected matching result.

Select Border Tips

D. Select border tips (Figure 3. 9)

D-1: Load the image of the neuron tissue section to search for border tips. (Note: Loading 3D image is only for the purpose of visual inspection.)

D-2: Launch 3D view of the image by pressing ctrl+v. Load the corresponding reconstruction of neuron fragments in this section by dragging the SWC file into the 3D view.

D-3: Launch the border tips searching tool: Plug-in->neuron_stitch->find_border_tips_SWC_image

D-4: Adjust related parameters and then click the “Search” button to automatically search for border tips. User can also manually define border tips by following D-6.

D-5: The automatically found border tips will be shown as bubbles (called Markers in Vaa3D). Visually inspect the border tips identified one by one by following the instructions in E. Accept or reject the border tips accordingly. The program will automatically jump to the next border tip after acceptance or rejection.

D-6: To add a border tip, right click on the corresponding location in 3D View and define a marker there. Then click the "Update" button in the dialog of the tool.

D-7: Click the "Save" button to save all the results. The accepted border tips will be saved in a single file for future usage.

E. Visually inspect border tips (Figure 3. 9)

Border tips will be shown as bubbles (called markers in Vaa3D). In 3D view, blue bubbles are the uncertain border tips that have not been inspected yet, green bubbles are the correct border tips that have been accepted, red bubbles are the wrong border tips that have been rejected, and the magenta bubble is the border tip under inspection (Figure 3. 9).

E-1: Global 3D view. In this view, users can inspect the global location and spatial distribution of border tips. Missing border tips can also be added here (D-6).

E-2: Local 3D view. In this view, users can inspect the detailed characters of the selected border tip in a zoom in view with the focus on the border tip. Only a local window of the 3D image will be shown in this view to allow high-resolution visualization. The size of the window is controlled by the "View Size" parameter in the tool dialog.

E-3: Slice view. The program will automatically focus on the selected border tip in this view. The neighbors of the border tip will be highlighted by dashed line squares. In this view, users can inspect the border tip through image slices.

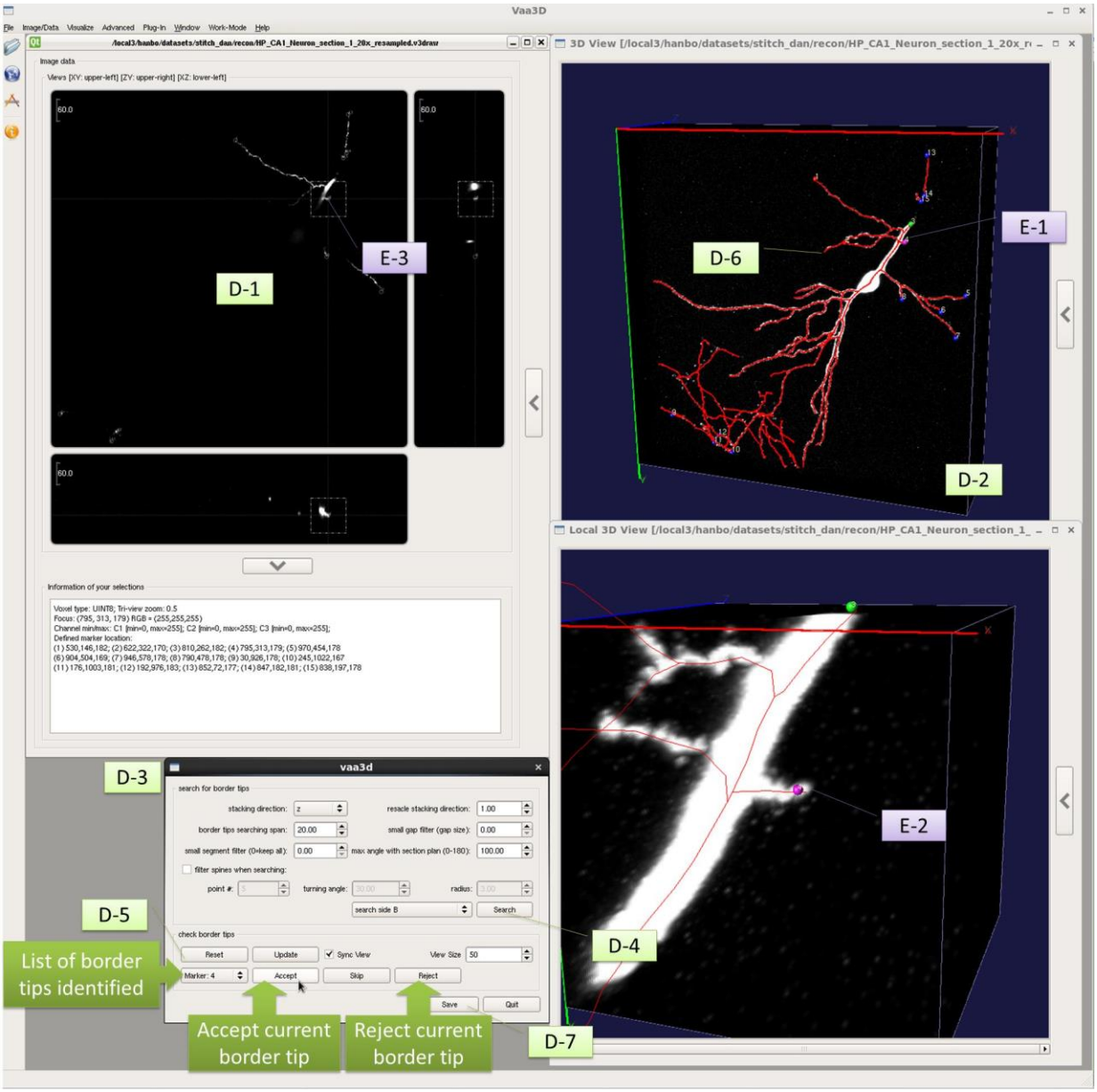

Figure 3. 9. Illustration of visual inspection and semi-automatic selection of border tips.

RESULTS

To comprehensively evaluate the performance of NeuronStitcher, we performed tests on three types of data – 1) ground-truth data, 2) real data, and 3) simulated data. The results of each fold are shown in following sections accordingly.

Validation on Ground Truth Data

We evaluated the accuracy of NeuronStitcher using carefully generated "ground truth" reconstructions from a piece of mouse brain tissue containing a labeled pyramidal neuron within the hippocampal CA1 region. This sample was first imaged and the neuron was thereafter semi-automatically reconstructed in 3D by Vaa3D and manually corrected by an expert as the ground truth reconstruction (Figure 3. 10(a), x, y, z dimensions were 602 μm, 271 μm, 274 μm, respectively). Then, we evenly sliced this sample into 3 serial sections in z direction, each of which was imaged. The reconstructions of neuron fragments from all such individual sections were generated by an expert with a similar approach and then stitched together using NeuronStitcher (Figure 3. 10(b-c)).

Using the automatic matching module, 6 pairs of matched border tips were identified between section #1 and #2 (Figure 3. 10(d)) and 2 pairs of matched border tips were identified between section #2 and #3 (Figure 3. 10(e)). A careful comparison of the ground truth reconstruction to the stitched reconstruction showed that 98% bifurcations of the 3D reconstructed, tree-like neuron morphology in the ground truth had their correspondence in the stitched reconstruction, and the minor amount (2%) of missing correspondence occurred at the section interfaces and was due to the sectioning process. Notably, the thinner 200 μm tissue sections reduced the signal loss resulting from light scattering from imaging through deep tissues. As a result, some deep neurites missing from the original reconstruction were captured after reimaging the 200 μm tissue sections (highlighted by yellow circles in Figure 3. 10(f)).

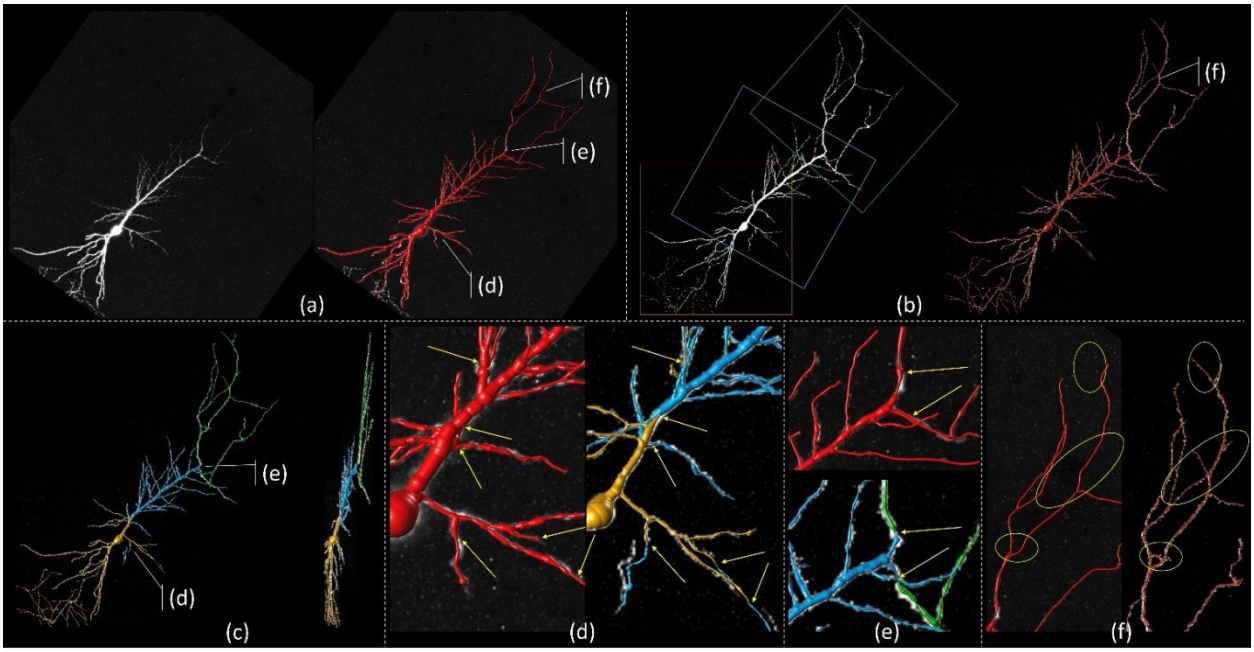

Figure 3. 10. Visual comparison between the reconstruction from the tissue before sectioning and the stitched reconstruction from sectioned tissues. (a) Maximum projection of 3D image acquired from complete tissue (left) and the corresponding reconstruction (right). The image has been rotated for better comparison with the stitching result. (b) Automatically aligned and stitched reconstructions from 3 successive sectioned tissues (right). The images of tissue sections were also aligned based on the stitching result and the section boundaries are highlighted by colored boxes accordingly (left). (c) Stitched reconstructions color-coded by sections (yellow: #1, blue: #2, green: #3) from different view angles. (d)-(f) Zoomed in view of regions shown in (a)-(c). The ground truth reconstruction is shown on the top/left of each subfigure. The stitched reconstruction is shown on the bottom/right of each subfigure. The matched and stitched border tips and their corresponding locations on original reconstruction are highlighted by yellow arrows.

Large Scale Neuron Image in Mammalian Brain

We used three sets of large-scale microscopy images obtained from mouse or human brains and their corresponding neuron reconstructions to test the performance of our neuron stitching framework (Table 3. 1). Dataset 1 was obtained from mouse brain V1 area and contains 11 adjacent sections in which the neurites of two neurons were densely twisted (Figure 3. 11). Dataset 2 contains a single mouse V1 neuron imaged in 4 adjacent sections. The reconstructions

in dataset 2 were automatically performed using the all-path-pruning 2 (APP2) algorithm (Xiao and Peng 2013) and spine segments were also reconstructed (Figure 3. 12). Dataset 3 contains 2 neurons from a human brain tissue imaged by bright field microscopy.

Table 3. 1. Information of data applied for stitching test cases.

ID	Species	Data Description	Imaging Method	# of Sections	x,y,z Resolution (μm)	Reconstruction Process
1	Mouse	Two adjacent neurons in V1.	Confocal	11	0.14,0.14,0.28	Neuron Crawler(Zhou et al. 2015), APP2(Xiao and Peng 2013), Manual Correction
2	Mouse	Single neuron in V1, border of layer 3 and 4.	Confocal	4	0.14,0.14,0.28	Neuron Crawler(Zhou et al. 2015), APP2(Xiao and Peng 2013)
3	Human	Two biocytin filled neurons.	Bright field	4	0.11,0.11,0.28	Adaptive Enhancement(Zhou et al. 2014), Neuron Crawler(Zhou et al. 2015), APP2(Xiao and Peng 2013)

We stitched each pair of adjacent sections using NeuronStitcher. After loading the reconstruction, we performed automatic matching and alignment. Based on visual inspections, we adjusted the parameters to obtain satisfactory matching results. In total, 16 pairs of sections were stitched. 411 pairs of border tips were automatically matched. After automatic matching, an expert manually corrected the errors by using our interactive proof-reading module when necessary. Among automatically matched border tips, 356 (86.6%) were accepted by the expert; and other 59 pairs of border tips were manually matched (Table 3. 2). NeuronStitcher typically finished the computation within seconds and the memory required for computation is less than 100Mb. The time to visually check and adjust the results depended on the complexity of the reconstruction. For the datasets here, the average time for stitching (including both automated computation and manual fine-tuning of the result) an adjacent pair of serial sections was 13’08”

(median: 9’41”, minimum: 0’13”, and maximum: 36’31”) (Table 3. 2). The final results are visualized with each section in different colors in Figure 3. 11-13.

Table 3. 2. Stitching results between sections based on the live stitching module: labor time is the time that experts took to adjust parameters, visually check matching and alignment results, and manually adjust matching results.

Data ID	Section ID		Border Tips Identified		Automatic Matched Pairs	Labor Time	Accepted Pairs	Rejected Pairs	Manually Matched Pairs
	A	B	A	B					
1	1	2	3	3	3	0'13"	3	0	0
1	2	3	14	15	11	2'20"	8	3	1
1	3	4	33	55	26	7'	23	3	5
1	4	5	81	47	41	31'50"	36	5	5
1	5	6	75	71	53	31'23"	45	8	6
1	6	7	72	71	43	22'47"	33	10	9
1	7	8	64	95	45	36'31"	36	9	5
1	8	9	39	34	27	14'47"	22	5	11
1	9	10	25	33	23	6'03"	20	3	4
1	10	11	23	23	19	3'09"	19	0	1
2	1	2	10	29	8	4'00"	6	2	2
2	2	3	45	85	22	11'45"	20	2	4
2	3	4	59	82	21	14'07	19	2	1
3	1	2	17	43	13	4'00"	11	2	2
3	2	3	44	69	23	7'36"	22	1	2
3	3	4	85	60	33	12'44"	33	0	1

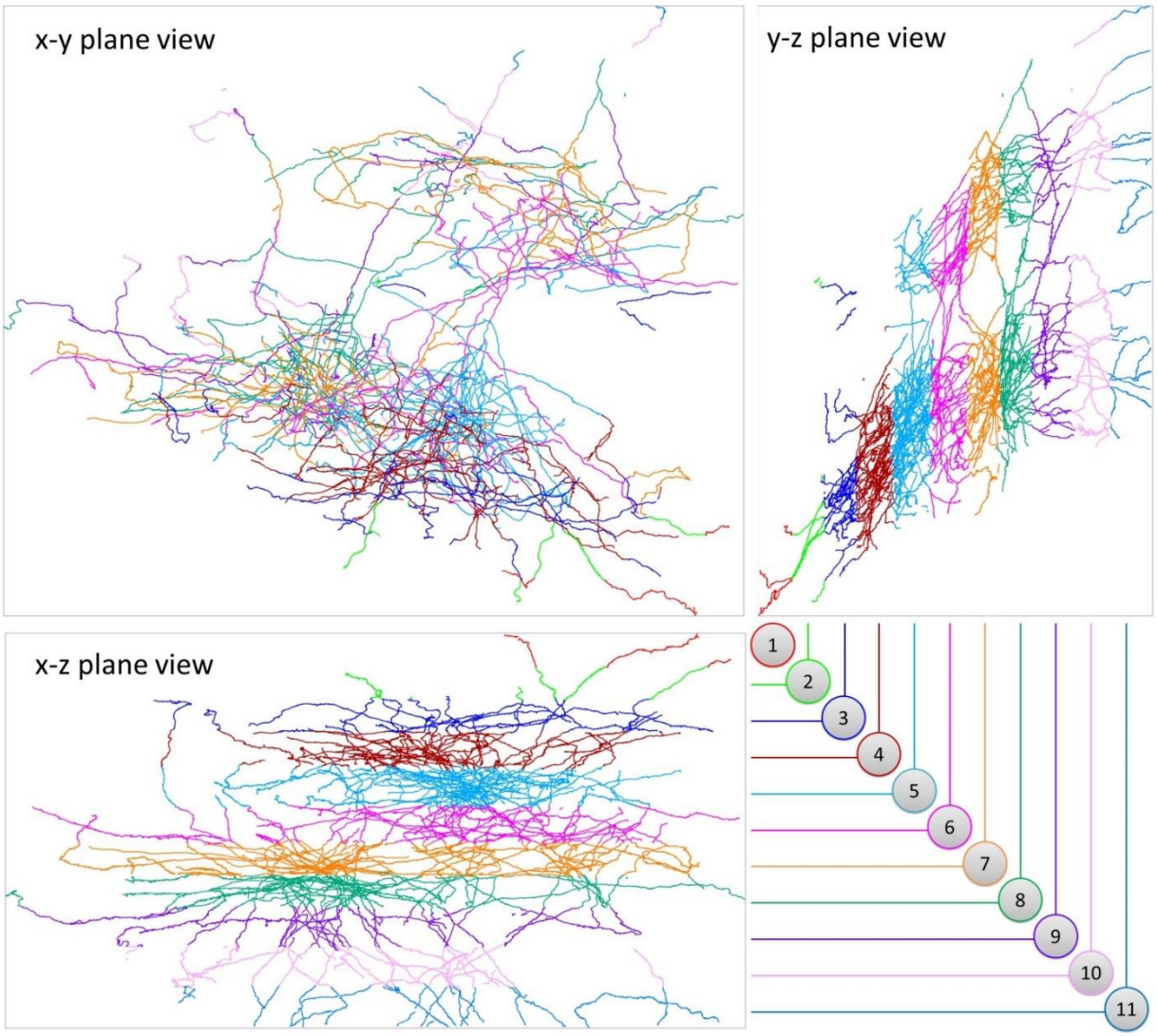

Figure 3. 11. Visualization of stitching results of dataset 1 from different views: reconstructions are displayed in skeleton; segments are color-coded for each section.

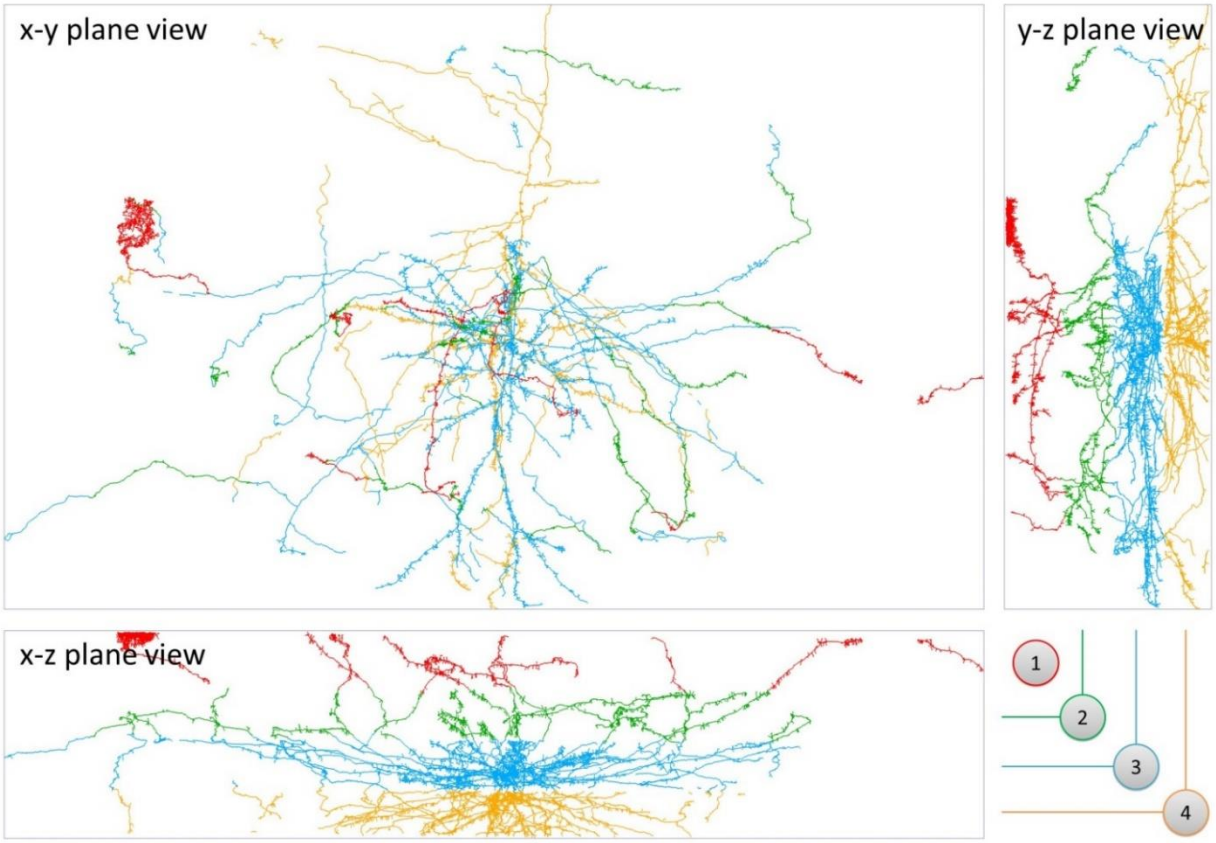

Figure 3. 12. Visualization of stitching results of dataset 2 from different views: reconstructions are displayed in skeleton; segments are color-coded for each section.

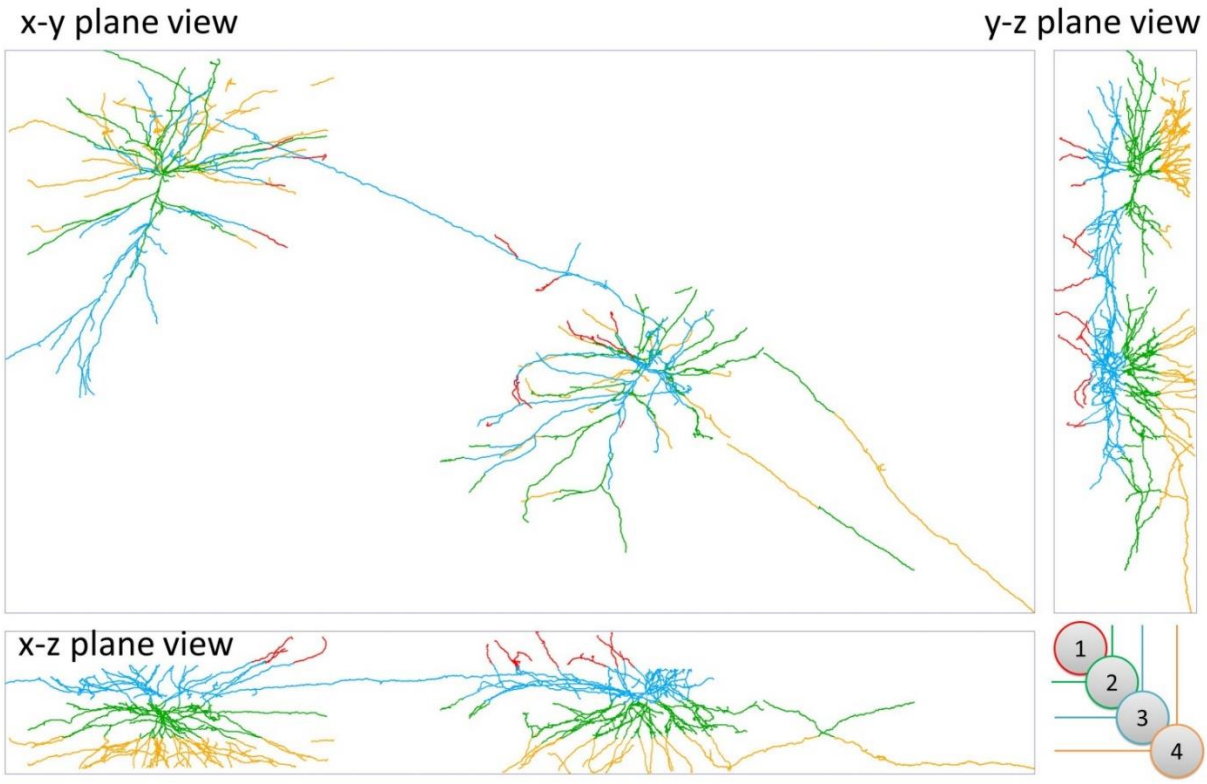

Figure 3. 13. Visualization of stitching results of dataset 3 from different views: reconstructions are displayed in skeleton; segments are color-coded for each section.

Simulated Testing Data

We also considered an alternative way to produce "ground truth" to evaluate the accuracy of NeuronStitcher. We chose 4 densely arborized reconstructions from the mouse visual cortex (dataset 1 previously used) and digitally "sectioned" each of them into two halves by deleting the vertices and the edges severed by the gap (black vertices and edges in Figure 3. 15) to generate the simulated data. Several different gap configurations (1, 2, 4, and 8 μm) were used to simulate the different levels of tissue loss during sectioning and one-half was randomly rotated and shifted in parallel to the sectioning plane to make those sections dis-aligned. An example of simulated data is shown in Figure 3. 14(b).

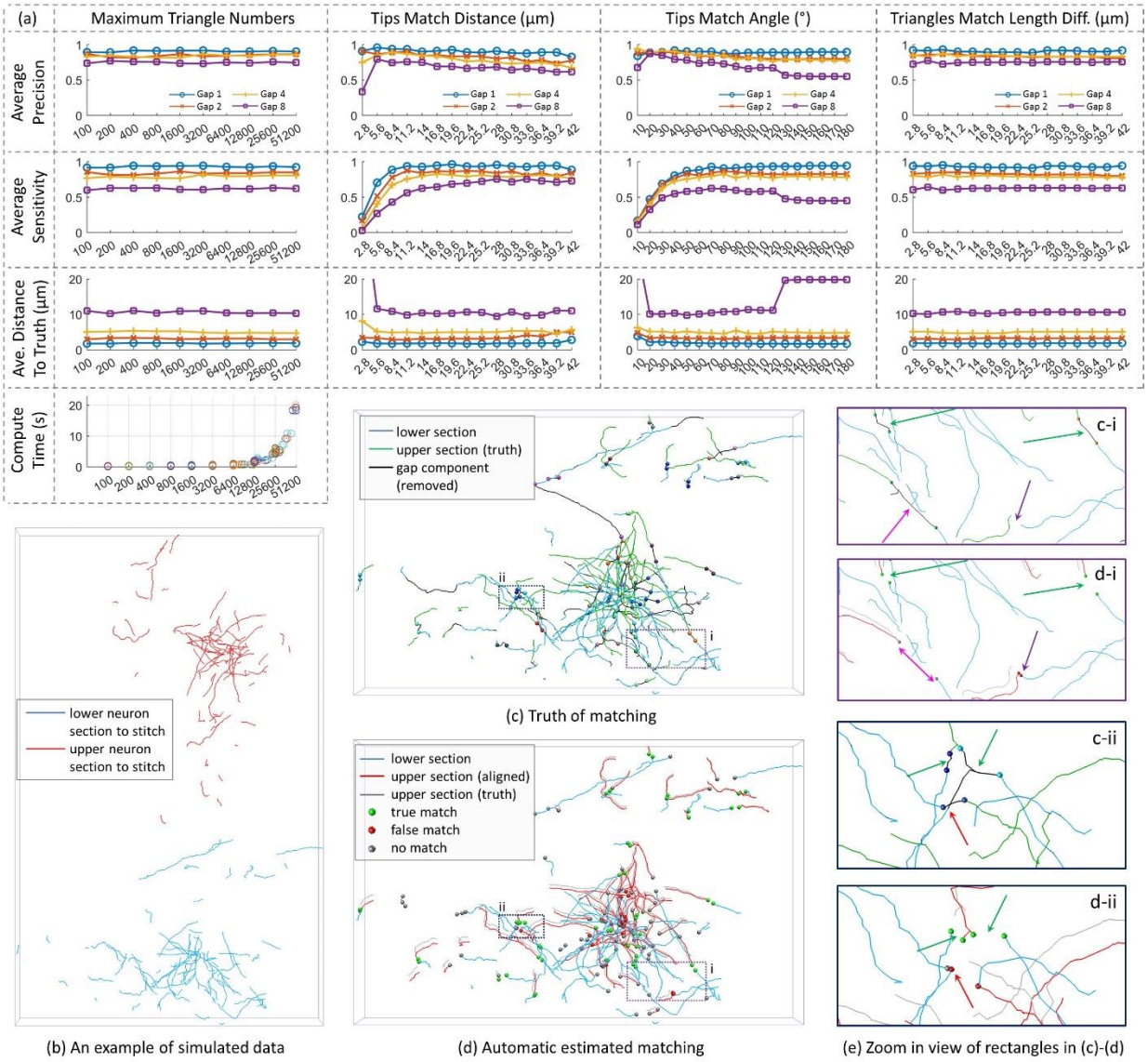

Figure 3. 14. Performance of automatic matching module on simulated data. (a) Quantitative assessment of performance with different parameter configurations. In each subfigure, the x-axis is the selected parameter and the y-axis is the performance measurement. Parameters are listed on the top of each column and the name of measurement is listed on the left of each row. The default values for the parameters are: maximum triangle number: 6400, distance to match tips: 14μm (100 voxels), angle to match tips: 70°, length difference to match triangles: 14μm (100 voxels). (b)-(e) An example of simulated data (b), truth data (c), and matching and alignment result (d)-(e). In (e), green arrows highlighted correctly matched border tips, magenta arrows highlighted the miss-matched border tips (false negative), purple arrows highlighted the matching of none-border tips (false positive), and red arrows highlighted falsely matched border tips.

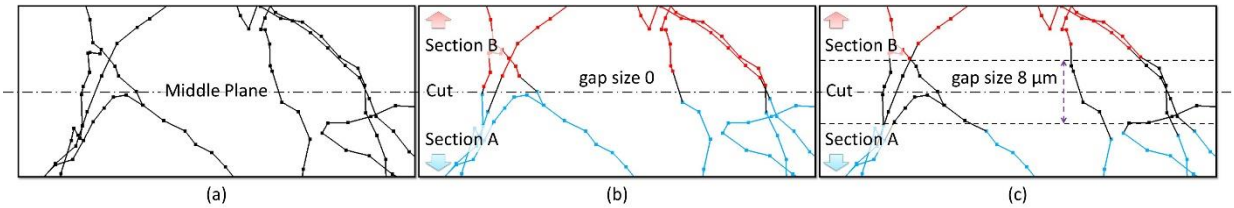

Figure 3. 15. Illustration of the generation of simulated data from experimental data. (a) Reconstruction of experimental data. (b) Simulated data with gap size 0. (c) Simulated data with gap size 8 µm. In (b) and (c), black lines are the removed components after separation. Red and blue lines are the sections after separation.

Then, we applied NeuronStitcher to the simulated data to automatically stitch the simulated datasets back together based on different parameter configurations. An example of automatic matching of simulated data is shown in Figure 3. 14(b-e). As shown in Figure 3. 14(d), even when a considerable amount of tissue is lost (black curves in Figure 3. 14(c)), the automatically estimated alignment is relatively close to the ground truth and most of the severed neurites were correctly matched. However, falsely matched border tips can still be observed. As highlighted by red and purple errors in Figure 3. 14 (e), some branches are falsely connected when the neurites are densely distributed in a small area. And some connections are missed when a long branch in parallel to the sectioning plane is severed (magenta errors in Figure 3. 14 (e)). To quantify the performance of proposed matching algorithm, we compared the result to the ground truth in the following two aspects:

1) Spatial similarity:

Because the topology structure of section B remains the same when moving it in the 3D space, we measured the average distance between corresponding vertices before moving (ground truth) and after alignment (results by proposed algorithm). When the distance was relatively small, the proposed algorithm estimated the correct alignment.

2) Topology correctness:

The proposed algorithm matched tips between section A and section B. After matching, we expected the vertices that were separated after separation (ground truth) to be reconnected (matched) and the vertices that were not connected at the beginning to remain disconnected. Thus, based on ground truth, precision and sensitivity defined below were measured:

$$Precision = \frac{\|Match^* \cap Match^{truth}\|}{\|Match^*\|} \tag{3.8}$$

$$Sensitivity = \frac{\|Match^* \cap Match^{truth}\|}{\|Match^{truth}\|} \tag{3.9}$$

where $Match^*$ is the set of matched pairs of border tips obtained by the proposed algorithm and $Match^{truth}$ is the set of pairs of vertices separated during separation. If a branch (fork vertices) was removed during separation that resulted in 3 or more vertices separated at a time, matching any pair of these vertices was counted as a successful match.

For different gaps, by using the default parameter configuration, the average precision in matching border tips gradually changed from 90% to 75% while the average sensitivity was between 93% and 62%- indicating the alignment result was accurate enough to recapitulate the original reconstruction. We then adjusted 4 critical parameters to examine the robustness of the proposed method. These 4 parameters and their default values were: maximum triangle number: 6400, distance to match tips: 14μm (100 voxels), angle to match tips: 70°, length difference to match triangles: 14μm (100 voxels). During each test, only 1 parameter was adjusted while the other 3 were fixed to the default values. As shown in Figure 3. 14(a), the parameter used for triangle matching did not significantly affect the final matching result. Notably, by only taking the first 100 triangles, the obtained results were similar to the results of using all triangles while the computational time was reduced from 20 seconds to less than 1 second. On the other hand,

the selection of border tips matching criteria (distance and angle) are crucial for an accurate result. Intuitively, if either the distance or angle criterion is too restrictive, a lot of severed neurites will be missed for matching. Conversely, with looser criteria, more false connections will be generated. Thus, users may need to pay close attention to these two parameters and select the optimal one for their dataset to achieve a balance between the false positive and false negative rates.

CONCLUSION

We present a novel neuron reconstruction stitching framework that features an efficient automatic matching and alignment algorithm, severed neurite filters, and a user-friendly interface for result proofreading and manual adjustment. With these tools, physically sectioned neuron reconstruction fragments can be matched, aligned, and stitched by the severed neurites on the sectioning plane to infer complete neuron morphology in a large-scale. In comparison with previous methods, NeuronStitcher has been comprehensively evaluated by both simulated data and complex mouse and human neurons. NeuronStitcher is accurate, robust, efficient, easy to use, and publicly available.

CHAPTER 4

OPTIMIZATION OF LARGE-SCALE MOUSE BRAIN CONNECTOME VIA JOINT EVALUATION OF DTI AND NEURON TRACING DATA [3]

[3] Hanbo Chen, Tao Liu, Yu Zhao, Tuo Zhang, Yujie Li, Meng Li, Hongmiao Zhang, Hui Kuang, Lei Guo, Joe Z. Tsien, Tianming Liu. 2015. *NeuroImage*, 115:202-213.
Reprinted here with permission of the publisher.

ABSTRACT

Tractography based on Diffusion tensor imaging (DTI) data has been used as a tool by a large number of recent studies to investigate structural connectome. Despite its great success in offering unique 3D neuroanatomy information, DTI is an indirect observation with limited resolution and accuracy and its reliability is still unclear. Thus, it is essential to answer this fundamental question: how reliable is DTI tractography in constructing large-scale connectome? To answer this question, we employed neuron tracing data of 1772 experiments in the mouse brain released by the Allen Mouse Brain Connectivity Atlas (AMCA) as the ground-truth to assess the performance of DTI tractography in inferring white matter fiber pathways and inter-regional connections. For the first time in the neuroimaging field, the performance of whole brain DTI tractography in constructing large-scale connectome has been evaluated by comparison with tracing data. Our results suggested that only with the optimized tractography parameters and the appropriate scale of brain parcellation scheme, DTI can produce relatively reliable fiber pathways and large-scale connectome. Meanwhile, a considerable amount of errors were also identified in optimized DTI tractography results, which we believe could be potentially alleviated by effort in developing better DTI tractography approaches. In this scenario, our framework could serve as a reliable and quantitative test bed to identify errors in tractography results which will facilitate the development of such novel tractography algorithms and the selection of optimal parameters.

INTRODUCTION

Mapping brain activity patterns and deciphering neural codes are the fundamental goals of the BRAIN project (http://www.nih.gov/science/brain/) (Tsien et al. 2013; NIH 2014). The achievement of the goal requires a comprehensive view of the structural connectivity patterns

from which neural activity patterns are generated. Since the early development of diffusion tensor imaging (DTI) (Basser et al. 1994) and tractography algorithms (Mori et al. 1999) in the 1990s, the technique has been widely applied to investigate white matter pathways of mammalian brains. As a magnetic resonance imaging (MRI) technique, DTI is able to infer axonal fiber orientations of living brains in 3D space by measuring restricted water diffusion in tissue. Based on the DTI tractography, many macro-scale fiber pathways of mammalian brains such as human (Assaf and Pasternak 2008; Mori et al. 2008; Bassett and Bullmore 2009), macaque (Rilling et al. 2008; Chen, Zhang, Guo, et al. 2013; Li, Hu, et al. 2013), or mouse (Zhang et al. 2002; Moldrich et al. 2010; Calamante et al. 2012) were reconstructed and analyzed. Later, it has been pointed out that in order to fully understand how the brain works, a comprehensive map of brain inter-regional wiring diagram on a large scale, namely connectome, is required (Sporns et al. 2005; Bullmore and Sporns 2009; Van Essen 2013). Moreover, several more advanced diffusion MRI approaches such as high angular resolution diffusion imaging (HARDI) (Tuch et al. 2002) or diffusion spectrum imaging (DSI) (Wedeen et al. 2005) were developed to overcome the limitation of DTI in reconstructing crossing fibers. As the only feasible neuroimaging approach to investigate structural connectome in living brain, DTI tractography as well as its advanced form has been used as a presumably reliable tool by a large number of large-scale studies. For example, the Human Connectome Project (Van Essen et al. 2012; Sotiropoulos et al. 2013) (http://www.humanconnectome.org/) is acquiring HARDI data of 1200 healthy subjects to build a connection map of brain; the CONNECT project (Assaf et al. 2013) has been developing tools to analyze the brain's macro- and micro- structure tissues and connectivities by combining tractography and micro-structural measurement in diffusion MRI data; the Brainnetome Project (Jiang 2013, 2014) (http://www.brainnetome.org) is comparing

DTI data of thousands of patients and the healthy controls to explore the brain's network-based biomarkers for brain diseases such as schizophrenia and Alzheimer's disease; the Brain Decoding Project (http://braindecodingproject.org/) is analyzing mouse brain data on different scales with different imaging modalities including DTI to unveil the myth of memory.

In spite of the growing exciting findings brought by DTI, the reliability of DTI-based tractography is still in question. DTI showed a variety of limitations, especially when it is applied to infer inter-regional connections. In the review article by Jbabdi and Johansen-Berg, DTI tractography is regarded as an "indirect, inaccurate, and difficult to quantify" observation approach (Jbabdi and Johansen-Berg 2011). Different from the traditional histology approach which directly observes neurons and axons under a microscope, DTI infers microanatomy indirectly from properties of restricted water diffusion in tissue, resulting in the loss of information on the microscale structures. For example, as reviewed in (Jbabdi and Johansen-Berg 2011), it is difficult to determine where a fiber tract should start or terminate. Long association tracts constructed by DTI tractography could be a long direct connection between remote cortical regions, or, alternatively, a succession of short fibers. Moreover, DTI tractography is unable to identify the polarity of a given connection. An afferent axon cannot be distinguished from an efferent axon based on their water diffusion pattern. Though one could argue that the detailed information like synapse structure or polarity is not necessary for analysis on a macro-scale. The accuracy of the approach is still questionable for such kind of analysis due to the empirical models and parameters applied to axonal fiber tractography. The classic DTI tractography methodology assumes that axonal fiber bundles move in parallel in a single voxel and thus models each voxel with single diffusion model. However, the assumptions can only be met if the resolution is high enough to monitor a single bundle of axons. In reality, a voxel

typically contains tens of thousands axons from different bundles. In addition to traveling in parallel, they could meet, merge, twist, bend, cross, etc. Therefore, a voxel cannot be modeled by a single diffusion model. Notably, some of the axon interactions such as crossing or diverging have been modeled by advanced tractography methods (Hess et al. 2006; Wedeen et al. 2008; Zhang, Schneider, et al. 2012). But due to a lack of the ground truth or alternative validation methods, the accuracy of the models remains untested, and the models and parameters applied by those approaches are highly empirical. Further, even with the most accurate model and optimal parameters have been applied, findings are still quite sensitive to the selection of brain parcellation scheme (Zalesky et al. 2010; Meskaldji et al. 2013). Given the limited resolution of DTI data, it is not clear on which scale (volume size of regions of interest) tractography gives the best performance. With all these limitations raised above and a large number of ongoing brain connectome-related studies based on DTI tractography, we believe that it is essential to re-examine the basic question: How reliable is large-scale connectome constructed by DTI?

So far, an ideal approach to validate DTI tractography is neuron tracing study. The merit of this approach is that it allows accurate observations of inter-regional connections and white matter fiber pathways in the brain of the sacrificed animal. Different from the dye applied in traditional histology study that targets on specific tissue/molecule, neuron tracers diffuse along axons and proliferate between neurons via synapses. Thus with the carried florescent protein, it could label the afferent/efferent projections to/from the injection site. In a group of recent works, comparisons between neuron tracing result and diffusion tractography result were compared in macaque brain (Dauguet et al. 2007; Jbabdi et al. 2013; Thomas et al. 2014), squirrel monkey brain (Gao et al. 2013), porcine brain (Dyrby et al. 2007), and human brain (Seehaus et al. 2013). These studies offered a new insight into approaches to validating DTI tractography on global

scales. However, due to the high cost and the large number of the neuron tracing experiments that are required to cover the whole brain, limited injections were performed in these studies and only connections between a few brain regions were analyzed. Until now, few works have been done to validate DTI tractography's performance in constructing large-scale connectome based on neuron tracing data.

Despite taking neuron tracing result as truth, other data were also applied to validate DTI tractography, but with limitations. Some recent studies validated the performance of DTI by comparing DTI findings with the stained histology data serving as the truth (Leergaard et al. 2010; Hansen et al. 2011; Choe et al. 2012). The difficulty with the histology approach is to construct a full 3D morphology of fiber pathways based on the many 2D image slices. Thus, only local white matter properties such as fractional anisotropic (FA) or diffusion orientation were examined in these studies. Meanwhile, DTI tractography's performance in identifying global connections was rarely examined in these studies. Instead of using real data, another approach is to use a phantom model that allows researchers to quantitatively examine and compare tractography algorithms' performances in constructing fiber pathways (Fillard et al. 2011; Côté et al. 2013). Notably, due to the absence of real data in such approach, possible problems in real scenarios might be overlooked. Moreover, none of these two types of data are proper to validate DTI tractography on constructing large-scale connectome.

In response, this chapter aims to fill in this knowledge gap via the recently released Allen Mouse Brain Connectivity Atlas (AMCA, http://connectivity.brain-map.org/). This dataset provides a map of neural connections in the mouse brain obtained by tracing axonal projections from defined regions via enhanced green fluorescent protein (EGFP)-expressing adeno-associated viral vectors and then by imaging the EGFP-labeled axons throughout the mouse

brain via high-throughput serial two-photon tomography (STPT). By March 2014, the data of 1772 tracing experiments across the whole mouse brain has been released, covering nearly all brain anatomical regions and axonal pathways. Such dataset enables accurate observations of large-scale connectome of the mouse brain in meso-scale (Oh et al. 2014). Moreover, after each tracing experiment, the imaged histology slices were preprocessed and assembled into a 3D image stack, a data type similar to DTI data, making the quantitative comparisons possible between these two types of data. Therefore, with the connectome constructed based on the AMCA as the benchmark, for the first time, we are able to validate DTI's performance in inferring axonal wiring diagram and large-scale structural connectome.

MATERIALS AND METHODS

Acquiring and Constructing Large-Scale Connectome

Reference atlas and parcellation schemes

To construct large-scale connectome, we toke anatomical brain regions across the whole brain as regions of interest (ROIs) and measured inter-regional structural connections between them. The annotation of mouse brain's anatomical structure was downloaded from Allen Mouse Brain Atlas (AMRA) (http://mouse.brain-map.org/static/atlas). These brain regions were manually annotated following the hierarchal structures in the 3-D reference atlas of AMRA, allowing brain parcellation scheme on different scales. On the finest scale, 300 regions were selected to parcellate the whole mouse brain. They were then combined to obtain 96 regions and 69 regions parcellation scheme. Notably, all the annotated regions were bi-partitioned by the left/right hemispheres. To enable comparisons, data obtained from different modalities were aligned to the space of AMRA before analysis.

Neuron tracing data and meso-scale connectome

Meso-scale connectomes were constructed based on the neuron tracing experiments. Neuron tracing data were downloaded from publicly available AMCA (Logothetis 2008) (http://connectivity.brain-map.org/). Images obtained from 1772 neuron tracing experiments covering the whole mouse brain were applied in this study. The experiments and preprocessing were carried out by Allen Institute for Brain Sciences (Oh et al. 2014). In each experiment, rAAV tracer was injected into target anatomical region of a mouse brain to label the projection from this region to the whole brain. For the purpose of efficiency, all the injection sites were located in the right hemisphere of mouse brain. After fixation and dissection, the mouse brain was then sliced (100 μm in thickness) and imaged (resolution 0.35 μm/pixel) with STPT (Ragan et al. 2012). Then the images were processed with injection volume manually annotated by experts and the traced neuronal projections segmented based on an algorithm. A 3-D image stack was then obtained and registered to the 3-D reference atlas space. The size of labeled volume and the injection volume in each annotation regions were then computed. To construct meso-scale connectome, we downloaded the table of labeled volume size and injection volume size from AMCA. Since the injection size in AMCA experiments is relatively large, it may label the projection from multiple anatomical regions simultaneously which will cause ambiguity in counting the projection from specific regions. Thus, a regression approach was applied to obtain pair-wise connection strength between annotated regions (Oh et al. 2014). Specifically, taken each experiment result as an observation, the correlation coefficient and the corresponding p-value between the injection volume size of anatomical region *i* and the labeled volume size of anatomical regions *j* was calculated to measure the connection strength from region *i* to region *j*.

When p-value is smaller than 0.05, then we assume that there is an axonal projection from region *i* to region *j*.

DTI data and macro-scale connectome

Macro-scale connectomes were constructed based on DTI data. Specifically, a high-resolution DTI data of an adult mouse brain was downloaded from the publicly available Mouse BIRN Data Repository and applied in this study. The specimen was fixed using 4% paraformaldehyde in phosphate-buffered saline (PBS) for over one month and was placed in PBS for 24 hours before imaging. During imaging, the specimen was placed in MR-compatible tubes filled with fombin (Fomblin Profludropolyether, Ausimont, Thorofare, New Jersey, USA) to prevent dehydration. Imaging was acquired in a Bruker Biospin 500MHz (11.7 Tesla) spectrometer with following parameters: matrix size = 420 x 210 x 230; pixel resolution = 0.0625 mm isotropic; 14 diffusion-weighted images were acquired by 3D fast spin echo imaging sequence and four signal averages were used; TR = 0.9s; TE = 35 ms, echo train length = 4 (Zhang et al. 2002). The preprocessing of data includes diffusion tensor estimation, fractional anisotropic (FA) estimation, and manually skull removal (Jiang et al. 2006). DTI data was aligned to the 3-D reference atlas in AMRA. Since the reference atlas is based on stitched sections of Nissl stain, its contrast is very different from FA image and non-diffusion (B0) image of DTI data (which are widely applied for the registration of DTI data) and there is zig-zag effect across sections, linear alignment based on FSL FLIRT (Jenkinson and Smith 2001) was applied and it works reasonably well in establishing correspondence between these two modalities. To further evaluate the performance of alignment, we quantitatively measured the overlap between manually annotated fiber tracts in AMRA and the fiber tracts in aligned DTI data detected based on FA value (FA>0.3). For all the annotated fiber tracts, 52.4% volume overlaps with DTI data

and for forebrain bundle system, 66.8% volume overlaps with DTI data. Streamline fiber tractography was performed via DTI Studio using the streamline model (Jiang et al. 2006). The connection strength between two anatomical regions is defined by the number of fibers passing through both regions.

Connectome Oriented Optimization of DTI Tractography Parameters and Parcellation Scheme Scales

In DTI tractography, the results largely depend on the selection of parameters and tractography algorithms (Dauguet et al. 2007; Moldrich et al. 2010; Jbabdi and Johansen-Berg 2011). Most of the previous studies selected their parameters empirically. The performance of the algorithm based on the selected parameters will thus be limited to one's knowledge and experience. Here, we propose an optimization scheme with a global view to obtain the optimal parameters for DTI tractography based on its accuracy in constructing large-scale connectome. For the DtiStudio (Jiang et al. 2006) on which we applied to perform tractography (and also for most state-of-art diffusion tensor tractography tools), the fiber tracking result is regulated by the FA threshold and angular threshold. 1) FA threshold: when the FA value of a voxel is larger than the threshold, the voxel will be taken as a seed point to initiate fiber tracks; and when the FA value is lower than the threshold, fiber tracks will terminate. 2) Angular threshold: when fiber tract bends in an angle larger than the threshold, tracking will terminate. We chose the minimum FA value to start/end fiber tracking from {0.1, 0.2, 0.3}; and the maximum angular value to terminate fiber tracking from {40°, 50°, 60°, 70°, 80°}. Moreover, the impact of the selection of parcellation scheme on constructing connectome based on DTI data was also analyzed based on the hierarchical parcellation scheme of AMRA. Specifically, connectivity strength matrices were constructed with each entry filled by the number of fiber streamlines connecting two brain

anatomical regions. By taking the whole brain connectome constructed based on neuron tracing data as the truth and changing the threshold of fiber streamline number to form connectivity, the rate of true positive (sensitivity) and false positive (1 - specificity) connections identified based on DTI tractography can be calculated. The well-established receiver operating characteristic (ROC) curve is then plotted for each connectivity strength matrix and the area under the curve (AUC) is computed to quantitatively measure the performance. Those parameters resulted in highest AUC will be viewed as the optimal ones. When selecting the fiber number threshold to binarize DTI based brain connectome, equal weights were assigned to the cost of false connections and missing connections (isocost lines are at 45°).

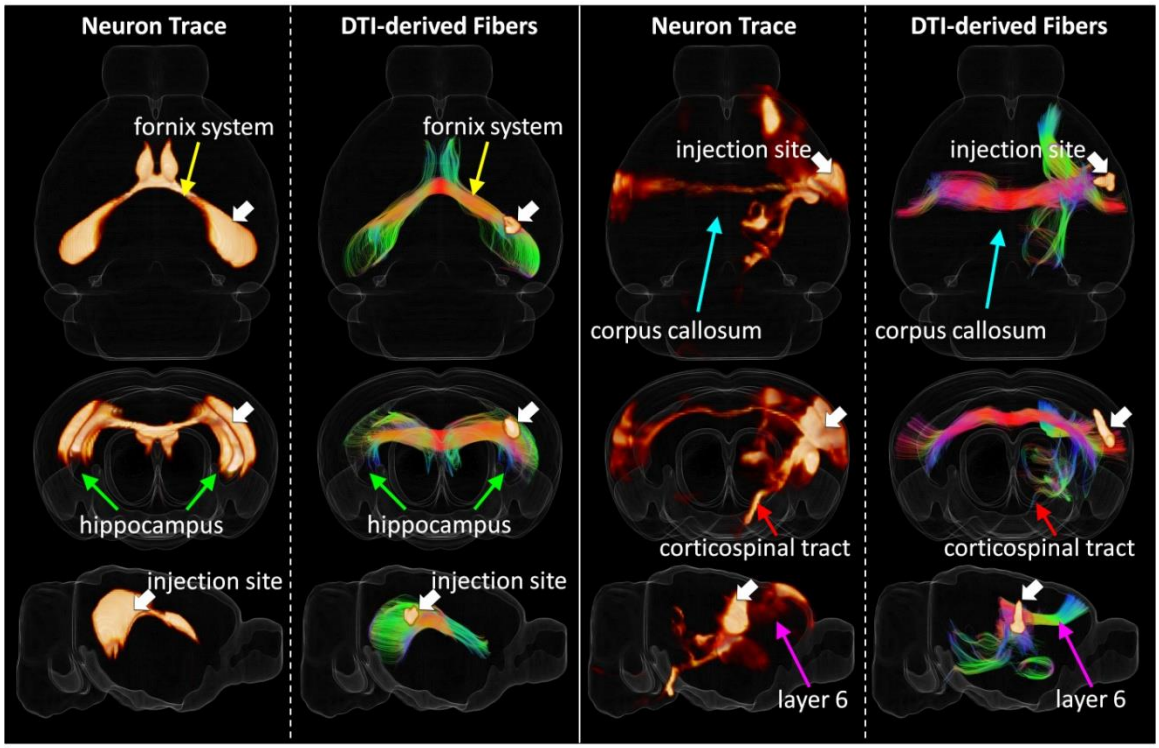

Figure 4. 1. Two examples of a joint 3D view of neuron tracers and the corresponding DTI derived axonal fibers (with Hausdorff distance smaller than 0.5 mm) from different views. For each sub-figure, 3D rendering of tracer density is shown on the left and the corresponding DTI fiber tracks are shown on the right together with injection sites highlighted by white arrows. A transparent reconstructed cortical

surface is also shown in each figure. (a) Injection site locates at CA3. (b) Injection site locates at the somatosensory area.

Validation of DTI Tractography based on Neuron Tracing Data

Validation of DTI tractography has been performed in two aspects. First, 3D morphology of fiber streamlines was compared with neuron trace track-wisely. Second, by taking neuron tracing experiments based connectome as truth, false connections in DTI derived large-scale connectome will be identified and analyzed across the whole brain.

In the AMCA, the images of histology slices were aligned into a 3D stack, which can be morphologically compared with fiber streamlines reconstructed on DTI tractography (Figure 4. 1). To quantitatively compare DTI-derived fiber tracts and neuron traces, we adopted the Hausdorff distance (Huttenlocher et al. 1993) to measure the distance or discrepancy between streamlines of DTI-derived fibers and the neuron trace in the AMRA space. Given a streamline ***F*** represented by a set of connected vertices (equation (2)) and a trace ***T*** represented by a set of voxels (equation (3)), for each voxel in ***T***, its shortest distance to ***F*** are calculated, denoted as distance D; and the Hausdorff distance is defined as the largest of D (equation (1)):

$$Hausdorff(F,T) = \max(\{D \mid D_i = \min(\{\|V_i - P_k\| \mid P_k \in F\}), V_i \in T\}) \quad (4.1)$$

$$F = \{(P, \vec{K}) \mid P_k \in \Re^3, k \in \vec{K}\} \quad (4.2)$$

$$T = \{(V, I) \mid V_i \in \Re^3, i \in I\} \quad (4.3)$$

where ***F*** is a set of 3D points ***P*** arranged in orders defined by $\vec{K}$, and ***T*** is a set of tracer labeled voxels ***V*** *indexed by* ***I***.

Relatively small Hausdorff distance between a pair of DTI derived fiber streamline and neuron trace indicates a close correlation between them. When the Hausdorff distance of a fiber streamline to a neuron trace is small, it can be concluded that the streamline successfully captures the white matter pathway detected by the neuron tracing experiment. On the other hand, with the large number of neuron tracing experiments in the AMCA covering the whole brain, we

premised that the majority of white matter pathways are captured by these experiments. Thus, if a DTI derived fiber streamline is detected to have a relatively large distance to all the neuron tracers, this fiber streamline is possible to be a false tracking. Based on this assumption, the smallest Hausdorff distance (SHD) of each fiber streamline to all the neuron tracing experiments is selected as the best quantifiable value to measure the reliability of DTI tractography. SHDs of all the DTI derived fiber streamlines were computed for quantitative analysis. Notably, as the injection sites only locate on the right hemisphere in the AMCA, the ipsilateral pathways on the left hemisphere were not labeled in these experiments. Thus only those DTI derived axonal fibers that project within/to/from right hemisphere were applied for analysis.

RESULTS

Optimal parcellation scheme and parameters to construct DTI based connectome

ROC curves on different scales with different parameters were shown in Figure 4. 2 and Figure 4. 3 for ipsilateral connection (right hemisphere) and contralateral connection accordingly, and the corresponding AUCs were listed in Table 4. 1. It can be seen that the FA threshold has more impact on reconstructed connectome than the angular threshold. As shown in Table 4. 1, AUCs were relatively higher with small FA threshold (0.1) and large angular threshold (50°-80°). Intuitively, smaller FA threshold and larger angular threshold will result in more fibers and increase the chance to establish connections, as highlighted by green arrows in figures, which results in higher AUCs. However, this may also increase the risk of false positive connections at the same time. On the other hand, an increasing amount of connections were missed by DTI tractography when more restrict tractography thresholds were selected, which results in horizontal lines in Figure 4. 2 and Figure 4. 3. Nevertheless, by looking at the overall trend of ROI curves, a clear tradeoff between sensitivity (true positive rate) and specificity (1 –

false positive rate) can be observed when tuning the threshold of fiber numbers and tractography parameters which agree with the findings in (Thomas et al. 2014). If we only focus locally on ROC curves as highlighted by the red arrows in the figures, we can see that smaller FA threshold (0.1) and angular threshold (40°) gives the best performance – to construct the largest number of correct connections with the fewest wrong connections. Thus, we took this parameter as the optimal one. In Figure 4. 4, we compared the obtained brain connectome based on optimal DTI tractography parameters with those none-optimized ones. Specifically, we extracted and highlighted those corrected connections after optimization in Figure 4. 4(d)-(f). It can be seen that a significant amount of connections have been corrected after optimization and suggests that applying optimal DTI tractography parameters is critical in generating accurate result when analyzing brain connectome. The fiber tracts and the corresponding connectome applied for comparison between DTI tractography and neuron tracing in the next sessions were obtained based on this optimal set of parameters.

Meanwhile, it is obvious that DTI performs much better in constructing connectome with coarser anatomical parcellation scheme in comparison with the finest anatomical parcellation scheme. As shown in Table 4. 1 and highlighted by the dark red and pink arrows in Figure 4. 2(d) and Figure 4. 3(d), parceling the mouse brain into 69 regions or 96 regions is more favored over 300 regions to construct brain connectome. Intuitively, for smaller brain region, less DTI-tracked fibers will go through it. With larger brain regions, connections could be more easily captured. However, with more fibers going through a region, the chance to generate wrong connections is also increased at the same time. Thus though DTI performs equally well for 96 regions and 69 regions when larger fiber number threshold was selected as highlighted by the dark/light red arrows in Figure 4. 2(d) and Figure 4. 3(d), the best performance was obtained

with 96 regions when smaller fiber number threshold was chosen and denser connections were obtained as highlighted by magenta arrows in both figures. This agrees with the observation based on AUCs in Table 4. 1 that the connectome generated based on middle scale parcellation scheme with 96 regions has the highest AUCs.

Table 4. 1. AUCs of DTI constructed connectome matrix

		Ipsilateral connection					Contralateral connection				
Regions	angular / FA	40	50	60	70	80	40	50	60	70	80
300	0.1	53%	60%	63%	65%	66%	42%	52%	57%	60%	61%
	0.2	41%	45%	48%	50%	52%	26%	32%	36%	39%	42%
	0.3	22%	23%	24%	24%	24%	9%	11%	11%	12%	13%
96	0.1	**67%**	**71%**	**72%**	**72%**	**71%**	**62%**	**67%**	**68%**	**68%**	**68%**
	0.2	61%	64%	65%	67%	67%	53%	58%	61%	63%	64%
	0.3	46%	47%	48%	48%	49%	30%	32%	33%	35%	36%
69	0.1	**68%**	**70%**	**69%**	**70%**	**69%**	**64%**	**65%**	**66%**	**65%**	**64%**
	0.2	62%	63%	64%	64%	65%	56%	59%	61%	62%	63%
	0.3	47%	48%	48%	49%	49%	36%	38%	39%	41%	42%

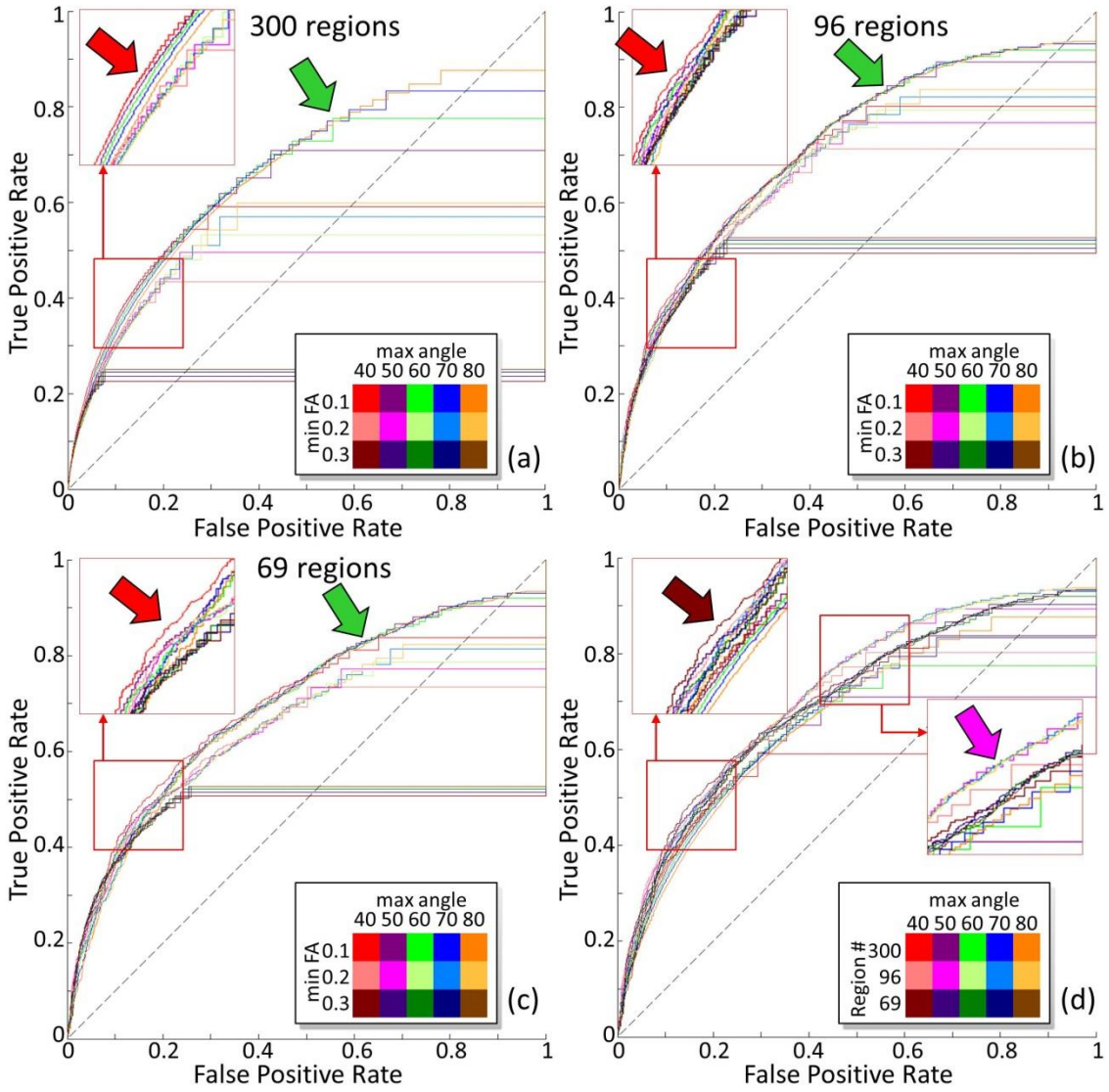

Figure 4. 2. ROC curve for DTI derived ipsilateral connectome on the right hemisphere with different parameters using different percolation schemes by taking tracing experiments based connectivity as truth. The fiber tracking termination angle varies from 40 degrees to 80 degrees. The FA threshold for fiber tracking to start and stop varies from 0.1 to 0.3. For each combination of tractography parameters, a ROC curve is generated with the threshold of fiber number to establish connectivity changes along the curve. Color legend is shown on the right bottom of each sub-figure. (a),(b),(c): the brain is parcellated into 300, 96, and 69 regions accordingly. (d) When the FA threshold is 0.1, comparisons across different parcellation scales are shown.

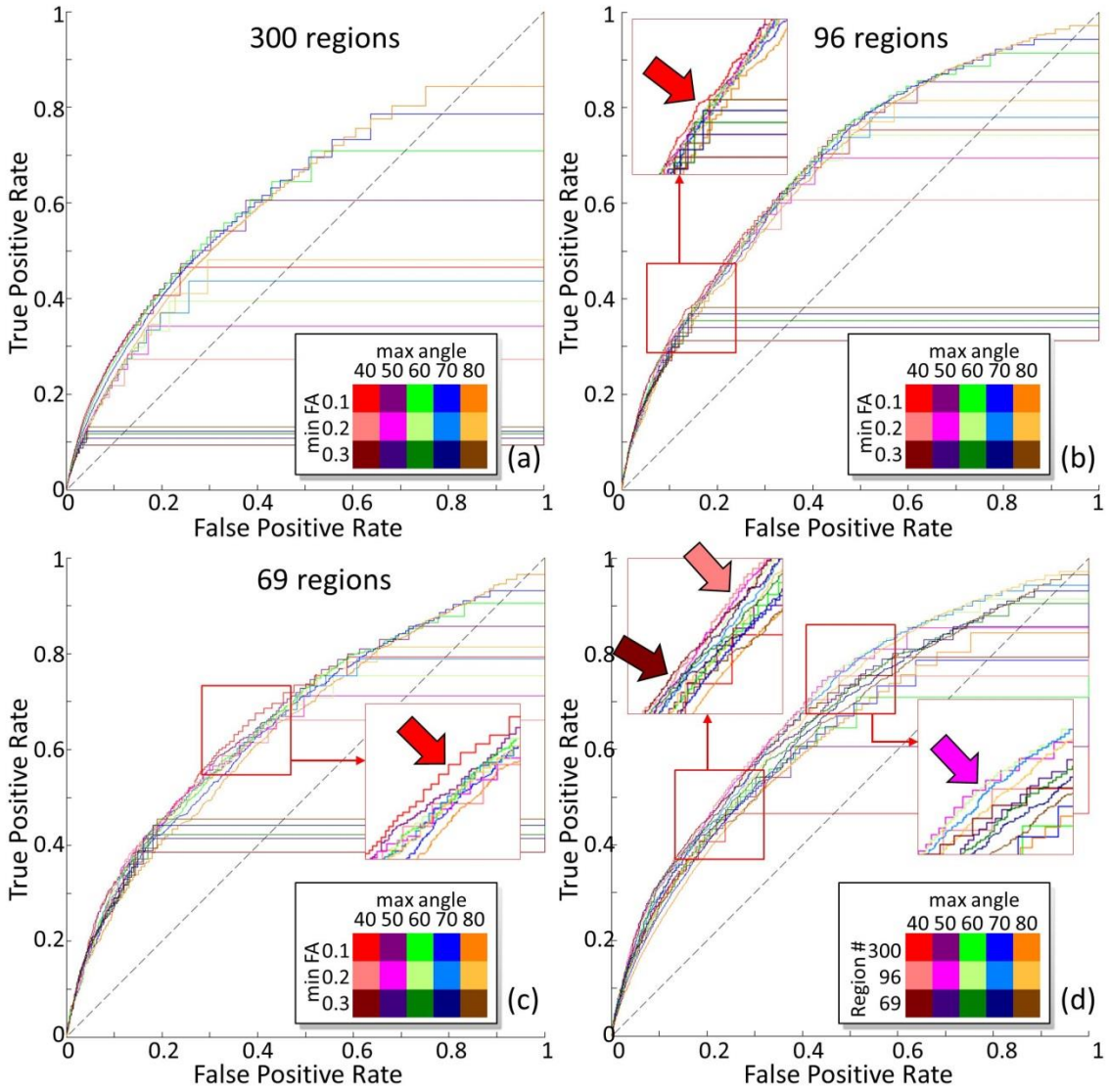

Figure 4. 3. ROC curve for DTI derived contralateral connectome with different parameters using different percolation schemes by taking tracing experiments based connectivity as truth. The fiber tracking termination angle varies from 40 degrees to 80 degrees. The FA threshold for fiber tracking to start and stop varies from 0.1 to 0.3. For each combination of tractography parameters, a ROC curve is generated with the threshold of fiber number to establish connectivity changes along the curve. Color legend is shown on the right bottom of each sub-figure. (a),(b),(c): the brain is parcellated into 300, 96, and 69 regions accordingly. (d) When the FA threshold is 0.1, comparisons across different parcellation scales are shown.

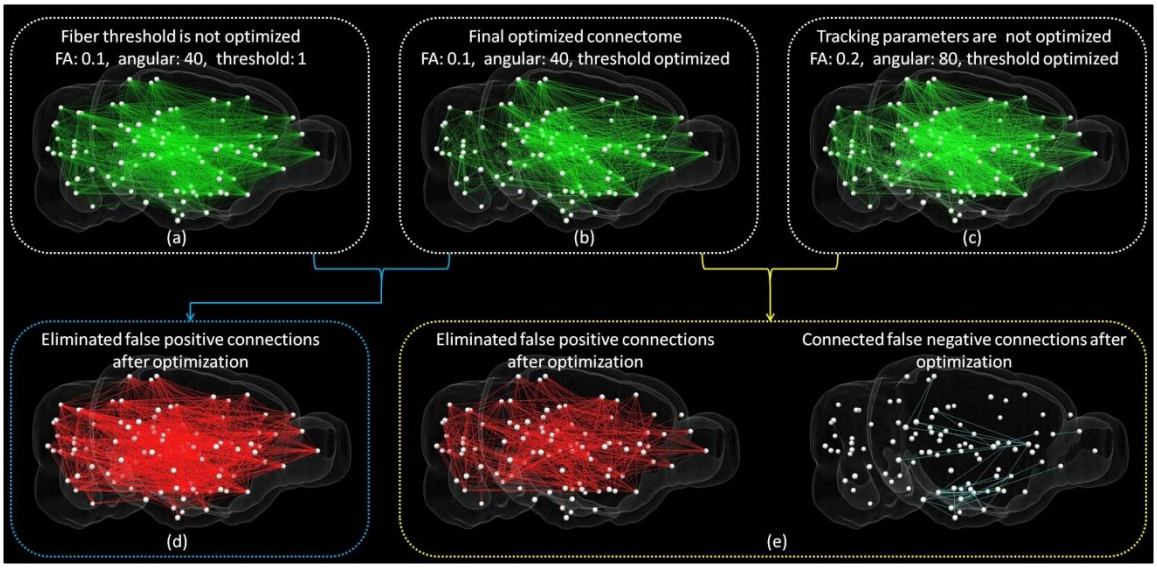

Figure 4. 4. Examples of improvements of DTI derived connectome after parameter optimization. The whole brain is annotated by 96 regions with the center of each one represented by a white sphere. (a)-(c): Visualization of ipsilateral connectome derived from DTI tractography when different parameters were selected. Result based on optimal parameters is shown in (b). In (a), the threshold of fiber number to establish a connection is not optimized and set to 1. In (c), the parameters for fiber tracking are not optimized. (d) Visualization of eliminated false positive connections from the result shown in (a) after optimizing fiber threshold. (e) Visualization of improvements from the result shown in (c) after optimizing tracking parameters.

In previous analysis, we did not specify the streamline length threshold. To further investigate the impact of streamline lengths on constructing accurate brain connectome, we separated fiber streamlines into 3 groups by their length (0-5mm, 5-10mm, longer than 10mm) and construct whole brain connectome based on different groups using similar approaches as previously. Then by taking tracing data derived connectivity as the truth, their reliability in constructing whole brain connectome was analyzed (Table 4. 2). Interestingly, similar to the findings in (Thomas et al. 2014), a different group of fibers has a different preference in higher specificity or higher sensitivity. Short streamlines have higher specificity while long streamlines have higher sensitivity (especially for contralateral connections). Another interesting finding is

that higher accuracy and precision were obtained with shorter fiber streamlines. Though long distance connection will be missing (false negative) when only considering short fiber streamlines, it will also reduce the number of false positive and increase the number of true negative at the same time. Since in our experiment, long distance connections reconstructed based on neuron tracer are relatively sparse, which means the chance to generate false positive long distance connection is relatively high, high accuracy and precision were obtained when excluding long fiber streamlines in the analysis. However, the overall connections identified were reduced by only consider part of the fiber streamlines (reduced AUCs). Thus in the successive analysis, the fiber streamlines were not filtered by length.

Table 4. 2. Analysis of DTI constructed connectome based on different length of streamlines.

Streamline Length		0-5 mm			5-10 mm			> 10 mm			All		
Parcellation Scheme		301	96	69	301	96	69	301	96	69	301	96	69
Ipsilateral Connection	Accuracy	**81%**	**72%**	**70%**	74%	62%	57%	71%	56%	49%	72%	73%	72%
	Precision	**46%**	**39%**	**46%**	35%	31%	35%	30%	28%	31%	33%	39%	47%
	Sensitivity	42%	64%	66%	**52%**	**74%**	**76%**	**50%**	**74%**	**78%**	54%	57%	58%
	Specificity	**89%**	**74%**	**72%**	79%	59%	50%	75%	52%	38%	76%	77%	77%
	AUC	40%	59%	61%	**48%**	**64%**	**65%**	45%	61%	62%	**53%**	**67%**	**68%**
Contralateral Connection	Accuracy	**85%**	**83%**	**80%**	81%	72%	69%	72%	57%	49%	72%	67%	64%
	Precision	**53%**	**34%**	**41%**	37%	25%	29%	24%	20%	22%	26%	23%	27%
	Sensitivity	20%	31%	29%	35%	53%	52%	**38%**	**72%**	**78%**	47%	60%	65%
	Specificity	**97%**	**91%**	**91%**	89%	75%	72%	79%	54%	43%	76%	69%	63%
	AUC	19%	30%	29%	34%	49%	48%	**34%**	**59%**	**61%**	**42%**	**62%**	**64%**

Tract-wise comparison

To evaluate the description power of Hausdorff distance and examine the performance of DTI tractography, we extracted DTI derived fiber streamlines with Hausdorff distances smaller than 0.5 mm to certain neuronal projection tracing for visual analysis (two examples showed in Figure 4. 1). By visual check, we found that the identified corresponding DTI derived streamlines are close to the neuron tracing result which suggests that Hausdorff distance is

powerful in measuring the similarity between these two sets of data. On the other side, it can be seen that DTI tractography performs reasonably well in identifying major axonal projection pathways such as the contralateral connections of hippocampus including fornix system (Figure 4. 1(a), the yellow arrows) and the projection pathways from somatosensory area (Figure 4. 1(b)) including corpus callosum (the azure arrows) and corticospinal tract (the red arrows). Intriguingly, in addition to the major white matter pathways, our observation suggested that DTI tractography is also able to infer detailed axonal connections such as the projection from the somatosensory area to the motor area through layer 6 detected by neuron tracer as highlighted by the magenta arrows shown in Figure 4. 1(b).

Our experiments showed that the correspondence can be precisely established between brain pathways identified by neuron tracing experiments and the DTI derived fiber streamlines in the case of small Hausdorff distances (smaller than 0.5mm) and when the Hausdorff distance is larger than 1mm, the correspondence between tracer labeled projections and fiber streamlines is not reliable (Figure 4. 5(e)). By taking SHDs of DTI derived fiber streamlines to tracing experiments as a measurement, the reliability of DTI tractography was examined quantitatively. Our result suggests that most of the DTI derived fibers have relatively small SHDs (Figure 4. 5(a)). 92.9% fibers have SHDs smaller than 0.5 mm and only 0.48% fibers have SHDs larger than 1 mm (Figure 4. 5(d)). This result suggests that DTI is in general reliable (>90% accuracy) in identifying meaningful axonal fibers. It is also worthwhile to examining further the remaining 7.1% of fibers with SHD larger than 1mm as where the causes of false tracking fibers embedded. By our observation, most of these possible false tracking fibers were relatively long and were likely to be caused by the false merging/linking to different pathways (type I error) (Figure 4. 5(b)). To better demonstrate it, we manually extracted those possible false tracking fibers

projected from/to the left main olfactory bulb (MOB) and visualized them with white curves in Figure 4. 5(c) . It can be seen that most of these fiber streamlines form contralateral projections from/to left MOB. Previous neuron tracing study has pointed that the only efferent projection of MOB to the contralateral half of the brain was to the anterior olfactory nucleus (Shipley and Adamek 1984), suggesting that those extracted DTI fiber streamlines with large SHDs are likely to be false tracking result – when the projection between MOB and hippocampal formation reconstructed, the algorithm mistakenly linked the streamline to the corpus callosum tracts and fornix system tracts, as highlighted by the dashed curves and red crosses in Figure 4. 5(c).

In addition to the above mentioned false connections (type I error), we also noticed false breaks (type II error) that cannot be detected by SHD in our analysis. For instance, in Figure 4. 1(b), though the corticalspinal tract has been successfully reconstructed by DTI tractography, if we manually highlight those corticalspinal tracts (Figure 4. 6(a)), a clear gap was observed between the tract and the isocortex. As a result, the connection between somatosensory area and the spinal regions identified by neuron tracers were not identified by DTI tractography. Another example is the efferent projection from the nucleus of reunions (RE) to hippocampal formations such as the entorhinal area (ENT) or CA1 (Herkenham 1978) identified by neuron tracers (highlighted by magenta curves in Figure 4. 6(c)). Even though, the pathway has been partially identified by DTI derived axonal fibers, as highlighted by different colors in Figure 4. 6(b), the pathway is composed of disjoint segments of DTI derived fibers. Thus no direct connection between RE and hippocampal formations can be identified by DTI tractography. Nevertheless, such type II error will be ignored by morphology descriptor such as SHDs proposed and can only be detected by analyzing regional connections. Facing such problem, in the next session, whole

brain connectome in large scale will be compared between two sets of data to count both types of error globally and guide the selection of optimal parameters.

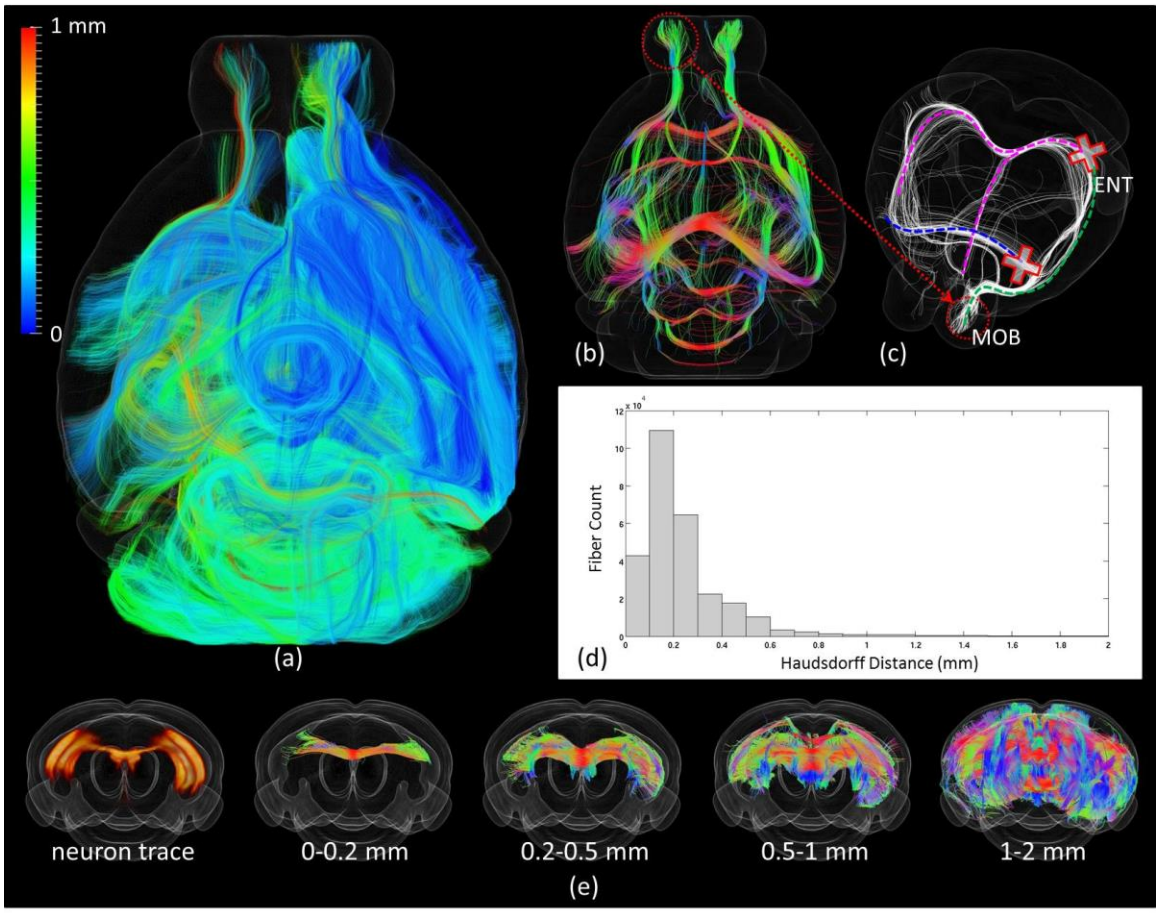

Figure 4. 5. (a) Visualization of fibers projected to/from the right hemisphere. Each fiber is color-coded by its SHD to all the neuron tracer volumes (color bar on the top left). Fibers were set transparent for better visualization. (b) Visualization of all the fibers with SHD larger than 1mm. Fibers are color coded by local orientations. (c) Manually selected fibers that have SHD larger than 1mm from the left main olfactory bulb (MOB) as highlighted by the red circle. (d) Histogram of SHD for all fibers projected to/from the right hemisphere. (e) Visualization of fibers with certain Hausdorff distance to the neuron trace shown on the left.

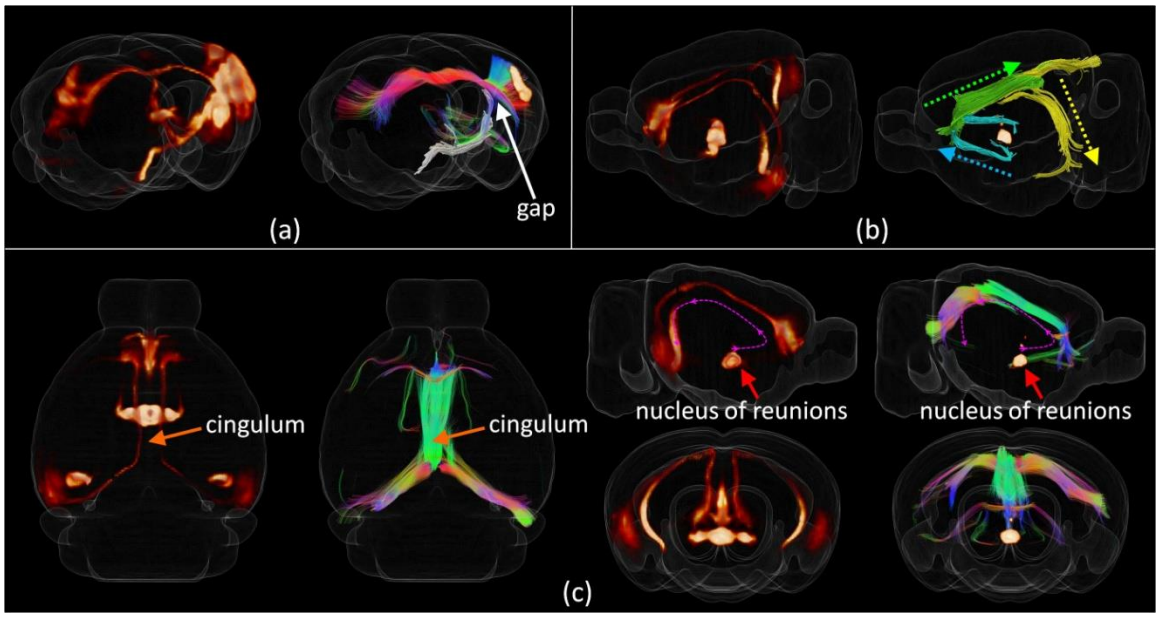

Figure 4. 6. 3D visualizations of the neuron tracing volume (left) and the corresponding fiber tracks (right) with type II error. (a) For the study shown in Figure 4. 1(b), cortical-spinal projections were manually selected and highlighted by the white curves. A gap can be clearly observed between fiber streamlines and the cortex as highlighted by the white arrow. (b)-(c) A neuron tracing study with injection site locates in the nucleus of reunions (RE). As highlighted by the magenta dash curve, the connection follows the cingulum and is projected to the entorhinal area and CA1. Though the corresponding DTI streamlines were identified successfully, it is broken down into 3 segments as represented by the azure, green, and yellow curves shown in (b).

Connectome-wise comparison

We then compared the obtained connectomes on different scales based on neuron tracing and DTI data. We jointly visualized the binarized connectome matrices obtained based on DTI and neuron tracing in different annotation scales for ipsilateral connection (Figure 4. 7) and contralateral connection (Figure 4. 8). Intriguing, by visual check, we can see that DTI performs better in constructing ipsilateral connection than contralateral connection. A similar observation can also be obtained by comparing ROC curves in Figure 4. 2 and Figure 4. 3 and the AUCs in Table 4. 1. It is also evident that a considerable amount of errors have been generated by DTI. Though DTI performs reasonably well when constructing connectome based on optimal

parameters, we could still see a considerable amount of disagreement between DTI derived connectome and neuron tracing derived connectome. For further analysis, we then clustered regions by their anatomical locations and computed the accuracy of DTI in constructing inner cluster connections and intra cluster connections. The result is shown in Table 4. 3. The overall performance of DTI is relatively good across the whole brain. However, as highlighted by the red boxes, DTI displayed poor performance in constructing connections for stratium (STR) and cerebellum (CB). For STR, this is partially because it is surrounded by white matter fiber pathways and penetrated by axonal fiber bundles which are more easily identified by DTI as connected via axonal fibers. Thus more connections than expected were identified in this region that resulted in overwhelmed false positive connections. However, as for cerebellum, it is partially because only a few neuron tracing experiments (40) has been taken in current released of AMCA and relatively small dose neuron tracer was injected for some of them. As a result, fewer connections than reality were identified for brain regions in the cerebellum and current incomplete data cannot tell us much about DTI's performance in the cerebellum. On the other side, as highlighted by the green box, DTI performed relatively well in identifying ipsilateral connections for the retrohippocampal region (RHP), while performed relatively poor for contralateral connections. This is partially because RHP locates at the lateral part of the brain and long distance connections are required to form contralateral connections which DTI tractography failed to construct. On the contrary, for regions locate at the hindbrain that is close to brain midline (e.g. pons (P), medulla (MY)), DTI performs equally well to construct both ipsilateral and contralateral connections in coarser scale.

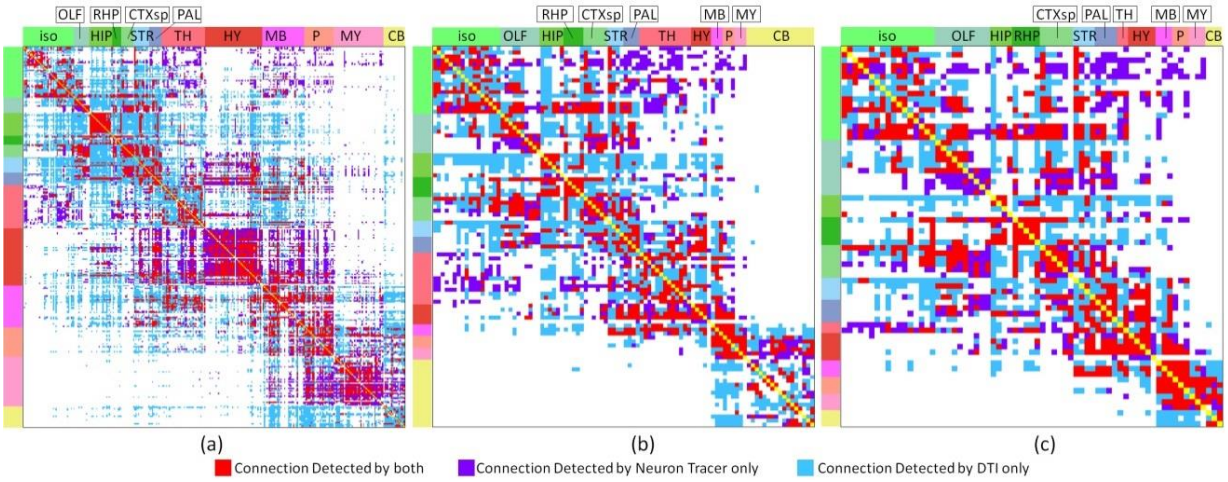

Figure 4. 7. Comparison of mouse brain ipsilateral connectome derived from neuron tracer or DTI using different parcellation schemes. For neuron tracer, when the p-value of the correlation coefficient between an injection site and a projection site is larger than 0.05, the projection will be identified as from the injection site to the projection site. For DTI, when the number of fibers connected between two regions is larger than the threshold, these two regions were identified as being connected. The optimal threshold is selected based on the ROC curve accordingly. DTI tractography was performed based on the following parameters: FA threshold: 0.1, angular threshold 40. (a) 300 regions. (b) 96 regions. (c) 69 regions. The red color represents common connections detected by both approaches. The violet color represents connections detected by neuron tracer only. The azure color represents connections detected by DTI only.

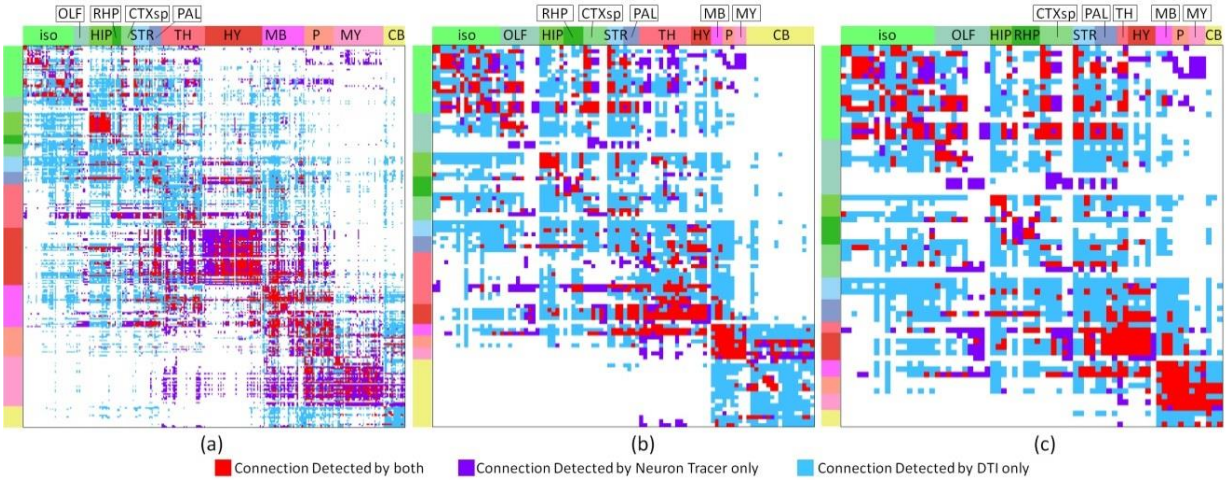

Figure 4. 8. Comparison of mouse brain contralateral connectome derived from neuron tracer or DTI using different parcellation schemes. For neuron tracer, when the p-value of the correlation coefficient between an injection site and a projection site is larger than 0.05, the projection will be identified as from the injection site to the projection site. For DTI, when the number of fibers connected between two regions is larger than the threshold, these two regions were identified as connected. The optimal threshold

is selected based on the ROC curve accordingly. DTI tractography was performed based on the following parameters: FA threshold: 0.1, angular threshold 40. (a) 300 regions. (b) 96 regions. (c) 69 regions. The red color represents common connections detected by both approaches. The violet color represents connections detected by neuron tracer only. The azure color represents connections detected by DTI only.

Table 4. 3. Accuracy of DTI constructed connectome for inner and inter regional connections.

Ipsilateral connection							Contralateral connection							color bar
	300 regions		96 regions		69 regions			300 regions		96 regions		69 regions		
	inner	inter	inner	inter	inner	inter		inner	inter	inner	inter	inner	inter	100%
iso	58%	78%	53%	72%	58%	74%	iso	55%	78%	50%	69%	52%	65%	90%
OLF	70%	77%	67%	79%	58%	75%	OLF	69%	77%	77%	74%	77%	68%	80%
HIP	83%	62%	67%	61%	75%	66%	HIP	77%	66%	75%	55%	75%	52%	70%
RHP	88%	63%	100%	68%	100%	71%	RHP	69%	68%	48%	68%	48%	66%	60%
CTXsp	89%	74%	67%	73%	60%	71%	CTXsp	68%	75%	67%	71%	67%	66%	50%
STR	37%	59%	17%	59%	17%	60%	STR	28%	59%	6%	47%	6%	39%	40%
PAL	67%	59%	75%	64%	92%	66%	PAL	51%	58%	38%	55%	38%	53%	30%
TH	46%	68%	65%	72%	100%	59%	TH	35%	69%	42%	69%	100%	54%	20%
HY	61%	77%	60%	79%	60%	83%	HY	55%	77%	64%	68%	64%	67%	10%
MB	69%	67%	83%	64%	83%	69%	MB	68%	66%	89%	46%	89%	54%	0%
P	65%	73%	100%	77%	100%	87%	P	55%	75%	100%	62%	100%	72%	
MY	61%	88%	100%	88%	67%	92%	MY	50%	86%	100%	83%	100%	89%	
CB	37%	80%	61%	94%	67%	89%	CB	20%	81%	31%	90%	33%	82%	

DISCUSSION

By taking neuron tracing data in mouse brain in the AMCA as a validation tool, we have investigated the performance of the whole brain DTI tractography and the corresponding large-scale connectome. A novel framework was presented for quantitative comparison between DTI data and tracing data. With quantitative measurement, we showed that over ninety percent DTI derived axonal fibers could identify corresponding fiber pathways, which suggested that DTI is a reliable tool in studying major brain pathways. Yet we have revealed that the optimal parameters and the right scale of parcellation scheme are critical in constructing a reliable large-scale brain connectome. In comparison with angular threshold, FA threshold was shown having more impact

on DTI tractography result. In our case, small FA threshold (0.1) generated the best result which agrees with the other's work (Dauguet et al. 2007). Our results also suggested that to construct large-scale connectome, right parcellation scheme is very important and the size of analyzed brain regions should neither be too small nor too big. For our data, annotating mouse brain with 96 regions is the best in comparison with finer and coarser parcellation schemes. With the optimal parameters, the overall performance of DTI tractography is reasonably good in constructing large-scale connectome.

Overall, DTI can be a substantially more reliable tool to investigate brain connectome on the conditions that optimal parameters and the appropriate parcellation scheme were carefully selected. Nevertheless, our framework still detected type I and type II errors with DTI tractography. This agrees with the findings in macaque brain in (Thomas et al. 2014). Not surprisingly, a considerable amount of disagreement between DTI constructed connectome and neuron tracing constructed connectome – especially in the contralateral connections and the connections of striatum and cerebellum – were noted. Though some type I errors can be accounted by the incompleteness of the neuron tracing data set such as those in the cerebellum, most of them might result from the inaccuracy of DTI tractography. These errors could be potentially caused by the complex wiring pattern in the brain (Jbabdi and Johansen-Berg 2011) that cannot be modeled by the classic diffusion tensor model applied in this work. Notably, more comprehensive multi-orientation models such as Q-ball (Tuch 2004; Hess et al. 2006), DSI tractography (Wedeen et al. 2005, 2008), or susceptibility tensor imaging (STI) (Liu et al. 2012) could be used to reduce the possibility of such breaking or missing fibers by considering fiber bundle cross in the model. On the other hand, instead of the limited accuracy of DTI tractography, some errors could also be caused by the registration error. Since it is quite

challenging to register images from different modalities and there is zig-zag effect in stitched sections of AMRA, current study applied linear registration and images were not perfectly aligned before analysis. Thus, with specially designed registration algorithm dedicated to this problem and the better quality data, it would be interesting to benchmark and compare the advanced tracing models on their performance in constructing fiber pathways (Fillard et al. 2011) and whole brain connectome and to investigate the effect of individual variability and acquisition variability on tractography results.

Notably, the evaluation of DTI tractography obtained based on the proposed framework may not be readily applicable to human brains at the current stage. Given the significant differences between the nature of human brain and mouse brain such as size and anatomical structures, it is still an open question on how to link the findings in the brain of these two species. From DTI data acquisition perspective, the image resolution is also very different (e.g. mouse: 50-100 micron resolution (Zhang et al. 2002; Calamante et al. 2012), human: 1-3 mm resolution (Hansen et al. 2011; Sotiropoulos et al. 2013)), thus the microstructures inferred by tractography in mouse and human brains have a magnitude difference (Mori and Zhang 2006; Xu et al. 2008). Also, the DTI data in mouse brains is post-mortem which allows long scanning time for more details and low SNR, but it will influence water molecule diffusion properties in comparison with live brain applied in the human study at the same time. However, the principles and methods of dMRI and the tractography approaches are virtually the same in all animal models. The findings in this chapter largely agree with the recent findings in macaque brain which is more comparable to human brain that dMRI tractography has limited accuracy in inferring brain structural connections and there is a tradeoff between sensitivity and specificity (Thomas et al. 2014). It is noteworthy to mention that the study in macaque brain was limited to only two tracer

injections. By comparison, our proposed framework and the corresponding findings are based on the AMCA dataset which includes 1772 tracer injections that cover the whole brain. Our proposed framework can be applied as a reliable test bed for dMRI tractography, and should be generally applicable to the assessments of the performance of advanced dMRI approaches, guiding a better design of tractography algorithms, and the optimization of parameters and parcellation schemes. On a higher level, as mammal animals, the mouse brain still shares a certain level of common anatomy and function mechanisms as the human brain (Song et al. 2014) which is an importance source of knowledge in understanding brain mechanisms. And to fully understand brain mechanisms, it is more desired to validate findings in different scales, different modalities, and different animal models including mouse (e.g. Jbabdi et al., 2013; Jiang, 2013; Rilling et al., 2008; Zhang et al., 2013).

Most importantly, based on our findings, we would like to draw attention to those studies that rely solely on DTI tractography to study brain connections: DTI can be a substantially more reliable and useful tool with optimized tractography parameters and brain parcellation schemes. If these conditions are not met and the performance is not tested, DTI-generated connection maps may contain numbers of the potential errors which can lead to erroneous conclusions.

CHAPTER 5

COEVOLUTION OF GYRAL FOLDING AND STRUCTURAL CONNECTION PATTERNS IN PRIMATE BRAINS [4]

[4] Hanbo Chen, Tuo Zhang, Lei Guo, Kaiming Li, Xiang Yu, Longchuan Li, Xintao Hu, Junwei Han, Xiaoping Hu, Tianming Liu. 2013. Coevolution of Gyral Folding and Structural Connection Patterns in Primate Brains. *Cerebral Cortex*, 23(5):1208-1217.

ABSTRACT

Both cortical folding and structural connection patterns are more elaborated during the evolution of primate neocortex. For instance, the cortical gyral shapes and structural connection patterns in human are more complex and variable than those in chimpanzee and macaque. However, the intrinsic relationship between gyral folding and structural connection and their coevolution patterns across primates remain unclear. Here, our qualitative and quantitative analyses of in-vivo diffusion tensor imaging (DTI) and structural magnetic resonance imaging (MRI) data consistently demonstrate that structural fiber connection pattern closely follows gyral folding pattern in the tangent direction to the cortical sphere, and this close relationship is well-preserved in the neocortices of macaque, chimpanzee, and human brains, despite the progressively increasing complexity and variability of cortical folding and structural connection patterns. The findings suggest a hypothesis that common axonal fiber pushing mechanism sculpts the curved patterns of gyri in tangent direction during primate brain evolution. Our DTI/MRI data analysis provides novel insights into the structural architectures of primate brains, a new viewpoint of the relationship between cortical morphology and connection, and a basis for future elucidation of the functional implications of coevolution of cortical folding and structural connection patterns.

INTRODUCTION

Brain evolution has been an intriguing research topic for centuries (Zilles et al. 1988; Deacon 1990; Schoenemann 2006; Rakic 2009; Rogers et al. 2010). Over the past decades, there has been increasing interests in applying non-invasive neuroimaging methods (Rilling and Insel 1999; Rilling and Seligman 2002; Woods et al. 2011) to study brain evolution because 3D morphological and anatomical attributes of mammalian brains can be effectively visualized and

measured. In particular, advanced neuroimaging techniques such as diffusion tensor imaging (DTI) (Mori and Zhang 2006) and functional magnetic resonance imaging (fMRI) (Friston 2009) have been recently used to study the connection and function of the primate brains. For instance, a recent comparative DTI study (Rilling et al. 2008) reported a prominent temporal lobe projection of the human arcuate fasciculus whose counterpart is significantly smaller or absent in nonhuman primates (Rilling et al. 2008). This work suggests that DTI is a powerful approach in revealing interesting structural connectivity patterns of brain evolution, and that DTI-derived fiber bundles can be potentially linked to brain function (Rilling et al. 2008). In another recent study (Vincent et al. 2007), fMRI was employed to examine the intrinsic functional architecture in anaesthetized macaque brains and resting state human brains. It was found that four functional networks including the oculomotor, somatomotor, visual, and default mode systems are well preserved across macaque and human brains (Vincent et al. 2007). These studies suggest that neuroimaging such as DTI and fMRI is a powerful approach to studying brain evolution.

In general, during the evolution of the neocortex of primate brains, the variability and complexity of gyral shape patterns are gradually pronounced, as illustrated in Figure 5. 1(a). Meanwhile, the axonal fiber connection patterns are much more elaborated during the evolution of primate cortex (Rilling et al. 2008; Krubitzer 2009). As an example, Figure 5. 1(b) illustrates the DTI-derived fibers emanating from the postcentral gyrus (Figure 5. 1(a)) in three primate brains. It is evident that there are much more DTI-derived axonal fibers connecting to the frontal and occipital lobes in the human brain than those in the macaque and chimpanzee brains. Based on the patterns in Figure 5. 1 and existing neuroscience knowledge of the relationship between corticogenesis and axonal wiring (Rakic 1988; Welker 1990; Van Essen 1997; Sur and Rubenstein 2005; Rash and Grove 2006; Nie et al., 2011), we hypothesize that gyral folding and

structural fiber connection patterns co-evolve in primate brains; and test this hypothesis via quantitative modeling and analysis of cortical surfaces reconstructed from MRI data and axonal fibers reconstructed from DTI data. Specifically, we developed novel computational methods to quantitatively measure the complexities of cortical gyral shape and fiber connection patterns, and performed statistical correlation analyses for three primates. Our results derived from quantitative modeling clearly showed the increasing complexities of gyral folding and fiber connection patterns in all of the three primates of macaque, chimpanzee, and human. In particular, the outcome of our analysis showed a well-preserved strong, positive correlation between the complexities of gyral folding and fiber connection patterns across the three primates, suggesting the coevolution of gyral folding and structural connection patterns in primates.

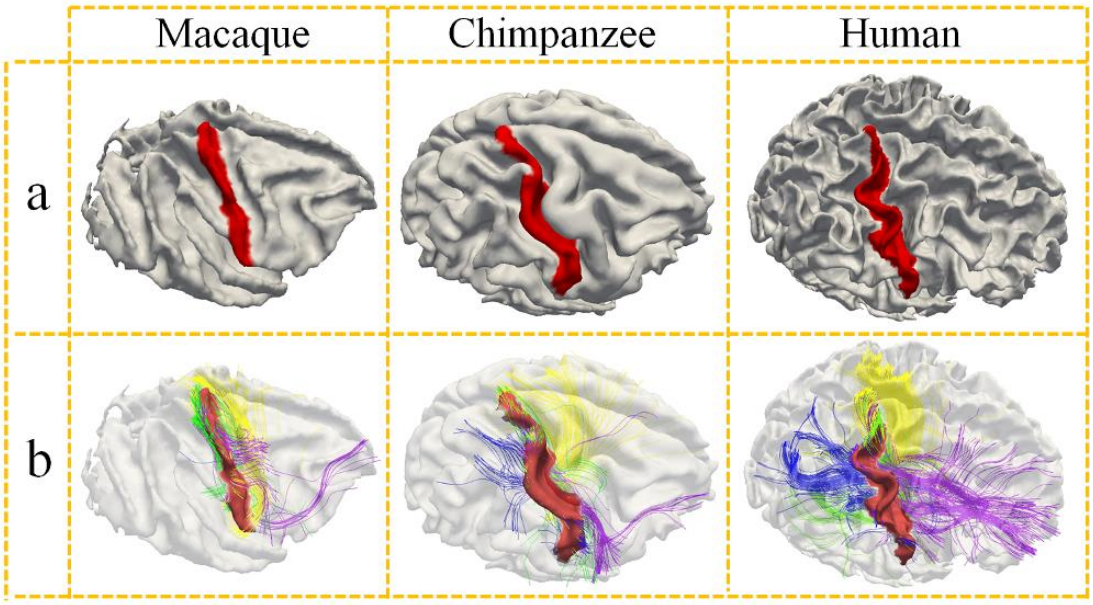

Figure 5. 1. (a): Rendering of the cerebral cortices reconstructed from MRI data of macaque, chimpanzee, and human brains respectively. The post-central gyrus is labeled in red to highlight the different levels of complexities and variabilities of gyral folding in three primate brains. (b): Joint visualization of post-central gyral shapes and the emanating DTI-derived fibers in three primate brains. The fibers connecting to the frontal lobes are colored in purple, those fibers connecting to the occipital lobes are represented in blue, those fibers connecting the other hemisphere are colored in yellow, and those fibers connecting to the subcortical regions are colored in green.

We further explored the possible underlying mechanism that can explain the clear coevolution of gyral folding and structural connections patterns across the three primate neocortices. Our previous studies already demonstrated that significantly denser DTI-derived axonal fibers are connected to the gyral regions than sulcal regions (Nie et al. 2012), as shown in Figure 5. 2(a). Our extensive quantitative DTI data analyses in human, chimpanzee and macaque brains replicated this observation (Nie et al. 2012) and based on this observation, we hypothesized that axonal fiber pushing (blue arrows in Figure 5. 2(a)) is a mechanism that induces or regulates the radial formation of gyral regions (dashed yellow curve in Figure 5. 2(a)) in the cerebral cortex (Nie et al. 2012). This hypothesis is specifically supported by the biomechanical experiment in the fruit fly and the cortex growth simulation experiment in (Nie et al. 2012). In this chapter, we report another interesting finding: the gyral folds in the tangent direction of cortical sphere (dashed green curve in Figure 5. 2(b)) are connected by dense axonal fibers that orient perpendicularly to the gyral crest curves, as demonstrated in Figure 5. 2(b) (red arrows). We replicated this close relationship between tangent gyral folds and axonal fiber orientation directions by extensive qualitative and quantitative analyses in all of the three primate brains in this chapter. Thus, we are inspired to extend the hypothesis in (Nie et al. 2012) to that axonal fiber pushing can also be a mechanism that induces or regulates the curved folding patterns in the tangent direction along gyral crest line, as illustrated in Figure 5. 2(b). Our results show that this hypothesis is supported by a series of experiments in the three primates based on DTI/MRI data. Therefore, the work reported in this chapter, together with our previous studies in (Nie et al. 2012), suggest a novel axonal fiber pushing mechanism of cortical gyral folding. This hypothesis can well explain not only the folding patterns of gyri along the radial direction (dashed yellow curve in Figure 5. 2(a)) (Nie et al. 2012) of the roughly spherically-shaped cortex

(e.g., Figure 5. 2(a)), but also the tangent folding of gyral crests on the cortical surface (e.g., Figure 5. 2(b)).

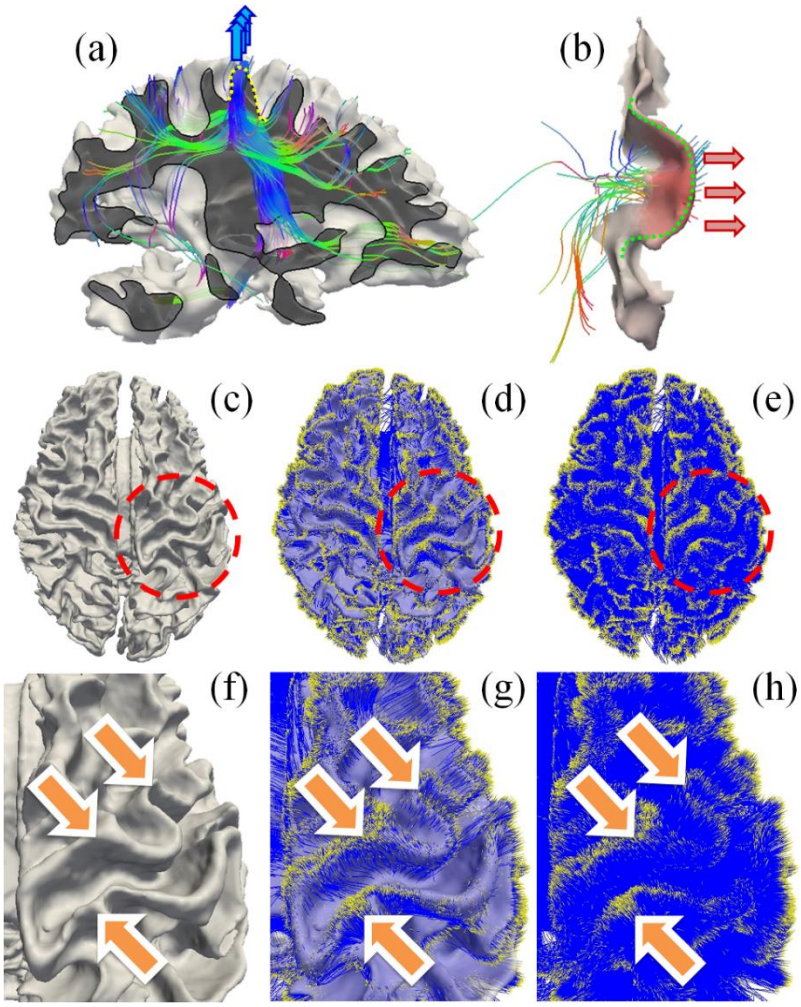

Figure 5. 2. (a): Demonstration that the end points of dominant percentages of DTI-derived fibers concentrate on gyral regions (Nie et al. 2012), instead of sulcal regions, suggesting a pushing mechanism of the formation of convex gyri (Nie et al. 2012). (b): Demonstration that the tangent cortical gyral folds (dashed green curve) are connected by dense fibers that orient perpendicularly to the gyral crest curves from concave side, as highlighted by the red arrows on the right. (c)-(h): Demonstration that the end points of DTI-derived axonal fibers closely follow the gyral folding pattern. (c). Cortical surface reconstructed from T1-weighted MRI data. (d). Projection of WM fibers to the cortex. It is the overlay of (c) and (e). (e). Rendering of WM fibers. Yellow dots represent fiber ends. Blue color represents fibers. (f)-(h): Zoomed views of the circled regions in (c)-(e).

The major contributions of this work are in the following two aspects. First, we developed, evaluated and applied a novel pipeline of computational approaches to quantify cortical gyral folding patterns and fiber orientation patterns in order to enable and facilitate the joint analysis of their co-evolution patterns. As a result, the correlation between fiber orientation patterns and tangent gyral folding patterns can be quantitatively accessed via a joint representation framework. These novel approaches have been shown to be effective in describing the three types of primate brains, and have revealed a well-preserved strong, positive correlation between the complexities of gyral folding and fiber connection patterns across three primates. Second, we revealed a novel finding that tangent gyral folds are connected by dense DTI-derived fibers orienting perpendicularly to the gyral crest curves, and replicated and confirmed across the three species of human, chimpanzee, and macaque we studied. This interesting finding provides novel insights into the underlying mechanism of co-evolution patterns of gyral folding and fiber connection in primate brains: a common axonal fiber pushing mechanism that sculpts the tangent folding patterns of cortical gyri during primate brain evolution.

MATERIALS AND METHODS

Data acquisition and preprocessing

Human brain imaging: Nineteen healthy volunteers were scanned in a GE 3T Signa MRI system (GE Healthcare, Milwaukee, WI) using an 8-channel head coil at the Bioimaging Research Center (BIRC) of The University of Georgia (UGA) under IRB approval. DTI data was acquired using the spatial resolution $2\times2\times2$ mm^3, matrix size=128×128, 60 slices, TR=15.5s, TE=min-full, b-value=1000 with 30 DWI gradient directions and 3 B0 volumes acquired. All slices were aligned to the AC-PC line. T1-weighted MRI images were acquired using a fast

spoiled gradient recalled echo (FSPGR) protocol; TE=min full, TR=7.5 ms, flip angle=20°, 154 axial slices, slice thickness=1.2 mm, and FOV=256 ×256 mm. For the anatomic data, pre-processing included brain skull removal, gray matter (GM) and white matter (WM) tissue segmentations (Liu et al. 2007). Then the GM/WM cortical surfaces were generated (Liu et al. 2008). For the DTI data, pre-processing included brain skull removal, motion correction, and eddy current correction. Fiber tracts were generated based on the DTI data using MedINRIA (Toussaint et al. 2007) .

Chimpanzees brain imaging: All chimpanzees were members of a colony in the Yerkes National Primate Research Center (YNPRC) at Emory University in Atlanta, Georgia. All imaging studies were conducted under IACUC approval of Emory University. MRI and DTI scans were obtained from adult female chimpanzees. Twenty-four cases of MRI/DTI scans were used for this study. Prior to MRI/DTI scanning, the chimpanzee subjects were immobilized with ketamine injections (2−6 mg/kg, i.m.) and were subsequently anesthetized with an intravenous propofol drip (10 mg/kg/hr) following standard veterinary procedures used at YNPRC. The subjects remained sedated for the duration of the scans as well as the time needed for transportation between their home cage and the scanner location. After completing the MRI/DTI scans, the chimpanzees were temporarily housed in a single cage for 6 to 12 hours to allow the effects of anesthesia to wear off before being returned to their home cage and cage mates. The veterinary staff and research staff assessed the general well-being (i.e., activity, food intake) of the chimpanzees twice daily after the scan for possible distress associated with aesthetic accesses.

Both anatomical MRI and DTI scans were acquired on a Siemens 3T Trio scanner (Siemens Medical System, Malvern, PA) with a standard birdcage coil. Foam cushions and

elastic straps were used to minimize head motion. Diffusion tensor imaging data were collected with two different imaging protocols: multi-shot double spin-echo echo planar imaging (MS-EPI) sequence and single-shot double spin-echo EPI (SS-EPI) sequence. For MS-EPI, a dual spin-echo technique combined with bipolar gradients was used to minimize eddy-current effects. The parameters used for diffusion data acquisition were as follows: diffusion-weighting gradients applied in 60 directions with a b value of 1000 sec/mm^2; repetition time/echo time of 5740/91 msec, field of view of 230×230 mm^2, matrix size of 128×128, resolution of 1.8×1.8×1.8 mm^2, 41 slices with no gap, covering the whole brain. For each diffusion direction, two diffusion-weighted images were acquired, each with one of the possible left-right phase-encoding directions and two averages, allowing for correction of susceptibility related distortion using an algorithm described in the literature (Andersson et al. 2003). For each average of diffusion-weighted images, six images without diffusion weighting (b=0 sec/mm^2) were also acquired with matching imaging parameters. The total MRI/DTI scan time was approximately 50 minutes. For SS-EPI, an SS-EPI sequence with reduced FOV in the phase-encoding direction and partial Fourier imaging technique were used to scan the chimpanzees. The parameters used for diffusion data acquisition were as follows: diffusion-weighting gradients applied in 60 directions with a b value of 1000 sec/mm^2; repetition time/echo time of 5900/84 msec, field of view of 129×230 mm^2, matrix size of 72×128, resolution of 1.8×1.8×1.8 mm^3, 41 slices with no gap, covering the whole brain. For each average of diffusion-weighted images, one image without diffusion weighting (b=0 sec/mm^2) were also acquired with matching imaging parameters. The total MRI/DTI scan time was 53.4 minutes. High-resolution T1-weighted MRI images were acquired with a 3D magnetization-prepared rapid gradient-echo (MPRAGE) sequence for all participants. For subjects scanned using MS-EPI sequence, the scan protocol,

optimized at 3T, used a repetition time/inversion time/echo time of 2400/1100/4.13 msec, a flip angle of 8°, a volume of view of 256×256×154 mm^3, a matrix of 256×256×192, and resolution of 1.0×1.0×0.8 mm^3, with 2 averages. Total T1 scan time was approximately 20 minutes. For subjects scanned using SS-EPI, the scan protocol is similar despite that the resolution is 0.8×0.8×0.8 mm^3 isotropic and volume of view is 154×154×154 mm^3. Pre-processing steps were similar to those used in the processing of human MRI/DTI data.

Macaques brain imaging: All macaques were members of a colony at YNPRC. All MRI and DTI scans were conducted under IACUC approval of Emory University. MRI/DTI data from 8 subjects were used for this study. Prior to scanning, the subjects were immobilized with ketamine injections (2−6 mg/kg, i.m.) and were subsequently anesthetized with an intravenous propofol drip (10 mg/kg/hr) following standard veterinary procedures used at YNPRC. The macaques remained sedated for the duration of the scans as well as the time needed for transportation between their home cage and the scanner location. After completing the MRI scan, the macaques were temporarily housed in a single cage for 6 to 12 hours to allow the effects of anesthesia to wear off before being returned to their home cage and cage mates. The veterinary staff and research staff observed the general well-being (i.e., activity, food intake) of the macaques twice daily after the scan for possible distress associated with anaesthetic accesses.

Both anatomical MRI and diffusion tensor imaging were performed on a Siemens 3T Trio scanner (Siemens Medical System, Malvern, PA) with a standard knee coil. Foam cushions and elastic straps were used to minimize head motion. A specially designed holding device was used to stabilize macaque's head during scanning, with two plastic screws anchoring in the macaque's ear canals tightly. High-resolution T1-weighted MRI images were acquired with a 3D magnetization-prepared rapid gradient-echo (MPRAGE) sequence for all participants. The

scan protocol used a repetition time/inversion time/echo time of 2500/950/3.49 msec, a flip angle of 8°, a volume of view of 128×128×96 mm^3, a matrix of 256×256×192, and resolution of 0.5×0.5×0.5 mm^3, with 3 averages. Total T1 scan time was approximately 33 minutes. Diffusion MRI data were collected with a diffusion-weighted, multi-shot (three segments), spin-echo echo planar imaging (EPI) sequence. A dual spin-echo technique combined with bipolar gradients was used to minimize eddy-current effects. The parameters used for diffusion data acquisition were as follows: diffusion-weighting gradients applied in 60 directions with a b value of 1000 sec/mm^2; repetition time/echo time of 6970/104 msec, field of view of 141×141 mm^2, matrix size of 128×128, resolution of 1.1×1.1×1.1 mm^3, 41 slices with no gap, covering the whole brain. Similar to that for the chimpanzees, diffusion-weighted images were acquired with phase-encoding directions of opposite polarity (left – right), each with 4 averages, to correct for susceptibility induced distortion. For each average of diffusion-weighted images, five images without diffusion weighting (b=0 sec/mm^2) were also acquired with matching imaging parameters. The total MRI and DTI scan time was approximately 90 minutes. Pre-processing steps were similar to those used in the processing of human data.

2.2. Joint representation of gyral shape and structural fiber connection

Since the major objective of this work is to assess the coevolution of gyral folding and structural fiber connection patterns, we employed a joint representation of gyral shape and structural fiber connection in this work. Specifically, our extensive recent studies (Li et al. 2010; Nie et al. 2012) have shown that DTI-derived white matter fiber end points closely follow the gyral folding patterns, as highlighted by the orange arrows in Figure 5. 2(f)-(h). This observation has been replicated in all of the DTI datasets of human, chimpanzee and macaque brains we analyzed, indicating that gyral shape pattern and structural connection pattern have

complementary information that can facilitate quantitative analysis of their coevolution brain patterns across primate species. Therefore, we performed whole-brain fiber tracking (via MEDINRIA, http://www-sop.inria.fr/asclepios/software/MedINRIA/) and aligned cortical surfaces reconstructed from T1-weighted MRI image to DTI space with linear transform matrix obtained from the volumetric registration (via FSL FLIRT). After linear alignment, the misalignment between anatomical space and DTI space caused by distortion is relatively small. Specifically, the average surface distances caused by the misalignment are 2.21 mm for human, 1.76 mm for chimpanzee, and 1.35 mm for macaque, respectively. Then, we performed segmentation of four major gyri, including precentral gyrus, postcentral gyrus, superior temporal gyrus and superior frontal gyrus in each hemisphere, from the above reconstructed cortical surfaces based on expert's interactive labeling. The open-source software Paraview (http://www.paraview.org/) was used for this interactive gyrus segmentation. After each gyrus is segmented from the cortical surface in the DTI image space, the emanating fibers were extracted from the results of whole-brain streamline tractography via a similar method detailed elsewhere (Zhu et al. 2012). As a result, each gyral shape and its structural fiber connections are co-localized and jointly represented on the same gyrus in the DTI space. It should be noted that the joint representation of gyral folding and structural connection patterns treats the brain as a whole via applying in vivo MRI and DTI to study the brain's gray matter (GM) and white matter (WM) architecture. By exploring the complementary information provided by gyral folding and connectivity patterns, this joint representation methodology offers advantages over other approaches that treat gray and white matter separately (Li et al. 2010; Nie et al. 2012), and could provide important insights into the regularity and variability of the brain structure.

Quantification of fiber orientation patterns

To quantitatively measure the relationship between fiber orientation patterns and gyral folding patterns based on the above joint representation, a coordinate system needs to be set up. However, a gyrus' orientation can vary in different ways; for example, the precentral gyrus and postcentral gyrus roughly follow a superior-inferior orientation, while the superior temporal gyrus and superior frontal gyrus have a rough anterior-posterior orientation. This makes it very difficult to set up a global coordinate system along the tangent direction for each gyrus. Instead, we defined a 3-dimensional local Cartesian coordinate system for each gyrus, as shown in Figs. 3a-3d. In each local coordinate system, the average normal direction of vertices on the gyral crest curves, which was obtained by thresholding principal curvatures on the cortical surface, is treated as the **Z** axis (Figure 5. 3(b)). Let **p**, **q** denote two points manually selected at each end of a gyrus, **Y** axis is defined by $\vec{Y} = \vec{Z} \times \overrightarrow{pq}$ and **X** axis is obtained by the right-hand rule (Figure 5. 3(d)). By default，the **Y** axis is identified as the tangent direction of a gyrus in this chapter.

After the local coordinate system has been constructed, we projected the DTI-derived fibers that intersect with the gyrus to the Y-Z plane. The fiber orientation pattern is defined by the angle between Z axis and the fiber's main direction vector on the end that intersects with the gyrus, as denoted by θ in Figure 5. 3(e). As shown in Figure 5. 3(e), if the projection of the main direction vector on Y axis is positive, θ is positive. Otherwise, it is negative. It should be noted that this chapter mainly focuses on the correlation between fiber orientation and gyral folding in the tangent direction, that is, along with the Y axis. Although we may lose certain fiber orientation information in other directions by projecting 3D fibers to the 2D Y-Z plan, this approach enables us to jointly examine the correlation between fiber orientation pattern and gyral folding pattern in the same local coordinate system.

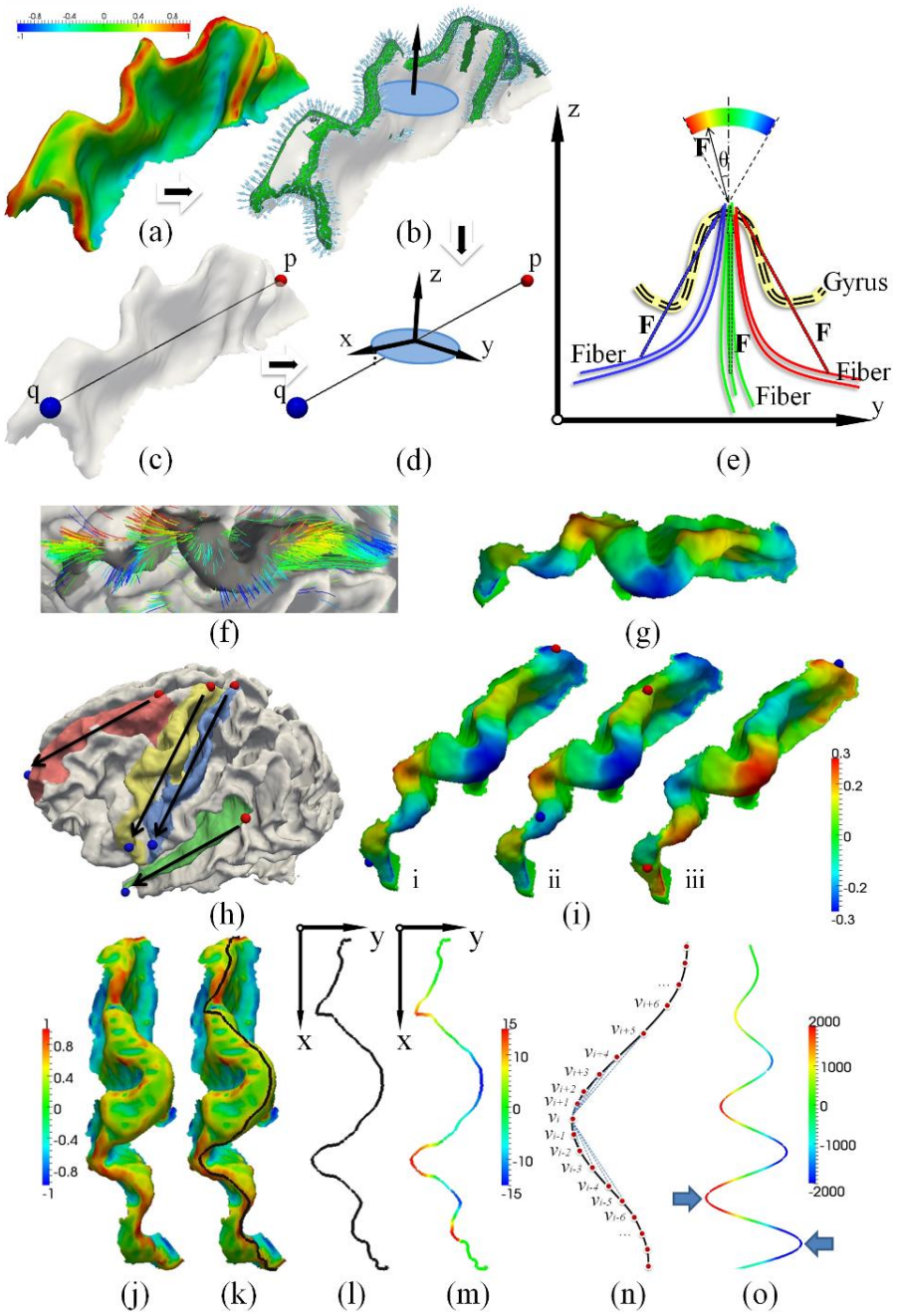

Figure 5. 3. Illustration of quantification of fiber orientation patterns and gyral folding patterns in local coordinate systems constructed on the gyral crest. (a)-(d): Definition of gyral local coordinate systems. (a) Principal curvature of the surface. (b) Gyral normal vectors. (c) Manually selecting two points from both ends of a gyrus. (d) Gyral local coordinate system. (e)-(i): Illustration of fiber orientation patterns. (e) Definition of fiber orientation patterns in the local coordinate systems. (f) Examples of orientation patterns of fibers. (g) Examples of mapping fiber orientation pattern onto the gyrus. (h) Illustration of endpoint pair selection on each gyrus. Black arrows indicate the X direction of each local coordinate

system. The red point is the start point, and the blue point is the end point. (i) Fiber orientation patterns for the same subject with different endpoint pairs. The red point is the start point, and the blue point is the end point. Fiber orientation pattern has been mapped to the gyrus. (j)-(o): Illustration of the methods for quantification of gyral folding patterns. (j) A precentral gyrus color-coded by maximum principal curvature. The color bar is on the left. (k) The gyral crest curve (black line) extracted and overlaid on the gyrus. (l) The gyral crest curve projected to the local coordinate system's X-Y plan. (m) The shape pattern of the crest curve. (n) Illustration of computing plane curve shape pattern. (o) Folding pattern descriptor on simulated curve: $Sin(x) * (x + 100)/(2\pi),\ 0 < x < 7$.

To facilitate quantitative measurements of the correlation between the fiber orientation pattern and the gyral folding pattern, we mapped the fiber orientation pattern (an example shown in Figure 5. 3(f)) to the gyrus that it intersects with, as shown in Figure 5. 3(g). Subsequently, the fiber orientation pattern is color-coded on the gyral crest for both visualization and quantification. It should be noted that the selection of gyral end points **p** and **q** may influence the direction of **X** and **Y** axis, and thus the fiber orientation patterns may vary slightly due to this influence. However, our extensive experience with this approach showed that this type of influence on our final analysis result is relatively small. For instance, Figure 5. 3(i) illustrates one example of how different selections of endpoints for the local coordinate system construction influence the computed fiber orientation patterns. It is evident that the fiber orientation maps in both cases are similar. But if we revert (**p**, **q**) as shown in Figure 5. 3(i), the fiber orientation pattern is flipped due to the flipping of **X** and **Y** axis. Thus, in order to unify the fiber orientation pattern and make the result reliable, we selected the (**p**, **q**) pair on two ends of a gyral ridge in all primate brains by following a superior-posterior to inferior-anterior rule as shown in Figure 5. 3(h).

Quantification of gyral folding patterns

The gyral folding pattern is quantified by the shape of its crest curve on the gyral ridge. We used the fast marching method in (Li et al. 2009) to find the shortest geometric path $\boldsymbol{L}$ weighted by $\boldsymbol{w(l)}$ which is inversely proportional to maximum principal curvature of surface between two manually selected gyral end points **p**, **q** on the surface (Figure 5. 3(j)-(k)) as follows.

$$\boldsymbol{L} = \{\bigcup_{i} \boldsymbol{l_i} \,|\mathbf{min}(\oint_{q}^{p} \boldsymbol{w(l)dl})\} \tag{5.1}$$

where l_i is a section of line on the surface of gyrus such that l_i and l_{i-1} are connected to each other. Denoting $\boldsymbol{L'}$ as the projection of $\boldsymbol{L}$ on the X-Y plan of the gyral local coordinate system defined previously, the shape pattern of each vertex on curve $\boldsymbol{L}$ is defined by the average determinant of the orientation matrix in each vertex's neighborhood on $\boldsymbol{L'}$ (Figure 5. 3(n)):

$$\boldsymbol{s_i} = \frac{\sum_{n}^{j=1} \mathbf{det}(\boldsymbol{O(i,j,L')})}{\boldsymbol{n}} \tag{5.2}$$

where *n* is the size of neighborhood, **det**() is the determinant function, and $O(i,j,\boldsymbol{L'})$ is the orientation matrix of vertex $\boldsymbol{v'_i}$ of $\boldsymbol{L'}$. Denote $(\boldsymbol{x'_i}, \boldsymbol{y'_i})$ as the coordinate of vertex $\boldsymbol{v'_i}$:

$$\boldsymbol{O(i,j,L')} = \begin{vmatrix} \mathbf{1} & \boldsymbol{x'_{i-j}} & \boldsymbol{y'_{i-j}} \\ \mathbf{1} & \boldsymbol{x'_i} & \boldsymbol{y'_i} \\ \mathbf{1} & \boldsymbol{x'_{i+j}} & \boldsymbol{y'_{i+j}} \end{vmatrix} \tag{5.3}$$

As examples, in Figure 5. 3(o), we showed the folding pattern values of a simulated curve of sine functions with linearly increasing amplitudes. We chose the average determinant of the orientation matrix as the folding pattern descriptor of a gyrus for the following reasons. First, it includes the orientation information of a gyral crest curve, e.g., negative values for clockwise or positive values otherwise, as illustrated by the blue arrows in Figure 5. 3(o). Second, it includes local curvature information. The larger its absolute value is, the larger the curvature of the curve

is. In other words, the higher the average absolute value of this descriptor is, the more curved the gyral folding pattern will be. Third, it is robust to noise. As we are considering a local neighborhood when computing this value, it is less influenced by local noises. With these properties, we use the determinant of the orientation matrix on the gyral crest curve as a cortical folding pattern descriptor, and compare its value with the fiber orientation patterns defined in Figure 5. 3(e)

The correlation between fiber orientation patterns and gyral folding patterns

To measure the correlation between fiber orientation patterns and gyral folding patterns, we used the gyral crest curve as a common reference along which we obtained the fiber orientation patterns and computed its Pearson correlation with the gyral folding patterns along the same gyral crest curve. The computational pipeline is illustrated in Figure 5. 4(a)-(d). Before comparison, the patterns in two ends of a gyrus were discarded since the defined folding pattern cannot be reliably computed at the end of a curve.

It should be noted that as the defined local coordinate system is relatively constant for each gyrus, for certain gyri (e.g., the superior temporal gyrus in this chapter), the normal directions on their top ridges may rotate from one end to the other. This could result in a global increasing or decreasing of fiber orientation patterns as shown in Figure 5. 4(e)-(f), which may cause inaccuracy when comparing them with the defined gyral folding patterns. As our gyral folding pattern descriptor only contains local shape information, the global trend of fiber orientation pattern has to be removed before computing their correlations with the gyral folding pattern. Our previous studies demonstrated that this type of trend can be effectively removed by a linear regression model as shown in Figure 5. 4(g)-(h). It is evident that after this de-trending, the fiber orientation pattern and folding pattern are closely correlated along the gyrus, as

highlighted by the purple arrows in Figure 5. 4(h)-(i). In this chapter, our experiments showed that only the superior temporal gyrus needs this de-trending preprocessing.

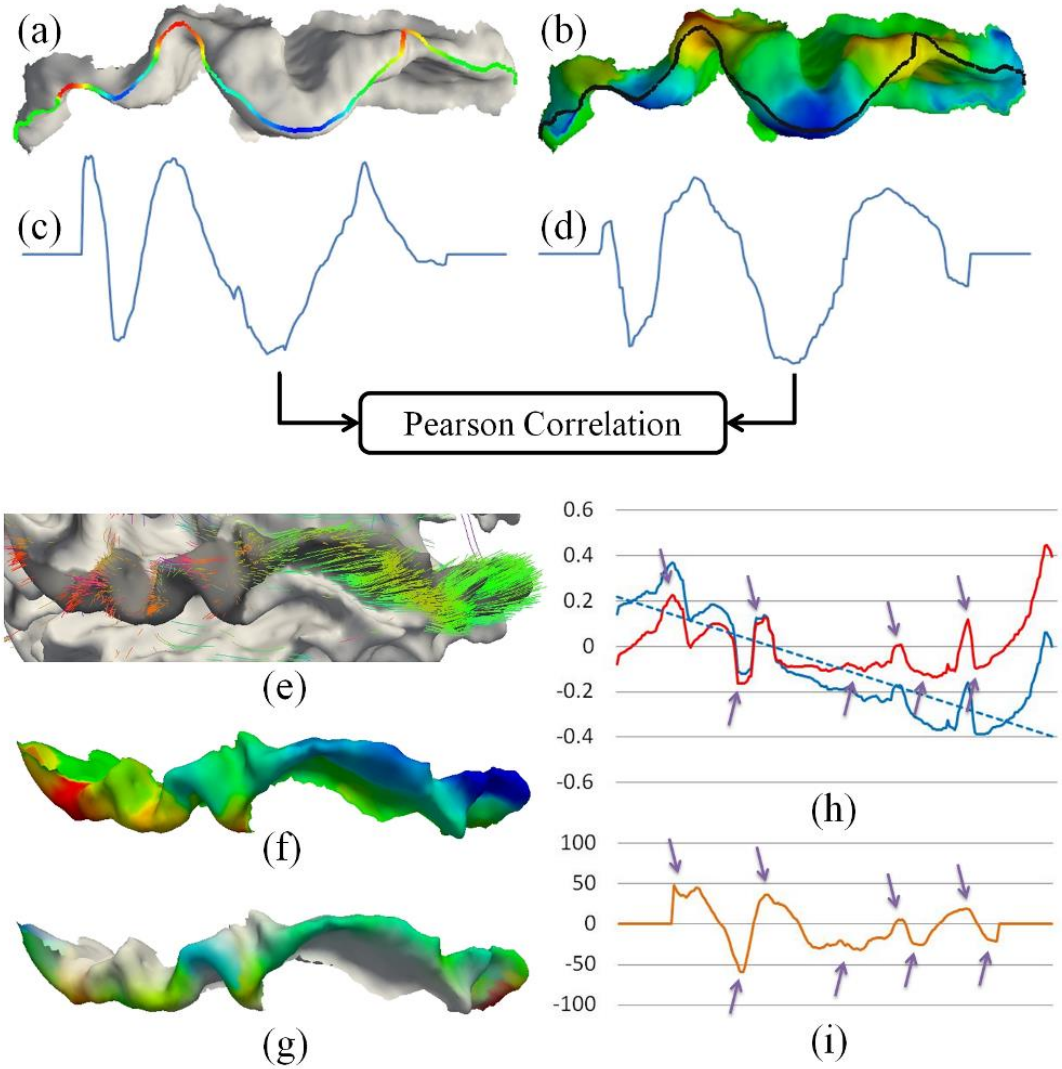

Figure 5. 4. Illustration of our methods for the quantification of correlation between fiber orientation patterns and gyral folding patterns. (a) Gyral folding pattern. (b) Fiber orientation pattern. (c) Gyral folding pattern function curve. (d) Fiber orientation pattern function curve. (e)-(f): An example of the global fiber orientation trend. (g) The fiber orientation patterns after de-trending. (h) De-trending fiber orientation patterns via linear model; blue line: original fiber orientation pattern; blue dash line: the linear model of the original fiber orientation pattern; red line: fiber orientation pattern after de-trending. The gyrus is the same as in (e-g) (i) Folding pattern description of the same gyrus in (h).

RESULTS

Based on the neuroimaging datasets and computational approaches described in the previous section, we investigated the coevolution of gyral folding and structural fiber connection patterns in the three primate species in three manners, allowing us to visually and quantitatively assess the relationships between gyral folding in the tangent directions and fiber orientations patterns. The specifics of these investigations and the results are described below.

Coevolution of cortical folding and structural fiber connection patterns

We compared the complexities of shape patterns of the precentral and postcentral gyri and their fiber connection patterns in three primate species. The average folding pattern description of the gyral crest defined in Eq. (5.3) was used as the gyral shape complexity. The fiber connection pattern complexity was quantified by the diversity of fiber end point destinations, that is, the ratio of end points of fiber connections to the frontal lobe and occipital lobe (purple and blue fiber bundles in Figure 5. 1(b)) out of the total number of fiber connections. Our rationale is that the precentral and postcentral gyri in the macaque brains have much fewer fiber connections to the frontal and occipital lobes, while the precentral and postcentral gyri in chimpanzee and human brains have more and more elaborated fiber connections to the frontal and occipital lobes (Figure 5. 1(b)). Therefore, we postulated that the percentage of fibers connecting the primary motor and sensory areas to the frontal lobe and occipital lobes is a good indicator of structural connectivity complexity for these areas and plotted the complexities of both gyral folding patterns and fiber connection patterns in a 2D diagram for each of the four gyri on both hemispheres in Figure 5. 1. For instance, Figure 5. 5(a) shows the complexities of the left precentral gyrus folding patterns (vertical axis) and fiber connection patterns (horizontal axis) for macaque (triangles), chimpanzee (rectangles) and

human (diamonds) brains. It is evident that there is an approximately linear increasing trend for both complexities of gyral folding patterns and fiber connection patterns, likely reflecting the coevolution of cortical gyral shape and fiber connection patterns. In Figure 5. 5(a), the trend is regressed by a black line. This linear trend can also be observed in the right precentral gyri in Figure 5. 5(b) and in the postcentral gyri on both hemispheres, as shown in Figure 5. 5(c)-(d).

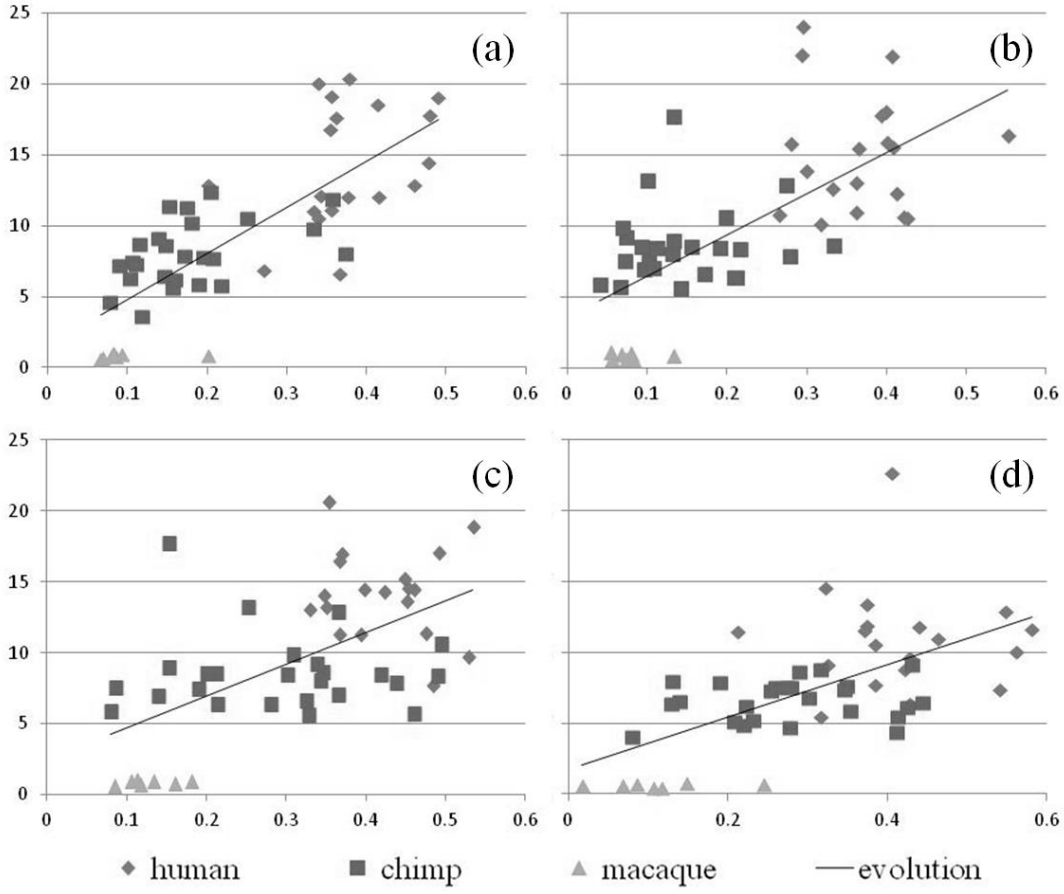

Figure 5. 5. Coevolution of gyral folding and structural connection patterns in four gyri. (a) Left pre-central gyri; (b) Right pre-central gyri; (c) Left post-central gyri; (d) Right post-central gyri. In each sub-figure, the vertical axis represents the fiber connection complexity, and the horizontal axis represents gyral folding pattern complexity.

Based on the results shown in Figure 5. 5, we conjecture that the gyral folding pattern complexity coevolutes with fiber connection pattern complexity in a close, positive relationship,

suggesting a deep-rooted evolutionarily-preserved mechanism underlying the structural fiber connection pattern and cortical gyral folding pattern. In further analysis described in the next two subsections, we further investigated the possible underlying mechanisms that underlie the clear coevolution of cortical folding and structural connections patterns across the three primate neocortices, and tested the hypothesis that the gyral folding pattern is induced or regulated by the axonal fiber pushing.

Visual examination of the relationships between gyral folding and fiber orientations patterns

We examined the relationship between gyral folding and fiber orientation patterns both qualitatively and quantitatively. First, we visually assessed the fiber orientation pattern and gyral shape pattern for four segmented gyri in the right hemisphere in Figure 5. 6. Specifically, Figure 5. 6(a)-(d) illustrate the precentral gyrus, postcentral gyrus, superior frontal gyrus, and superior temporal gyrus, respectively. For each sub-figure, the first column demonstrates the joint visualization of gyral shape and the emanating DTI-derived fibers, the second column shows the color-coded fiber orientation in the local coordinate system, and the last column illustrates the color-coded gyral shape patterns quantified by the descriptor. Each row shows the result for one example of macaque, chimpanzee, and human brains, respectively. By visual examination of these four gyri, it is clear that there is a close relationship between the fiber orientation and cortical folding along the gyral crest curve. For instance, in Figure 5. 6(a), the blue arrows highlight negative fiber orientations in the second column, which co-localize well with the negative folding patterns in gyral shapes, as highlighted by the blue arrows in the third column as well. Meanwhile, the positive fiber orientations highlighted by the oranges arrows in the second column also co-localize well with the positive folding patterns in the third column, which are

pointed to by the orange arrows. For comparison, the corresponding blue and orange arrows are also provided in the first column of joint visualizations in Figure 5. 6. These similar positive correlations between fiber orientation patterns and gyral folding patterns have been replicated in other gyri, as shown in Figure 5. 6(b)-(d). Our extensive observations in all of the three primate cases we studied overwhelmingly demonstrate that there is an evolutionarily-preserved positive correlation between the cortical folding and fiber connection orientation patterns, which support the concept of co-evolution of cortical folding and fiber connection patterns.

Similarly, Figure 5. 7 shows the visualization of fiber connection orientation and cortical gyral folding patterns for four gyri in the left hemisphere. Again, the positive correlation between fiber orientation and gyral folding patterns is evident, as highlighted by the blue and oranges arrows in Figure 5. 7(a)-(d). By joint visualizations shown in Figure 5. 6 and Figure 5. 7, it is clear that for all eight gyri on both hemispheres of three primates, we observed that there exists a positive relationship between fiber orientations and gyral folding patterns. Therefore, we conjecture that the axonal fiber pushing forces induce or regulate the tangent folding patterns of gyral crest curves, as illustrated in Figure 5. 2(b). This conjecture can not only explain the close positive relationships between fiber orientations and folding patterns as shown in Figure 5. 6 and Figure 5. 7, but also well interpret the increasing complexities of cortical gyral folding patterns across primates. For instance, the precentral gyrus in Figure 5. 6(a) exhibits increasing complexity of shapes across primates, e.g., three clear positive folds and three clear negative folds in human, one clear negative fold and two positive folds in chimpanzee, and no clear folds in the macaque. These increasing complexities of cortical gyral folding are exactly mirrored by the increasing complexities of fiber connection patterns, e.g., the denser and complex fiber connections in human and much simpler and sparser fiber connections in chimpanzee and

macaque, as shown in the first column in Figure 5. 6(a). From a biomechanical perspective, it is reasonable to hypothesize that the increasingly complex fibers "push" the gyri into increasingly complex shape patterns, such as more and more positive and negative folds during the evolution of primate brains.

Similar, axonal fiber pushing of tangent gyral folding can well explain other gyri on both hemispheres of three primates, as shown in Figure 5. 6 and Figure 5. 7, e.g., the post-central gyrus in Figure 5. 6(b) and the precentral gyrus on the left hemisphere in Figure 5. 7(a). It should be noted that although the gyral folding patterns and fiber orientation patterns are increasingly complex across the species, the same observation that fiber orientations are positively correlated with tangent gyral folding patterns is well preserved across three primates suggests that axonal fiber pushing might be an evolutionarily preserved mechanism of brain architecture formation and organization. In addition, our approaches have been tested on the same group of chimpanzee subjects scanned with both scan sequence. The results are similar in different scans, thus confirming that our approaches are not sensitive to scan parameters. Finally, the influence of DTI parameters is tested by using different diffusion-weighting gradient directions for tractography for the same subject. Specifically, for the DTI data with 60 directions scanned, we separated the image into two groups by the order of direction. One group contains 30 directions with the odd index from the original file, while the other group contains the rest of 30 directions. The results are very similar in different groups, thus further confirming that our approaches are not sensitive to scan protocols and parameters.

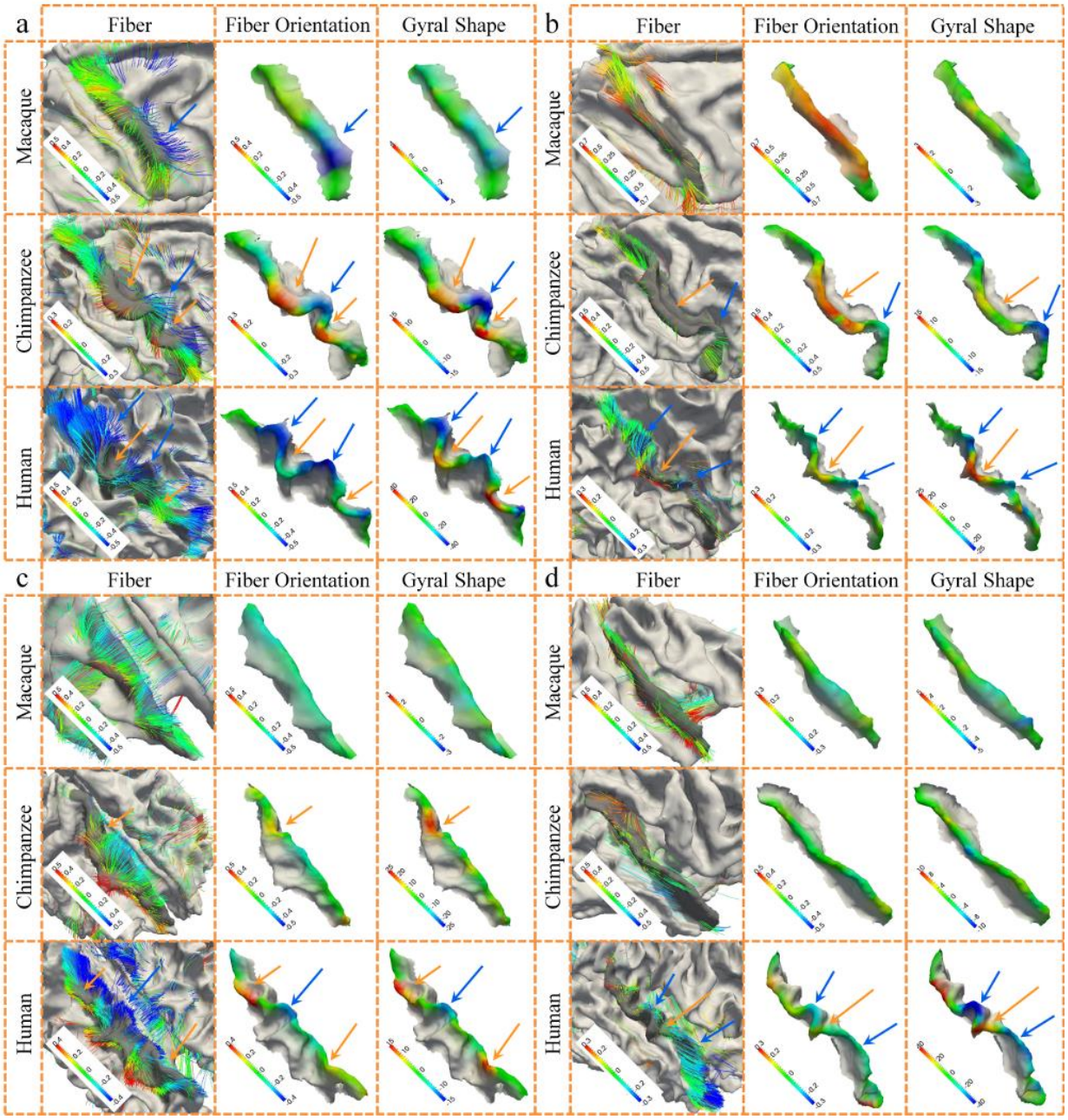

Figure 5. 6. Joint representation of fiber orientation patterns and gyral shape patterns on the right hemisphere. The color bar is on the left bottom and the range varies between subjects for better visualization. (a) Precentral gyrus. (b) Postcentral gyrus. (c) Superior frontal gyrus. (d) Superior temporal gyrus.

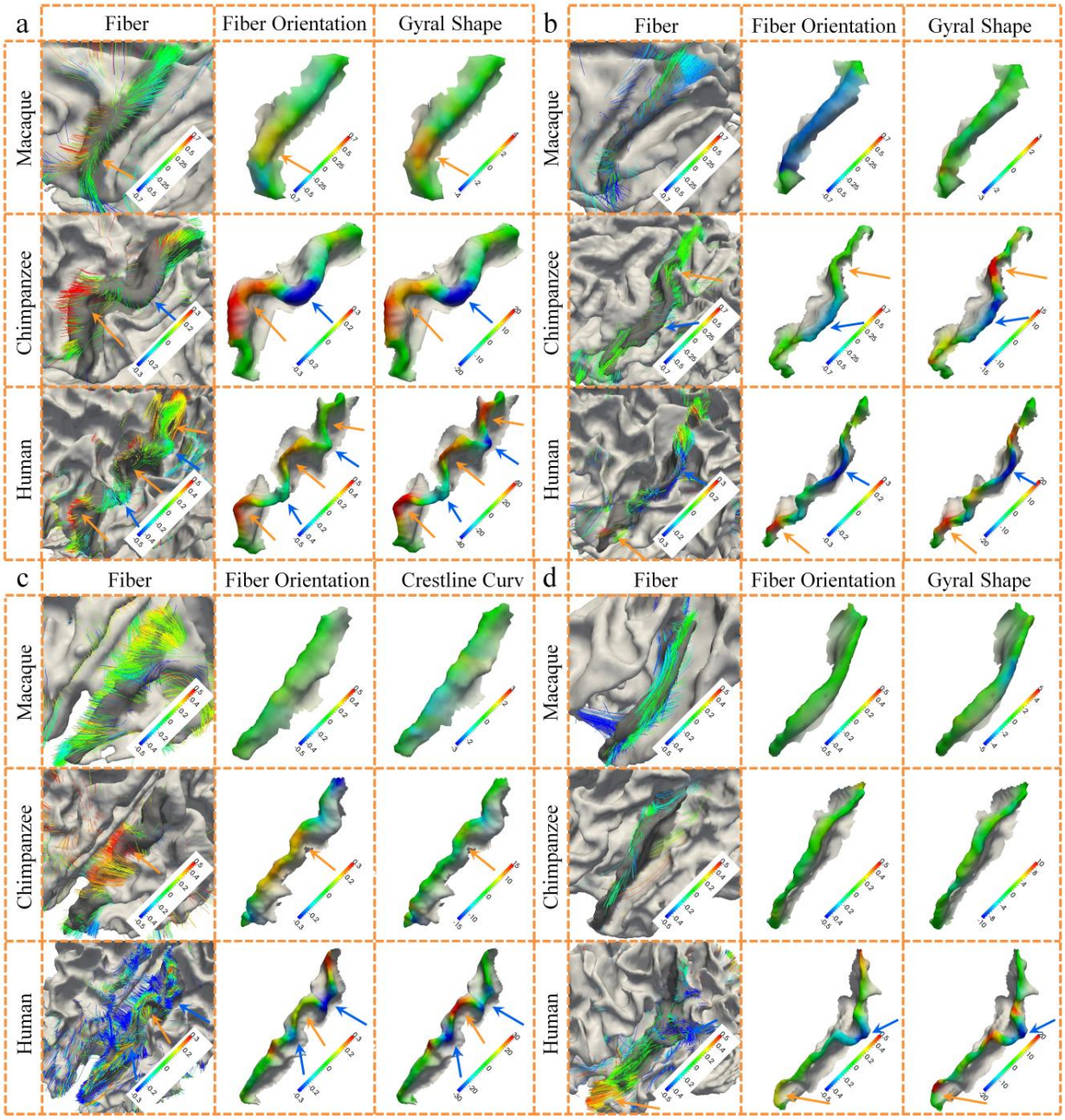

Figure 5. 7. Joint representation of fiber orientation patterns and gyral shape patterns on the left hemisphere. The color bar is on the left bottom and the range varies between subjects for better visualization. (a) Precentral gyrus. (b) Postcentral gyrus. (c) Superior frontal gyrus. (d) Superior temporal gyrus.

Quantification of the relationships between gyral folding and fiber orientations patterns

In addition to the visual examinations aided by Figure 5. 6 and Figure 5. 7, we performed quantitative measurements of the correlation between gyral folding and fiber connection patterns. Specifically, Pearson correlations between the gyral folding patterns and the fiber orientation patterns were measured, and the results are shown in Figure 5. 8. Figure 5. 8(a)-(d) present the results for the right precentral gyrus, the right postcentral gyrus, the left precentral gyrus, and the left postcentral gyrus, respectively. For each sub-figure, the results for chimpanzee and human brains were provided in the first and second rows, respectively. The average correlations for the right precentral gyrus, the right postcentral gyrus, the left precentral gyrus, and the left postcentral gyrus in chimpanzee brains are 0.69, 0.68, 0.75, and 0.73, respectively. The average correlations for the right precentral gyrus, the right postcentral gyrus, the left precentral gyrus, and the left postcentral gyrus in human brains are 0.72, 0.66, 0.69, and 0.64, respectively. Statistical measurements of mean values and standard deviations are displayed on the top of each set of results in Figure 5. 8. In total, the average Pearson correlation for four gyri is 0.67 for 19 human brains we tested, and 0.71 for 24 chimpanzee brains. These relatively high positive correlations between gyral folding patterns and fiber orientation patterns in both chimpanzee and human brains further suggest that axonal fiber pushing might be an evolutionarily-preserved mechanism of brain architecture formation and organization.

It should be noted that due to the relatively straight shapes of gyri in macaques, e.g., as shown in the third columns in Figure 5. 6 and Figure 5. 7, their gyral folding patterns quantifications are more prone to noises and not reliable. Hence, we did not include Pearson correlations of macaques' gyral folding and fiber orientation patterns in our result reports. The positive relationship between gyral folding patterns and fiber orientation patterns in macaque

brains can still be clearly appreciated in the first rows of the sub-figures of Figure 5. 6 and Figure 5. 7, although the closeness of this positive relationship is less pronounced than those in the chimpanzee and human brains.

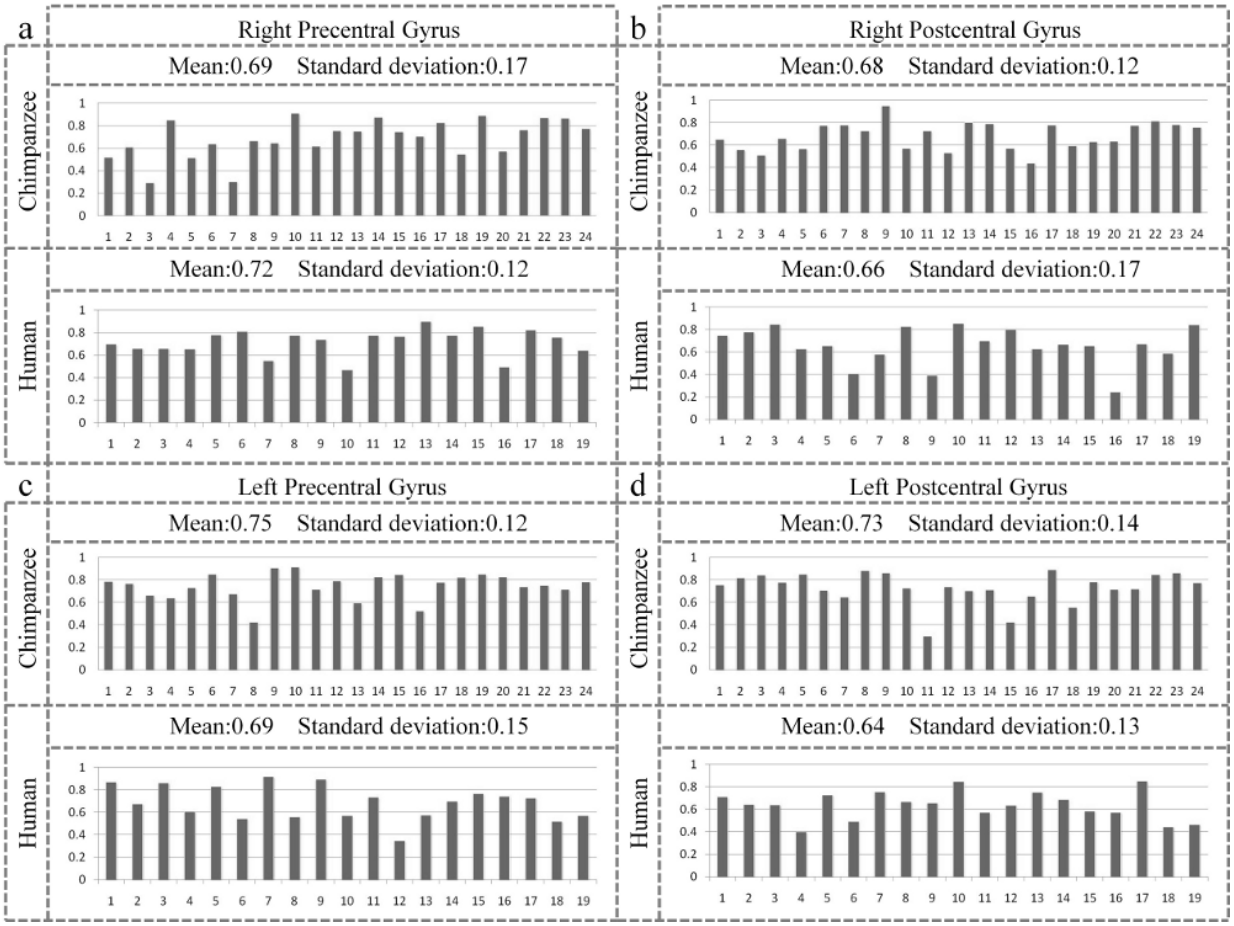

Figure 5. 8. Pearson correlations between fiber orientation patterns and gyral shape patterns of the precentral gyri and postcentral gyri on both hemispheres of 24 chimpanzee and 19 human brains separately. In each sub-figure, the result of chimpanzee is displayed on the top panel, while the human's is on the bottom panel. The mean value and stander deviation are displayed on the top of each panel. The horizontal axis represents the index of primate subject and the vertical axis stands for the Pearson correlation. (a) Right precentral gyrus. (b) Right postcentral gyrus. (c) Left precentral gyrus. (d) Left postcentral gyrus.

DISCUSSION AND CONCLUSION

In this work, we developed, evaluated and applied a novel computational pipeline of algorithms for quantifications of tangent gyral folding patterns and fiber orientation patterns based on a joint representation approach. These quantifications are then mapped onto the same gyral crest curves to enable and facilitate the quantitative measurements of correlations between fiber orientation patterns and tangent gyral folding patterns. Application of these approaches to experimental data obtained from human, chimpanzee and macaque subjects revealed a well-preserved strong, positive correlation of the complexities of tangent gyral folding and fiber connection patterns across three the primate species. Our qualitative and quantitative analyses also found that tangent gyral fold shapes are connected by dense DTI-derived fibers orienting perpendicularly to the gyral crests curves, which has been replicated and confirmed in four major gyri on both hemispheres across the three species. Both of these findings motivated us to hypothesize an underlying mechanism of axonal fiber pushing that drives the co-evolution patterns of gyral folding and fiber connection in primate brains and sculpts the tangent folding patterns of cortical gyri during primate brain evolution. This axonal fiber pushing conjecture well explains not only the folding patterns of gyri along the radial direction of the spherically-shaped cortex, but also the folding of gyral crest along the tangent direction on the cortical surface.

Nevertheless, it should be pointed out that our current study only examined the association between axonal orientation patterns and gyral folding patterns, and the potential causal relationship has not be investigated yet. Future studies of the potential causal relationships entail a combination of different experimental and computational approaches. We conjecture that at least the following two lines of research efforts are worth pursuit in the future. First, DTI and MRI datasets of human genetic disorders with abnormal axonal wiring patterns can be analyzed

and modeled to examine whether or not disrupted axonal connections would be associated with abnormal cortical folding patterns. If it turns out that abnormal axonal wiring caused disrupted cortical folding pattern, it can be considered as a supporting evidence of the causal relationship. For example, the agenesis of the corpus callosum (AgCC) (Tyszka et al. 2011) is a congenital disorder in which corpus callosum is absent. Then, we can compare the differences between the cortical folding pattern of AgCC patients and those of normal controls to see whether or not abnormal axonal wiring would result in disrupted gyral folding pattern. Second, biomechanical experiments and simulations can be performed to further elucidate the possible pushing forces within the wiring axons and their mechanical effects on the growing cortical layers. For instance, by using the atomic force microscopy (AFM) tip as a scalpel to cut axons in cultured neurons, we can release the stress and thus will be able to directly discern between positive and negative tension by observing the relaxation of the axon. The experimental settings could be similar to those in (Xiong et al. 2009). In addition, extensive mechanical modeling and simulations can be performed in the future to further gain mechanical evidences and feasibility of the axonal pushing mechanism of cortical folding.

To date, our axonal fiber pushing theory of cortical folding has been based on the qualitative and quantitative analyses of in-vivo DTI datasets of macaque, chimpanzee, and human brains. In the future, our hypothesis can be further tested using independent micro-scale microscopic bioimaging studies. For instance, the axonal fiber wiring patterns in gyral and sulcal regions could be verified by microscopic histology studies using animal models in the future, which can provide independent and reliable confirmation of our macro-scale neuroimaging studies. It can even be considered to apply the similar electron microscopy (EM) techniques in (Bock et al. 2011) to examine the axonal wiring patterns at the single axon resolution, and test if

the axonal terminations are concentrated on cortical gyri. In addition, time-lapsed confocal microscopic imaging studies could be performed on fast-growing animal models or cultured neurons to probe whether or not there are real axonal pushing forces induced by the wiring axonal cones.

As for data analysis, in the present, we only analyzed four major gyri including the precentral gyrus, postcentral gyrus, superior frontal gyrus, and superior temporal gyrus on both hemispheres to demonstrate the major findings and hypotheses in this chapter. In the future, other major gyri such as middle temporal gyrus, middle frontal gyrus and cingulate gyrus will be investigated for additional confirmation of our findings and theory. Also, other cortical surface shape descriptors and fiber bundle pattern descriptors can be incorporated to measure the complexities of cortical folding and fiber connection patterns. For instance, the curvedness of the gyral crest curve can be quantitatively modeled by a combination of accumulative integral of angles of tangents, bend, centroids ratio, curve bend angle, and concave/convex via the methods in (Hu et al. 2010). Meanwhile, the fiber connection pattern can be quantitatively described by the novel trace-map models (Zhu et al. 2011, 2012). Once both gyral folding patterns and fiber connection patterns are quantitatively modeled, computational simulation models (Nie et al. 2012) based on these quantitative measurements can be adopted to verify the axonal pushing mechanism of cortical folding.

To summarize, our DTI and MRI studies have revealed a positive correlation between axonal fiber orientation and tangent gyral folding pattern across three primate species (macaque, chimpanzee, and human), which suggests a hypothesis of axon fiber pushing mechanism of cortical folding. To further test this hypothesis, many future studies should be performed to replicate the existing findings in other primate species via different imaging modalities, to

reproduce the existing findings in multiple scales, to and investigate the causal relationships between axonal pushing and cortical folding. Once these biological and biomechanical supports are obtained, we can then possibly establish the axonal pushing mechanism as an underlying theory in the future to uniformly explain the co-evolution of gyral folding and axonal fiber connection patterns across primate or mammalian brains. Finally, the potential interactions between the proposed axonal pushing mechanism and other cortical folding mechanisms such as the brain skull constraint (Nie et al. 2012) and behaviors of neurons (Rakic 1988, 2009) and glial cells (Hevner and Haydar 2012), should be studied in the future.

ACKNOWLEDGEMENTS

T Liu was supported by the NIH Career Award EB 006878, NIH R01 HL087923-03S2, and The University of Georgia start-up research funding. K Li was supported by the NWPU Foundation for Fundamental Research. L Li and X Hu were supported by NIH PO1 AG026423. K Li and T Zhang were supported by the China Government Scholarship. The authors would like to thank the anonymous reviewers for their constructive comments that have helped to significantly improve this chapter.

CHAPTER 6

IDENTIFYING GROUP-WISE CONSISTENT WHITE MATTER LANDMARKS VIA NOVEL FIBER SHAPE DESCRIPTOR [5]

[5] Hanbo Chen, Tuo Zhang, Tianming Liu. 2013. Identifying Group-wise Consistent White Matter Landmarks via Novel Fiber Shape Descriptor. *International Conference on Medical Image Computing and Computer Assisted Intervention, Lecture Notes in Computer Science*, 8149:66-73
Reprinted here with permission of the publisher.

ABSTRACT

Identification of common and corresponding white matter (WM) regions of interest (ROI) across human brains has attracted growing interest because it not only facilitates comparison among individuals and populations, but also enables the assessment of structural/functional connectivity in populations. However, due to the complexity and variability of the WM structure and a lack of effective white matter streamline descriptors, establishing accurate correspondences of WM ROIs across individuals and populations has been a challenging open problem. In this chapter, a novel fiber shape descriptor which can facilitate quantitative measurement of fiber bundle profile including connection complexity and similarity has been proposed. A novel framework was then developed using the descriptor to identify group-wise consistent connection hubs in WM regions as landmarks. 12 group-wise consistent WM landmarks have been identified in our experiment. These WM landmarks are found highly reproducible across individuals and accurately predictable on new individual subjects by our fiber shape descriptor. Therefore, these landmarks, as well as proposed fiber shape descriptor has shown great potential to human brain mapping.

INTRODUCTION

Identification of common and corresponding white matter (WM) regions of interest (ROIs) across human brains has attracted growing interest not only in that it facilitates comparison among individuals and populations, but also because it makes it possible to assess structural/functional connectivity in populations (Derrfuss and Mar 2009). One mainstream of previous methods developed in the field so far largely relies on building white matter atlases via registration methods (Mori et al. 2008; Yap et al. 2009) to establish correspondence across subjects. Alternatively, voxel based or fiber tract based features have been newly applied to

identify WM ROIs. For instance, in (Bloy et al. 2011), FOD (fiber orientation distribution) has been applied to identify pathologies. In (O'Donnell et al. 2009), group-wise shape analysis based on fiber tracts has been performed to study WM. In (Zhu et al. 2011), an effective fiber bundle shape descriptor called trace-map has been developed. Base on the trace-map feature (Zhu et al. 2011), a map of discrete cortical landmarks named DICCCOL (Zhu, Li, Guo, et al. 2013) that possess group-wise consistent white matter fiber connection patterns across individuals has been identified.

However, identifying reliable WM landmarks is still a challenging open problem due to the complexity and variability of the brain structure and a lack of effective white matter streamline descriptors (Derrfuss and Mar 2009). For instance, the accuracy and reliability of registration based method are limited due to the substantial variability in brain anatomy and structure between individuals. As for most voxel based methods, they are based on local information and have difficulty in establishing between-subject correspondences. In (Zhu, Li, Guo, et al. 2013), the authors successfully solved the above mentioned issues by introducing an effective fiber bundle shape descriptor of trace map (Zhu et al. 2011). However, since those identified DICCCOL landmarks locate on the cortical surface, the remarkable cortical folding pattern variation may be a major barrier to further improvement.

Motivated by the achievements and the challenges in (Zhu et al. 2011), we developed a novel shape descriptor to characterize the connection patterns of a fiber bundle. Instead of focusing on the shape of streamline fibers as in (Zhu et al. 2011), our descriptor centers on the global connection pattern of fibers. In particular, our proposed descriptor is based on probability density which enables the measurement of directional statistic features. Based on this descriptor, an effective searching/optimization framework is designed to identify WM landmarks that: 1) are

highly connected hubs in the brain; 2) are reproducible across individuals. The reason we aim to identify hubs as landmarks lies in that the human brain networks have been shown to be a small-world network (Bullmore and Sporns 2009). In such network, hubs are more robust, consistent, and could be used to identify sub-nodes. Thus, by identifying hubs in WM, those landmarks can be potentially used as initial points to establish correspondences across individuals, which will bring great potential to the study of human brain mapping, such as WM landmark-guided image registration. In comparison to existing model-driven WM landmark identification methods (Mori et al. 2008; Yap et al. 2009), the major novelty of our work is that it is data-driven and thus can better handle the complexity and variability of the WM architecture.

METHODS

In this chapter, brain ROI is defined as a sphere in the space. To identify WM landmarks with abovementioned properties from ROIs, first, we borrowed the idea from (Zhu et al. 2011) and defined a novel spherical probabilistic distribution based connection map feature vector to describe the fiber profile (Figure 6. 1(b)). Then, the connection pattern complexities of ROIs are measured to identify WM landmarks (Figure 6. 1(c-d)). Finally, the locations of landmarks are iteratively optimized in each subject's own space to increase group-wise consistency of these landmarks' connection profiles (Figure 6. 1(e)). The computational pipeline of the proposed framework is summarized in Figure 6. 1.

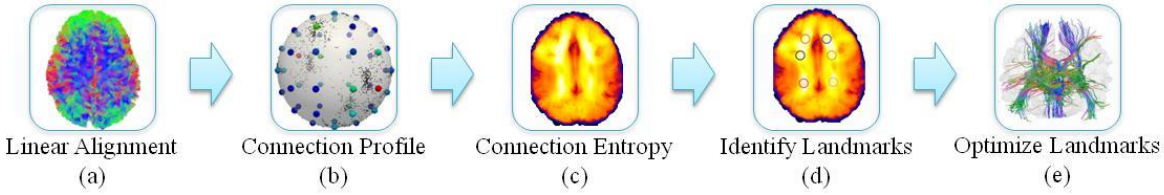

Figure 6. 1. Illustration of the computational pipeline, consisting of 5 steps.

ROI Connection Map

First, definitions of several key concepts and terms are given.

ROI fiber bundle: An ROI is defined as a sphere with a predefined radius (5mm in this chapter). The fiber streamlines passing through this sphere is viewed as the fiber bundle of the corresponding ROI.

Fiber principal orientation: For each fiber, its principal orientation is described by a norm vector $\boldsymbol{v}$ which is the first principal component of the points $\boldsymbol{X}$ along the fiber such that:

$$\max(\sum_{x_i \in X} (v \cdot (x_i - \bar{x}))^2 \mid |v| = 1) \tag{6.1}$$

where $\bar{x}$ is the center of the points in $\boldsymbol{X}$.

Fiber connection profile: For a bundle of fibers, by projecting the principal orientation $\boldsymbol{v}$ of each fiber to a unit sphere, the connection profile of this fiber bundle can be represented and interpreted by the points distributed on the sphere. As illustrated in Figure 6.2(a-b), the complex fiber bundle connection pattern is mapped to the surface of a sphere without the loss of global information and could be further reduced in dimension via directional statistics method. Notably, as the fiber is non-directional connection, both its principal direction $\boldsymbol{v}$ and the opposite direction $-\boldsymbol{v}$ will be projected onto the sphere.

Connection map: The probability density of orientation vector on the sphere is applied to describe the connection map of fiber bundles. Specifically, the sphere is subdivided into 48 equal sized pixels as defined in the HEALPix (Gorski et al. 2005). The number of points within each pixel out of the total number of points is calculated as the probability density. In this way, the fiber connection profile is represented by a connection map with a vector of 48 numbers such that:

$$P(V) = \{P_1(V), P_2(V), \cdots, P_{48}(V)\} \tag{6.2}$$

$$P_k(V) = \frac{\|V \cap R_k\|}{\|V\|} \quad (k = 1 \cdots 48) \tag{6.3}$$

where R_k is the area covered by pixel k, and $\|\boldsymbol{V}\|$ is the number of points on the unit sphere. The advantage of this representation is the capability of representing complex fiber bundle connection pattern with a simple one dimensional feature vector without the loss of major information. As shown in Figure 6.2, the connection maps are similar for the fiber bundles sharing similar shapes. For the bundles with different shapes, the connection maps would be distinct. Notably, this representation may have difficulty in distinguishing the fiber bundles with similar shapes but connecting in the opposite direction, or the fiber bundles with similar orientations but different lengths (e.g. the anterior thalamic projection V.S. the inferior frontal-occipital and uncinate fasciculus). These issues could potentially be solved by defining fiber connection direction and introducing multiple spherical shells for fiber bundles with different lengths.

Connection entropy: As the HEALPix pixels (Gorski et al. 2005) are the squares evenly distributed on the sphere with equal size, the entropy of orientation vectors $\boldsymbol{V}$ distributed on the sphere could be directly obtained from ***P(V)***:

$$H(V) = \sum_{i=1 \cdots 48} - P_i(V) \log_{48} P_i(V) \tag{6.4}$$

Connection similarity: The similarity between two connection maps is measured by cosine similarity:

$$S(P(V_i), P(V_j)) = \frac{P(V_i) \cdot P(V_j)}{\|P(V_i)\| \cdot \|P(V_j)\|} \tag{6.5}$$

Both connection entropy and similarity are values between 0 and 1. As shown in Figure 6.2, higher connection entropy indicates higher connection pattern complexity, and higher similarity value indicates higher similarity between fiber bundles.

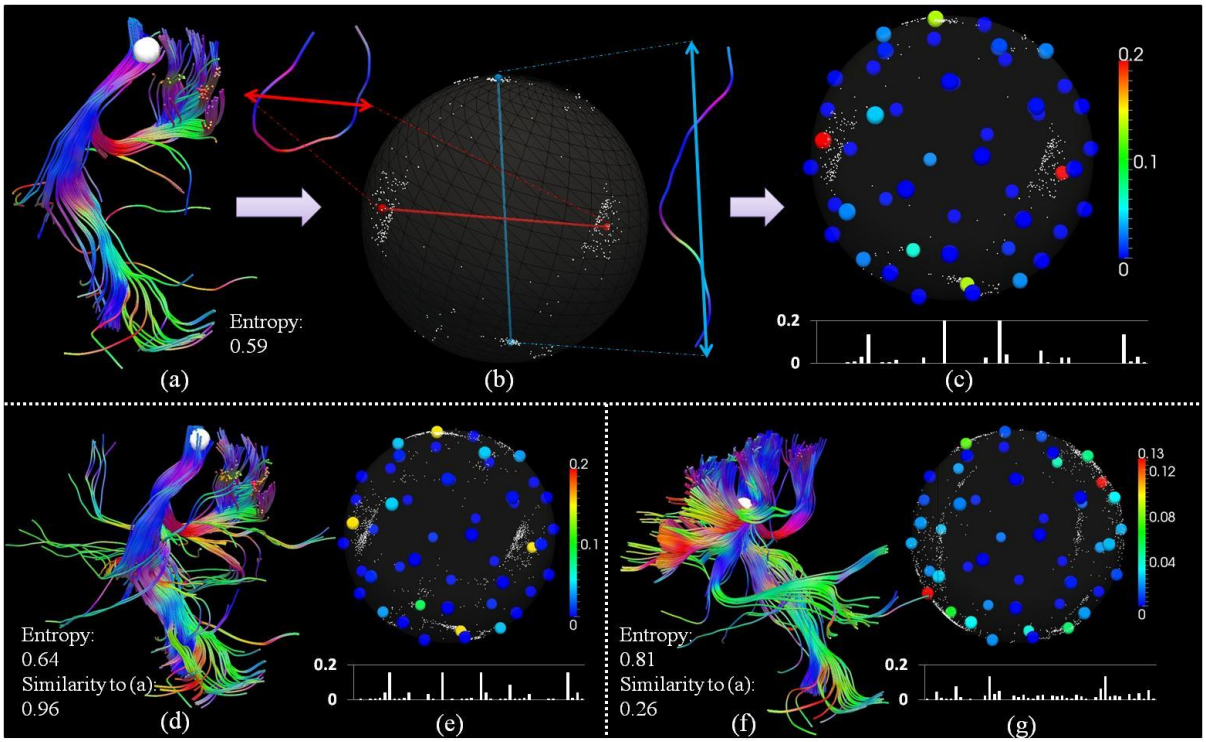

Figure 6.2. Illustration of ROI connection profile. (a), (d), (f): DTI-derived fibers connected to an ROI. The ROI is defined by a sphere in space (white bubble). (b) Illustration of projecting fibers' orientations to a sphere to obtain connection profile. The white dots are the projection points of fibers. The red and blue lines indicate the main orientation of the corresponding fibers and their projections on the unit sphere. (c), (e), (g): The probabilistic distributions of connection profiles of the fiber bundles shown on their left. The center of each sampling pixel is shown and color-coded by the probability density. Corresponding connection map feature vector is shown at the bottom by the histogram.

Identify, Optimize and Predict WM Landmarks

To identify the group-wise consistent WM landmarks that play the hub roles, we need to find the ROIs that maximize the connection entropy (meaning more diverse connections) and cross-subject connection similarity (meaning group-wise consistency) at the same time. The optimization is thus designed to maximize the energy function (equivalent to minimizing the distance function) described below:

$$E(X) = \sum_{x_i \in X} (E_{\text{int}}(x_i) + \lambda E_{ext}(x_i)) \tag{6.6}$$

$$E_{\text{int}}(x_i) = \sum_{j=1\cdots n} H(V(F(x_i^j))) \tag{6.7}$$

$$E_{ext}(x_i, \bar{X}) = \sum_{j=1\cdots n} S(V(F(x_i^j)), \overline{V(F(X))}) \tag{6.8}$$

where $\boldsymbol{X}$ is the set of a landmark in all subjects. $E_{int}(x_i)$ is the internal energy function of connection entropy. $E_{ext}(x_i)$ is the external energy function of connection similarity. λ is the tradeoff (empirically set to 1 in this chapter). $F(x_i^j)$ is the fiber bundle passing through the landmark x_i of subject j.

Algorithm 6.1

Input:	Initial Landmarks **X**, Streamline Fibers **F**
1	For landmark i
2	For subject j
3	For k=1…N
4	Generate random vector v_{random}
5	If $E(x_{ij}+v_{random})>E(x_{ij})$
6	$x_{ij}=x_{ij}+v_{random}$
7	Re-do step 2 to 6 if location of x_i changed

The landmark searching framework follows the pipeline shown in Figure 6. 1. First, the subjects are initially aligned to the same space by linear registration (FSL FLIRT (Jenkinson et al. 2012)). Then, taking each voxel in the space as the center of an ROI, the connection map entropy of fiber bundles passing through each ROI is computed for each subject. By averaging these connection entropy images, a group-wise connection entropy map is obtained (Figure 6.3(a)). Distinguishable regions with high average connection entropy values in this map are visually identified as the initial landmarks. Due to the individual variability and misalignment, the fiber profiles of these initial landmarks could be different. To solve this problem, the landmarks' locations are optimized iteratively with random walks in each subject to maximize the energy function in Eq. (6.6) as described in Algorithm 6.1. After optimization, the converged landmarks are then used as templates for the prediction on new individual brains. The prediction

process used a similar framework as an optimization. First, the brain of a new subject with DTI data is registered to the template space. Then, the space around the initial location of each landmark is searched for the point that maximizes external energy $E_{ext}(x^*, \overline{X}_{template})$ defined in Eq. (6.8) to guarantee the similarity with the template.

EXPERIMENT RESULTS

Two sets of data are applied. One is acquired from 18 healthy young adults who are equally distributed as training subjects and prediction testing subjects. The parameters are: matrix size 128×128, 60 slices, image resolution 2×2×2mm^3 isotropic, TR=15s, ASSET=2, 3 B0 images, 30 optimized gradient directions, b-value=1000. Another dataset publicly released by Human Connectome Project (HCP)(Van Essen et al. 2012) contains DTI data of 64 healthy subjects. This dataset is applied to test the prediction of trained landmarks. The DTI data preprocessing was performed via FSL (Jenkinson et al. 2012) which includes eddy current correction, skull removal, computing FA image, tissue segmentation, and linear registration. Fiber tracking was performed via MedINRIA (Toussaint et al. 2007) using streamline model and then registered to the same space.

After preprocessing, entropy map is computed for randomly picked subjects with different subject numbers (6/8/9/10/12/14). The result is similar and consistent between different groups with different sizes Figure 6.3(a,c). Thus we randomly picked 9 subjects for training. Finally, 12 landmarks with high connection entropy were visually identified and then automatically optimized as shown in Figure 6.3(a-b). Taking the training subjects as the template, these 12 landmarks are predicted on other 9 subjects as well as 64 subjects from HCP data for validation. The average internal energies and external energies are shown in Figure 6.4. For training data, both internal and external energies are relatively high, which indicates that

these landmarks are consistent connection hubs in brain WM. For prediction data, compared with initial landmarks (obtained via linear registration), the energies of finally optimized landmarks are much higher, which suggests that these landmarks are very reproducible in new subjects and could be predicted with our proposed framework.

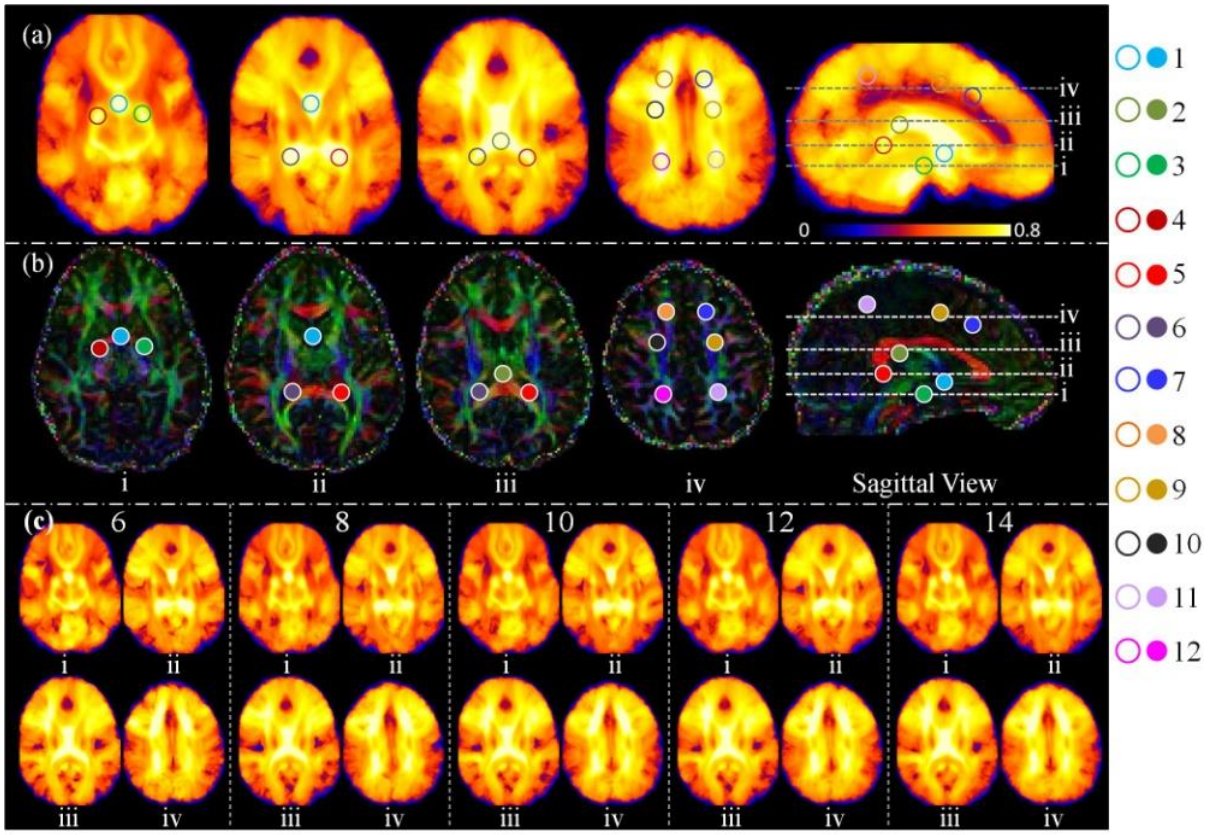

Figure 6.3. Visualization of average entropy map and the location of 12 landmarks. The location of each landmark is indicated by colored ring/bubble. The location of each axial plan is illustrated by the dash line in the sagittal view on the right. (a) Average entropy map of 9 randomly picked subjects. (b) Slices of RGB color-coded principal diffusion tensor direction of template subject volume with the corresponding view to (a). (c) Average entropy map of randomly picked subjects with different numbers (6/8/10/12/14). The view is the same as (a).

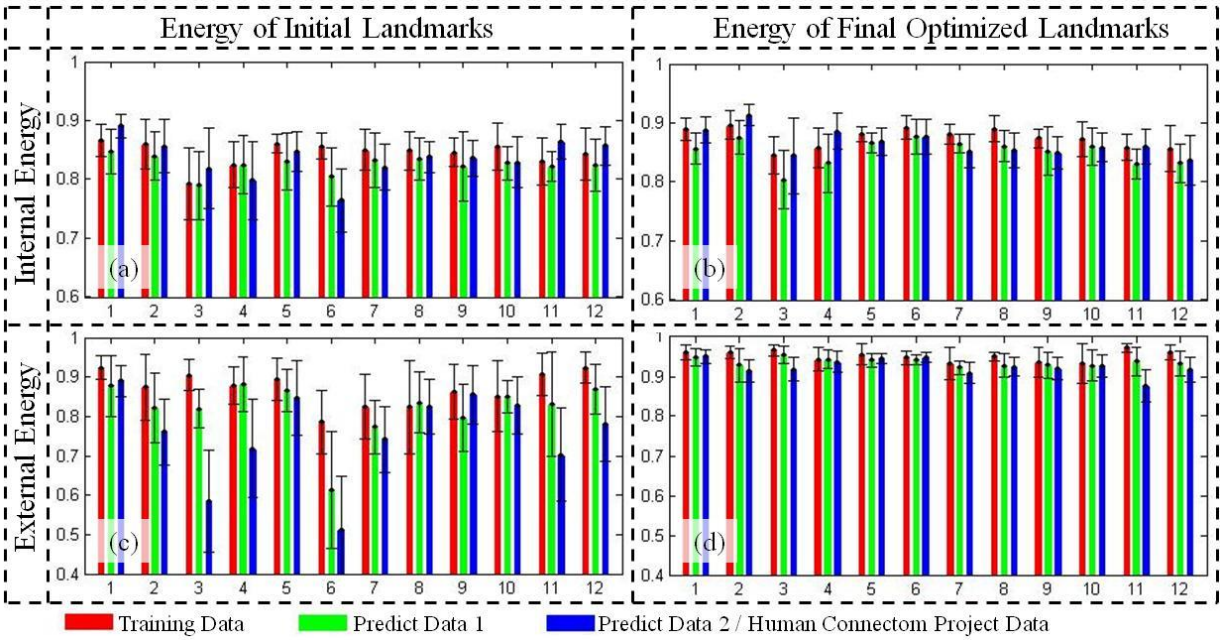

Figure 6.4. Average internal and external energy of each landmark in a different dataset.

To further examine the anatomical meaning of these landmarks, we randomly picked one training subject and one prediction subject to visualize major pathways passing these landmarks (Figure 6.5). By observation, all these landmarks locate at the intersection point or the connection concentration regions of major fiber pathways. For instance, landmark 3 and 4 are close to the thalamus of each brain spheres, and the fiber tracts such as thalamic radiations, corticopontine tract and corticalspinal tract concentrate around this region. For landmark 5 and 6, the fiber pathways from different lobes intersect at this region, e.g. corpus callosum, posterior thalamic radiation, superior longitudinal fasciculus, and superior longitudinal fasciculus, and stria terminalis/fornix. The pathways that go through these landmarks will be further examined in our future work.

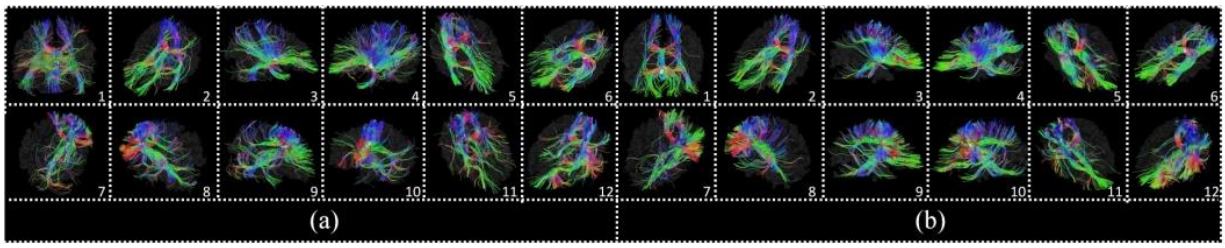

Figure 6.5. Visualization of the fiber bundle of 12 landmarks of (a) a training subject and (b) a testing subject. The landmarks are represented by white bubbles in each sub-figure. The IDs of the landmarks are listed in the right-bottom corner.

CONCLUSION AND DISCUSSION

A novel fiber shape descriptor has been proposed to characterize the connection patterns of a fiber bundle. The advantage of this descriptor lies in that: (1) it is based on orientation probability density distribution, thus enabling direct calculation of directional statistic features such as similarity or entropy; (2) it can be efficiently calculated with a decision tree which makes it fast to compute. Our validation experiment suggests that this descriptor can quantitatively measure the similarity and connection complexity of fiber bundles with high accuracy. Based on proposed descriptor, a novel computational framework has been developed to identify and predict landmarks that are group-wise consistent connection hubs in WM region. Finally, 12 landmarks with dense connection and high reproducibility across individuals are identified and validated. The major novelty and contribution of WM landmark discovery framework lie in its data-driven nature that can better handle the complexity and variability of the WM structures, in comparison to existing model-driven methods.

In the future, these WM landmarks will be used as initial points to establish cross-individual correspondences for brain image registration. Also, a hierarchical brain connection map will be built based on these WM landmarks to facilitate brain structural/functional connection studies in population. For instance, with each individual, we will first recognize their

WM landmarks and then the consistent cortical regions that are connected to these landmarks. Afterward, the sub-connected regions between these consistent cortical regions could be recognized iteratively to populate the landmarks on the cortical brain with consistent connectomes. Finally, it is noted that future applications of the proposed fiber shape descriptor are not limited to the framework introduced. It has broader potential to be applied in fiber shape related clustering problems such as connection based cortical segmentation optimization (Clarkson et al. 2010) or diffusion tensor image based functional ROIs prediction (Zhang, Guo, et al. 2012).

ACKNOWLEDGEMENTS

Data were provided [in part] by the Human Connectome Project, WU-Minn Consortium (Principal Investigators: David Van Essen and Kamil Ugurbil; 1U54MH091657) funded by the 16 NIH Institutes and Centers that support the NIH Blueprint for Neuroscience Research; and by the McDonnell Center for Systems Neuroscience at Washington University.

CHAPTER 7

INFERRING GROUP-WISE CONSISTENT MULTIMODAL BRAIN NETWORKS VIA MULTI-VIEW SPECTRAL CLUSTERING [6]

[6] Hanbo Chen, Kaiming Li, Dajiang Zhu, Xi Jiang, Yixuan Yuan, Peili Lv, Tuo Zhang, Lei Guo, Dinggang Shen, Tianming Liu. 2013. Inferring Group-wise Consistent Multimodal Brain Networks via Multi-view Spectral Clustering, *IEEE Transactions on Medical Imaging*. 32(9):1576 - 1586.

ABSTRACT

Quantitative modeling and analysis of structural and functional brain networks based on diffusion tensor imaging (DTI) and functional MRI (fMRI) data have received extensive interest recently. However, the regularity of these structural and functional brain networks across multiple neuroimaging modalities and also across different individuals is largely unknown. This chapter presents a novel approach to inferring group-wise consistent brain sub-networks from multimodal DTI/resting-state fMRI datasets via multi-view spectral clustering of cortical networks, which were constructed upon our recently developed and validated large-scale cortical landmarks - DICCCOL (Dense Individualized and Common Connectivity-based Cortical Landmarks). We applied the algorithms on DTI data of 100 healthy young females and 50 healthy young males, obtained consistent multimodal brain networks within and across multiple groups, and further examined the functional roles of these networks. Our experimental results demonstrated that the derived brain networks have substantially improved inter-modality and inter-subject consistency.

INTRODUCTION

Studying structural/functional brain networks via diffusion tensor imaging (DTI)/functional magnetic resonance imaging (fMRI) has attracted increasing interest recently due to their potential in elucidating fundamental architectures and principles of the brain (Bassett and Bullmore 2009; Bullmore and Sporns 2009). Taking brain regions as nodes and the structural connections or functional correlations between these regions as edges, the brain can be viewed as a graph, and thus can be analyzed using graph theory principles in computer science (Watts and Strogatz 1998). For instance, a variety of recent analysis on brain networks via graphical approaches have shown that both functional and structural networks of human brain

share multiple properties with common complex networks (e.g., social network), including small-worldness, scale free (a few highly-connected hubs) and modularity (Sporns and Zwi 2004; Salvador et al. 2005; Achard et al. 2006; He et al. 2007; Iturria-Medina et al. 2007, 2008; Hagmann et al. 2008; Bullmore and Sporns 2009). Furthermore, it is reported that the structural network modularity plays a key role in generating persistent and dynamic functional patterns (Kaiser et al. 2007) and also determining the hierarchical functional architectures (Zhou et al. 2006; Müller-Linow et al. 2008). Thus, constructing brain networks that are structurally and functionally meaningful and consistent is crucial to unveiling the brains' fundamental principles (Supekar et al. 2009; Zhang, Guo, et al. 2012).

Among tremendous efforts in the exploration of brain networks, many of them adopt the single MRI imaging technique, although their approaches may be different. For instance, some studies used information from MRI to obtain brain modules. In (Chen et al. 2008), six structural modules in the brain that have the firm correspondences with brain functional regions were revealed by comparing brain cortical thickness measured by MRI. In addition, more studies used the advanced diffusion imaging technique such as diffusion tensor imaging (DTI) and diffusion spectrum imaging (DSI) to construct brain structural networks and obtain corresponding structural clusters. In (Hagmann et al. 2008), an analysis of large-scale brain structural networks constructed by DSI reveals a structural core in the posterior medial and parietal cerebral cortex, together with several modules. On the other hand, thanks to the powerful technique of fMRI, *in vivo* analysis of human brain functional network becomes possible. For instance, in (Greicius et al. 2003), the resting state module of the human brain has been analyzed by comparing fMRI BOLD signals under task with the ones in resting state (R-fMRI).

Essentially, these studies might be substantially improved by integrating multimodal information (Bassett and Bullmore 2009). It has been shown that anatomical structural network connections play a key role in determining and maintaining functional patterns (Bullmore and Sporns 2009). In general, better quantitative characterization of the relationship between multimodal brain networks and its consistency across individuals could significantly advance our understanding of the human brain architectures. However, this important issue has been rarely investigated due to the following challenges. First, the variability across individuals makes it difficult to define reliable regions of interest (ROIs) that has group-wise consistency. In general, most brain parcellation approaches have difficulty in establishing across-subjects correspondences. This problem has been overcome by warping brains into an atlas space via image registration algorithms and further use the manually-segmented regions in the atlas as ROIs despite its limitations in accuracy and robustness (Hellier et al. 2003). Another set of methods from the functional perspective is using task-based fMRI to detect functionally-corresponding ROIs (Greicius et al. 2003). Nevertheless, the cost and time in fMRI data acquisition is the major restriction in obtaining data for large-scale networks and for large populations. Thus, it is very challenging to acquire large-scale group-wise consistent ROIs upon which to construct brain networks. Second, it is also very challenging to achieve the consistency between structural and functional brain networks that are derived from the different imaging modality, i.e., DTI and R-fMRI, respectively. As shown in Figure 7. 1, and also as reported by Honey et al.(Honey et al. 2009), there is significant variability between functional and structural networks which makes it difficult to define and detect common networks between modalities.

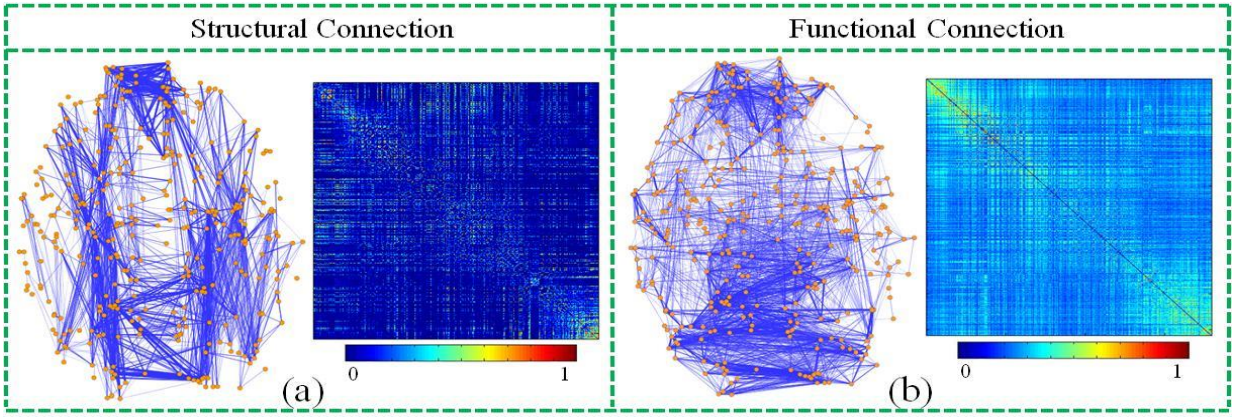

Figure 7. 1. An example of the constructed structural (a) and functional (b) brain networks. Both networks were composed of the same set of 358 DICCCOL ROIs as nodes. Each sub-figure shows a joint view of ROIs (orange dots) and their connections (blue lines), along with the corresponding connectivity matrix on the right.

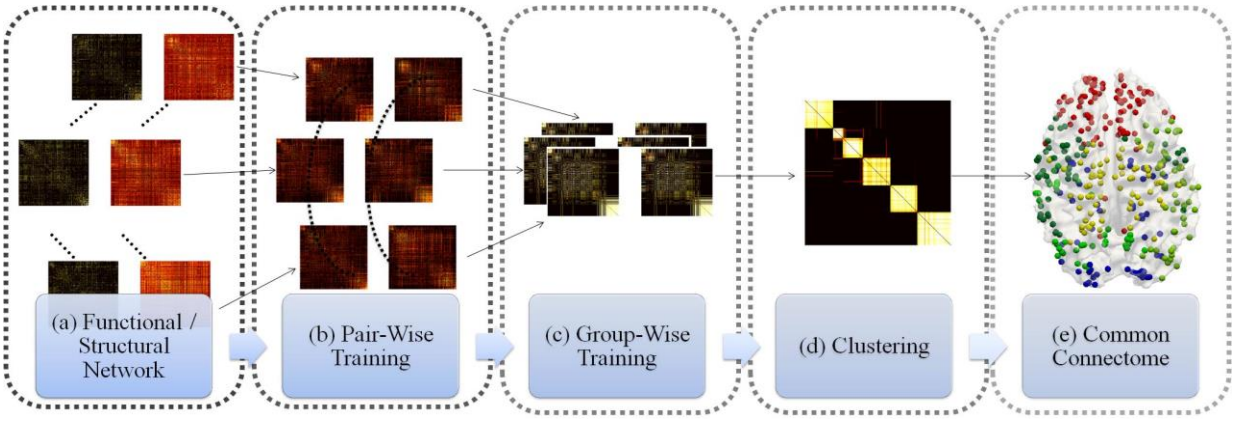

Figure 7. 2. Illustration of the computational pipeline of the proposed method.

In response to the abovementioned challenges, this chapter presents a novel approach to infer group-wise consistent brain networks from multimodal DTI/R-fMRI datasets via multi-view spectral clustering of large-scale cortical landmarks and their connectivity graphs. Specifically, we defined network nodes by our recently developed and validated brain landmarks, namely DICCCOL (Dense Individualized and Common Connectivity-based Cortical Landmarks) (Zhu, Li, Guo, et al. 2013). As shown in Figure 7. 1, the DICCCOL system at the

current stage is composed of 358 cortical landmarks, each of which was optimized to possess consistent group-wise DTI-derived fiber connection patterns across populations (Zhu et al. 2012; Zhu, Li, Guo, et al. 2013). The neuroscience basis is that each cortical region's cyto-architectonic area has a unique set of extrinsic inputs/outputs (called the "connectional fingerprint" (Passingham et al. 2002)), which generally predicts the function that each cortical area could possibly possess. According to our extensive structural and functional validations (Zhu, Li, Guo, et al. 2013), these landmarks possess structural and functional consistency and preserve correspondences across individuals. Based on these landmarks, we constructed both structural and functional brain networks using multimodal DTI/R-fMRI data for 150 healthy young adult brains (aged 17-28 years old, with 100 females and 50 males) (Yan et al. 2011). We equally separated these subjects into three groups (2 groups of females and 1 group of male) for the purpose of comparison and reproducibility examination. Then, we developed and applied an effective multi-view spectral clustering algorithm to derive the consistent multimodal brain networks. Specifically, we considered each structural or functional network in a subject as a separate view of the studied large-scale network, and then modeled the clustering of group-wise consistent multimodal brain sub-networks in an unified multi-view clustering framework, by which the substantial variability of large-scale brain networks across modalities (DTI and R-fMRI) and different individuals (50 subjects in each training group) can be modeled and handled by the powerful multi-view spectral clustering method. The prominent advantage of multi-view spectral clustering methodology is that it can effectively deal with heterogeneous features by maximizing the mutual agreement across multimodal clusters in different views (Kumar and III 2011). This is actually the major methodological novelty and contribution of this chapter.

METHOD

In this section, we will introduce our computational pipeline of the proposed algorithm, which is summarized in Figure 7. 2. First, after obtaining 358 whole-cortex dense landmarks based on our recently developed DICCCOL (Zhu, Li, Guo, et al. 2013), we constructed the functional connections and structural connections between these DICCCOL landmarks with the R-fMRI and the DTI. Based on this, we trained each pair of connectivity matrices, subject by subject, to obtain the common connections across modalities while retaining individual information of each subject, and then trained and combined these pair-wise common matrices group-wisely. The respective co-training algorithms will be introduced. In the end, the final group-wise multi-modality common connectomes are obtained using spectral clustering.

Multimodal Brain Network Construction

In response to the first challenge, i.e., to acquire large-scale group-wise consistent ROIs upon which to construct brain networks, we recently developed and validated 358 cortical landmarks that have intrinsically-established structural and functional correspondences in different brains (Zhu, Li, Guo, et al. 2013), which provides the natural and ideal nodes for brain network construction. Based on these 358 cortical landmarks/ROIs (Figure 7. 1), we constructed both structural (Figure 7. 1(a)) and functional (Figure 7. 1(b)) networks for 150 healthy brains with multimodal DTI/R-fMRI data. Specifically, to construct structural connection matrix, the connection strength between each pair of ROIs is defined as the average FA (fractional anisotropy) value along the fiber bundle connecting these two ROIs. If there is no connecting fiber bundle between two ROIs, the connection strength is set to 0. As for the connectivity matrix of functional networks, they are constructed based on R-fMRI data as follows. First, we performed brain tissue segmentation directly on DTI data (Liu et al. 2007), and used the gray

matter segmentation map as a constraint for R-fMRI BOLD signal extraction. A principal component analysis was then conducted for the R-fMRI time series of all gray matter voxels within an ROI, and the first principal component was adopted as its representative R-fMRI BOLD signal. Finally, the functional connection strength between ROIs is defined as the Pearson correlation of their R-fMRI BOLD signals. An example of the constructed structural and functional networks is shown in Figure 7. 1.

Spectral Clustering

Taking a graph $G=(V,E)$ with $\|V\|=n$ nodes, the objective of clustering problem is to find cluster indicator matrix $C=\Re^{n\times k}$ such that for the i^{th} column of C, $c_{ij}=1$ iff. the j^{th} node belongs to the i^{th} cluster. Otherwise, $c_{ij}=0$. The spectral clustering algorithm solves this problem by solving the following equation (Shi and Malik 2000):

$$(D-W)y=\lambda Dy \tag{7.1}$$

where $W=\Re^{n\times n}$ is the affinity/similarity matrix of G, which is a semi-positive definite matrix. D is a diagonal matrix with the degree $d_i=\sum_{j=1}^{n} w_{ij}$ for the corresponding vertex v_i on its diagonal. Meanwhile, Eq. (7.1) can be formulated as eigen problem of Laplacian matrix $L=I-D^{-1}W$ (Luxburg 2007). When the eigenvalue of L equals to 0, the corresponding eigenvector y is the cluster indicator vector c of the graph. For the non-zero eigenvalue of L, the first k eigenvectors of L, corresponding to the k smallest eigenvalues, is the approximation of C that partitions the graph into k components. The objective of this solution is to partition the graph by the *normalized cut* (*Ncut*) (Luxburg 2007), which is defined as:

$$Ncut(A,B)=\frac{cut(A,B)}{assoc(A,V)}+\frac{cut(A,B)}{assoc(B,V)} \tag{7.2}$$

where $A \cup B = V$, and $A \cap B = \Phi$. $cut(A,B) = \sum_{u \in A, v \in B} w_{uv}$ is the sum of edges connecting partitions *A* and *B*, which is called *cut* in graph theory. $assoc(A,V) = \sum_{i \in A} d_i$ is the total connections from nodes in *A*, and $assoc(B,V)$ is defined in a similar way. By minimizing *Ncut* value, one tends to obtain a balanced partition with relatively low *cut*.

In practice, the second eigenvector of graph Laplacian is often used to bi-partition the graph. As shown in Figure 7. 3, we can partition the nodes by their signs in the second eigenvector – that is, assigning the nodes with the positive value in the eigenvector to one cluster and the rest to the other. However, to achieve a more meaningful result, *k-means* algorithm is applied to bi-partition the graph based on the second eigenvector. Then, the sub-graph can be further partitioned by recalculating the eigenvector of the graph Laplacian of sub-graph if necessary. By doing so recursively, the graph will be partitioned into multiple clusters. Specifically, we applied *Ncut* as determinant condition for bi-partitioning. We will stop bi-partitioning sub-graph if *Ncut* value is larger than the pre-set threshold. Thus, the number of clusters will be determined by the threshold we set. The outline of this partition algorithm is listed below, by following (Shi and Malik 2000).

Algorithm 7.1. Spectral Clustering

Input: Connectivity matrix W with size $n \times n$, and the threshold *T* of *Ncut* for partitioning.
Output: Clusters of nodes.

1. Compute the normalized Laplacian *L* of *W*.
2. Solve eigenvectors of L with the smallest eigenvalues.
3. Use the eigenvector with the second smallest eigenvalue to bi-partition the graph, and then compute the corresponding *Ncut* value.
4. **If** *Ncut* < T, bi-partition the graph, and repeat the algorithm on two bi-partitioned sub-graphs.
5. **Else** Return without bi-partitioning the graph.

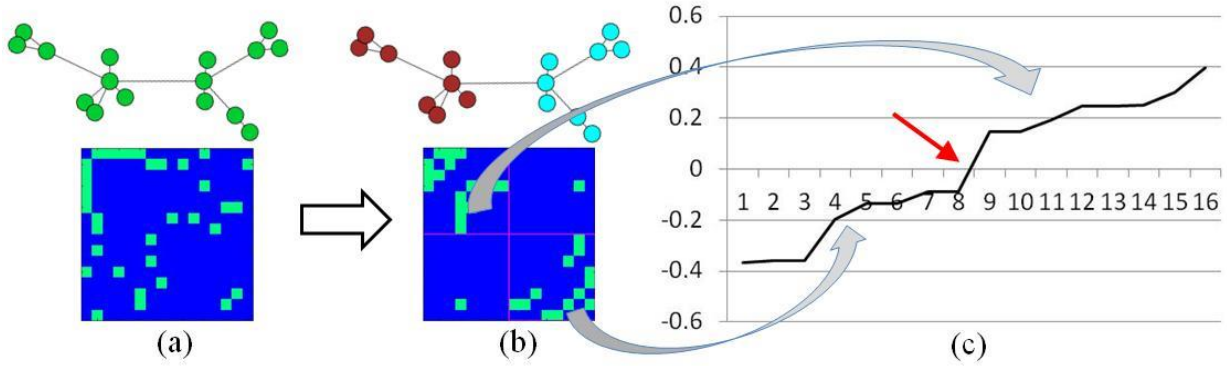

Figure 7. 3. Illustration of spectral clustering. (a) The original graph and the corresponding affinity matrix. (b) The clustered graph and the corresponding affinity matrix re-arranged by clusters. (c) The second eigenvector of the graph after sorting.

Co-Training Approach Based on Spectral Clustering

In our research problem, we have both structural connectivity and functional connectivity for large-scale brain network clustering. To find common brain sub-networks across different modalities, an intuitive way is to assign a weight to each view or modality and then combine them together. However, it is difficult to define optimal weights, especially when there exists significant variability across modalities – the common connection obtained may be biased when the connection is strong in one modality but absent in the other modality. Thus, how to fuse these multimodal networks to achieve the relatively consistent sub-networks becomes an important issue. Recently, a clustering methodology called *multi-view clustering* has been developed to solve this type of problem (Cai et al. 2011; Kumar and III 2011). In this chapter, we designed a co-training approach based on spectral clustering to maximize, first, the agreement between the structural network and functional network, and then the agreement between subjects, to find the group-wise consistent multimodal connectomes of the human brain.

As shown in the previous section, when the eigenvalue is 0, the corresponding eigenvector of normalized Laplacian of a graph is the cluster indicator vector. For a fully-

connected graph, spectral clustering solved a relaxed solution of min *cut* problem. That is, the top eigenvectors carry the most discriminative information for graph clustering. In (Kumar and III 2011), the authors have shown that, by projecting the affinity matrix to the eigenspace of the first *k* eigenvectors corresponding to the *k* smallest eigenvalues, the inter-cluster details will be discarded and only the essential information required for clustering retains. Thus, we can achieve the agreement between two views by projecting the affinity matrix of one view to the eigenspace of the other view. As the eigenvectors are orthogonal, the affinity matrix in eigenspace can be easily projected back by multiplying the transpose of eigenvectors matrix. It should be mentioned that the post-projected affinity matrix obtained in this way is not symmetric. To make it symmetric, we added the post-projected affinity matrix with its transpose and then divide it by 2. The whole projection process can be summarized as follows:

$$proj(W,U) = (UU^T W + (UU^T W)^T)/2 \tag{7.3}$$

where $U = \Re^{n \times k}$ is the first *k* eigenvectors corresponding to the top *k* smallest eigenvalues of graph Laplacian of affinity matrix.

To further illustrate how this approach works, we assume that there exist two discriminate clusters *A* and *B* in a graph *G*, and also that the affinity matrix of *G* has been rearranged by clusters as follows:

$$W = \begin{bmatrix} W_A & W_{AB} \\ W_{AB}^T & W_B \end{bmatrix} \tag{7.4}$$

where $W_A = \Re^{\|A\| \times \|A\|}$ are the edges between nodes in cluster *A*, with W_B defined similarly. $W_{AB} = \Re^{\|A\| \times \|B\|}$ are the edges between clusters *A* and *B*. Then the corresponding cluster indicator matrix *C* is:

$$C = \begin{bmatrix} I_A & 0 \\ 0 & I_B \end{bmatrix} \tag{7.5}$$

where $I_A = 1^{\|A\|}, I_B = 1^{\|B\|}$. As W_A and W_B are the symmetric matrices, let's define $E_A = I_A I_A^T = 1^{\|A\| \times \|A\|}$ and $E_B = I_B I_B^T = 1^{\|B\| \times \|B\|}$. Then, we can get:

$$\begin{aligned} W^* &= proj(W, C) \\ &= (CC^T W + (CC^T W)^T)/2 \\ &= \frac{1}{2}\begin{bmatrix} E_A W_A & E_A W_{AB} \\ E_B W_{AB}^T & E_B W_B \end{bmatrix} + \frac{1}{2}\begin{bmatrix} E_A W_A & E_A W_{AB} \\ E_B W_{AB}^T & E_B W_B \end{bmatrix}^T \\ &= \frac{1}{2}\begin{bmatrix} E_A W_A + W_A E_A & E_A W_{AB} + W_{AB} E_B \\ E_B W_{AB}^T + W_{AB}^T E_A & E_B W_B + W_B E_B \end{bmatrix} \\ &= \begin{bmatrix} W_A^* & W_{AB}^* \\ W_{AB}^{*\,T} & W_B^* \end{bmatrix} \end{aligned} \tag{7.6}$$

We can see that the element w_{ij} of W_A^* is the average degree of entry *i* and entry *j* of sub-matrix W_A, which are similarly done for W_B^* and W_{AB}^*. This indicates that the projection process tends to fuse and smooth the inter-cluster connections or intra-cluster connections independently. As we know, the intra-cluster connections tend to be high and inter-cluster connections are relatively low. By smoothing inter/intra-cluster connections separately, we can expect the increase in intra-cluster connection strength and vice versa. However, in practice, the eigenvectors obtained are approximations of cluster indicators, and the clusters are indicated by their signs approximately as shown in Figure 7. 3. Then, for the above affinity matrix *W*, the corresponding second eigenvector should be:

$$U = \begin{bmatrix} P \\ N \end{bmatrix} \tag{7.7}$$

where $P = \Re^{\|A\|}$ is a vector containing the positive real numbers and $N = \Re^{\|B\|}$ is a vector containing the negative real numbers. Then we will have:

$$
\begin{aligned}
W^* &= proj(W,U) \\
&= (UU^T W + (UU^T W)^T)/2 \\
&= \frac{1}{2}\begin{bmatrix} PP^T W_A + PN^T W_{AB}^T & PP^T W_{AB} + PN^T W_B \\ NN^T W_{AB}^T + NP^T W_A & NN^T W_B + NP^T W_{AB} \end{bmatrix} + \\
&\quad \frac{1}{2}\begin{bmatrix} PP^T W_A + PN^T W_{AB}^T & PP^T W_{AB} + PN^T W_B \\ NN^T W_{AB}^T + NP^T W_A & NN^T W_B + NP^T W_{AB} \end{bmatrix}^T \\
&= \frac{1}{2}\begin{bmatrix} PP^T W_A + W_A^T PP^T & PP^T W_{AB} + W_{AB} NN^T \\ NN^T W_{AB}^T + W_{AB}^T PP^T & NN^T W_B + W_B^T NN^T \end{bmatrix} + \\
&\quad \frac{1}{2}\begin{bmatrix} PN^T W_{AB}^T + W_{AB} NP^T & PN^T W_B + W_A^T PN^T \\ NP^T W_A + W_B^T NP^T & NP^T W_{AB} + W_{AB}^T PN^T \end{bmatrix} \\
&= \begin{bmatrix} W_A^* & W_{AB}^* \\ W_{AB}^{*T} & W_B^* \end{bmatrix}
\end{aligned}
\tag{7.8}
$$

In the above equation, W_A^* can be separated into two parts. The first part $(PP^T W_A + W_A^T PP^T)/2$ is the fuse of connections within cluster *A*, and the second part $(PN^T W_{AB}^T + W_{AB} NP^T)/2$ is the fuse of connections between clusters *A* and *B*. It should be noted that the first part is all positive and the second part is all negative, which means W_A^* is the sum of intra-cluster connections of cluster *A* minus the inter-cluster connections between *A* and *B*. Similarly, W_B^* is the sum of connections in *B* minus the inter-cluster connections. And W_{AB}^* is the sum of inter-cluster connections minus the intra-cluster connections. As we know, W_A and W_B are the matrices that are relatively dense with large values, and W_{AB} is sparser with low values. Thus, we can expect high positive values evenly distributed in W_A^* and W_B^*, while low or even negative values in W_{AB}^*. Since the negative values in W^* are caused by strong inter-cluster connections which are the disagreed part between the matrices and are in conflict with the definition of the affinity matrix, we set all negative values in W^* to 0 after projection.

Algorithm 7.2

Input: Connectivity matrices of two views W_1^0, W_2^0, and the number of eigenvectors to consider *k*.

Output: Co-trained connectivity matrices W_1^*, W_2^*.

Compute the initial normalized Laplacian L_1^0, L_2^0 of each connectivity matrix, and the first *k* eigenvectors U_1^0, U_2^0 with the *k* smallest eigenvalues of L_1^0, L_2^0.

for *i* = 1 to *iter*

$W_1^i = proj(W_1^{i-1}, U_2^{i-1})$

$W_2^i = proj(W_2^{i-1}, U_1^{i-1})$

Compute Laplacian and the corresponding first *k* eigenvectors U_1^i, U_2^i of W_1^i, W_2^i.

If converge, **return** $W_1^* = W_1^i, W_2^* = W_2^i$.

Let $U = [u_1 \quad u_2 \quad \dots \quad u_k] = \Re^{n \times k}$ be the combination of the first *k* eigenvectors, and then we will have:

$$proj(W, U) = \sum_{i=1}^{k} proj(W, u_i) \tag{7.9}$$

Thus, by projecting the graph affinity matrix to the eigenspace of top eigenvectors of corresponding graph Laplacian matrix, we can smooth and thus increase the intra-cluster connections and also decrease or remove inter-cluster connections. Let $M = \sum_{i=1}^{k} u_i u_i^T$ be the projecting matrix. For pair-wise co-training of functional and structural connectivity matrices, we can project functional matrix to the spectral eigenspace of structural matrix and vice verse at the same time by using above steps iteratively. While for group-wise co-training process, we can project the matrices of one subject to the spectral eigenspace of the rest subjects. The group-wise co-training step for *p* subjects with single view for each subject is defined as follows:

$$gproj(W_i, U_{all}) = ((\sum_{j=1, j \neq i}^{p} M_j) W_i + ((\sum_{j=1, j \neq i}^{p} M_j) W_i)^T) / 2 \tag{7.10}$$

where W_i is the affinity matrix of subject *i*; U_j is the spectral eigenvector matrix of subject *j*; $M_j = U_j U_j^T$ is the corresponding projecting matrix of subject *j*. When we have both structural matrix and functional matrix for each subject, M_j is re-defined as $U_{Sj}U_{Sj}^T + U_{Fj}U_{Fj}^T$, where U_{Sj} is the eigenvector matrix of structural matrix spectrum, and U_{Fj} is the eigenvector matrix of functional matrix spectrum. W_i is then either the functional matrix or structural matrix. The detailed algorithm for pair-wise co-training is as Algorithm 7.2.

As shown previously, during the projection process, the within-cluster connection will be smoothed (increasing the positive agreement between matrices) and the disagreed connections will be broken (increasing the negative agreement between matrices). As a result, only the agreed connections will be retained during the iterative projection. As the algorithm will converge when no more agreement could be further achieved, the convergence could be assessed by the measurement of similarity between matrices. Particularly, we applied different measurements for different scenarios and will discuss this important issue in details in the next section.

The algorithm for the group-wise co-training algorithm is similar to the above by replacing the pair-wise projection function $proj()$ to the group-wise projection function $gproj()$ in Eq. (7.10). After co-training, the trained matrices are similar as shown in the result section. The final fused connection matrix can be obtained by calculating the average normalized matrix between different subjects and views. Base on fused connection matrix, the final multi-modal connectomes of the human brain will be obtained directly by applying spectral clustering algorithm introduced previously.

EXPERIMENT MATERIAL AND PARAMETER SELECTION

Experiment Materials

Our experiment was performed on 150 healthy adults (100 females and 50 males) from the publicly released dataset by the Beijing Normal University, China (Yan et al. 2011). Both DTI and R-fMRI were acquired for each subject. The parameters are as follows. R-fMRI: 33 axial slices, thickness/gap = 3/0.6mm, in-plane resolution = 64×64, TR = 2000ms, TE = 30ms, flip angle = 90º, FOV = 200×200mm. DTI: single-shot Echo-Planer Imaging-based sequence, 49 axial slices, 2.5mm slice thickness, TR = 7200ms, TE = 104ms, 64 diffusion directions, b-value = 1000s/mm^2, matrix = 128×128, FOV = 230×230mm^2. Preprocessing steps include tissue segmentation, surface reconstruction, and fiber tracking, which are similar to the methods in (Zhu, Li, Guo, et al. 2013). Then a set of large-scale, group-wise consistent ROIs were obtained for each subject using the method in (Zhu, Li, Guo, et al. 2013). The structural and functional connectome matrices were then computed using the method described previously. Examples of ROIs and connectivity matrices are shown in Figure 7. 1. To test the reproducibility of our proposed method, we randomly separated the female subjects into two training groups: female group 1 and female group 2.

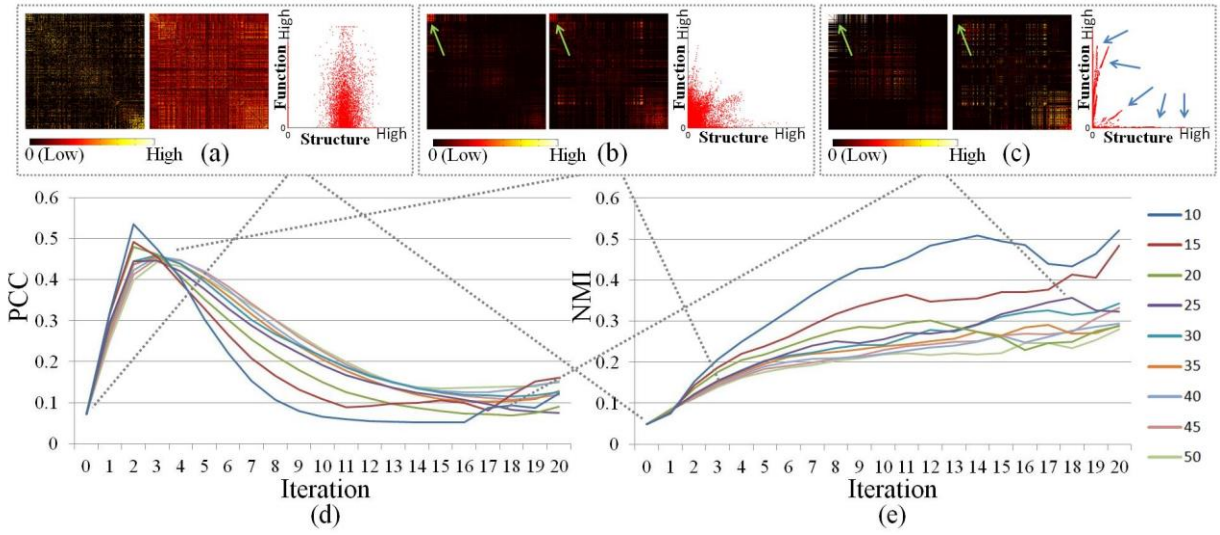

Figure 7. 4. Illustration of parameter selection for pair-wise training. (a)-(c) Original structural and functional connections and the co-trained connections in the 3rd and 18th iteration when the top 25 eigenvectors are considered. In each subfigure, the left figure is structural matrix; the middle figure is functional matrix; the right figure is functional connection vs. structural connection with each dot representing an edge. (d) Changes of PCC during co-training iteration with different numbers of eigenvectors considered. (e) Changes of NMI during co-training iteration with different numbers of eigenvectors considered.

Parameter Selection

Normalized mutual information (NMI) (Witten and Frank 2005) and Pearson correlation coefficient (PCC) are applied as measurements to assess the level of agreement between two affinity matrices. NMI between two affinity matrices A and B is defined as follows:

$$NMI(A,B) = \frac{I(A,B)}{[H(A)+H(B)]/2} \tag{7.11}$$

where $H(A) = -\sum_{i,j} P(a_{ij}) \log P(a_{ij})$ is the entropy of A. $I(A,B)$ is the mutual information between A and B, and is defined as:

$$I(A,B)=\sum_{i,j}\sum_{p,q}P(a_{ij},b_{pq})\log\frac{P(a_{ij},b_{pq})}{P(a_{ij})P(b_{pq})} \tag{7.12}$$

The values of NMI and PCC are both between 0 and 1. The higher the value is, the more the two matrices agree with each other (Witten and Frank 2005).

Number of eigenvectors

During the co-training process introduced in the previous section, the affinity matrix will be projected to the first *k* eigenvectors of the graph Laplacian. In the ideal case, *k* should be set equal to or larger than the true cluster number. However, due to the lack of prior knowledge, we tested the result with different *k* values on the pair-wise training of single subject networks. As shown in Figure 7. 4(d)-(e), by using small *k* value, more information will be removed and thus the agreement between two views will be higher. However, small *k* value will cause the loss of useful information and results in over-training. Also, small *k* value may cause oscillation during training process which is vulnerable. On the other hand, large *k* value will keep too much information including the uncommon information between views that we want to remove and thus may cause under-training. Considering that the number of nodes in our network is 358, we set *k* to 25 empirically. By using this *k* value, we can ensure the useful information retained, and also the accuracy and smoothness during the training process.

Convergence criterion

During the training process, our goal is to maximize the agreement between different views. In Figure 7. 4(e), we can see that the NMI between two networks is increasing during the training process. In general, PCC between two networks increases in the first several iterations rapidly and then decreases slowly. This is mainly because there is a certain amount of disagreement between two networks. Though the intra-cluster connections will be smoothed to

increase the agreement between two matrices, some connections may still be relatively weak compared with other connections as highlighted by green arrows in Figure 7. 4(b)-(c). Also, as highlighted by the blue arrows in Figure 7. 4(c), we can see that, after training, certain sets of edges are highly correlated, but there may exist multiple correlation models between two views and thus the overall correlation is low. This indicates that, compared with PCC, NMI is a better measurement as the criterion of co-training convergence. However, the pair-wise trained result will be used for successive group-wise training. If the training process iterates for too many times, the group-wise information will also be smoothed out at the same time, although we maximize the agreement between two matrices of each subject. Thus, we use PCC value as a convergence criterion for pair-wise training (Figure 7. 2(b)). The mean NMI between each pair of subjects of each view is used as a convergence criterion of group-wise training (Figure 7. 2(c)). As shown in Figure 7. 5, it takes about 30 iterations for the group-wise co-training algorithm to converge. For pair-wise training, it takes either 3 or 4 iterations to converge.

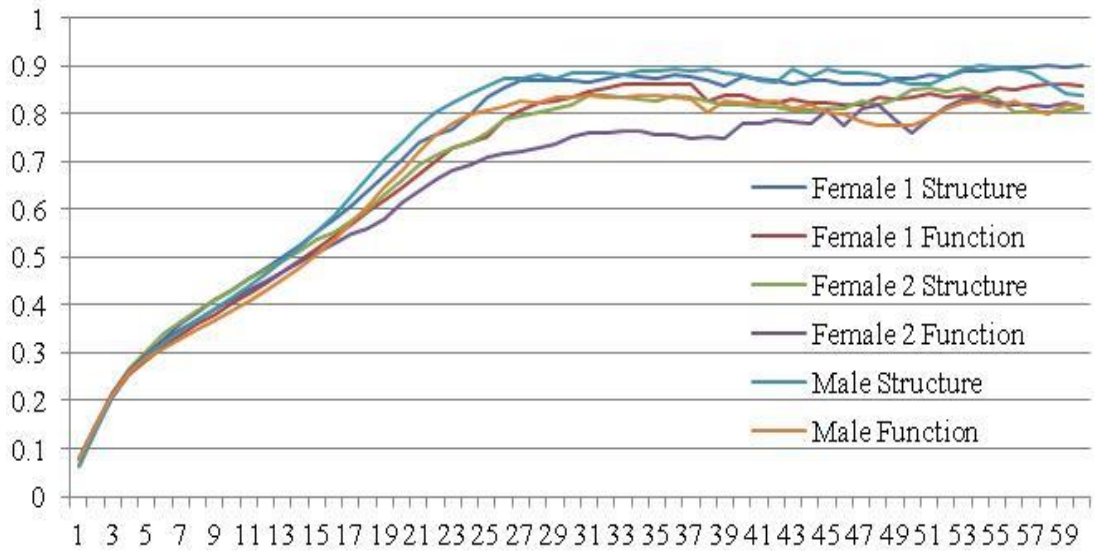

Figure 7. 5. Changes of average NMI in each iteration of group-wise co-training process for each training group.

RESULTS

Clustered Multi-modal Networks

We obtained 8 multi-modal clusters upon 358 DICCCOL landmarks using the proposed methods and the parameters described above. The clustering results are similar when set the threshold of *Ncut* in spectral clustering algorithm from 0.2 to 0.9, thus we set it 0.5 specifically. We randomly picked 4 subjects in female group 1 and visualized their affinity matrices before and after training in Figure 7. 6, where the matrices are all rearranged by clusters. Each cluster is highlighted by a green box. As the connection strength of edges in the certain cluster may be relatively higher which makes it difficult to visualize other clusters (Figure 7. 4 (d)-(e)), the connection strength of co-trained matrices are adaptively normalized for the purpose of visualization in the following way. First, each row of the matrix is scaled independently such that the largest element in each row is 1 (i.e., by normalizing the largest connection to each node). Then, add the row-normalized matrix to its transpose to obtain the adjusted matrix (symmetrizing matrix). By observation, we can see that the connection matrices vary substantially between subjects and modalities before optimizations (the second row of each panel). After pair-wise co-training, the structural connection matrix and functional connection matrix of each subject are more similar to each other, but there still exists disagreement. However, after group-wise training, the matrices are similar across subjects and modalities. A clear boundary of eight clusters can be observed (at the third row of each panel). To validate the performance of the proposed algorithm in identifying common clusters, the strengths of the original structural/functional connections within each cluster are measured as shown in Table 7. 1. Obviously, both of the average structural connection and the average functional connection within each cluster are substantially higher than the average connection strength of the whole

brain network. A similar observation can also be observed in the first rows of the matrices in Figure 7. 6 that the clusters inferred by the proposed algorithm have relatively stronger within-cluster connections than the whole network for both connection matrices.

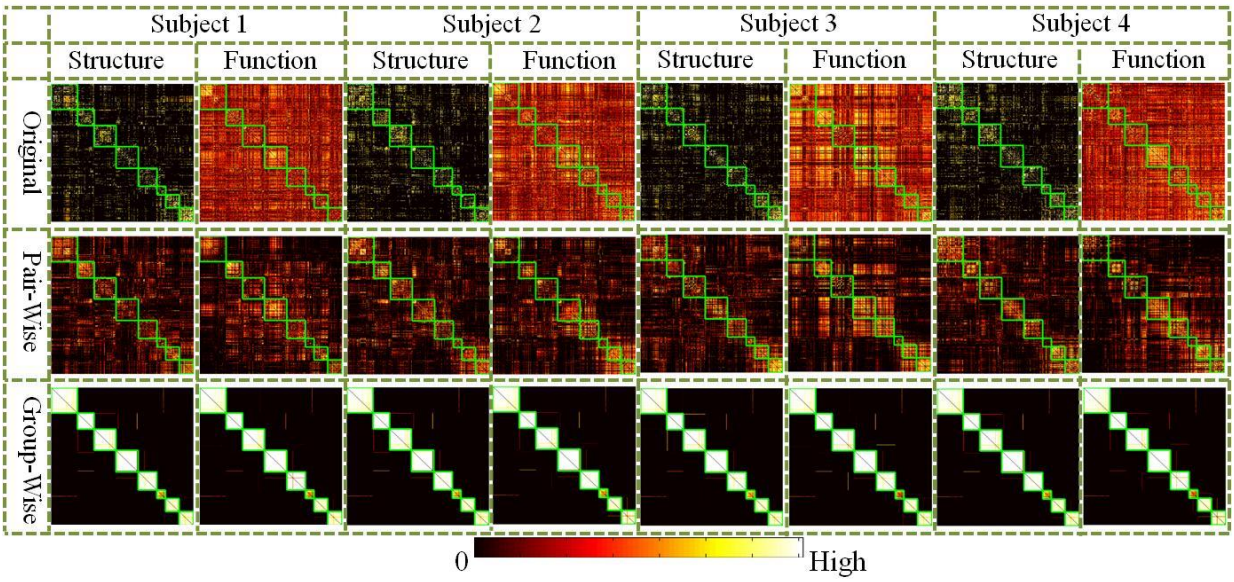

Figure 7. 6. Visualization of original and trained connection matrices of 4 randomly selected subjects from the first female group. The matrices are re-arranged by group-wise consistent clusters. Each cluster is highlighted by a green box. The matrices are adaptively normalized node by node to give better visualization.

Table 7. 1. Average connection strengths.

	Whole Brain	Cluster 1	Cluster 2	Cluster 3	Cluster 4	Cluster 5	Cluster 6	Cluster 7	Cluster 8
Structure	0.037	0.118	0.104	0.098	0.062	0.070	0.090	0.092	0.193
Function	0.249	0.284	0.353	0.264	0.348	0.301	0.263	0.334	0.329

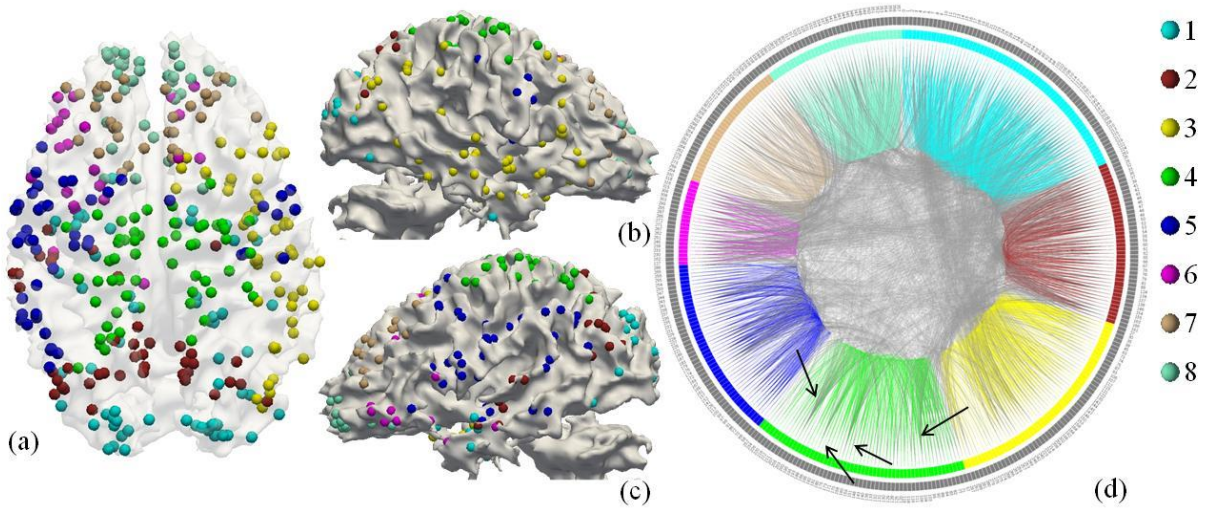

Figure 7. 7. Visualization of group-wise multimodal brain networks computed based on the female training group 1. The color-coding of sub-networks is provided in the right side of subfigure (d). (a)-(c) Visualization of multi-modal sub-networks on template cerebral cortex. The visualization was generated by ParaView (Henderson 2007). (d) Visualization of average structural connections between ROIs. Only the top 9.17% connections *(*the average connection density of 150 structural matrices applied*)* are retained. ROIs are rearranged and color-coded by sub-networks and listed around the circle. Between sub-networks connections are represented by gray lines and within sub-network connections are represented by corresponding color lines. The visualization was generated using the Circos toolkit (Krzywinski et al. 2009). It should be noted that the short distances of the re-arranged connections in this sub-figure do not necessarily mean that their actual structural connections have short distances, as shown in (a).

We visualized the 8 clusters trained from the female group 1 on the cerebral cortex surface in Figure 7. 7(a)-(c). By observation, most of the clusters are composed by ROIs that are geometrically close to each other or structurally/functionally connected. It is interesting that the parcellation of the cortical landmarks in Figure 7. 7(a)-(c) largely coincides with the recently published clusters obtained via genetic similarity by Chen et al. (Chen, Gutierrez, et al. 2012) and is consistent with current neuroscience knowledge. For instance, the major part of cluster 1 includes the visual cortex (Salvador et al. 2005; Damoiseaux et al. 2006; De Luca et al. 2006; Sorg et al. 2007; van den Heuvel et al. 2008). The major part of cluster 4 includes the sensory-

motor systems including pre- and post-central gyrus (BAs 1/2/3/4), and the Supplementary Motor Area (SMA) (BA 6) (Salvador et al. 2005; Damoiseaux et al. 2006; De Luca et al. 2006; van den Heuvel et al. 2008). Cluster 8 includes the prefrontal cortex (BA 11) and dorsal anterior cingulate (BA 32) (Damoiseaux et al. 2006). Figure 7. 7(d) shows the average structural connections between clusters. More intra-cluster connections than inter-cluster connections can be observed. We can also observe connection hubs within each cluster such as DICCCOL #104, #170, #185, #200 in cluster 4 as highlighted by black arrow. For details of the location of these DICCCOL ROIs on the cerebral cortex, please refer to the website (http://dicccol.cs.uga.edu).

Reproducibility and Between-Gender Similarity

The female training group 2 also generated 8 clusters. The visualization of these 8 clusters on the template cortex surface is shown in Figure 7. 8(a). The IDs of clusters are calibrated according to their overlap degree with the clusters of female group 1. The nodes with consistent cluster labels between two female training groups are shown in Figure 7. 8(b). By observation, we can clearly see that these eight clusters are similar to those obtained from female group 1. Besides, we further computed the Rand Index (RI) (Rand 1971) and NMI (Witten and Frank 2005) between clustering results of these two sets of subjects. Both RI and NMI range between 0 and 1. The higher value indicates higher similarity between clustering results. As shown in Table 7. 2, the RI value between these two results is 0.93 and the NMI value is 0.72. These relatively high RI and NMI values suggest that the proposed method is stable and robust, and the results are highly reproducible across different training groups.

The training results on male groups also gave eight similar clusters. As shown in Figure 7. 9, it is evident that the male's multi-modal clusters are similar to those of females. The RI and NMI values between the clustering results of male and female groups are also high (Table 7. 2).

There are 298 nodes that are consistent in cluster labels between two female training groups and 282 consistent nodes across all three training groups. As previous neuroscience studies suggested that there is a certain degree of difference in brain function and structure between genders (Cahill 2006), it is intriguing that no significant difference can be observed between the obtained network clusters of male and female. Our interpretation is that the DICCCOLs we applied as ROIs do not carry much gender-specific information (Zhu, Li, Guo, et al. 2013). To further quantitatively show this point, we measured the NMI between the original connection matrices and no significant differences between genders can be observed. As for the network disagreement between females and males, it is still not clear whether they are caused by sexual difference, or by the variability in the data acquisition, preprocessing and analysis. However, as shown in Figure 7. 8(b) and Figure 7. 9(b), the most inconsistent nodes locate on the boundary region between clusters. It is more likely that the variability between cluster results is caused by the individual variability. This observation, together with previous results, suggests that the proposed multi-view spectral clustering algorithm is robust and powerful in identifying group-wise consistent clusters.

Table 7. 2. RI and NMI Between Joint Clustering Results

Index Type	RI	NMI
Female 1 VS. Female 2	0.93	0.72
Female 1 VS. Male	0.94	0.77
Female 2 VS. Male	0.93	0.74

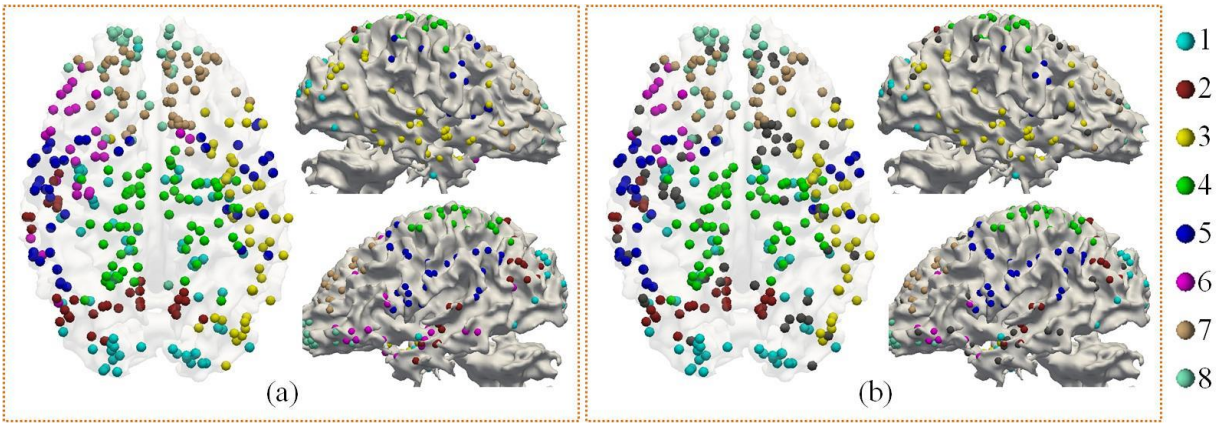

Figure 7. 8. Visualization of group-wise multimodal brain networks computed based on female training group 2. The visualization is performed on the template brain with Paraview (Henderson 2007). Corresponding sub-networks are color-coded by the same color. (a) Networks of female training group 2. (b) Nodes with consistent clusters between two female training groups. Inconsistent nodes are color-coded by gray.

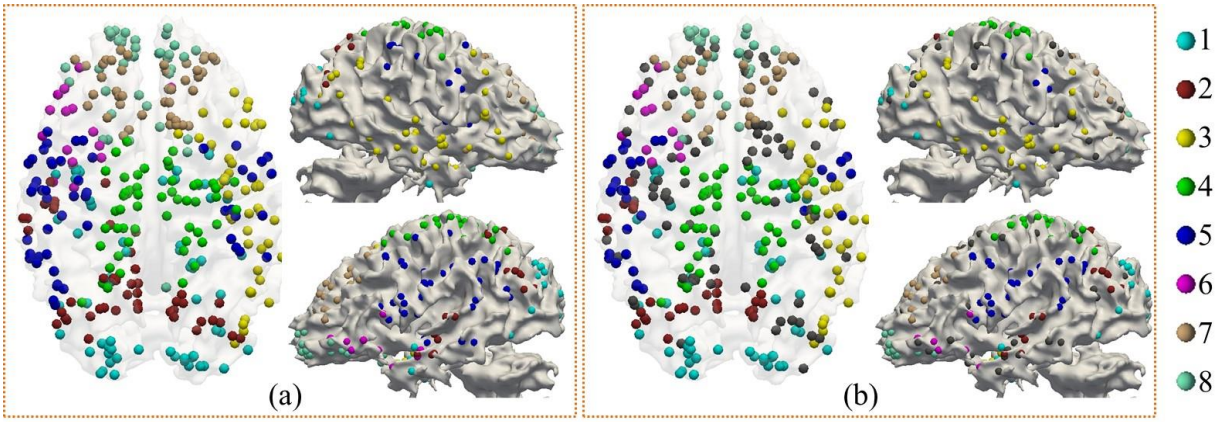

Figure 7. 9. Visualization of group-wise multimodal brain networks computed based on male training group. The visualization is performed on the template brain with ParaView (Henderson 2007). Corresponding sub-networks are color-coded by the same color. (a) Networks of male training group. (b) Nodes with consistent clusters across three training groups. Inconsistent nodes are color-coded by gray.

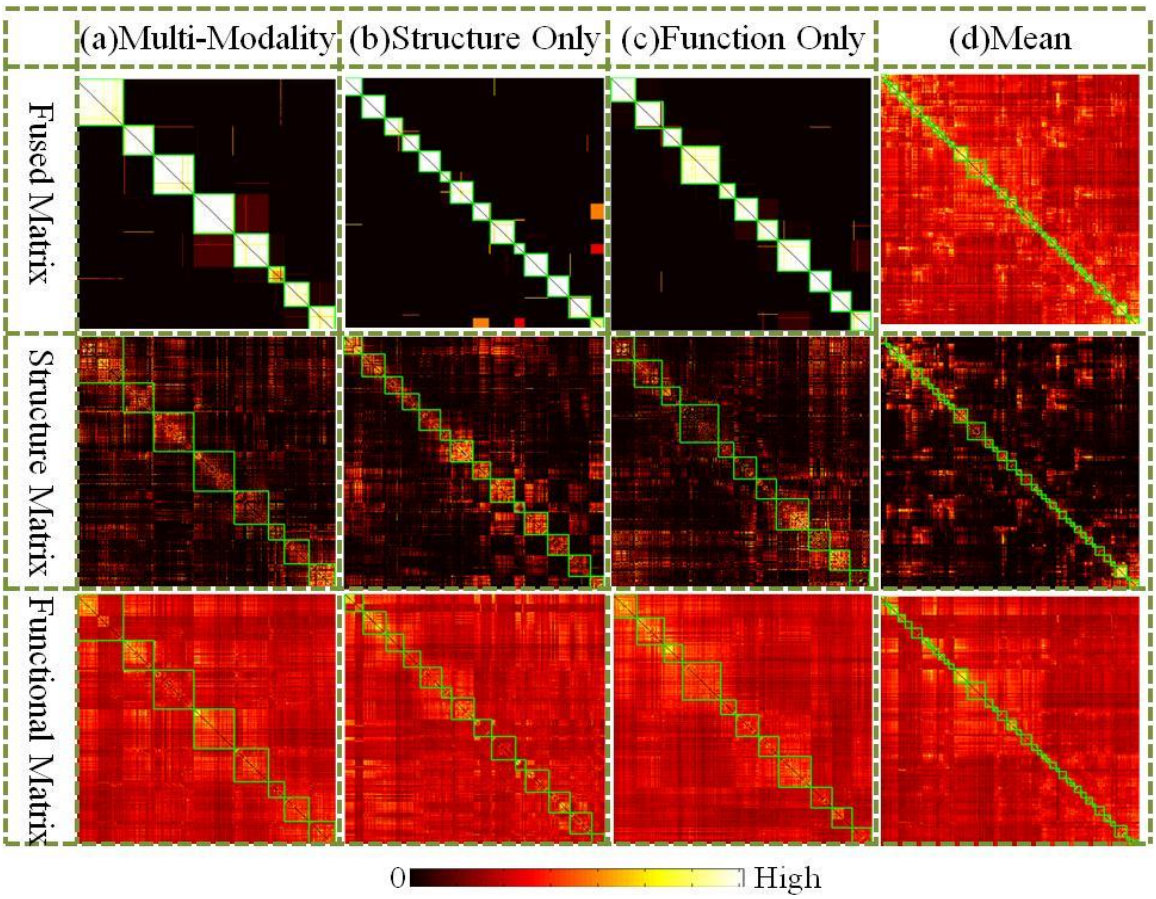

Figure 7. 10. Visualization of clusters on matrices obtained by different approaches from female group 1. Matrices including adaptively normalized fused matrix (top row), average structure matrix (middle row), and average functional matrix (bottom row) are visualized and rearranged by corresponding clusters. Each cluster is highlighted by a green box. In each sub-figure, the IDs of the clusters from top-left to bottom-right are from 1 to *n* successively. (a) Fused matrix using the proposed group-wise multi-view co-training approach using multi-modality matrices. (b) Group-wise co-trained matrix fused by the proposed method with structure connection matrices only. (c) Group-wise co-trained matrix fused by the proposed method with functional connection matrices only. (d) Average matrix of both connection matrices of all the subjects in the training group.

Comparisons between Approaches

For the purpose of comparison, sub-networks obtained by different approaches are computed. We computed the group-wise sub-networks based only on structural information or

only on functional information. The group-wise consistent connection matrix for each modality is obtained respectively using the proposed multi-view spectral co-training approach. The parameters are selected in a way similar to those described previously. As there is only one connection matrix considered for each subject, group-wise co-training is performed directly on the original matrices without pare-wise co-training. On average, it took 42 iterations for structural matrices to converge and 36 iterations for functional matrices to converge. The threshold of *Ncut* in the spectral clustering is set to 0.5. Also, an average matrix of both modalities' connection matrices of the training group is obtained for comparison. Based on the average matrix, the cluster is obtained by the spectral clustering method. As the matrix is more densely connected compared with the final fuse matrices obtained by proposed approach, the threshold of *Ncut* is set to 0.9 here. In this section, our analysis will mainly focus on the results of female group 1.

In total, 14 structural clusters and 11 functional clusters were obtained. These clusters can be visually observed with clear boundaries in Figure 7. 10(b)-(c). The visualization of clusters on the template cortex is shown in Figure 7. 11. Interestingly, functional regions are symmetric in certain degree between the left and right spheres. Another intriguing observation is that, though structure connection matrix generated more clusters, these clusters are highly reproducible across three training groups we have. As shown in Table 7. 3, the average RI value is 0.97 and average NMI value is 0.83, which are relatively high.

It is evident that the derived brain sub-networks via the multi-view spectral clustering method have substantially improved inter-modality consistency in comparison with the clustering results by any single modality. As shown in Figure 7. 10, the clusters based only on structural connection matrices failed to give functional meaningful clusters. On the other side,

functional clusters also failed to generate significant structural clusters. During the multi-modal co-training process, these single modality clusters are split and then recombined considering the mutual clusters between modalities. Thus, as shown in Figure 7. 10(a), the multi-modal clusters carry dense intra-cluster connections for both structural and functional connections.

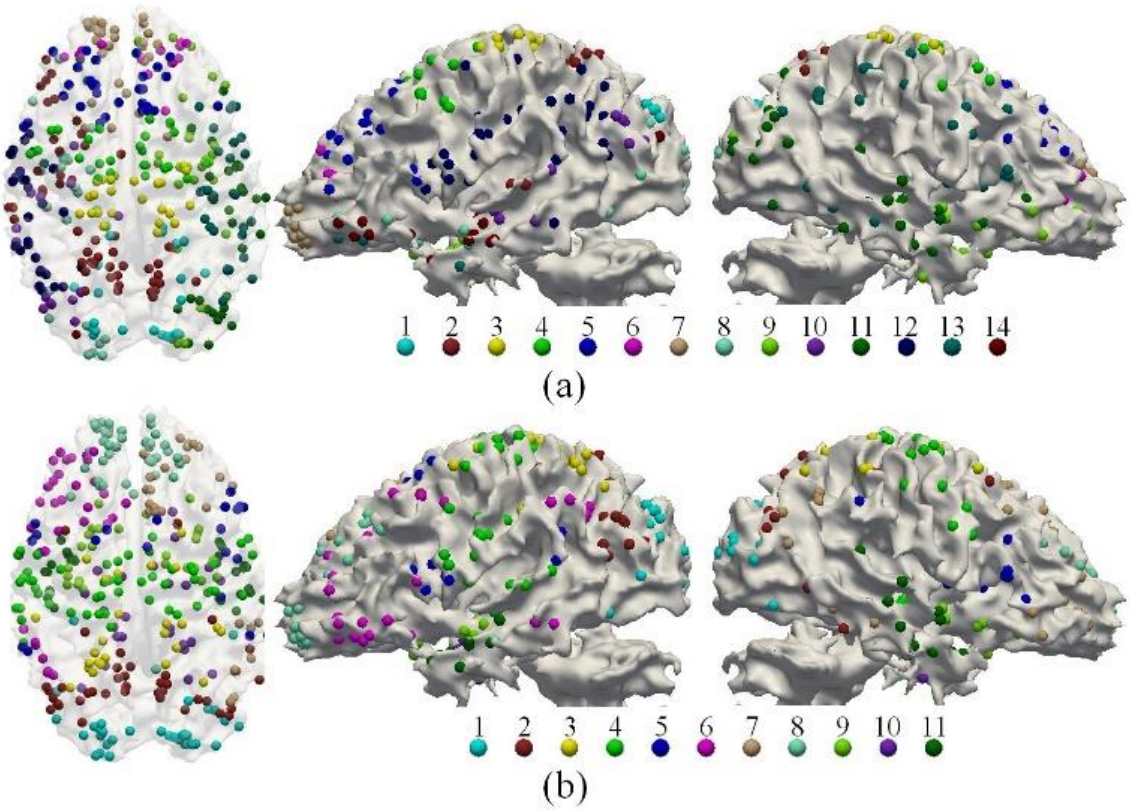

Figure 7. 11. Visualization of group-wise structural/functional brain networks computed based on female group 1. The visualization is performed on the template brain with ParaView (Henderson 2007). (a) Structural networks. (b) Functional networks.

However, as shown in Figure 7. 10(d), the average matrix failed to offer meaningful information for clusters, which might be caused by the following reasons. 1) The variability across individual connection matrices might be relatively high. Thus, by averaging individual matrices, useful information might be smoothed out. 2) The structural connection matrix is too sparse compared with functional connection matrix. Thus, the structural information may be

overwhelmed by functional information. 3) The disagreement between two modalities is relatively high. For the edges between certain nodes, only the connection in one modality is strong. But the connection strength of these edges will still remain strong if taking the average value as the common connection strength.

Table 7. 3. RI and NMI Between Separate Clustering Results

	Structure		Function	
Index Type	RI	NMI	RI	NMI
Female 1 VS. Female 2	0.97	0.84	0.93	0.73
Female 1 VS. Male	0.97	0.83	0.92	0.69
Female 2 VS. Male	0.96	0.82	0.92	0.70

DISCUSSION AND CONCLUSION

We inferred eight group-wise consistent multi-modal brain sub-networks via a novel multi-view spectral clustering approach based on our recently developed cortical landmark system - DICCCOL. The DICCCOL system is composed of 358 cortical landmarks, which are optimized and predicted via brain white matter connection patterns such that they possess correspondence between individuals. Structural/functional networks are composed of connections between these landmarks derived from DTI/R-fMRI data. Then a co-training framework based on the novel multi-view spectral clustering algorithm is applied to obtain the group-wise consistent and cross-modality common brain network clusters. The advantage of multi-view spectral clustering methodology is that it can effectively deal with heterogeneous

features by maximizing the mutual agreement across clusters in different views (Kumar and III 2011).

Our experiment results have shown that the algorithm converges well on the data used. Eight multi-modal brain sub-networks that are reproducible across different training groups have been identified. They are also shared by both males and females. Compared with clusters derived from the structural connection or functional connection only, the sub-networks obtained by our proposed method have improved inter-modality consistency significantly.

To conclude, the major technical contribution of this work is the proposed novel clustering framework for multi-view brain networks. Based on this framework, eight sub-networks are derived from the DICCCOL system via connection matrices based on DTI/R-fMRI data. Our experimental results suggest that the derived sub-networks are functionally/structurally meaningful. Also, we demonstrated the possible usage of DICCCOL system in studying brain networks patterns. Further and intensive studies based on the DICCCOL system and those eight inferred multi-modal sub-networks can potentially help elucidate brain functions and dysfunctions in the future.

ACKNOWLEDGEMENT

T Liu was supported by the NIH Career Award EB006878 (2007-2012), NIH R01 HL087923-03S2 (2010-2012), NIH R01 DA033393 (2012-2017), NSF CAREER Award IIS-1149260 (2012-2017) and The University of Georgia start-up research funding.

CHAPTER 8

LONGITUDINAL ANALYSIS OF BRAIN RECOVERY AFTER MILD TRAUMATIC BRAIN INJURY BASED ON GROUPWISE CONSISTENT BRAIN NETWORK CLUSTERS[7]

[7] Hanbo Chen, Armin Iraji, Xi Jiang, Jinglei Lv, Zhifeng Kou, Tianming Liu. 2015. Longitudinal Analysis of Brain Recovery After Mild Traumatic Brain Injury Based on Groupwise Consistent Brain Network Clusters. *International Conference on Medical Image Computing and Computer Assisted Intervention, Lecture Notes in Computer Science*, 9350:194-201.

ABSTRACT

Traumatic brain injury (TBI) affects over 1.5 million Americans each year, and more than 75% of TBI cases are classified as mild (mTBI). Several functional network alternations have been reported after mTBI; however, the network alterations on a large scale, particularly on connectome scale, are still unknown. To analyze brain network, in a previous work, 358 landmarks named dense individualized common connectivity based cortical landmarks (DICCCOL) were identified on the cortical surface. These landmarks preserve structural connection consistency and maintain functional correspondence across subjects. Hence DICCCOLs have been shown powerful in identifying connectivity signatures in affected brains. However, on such fine scales, the longitudinal changes in brain network of mTBI patients were complicated by the noise embedded in the systems as well as the normal variability of individuals at different times. Faced with such problems, we proposed a novel framework to analyze longitudinal changes from the perspective of network clusters. Specifically, the multiview spectral clustering algorithm was applied to cluster brain networks based on DICCCOLs. And both structural and functional networks were analyzed. Our results showed that significant longitudinal changes were identified from mTBI patients that can be related to the neurocognitive recovery and the brain's effort to compensate the effect of the injury.

INTRODUCTION

Mild traumatic brain injury (mTBI) accounts for over one million emergency visits each year in the United States (McCrea et al. 2009). Most mTBI patients have normal findings in clinical neuroimaging. Advanced magnetic resonance imaging (MRI) has detected microstructural damage in major white matter tracts by diffusion tensor imaging (DTI), and functional network alternations by functional MRI (fMRI) (Eierud et al. 2014; Iraji et al. 2015).

However, the field is still short of investigations on the overall extent of structural and functional network disruptions after mTBI and its recovery process. Moreover, there is a lack of investigation in the alteration of connectivity on large-scale brain networks after mTBI and their recovery process. We hypothesize that mTBI results in network connectivity changes, and brain structural and functional recovery occurs over time.

In a literature work, Zhu et al. identified 358 landmarks on the cortical surface that preserve structural connection consistency across subjects named dense individualized common connectivity-based cortical landmarks (DICCCOL). The previous studies have shown that DICCCOLs are highly reproducible across individuals (Chen, Li, Zhu, Jiang, et al. 2013; Zhu, Li, Guo, et al. 2013) and they also preserves structural and functional correspondence across individuals (Yixuan et al. 2012). Moreover, in recent studies, Zhu et al. have shown that, by taking these DICCCOLs as network nodes, the connections between them could be taken as connectome signatures of mental diseases such as mild cognitive impairment (Zhu, Li, Terry, et al. 2013) or prenatal cocaine exposure (Li, Zhu, et al. 2013). With DICCCOL framework, the brain network alternations after injury and its recovery process of mTBI patients could be analyzed.

Intuitively, the changes in network connections during brain recovery can be derived by comparing the MRI scans of healthy subjects and the mTBI patients using t-test. Yet a considerable amount of changes in brain network connections were also seen in the two scans of the same group of healthy control (HC) subjects (E.g. the functional connection changes shown in Figure 8. 1). This result suggested that pairwise network connections comparison is sensitive to individual variability as well as system noise on a fine scale and thus cannot serve our purpose.

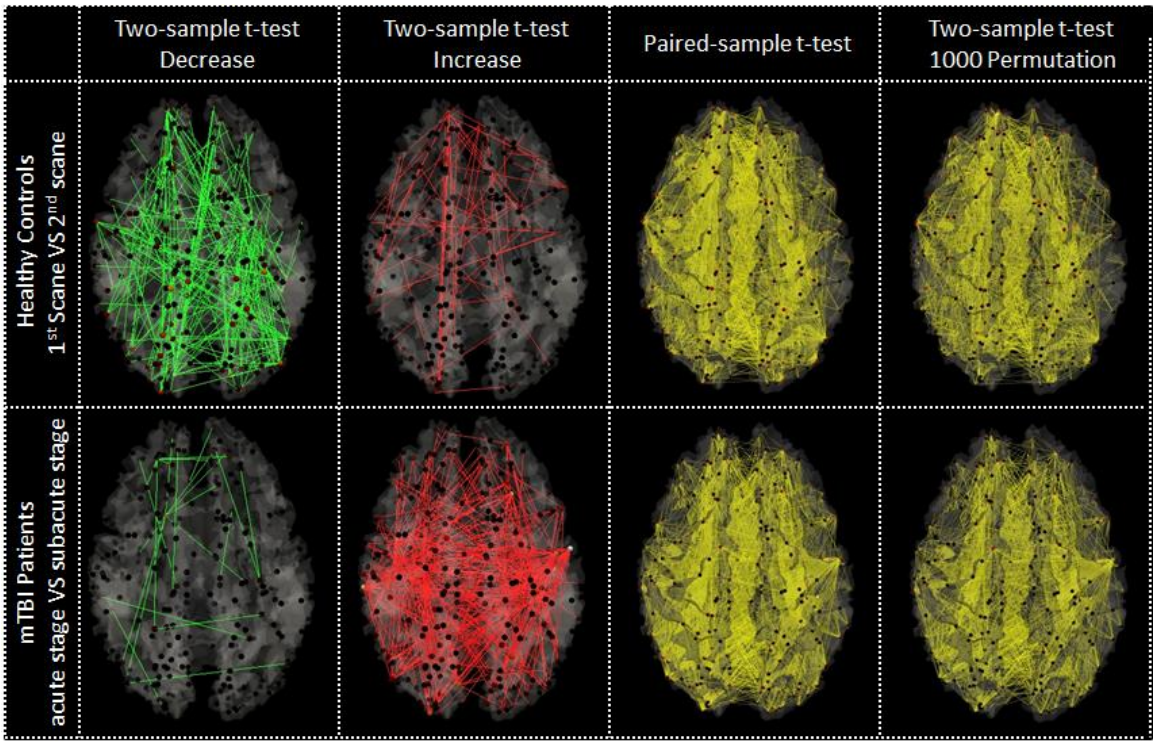

Figure 8. 1. Significantly different ($P<0.05$) pairwise functional connections among DICCCOLs between two scans of each population identified by different types of t-test.

Faced with such problem, we addressed the issue from the level of connectivity changes of brain network clusters. Whole brain networks were clustered into group-wisely common sub-networks based on the multiview spectral clustering algorithm. Each network cluster is a subset of nodes that are more densely connected within the cluster than between clusters. By comparing the connection changes within and between the clusters, the noises due to individual variability were greatly diminished and we have observed a consistent pattern of disruption in structural and functional networks after mTBI. Interestingly, over time the decrease in structural connectivity is accompanied by the increase in functional connectivity. This finding is in agreement with the temporally evolving and deteriorating nature of brain injury. On the other hand, the increase in functional connectivity suggested that brain is highly plastic as it tries to recruit more regions and remodel the functional connectivity to compensate the alteration in structural connectivity.

Together, these results may shed light on the network alteration mechanism of brain recovery and plasticity.

DATA ACQUISITION

This study was approved by the local Human Investigation Committee. Written informed consent was obtained from each subject before enrollment. In this study, the DTI and rsfMRI data were acquired from 24 healthy subjects twice in two independent scans and from 16 mTBI patients at both acute and subacute stages after injure. In acute stage, patients were scanned 82.64/17 (average/median) hours after injury. For subacute stage, patients returned 4-6 weeks after injury to take the second scan.

Data were collected on a 3-Tesla Siemens Verio scanner with a 32-channel radiofrequency head-only coil. Diffusion imaging was acquired using a gradient echo EPI sequence in 30 diffusion gradients directions with the following parameters: b = 1000, TR = 13300 ms, TE = 124 ms, slice thickness = 2 mm, pixel resolution =1.333 x 1.333 mm, matrix size = 192 x 192, flip angle = 90°, and number of averages (NEX) =2. Resting state functional imaging was performed by a gradient echo EPI sequence with the following imaging parameters: TR/TE = 2000/30 ms, slice thickness = 3.5 mm, slice gap = 0.595 mm, pixel spacing size = 3.125 x 3.125 mm, matrix size = 64 x 64, flip angle = 90°, 240 volumes for whole-brain coverage, NEX = 1. During resting state scans, subjects were instructed to keep their eyes closed.

METHOD

Each DICCCOL node is a region of interest (ROI) (Zhu, Li, Guo, et al. 2013). The connectivity between DICCCOLs was obtained based on DTI/rsfMRI data to construct structural/functional networks. The group-wise common clusters were calculated based on multi-view spectral clustering algorithm (Chen, Li, Zhu, Jiang, et al. 2013) for structural or functional

networks separately by taking the brain network of each subject as a 'view'. Based on those clusters, we further analyzed the connection changes of mTBI patients over the recovery period.

Preprocessing

Preprocessing of DTI data was performed using FSL toolbox (Jenkinson et al. 2012) which includes eddy current correction, skull and background removal, fractional anisotropic (FA) estimation. The white matter (WM)/grey matter (GM) was segmented based on FA image and WM surface was then reconstructed (Liu et al. 2007, 2008). DTI tractography was performed based on MedINRIA (Toussaint et al. 2007) to reconstruct fiber streamlines. For rsfMRI data, the first 5 volumes were removed before preprocessing. Then, brain extraction, motion correction, slice-time correction, spatially smoothing (FWHM=5mm), temporal prewhitening, grand mean removal, and temporally high-pass filter were applied on rsfMRI data accordingly in FSL (Jenkinson et al. 2012).

Predict DICCCOLs and Construct Brain Networks

DICCCOLs were predicted based on the DTI derived fiber streamlines and the reconstructed cortical surface by using the tool downloaded from http://dicccol.cs.uga.edu/. In brief, DICCCOL is composed by 358 cortical landmarks obtained based on group-wise training process described in (Zhu, Li, Guo, et al. 2013). These landmarks were defined as a patch on cortical surface and the DTI derived fiber connection profile of each patch is consistent across individuals. To predict DICCCOLs on a new subject, the subject's brain will be aligned to the template space. Then for each ROI, the closest point to the template center will be identified on the subject's reconstructed cortical surface as an initial location. By searching around the neighborhood of this initial location, the patch with similar structural connection profile to the template will be identified as the location of this ROI on the new subject.

Based on obtained 358 ROIs, brain networks were reconstructed by similar approaches in (Chen, Li, Zhu, Jiang, et al. 2013; Zhu, Li, Terry, et al. 2013). The average fractional anisotropy (FA) value along the fiber streamlines connecting each pair of DICCCOLs was taken as the structural connection strength. And if there is no fiber streamline connecting two DICCCOLs, the connection strength between them will be set 0. The functional connection strength between each pair of DICCCOLs was defined by the Pearson correlation between preprocessed rsfMRI signals derived from GM area of DICCCOLs. The obtained structural and functional connection matrices were represented by symmetric affinity matrices.

Multi-view Spectral Clustering

To analyze brain network alternations of mTBI patients as well as the network longitudinal changes during recovery, common network clusters were needed for comparison between different populations and different stages. Thus, we applied multi-view spectral clustering which has been shown to be reliable in obtaining group-wisely consistent brain network clusters (Chen, Li, Zhu, Jiang, et al. 2013). Specifically, the brain network of each subject was taken as a view. Its affinity matrix W will be projected to the eigenspace of the graph Laplacian of other views and then projected back such that:

$$proj(W,U) = (UU^T W + (UU^T W)^T)/2 \tag{8.1}$$

where $U = \Re^{n\times k}$ is the first k eigenvectors corresponding to the top k smallest eigenvalues of graph Laplacian of other affinity matrices and n = 358. The idea is similar to principal component analysis. Since the space represented by the top eigenvectors of graph Laplacian of affinity matrices can be viewed as the principal direction of corresponding graphs in which the graph expands most, by projecting other graphs to this space, the common part (the connections within clusters) will be retained and the disagreed part (the connections between clusters) will be

eliminated. Then by doing so iteratively, the networks will converge to common connections and the common clusters across individuals will be retained. For the detailed mathematical derivation, algorithm description, and experimental validations, one can refer to (Chen, Li, Zhu, Jiang, et al. 2013).

RESULTS

By performing multi-view spectral clustering on all the 80 affinity matrices derived from the data obtained from the two scans of 24 healthy controls and 16 mTBI patients, the clustering algorithm has converged to 13 common structural network clusters and 8 common functional network clusters (Figure 8. 2). The network clusters largely agree with the ones obtained from young healthy subjects in previous works (Chen, Li, Zhu, Jiang, et al. 2013). The average within and between clusters connectivity are shown in Figure 8. 3(a) for structural networks and Figure 8. 3(c) for functional networks, respectively. It is obvious that within cluster connections is stronger than between cluster connections.

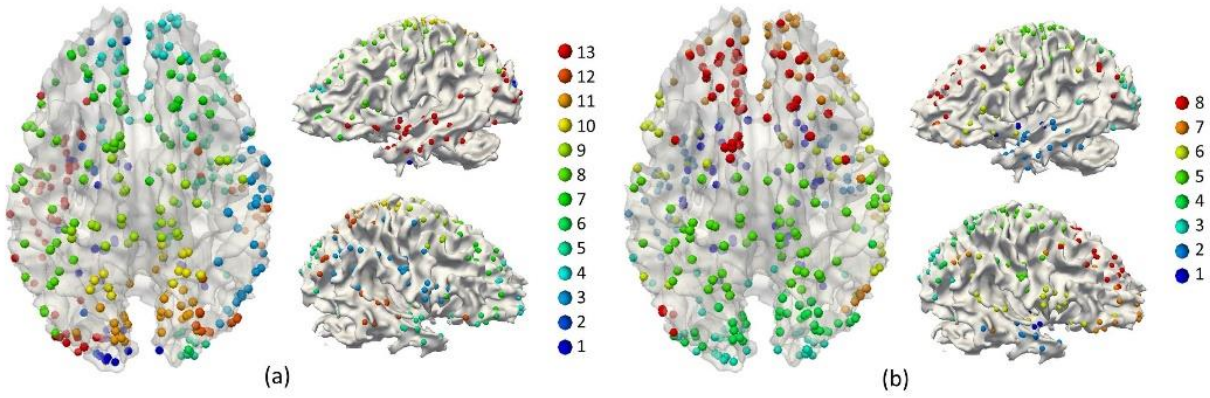

Figure 8. 2. Visualization of brain network clusters. Each DICCCOL is represented by a bubble color-coded by clusters (color legend on right). (a) 13 group-wise consistent structural network clusters. (b) 8 group-wise consistent functional network clusters.

For structural connections, the connectivity pattern is relatively similar between patient and control populations. Comparing the differences between the two scans of the same group (Figure 8. 3(b)), the brain network of normal controls is relatively consistent between two scans while those of mTBI patients from the acute stage to the subacute stage presented significant changes in brain networks. However, it is intriguing that the majority of the changes are the decreased connection strength during recovery such as those highlighted by green and red arrows in Figure 8. 3(b). Another intriguing observation is that, some of these changes were not detected by paired-sample t-test (as highlighted by red arrows in Figure 8. 3(b)). Meanwhile, with paired-sample t-test, the connections that do not change significantly could be selected (magenta arrows in Figure 8. 3(b)). This is partially because though the strength of the connection is extremely small, the t-test will still pick up the connections when there is a relative significant difference between groups (E.g. average connection is 0.01 for one set of data and 0.005 for another set). However, we are not interested in such connection in our analysis. And we would like to call attention on the usage of t-test in such applications.

A similar observation has also been obtained in functional connection between clusters. The network connection between and within clusters remained similar between two scans of healthy subjects while significant changes in cluster connections were observed between two stages of mTBI patients Figure 8. 3(d)).

In our analysis, we noticed that the connection within and between structural cluster 5 and cluster 12 both decreased in subacute stage. By comparing the structural network of mTBI patients and healthy controls, the connections related to these two clusters is also weaker than normal controls for patients (Figure 8. 4). These two clusters locate at the occipital lobe and temporal lobe of right hemisphere Figure 8. 5(a). Since the major fiber pathway in this area is

inferior longitudinal fasciculus (ILF) and uncinate fasciculus (UF), it may suggest longitudinal degradation of these tracts over time. Interestingly, the functional connection between cluster 2 (temporal lobe, Figure 8. 5(b)) and other clusters increased significantly during brain recovery, which is consistent with the observation based on structural networks.

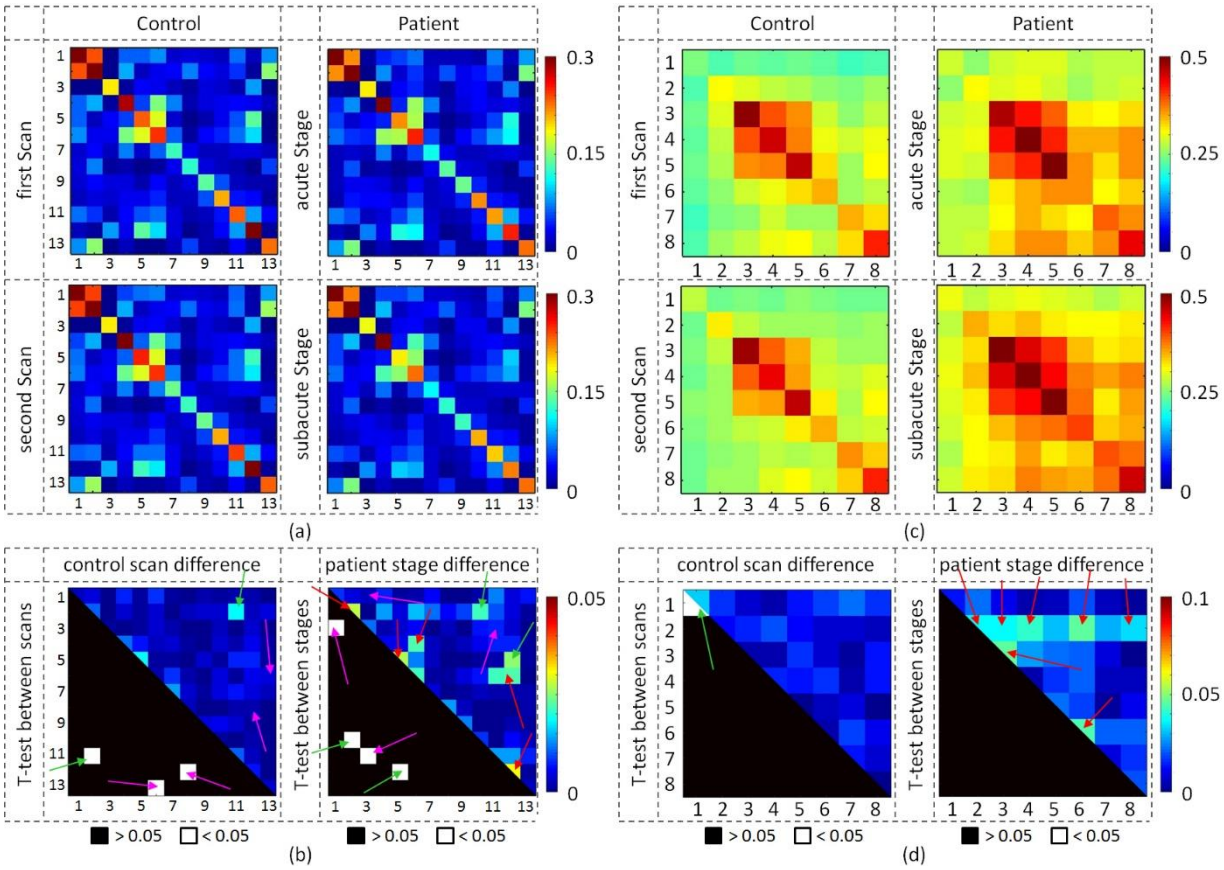

Figure 8. 3. Average (a) structural connection density or (c) functional connection strength within and between clusters for each group of scans. Comparison between two scans for each population for (b) structural or (d) functional connection were shown on the bottom accordingly. In the matrix shown in (b) and (d), top right part is the absolute difference between the average connection densities of two scans/stages; and bottom left part is the significantly changed connections ($P<0.05$) tested by paired-sample t-test.

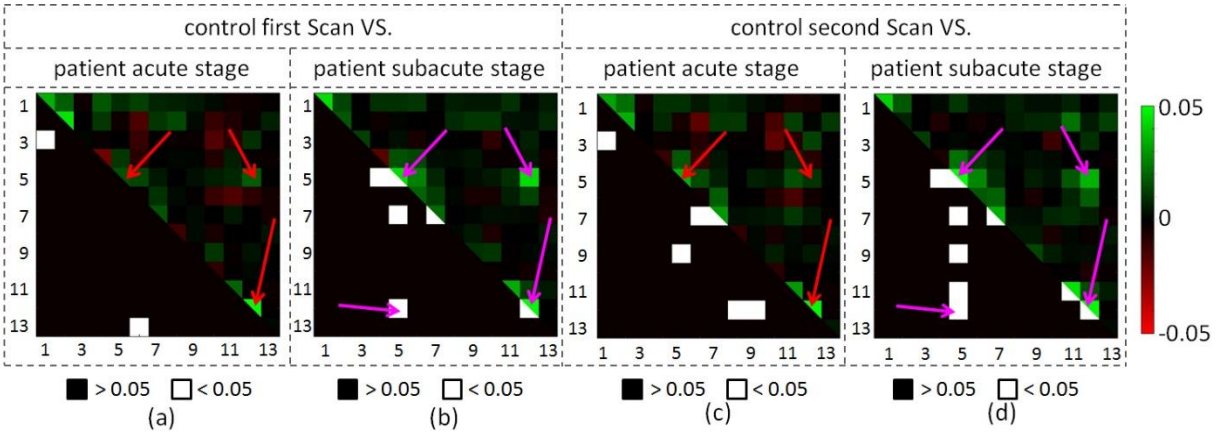

Figure 8. 4. Comparison of average structural connection densities between healthy controls and mTBI patients. In each subfigure, top right part of the matrix is the difference (control minus patient) and bottom left part is the significant different connections tested by two-sample t-test with 1000 permutations.

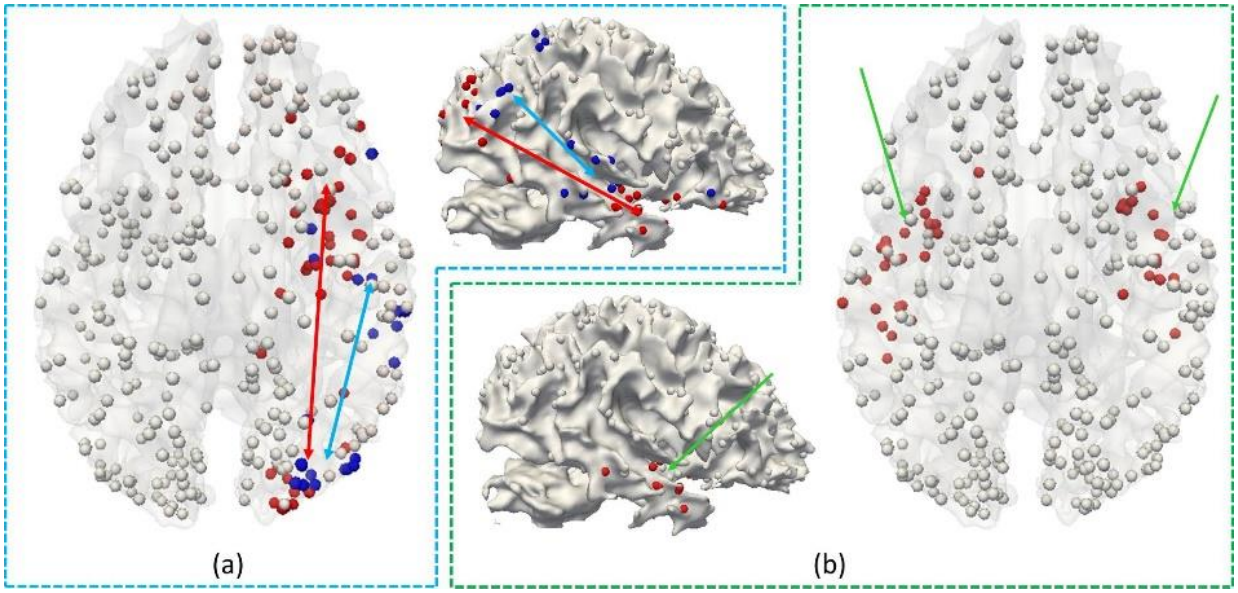

Figure 8. 5. (a) Visualization of structural network cluster 5 (red) and 12 (blue). (b) Visualization of functional network cluster 2 (red). Each cluster is highlighted by arrows of different colors.

DISCUSSION AND CONCLUSION

Mounting evidence in histopathology demonstrates that TBI has a progressive nature. After initial traumatic insult, the axons will undergo a temporal progression of degradation to final disruption. Recent evidence demonstrates that a prior history of brain injury, even a

concussion, will make the patient more vulnerable to poor outcome after the second insult. Our structural network finding also demonstrates the progressive degradation nature in large-scale networks in mTBI. Furthermore, despite brain concussion, most mTBI patients enjoy a full recovery within several months from a neurocognitive assessment perspective. This leads to the hypothesis that brain is highly plastic. Our data further support this hypothesis. In spite of structurally reduced connectivity in the temporal white matter, this area tends to increase functional connectivity with other regions of the brain to compensate. Putting together, our work represents the first finding on the progressive pathology of brain injury and functional compensation after mTBI from a large scale network perspective. Particularly the identification of brain networks undergoing structural degradation and functional plasticity would help clinicians to make proper neurorehabilitation plan to proactively treat the patient for a speedy recovery.

ACKNOWLEDGEMENTS

This research was supported in part by the National Institutes of Health (R01DA033393, R01AG042599), by the National Science Foundation Graduate Research Fellowship (NSF CAREER Award IIS-1149260, CBET-1302089, BCS-1439051), by the Department of Defense (award number W81XWH-11-1-0493), and by International Society for Magnetic Resonance in Medicine (ISMRM) Seed Grant award (PI: Zhifeng Kou).

CHAPTER 9

DISCUSSION AND CONCLUSION

This thesis systematically introduced my Ph.D. studies on brain connectome in different scales ranging from micro-scale to macro-scale. A wide range of topics has been covered including different imaging modalities, different resolution scales, different species and objects, and different analysis methods. Figure 9. 1 shows a summary of these topics involved. Such variability is due to the interdisciplinary nature of brain connectome study and is also the major challenging of brain connectome studies and also requires researchers equipping a comprehensive background of neuroscience.

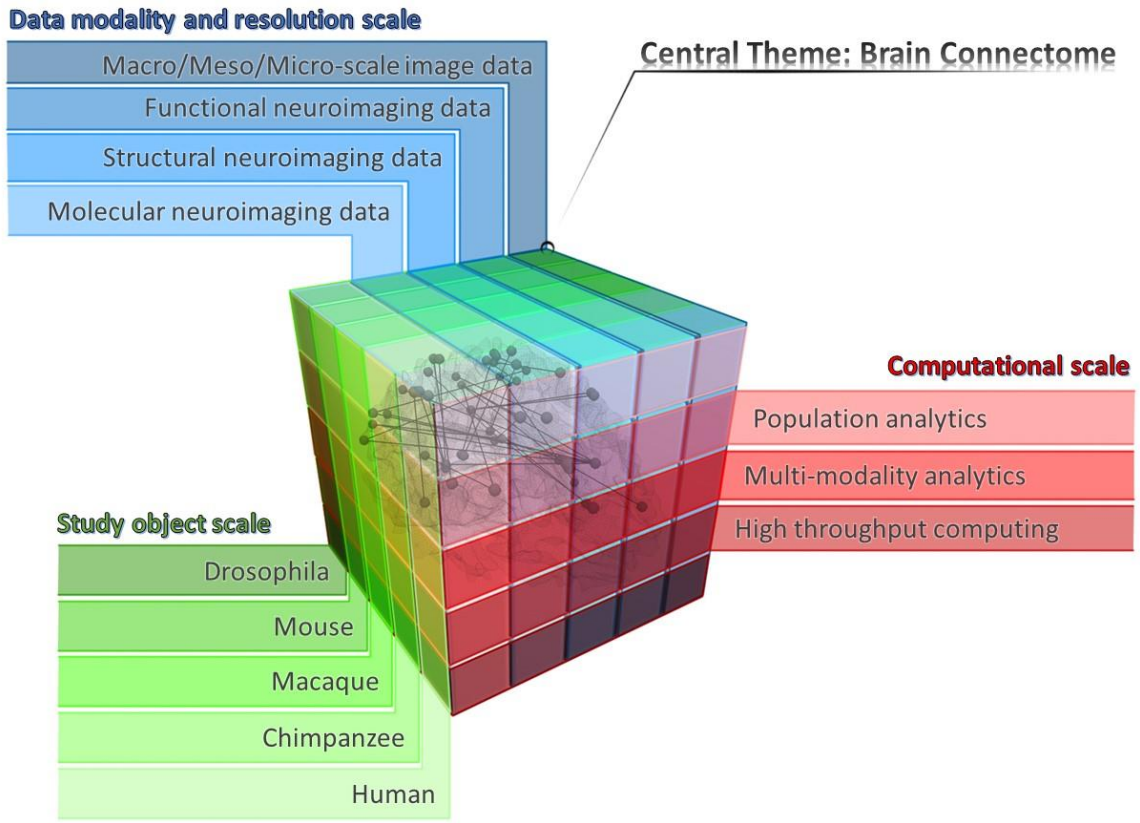

Figure 9. 1. Summary and overall vision of my research topics on brain connectome.

In this chapter, I will summarize my contributions in computational scale and research philosophies as a computer scientist. The major contributions of my Ph.D studies includes high-throughput computing tools for neuroimage analysis, automatic neuron reconstruction software (chapter 2, 3), computational analysis frameworks for across scales (chapter 4), across species (chapter 5), and group-wise (chapter 6) comparison of neuron wiring, multi-modalities learning algorithms for brain network fusion (chapter 7, 8), and the corresponding novel neurology findings. They can be further summarized into three major topics as shown in Figure 9. 1: (1) high throughput computing, (2) multi-modality analytics, and (3) population analytics.

HIGH-THROUGHPUT COMPUTING

Thanks to the development of bio-imaging techniques, acquiring a large population of neuroimaging data in good quality are more feasible than ever. And thanks to the trend of open source in neuroscience field, more and more neuroimaging data are now shared online or between labs. Data availability is no longer the major reason that slows the findings in the neuroscience field. Instead, the lack of efficient computational pipelines is becoming the bottleneck. Despite the previously mentioned approaches from the perspective of analytical strategy, the throughput of the computational tool is also very important. To increase the throughput, two features are very important for tool design: 1) 'smart'; 2) high-performance computing.

Smart Softwares

Today, Google cars can already handle complicated road conditions and drive automatically on the road without human intervention. However, in most biology labs, scientists still have to repeat their experiments again and again to acquire data. As a computer scientist, I would like to build smarter tools to free those great minds from labor works so they can focus on

more intelligent activities. For instance, I developed NeuronStitcher which is the first tool that allows neuroscientists to automaticaly/semi-automaticaly stitch neuron fragments from sliced brain tissues (Chapter 3). Due to the limited imaging depth of microscopic, to study complete neuron morphology, researchers need to 1) physically section brains, 2) image such sections under the microscope, and 3) stack and align image sections one by one to generate a very big image volume. Before NeuronStitcher, step 3 can only be manually accomplished for confocal microscopic sections. Yet an accurate alignment is extremely difficult. The tool provided an efficient solution to this problem and has been integrated in the IVSCC pipeline of Allen Institute for Brain Science. In another work, I developed one of the first fully automatic software based on machine learning algorithms to reconstruct a 3D digital representation of neuron morphology (Chen, Xiao, et al. 2015) (Chapter 2). SmartTracing is a very powerful tool in that it is self-adaptive and does not need human intervention such as parameter tuning to generate results.

High-performance computing

Advanced computing framework such as network clusters, computer clouds, or graphic processing unit (GPU) is usually needed to speed up computations for big data. In my recent work in collaboration with Yu Zhao, we successfully reduced the running time of pairwise comparison between 35600 3-dimensional images of brain functional networks from 1280 hours to 3 days (Zhao et al. 2016). Our computational framework was implemented on Apache Spark, which provides a fast and general engine for big data processing. To our best knowledge, this is one of the earliest works in applying SPARK scalable computing framework in processing fMRI images. In the future, we will complete this high-performance fMRI analysis framework and release it to the field.

Cross validate findings between different resolution scales

Advanced neuroimaging techniques allow researchers to investigate brain on different scales which offer complementary pictures of the brain. Coarse scale images enable a global and population-wise view of the brain, while finer scale images carry more details and can be used to validate findings on coarser scales. For instance, diffusion imaging and tractography have been widely used to investigate structural connectome on macro-scale. Despite its capability in none-invasively capturing whole-brain structural networks, the technique has been questioned for its limitations and biases for a long time. By comparing whole brain connectome derived from DTI tractography with the connectome derived from meso-scale neuron tracing study released by Allen Mouse Connectivity Atlas, my recent study has showed that a limited agreement between two scales can be achieved with gains in reliability and sensitivity that depend on the selection of optimal tractography parameters and parcellation schemes (Chen, Liu, et al. 2015) (Chapter 4). In the future, this framework can be applied in designing better DTI acquisition parameters and tractography models.

Link findings across species

The rationale for studying and comparing neuroimaging data across species are mainly two-fold: 1) the differences across species allow us to investigate how the brain evolves and how human-specific brain functions emerge; 2) the common brain mechanisms and anatomical regions across species allow us to investigate human brain based on animal models. In my previous studies in collaboration with Dr. Tuo Zhang, by analyzing MRI and DTI data across macaque, chimpanzee, and human brain, we found that the complexity of wiring patterns and folding patterns jointly evolves across species (Chen, Zhang, Guo, et al. 2013; Zhang, Chen, et

al. 2014) (Chapter 5). Further investigations showed that fiber orientation coincides with the bending direction of the gyral crest. This observation is consistent across the brains of three species we analyzed and support the theory that the wiring progress may regulate cortical convolution during brain development. In another study in collaboration with Xiao Li, we analyzed the gyral folding patterns across these three species (Li et al. n.d.) and quantified both preserved and evolved patterns. In the future, this comparison can be extended to more animal models such as mouse and rat brain. And we should also include more imaging modalities into analysis such as functional data or molecular data.

Compare functional and structural connectome

If we view the brain as a computer, then the structural (anatomical) connectome is the hardware of brain and the functional connectome is the software in the brain. Most of the previous studies on mental disorders largely rely on a single imaging modality and thus only focused on one aspect of the brain. However, a comprehensive understanding of brain requires viewing brain from both aspects. Based on the group-wise analysis approaches (Zhu, Li, Guo, et al. 2013), I found that structural connectivity is more consistent across individuals in comparison with the functional connectivity (Chen, Li, Zhu, Jiang, et al. 2013). This finding is expected given that the functional connectivity may dynamically alter between different brain states. By fusing the connectome across individuals, we can reproducibly identify brain network clusters for both functional and structural connectivity among different groups of subjects. This framework offered new insight on the joint analysis of brain connectome and has been successfully applied to mTBI studies (Chen, Iraji, et al. 2015). In the future, the method will be extended to the analysis of different brain disorders as well as joint analyses across multiple brain diseases.

GROUP-WISE ANALYTICS

Defining reliable, reproducible and accurate brain regions of interest (ROIs) is the first and fundamentally important step in performing group-wise analysis of brain connectome. Traditional approaches rely on registering individual brains to a common template brain with atlas derived from domain knowledge (E.g. Brodmann area) to define common ROIs. However, automatic registration algorithm has limited accuracy in mapping ROIs due to the variability across individuals. Although more precise ROIs can be obtained by manual annotation of experts, it is not applicable to large populations. Moreover, finer parcellation of ROIs beyond current domain knowledge is required for accurate mapping of functional ROIs (E.g. pre-central gyrus should be further parcellated into different functional regions).

Facing this challenge, my colleagues and I have made great progress on defining brain ROIs (Liu 2011) in the past 6 years. Together with my colleague Dr. Dajiang Zhu and Dr. Kaiming Li, we reproducibly and accurately identified and predicted brain ROIs with consistent structural connectivity across individuals (Chen, Zhang, and Liu 2013; Zhu, Li, Guo, et al. 2013). Specifically, we defined a set of accurate and efficient descriptors for brain connectivity profiling. Then based on a data-driven exhaustive search, regions with common connectivity profiles were identified. For instance, in my works, 12 consistent white matter hubs were reproducibly identified (Chen, Zhang, and Liu 2013) (Chapter 6) and pre-central/post-central gyri were consistently parcellated into multiple sections (Chen, Cai, et al. 2012). I also included different metrics to further refine ROIs including functional connectivity profile (Chen, Li, Zhu, and Liu 2013), inter-regional connectivity profile (Chen et al. 2014), and global distance constraint (Yuan et al. 2015). These ROI systems will serve as a GPS map of brains. In the

future, the similar approach can be extended to identify ROIs that are not only consistent across individuals but also consistent across species.

According to the 'fingerprint' concept suggested by Passingham that each brain's cytoarchitectonic area has a unique set of extrinsic inputs and outputs that largely determines the functions that each brain area performs, those ROIs with consistent structural connectivity are ideal for both functional and structural connectome studies. With the identified ROIs as foundations, I studied the regularity and variability of both functional and structural connectome across populations in both healthy brains and diseased brains. Specifically, I adopted a novel algorithm called multi-view spectral clustering to fuse functional connectome and structural connectome across individuals to identify common brain network modules (Chen, Li, Zhu, Jiang, et al. 2013) (Chapter 7). Based on this framework, I performed longitudinal and group-wise analysis on mild traumatic brain injury subjects and found that after brain injury decreased inter-regional structural connectivity will be complemented by increased functional connectivity (Chen, Iraji, et al. 2015; Iraji et al. 2016) (Chapter 8). In the future, the method can be widely applied to larger database analysis which includes many more subjects of variety brain diseases across different imaging sites for a deep understanding of abnormal connectome in mental disorders.

Besides model driven approaches, machine learning algorithms are also powerful tools in identifying brain regions of interest (Lv, Jiang, Li, Zhu, Chen, et al. 2015; Lv, Jiang, Li, Zhu, Zhang, et al. 2015). Specifically, in collaboration with Yu Zhao, we have developed a large-scale computing framework to study functional network alternations in Autism patient brains (Zhao et al. 2016). By applying sparse representations and dictionary learning on resting-state fMRI images, the brain was decomposed into hundreds of functional networks. After pair-wisely

comparing decomposed networks across 178 subjects, we identified 144 group-wisely common functional networks. Further analysis of these networks showed abnormality in both inner-network connectivity and inter-network interactions. Traditional fMRI analysis only focused on a few brain networks such as default mode networks. The novel techniques proposed in this work may revolute future fMRI studies on brain functional connectome such that a more comprehensive understanding of brain functional networks than before is possible. In another work with Yujie Li, we found that machine learning approach can also identify ROIs from gene expression data. By applying the data-driven sparse coding framework on genome-wide in situ hybridization image data set released by Allen Mouse Brain Atlas, we identified transcriptome organization of mouse brain that displayed robust regional specific molecular signatures and corresponded to canonical neuroanatomical subdivisions consisting of discrete neuronal subtypes. In the future, similar methods can be applied on different imaging modalities. Moreover, it is also important to correlate those ROIs obtained from different imaging modalities. Traditionally, brain ROIs are defined and predicted based on a single image modality (e.g. manually annotated on averaged MRI templates). My colleagues have shown that by using structural connectivity consistency as constraint, we can more accurately identify brain ROIs computed from task fMRI data. My work further showed that by including the predictability of functional connectivity from structural connectivity into object function, the brain ROIs initially obtained based on structural information can be optimized to preserve better anatomical consistency across individuals (Chen, Li, Zhu, and Liu 2013). In the future, it is necessary and much more meaningful to define and optimize brain ROIs by including joint information from multiple modalities such as functional connectivity (fMRI), structural connectivity (DTI), anatomical information (MRI, Nissle stain), and gene expression data.

REFERENCES

Achard S, Salvador R, Whitcher B, Suckling J, Bullmore E. 2006. A Resilient, Low-Frequency, Small-World Human Brain Functional Network with Highly Connected Association Cortical Hubs. J neurosicience. 26:63–72.

Andersson JLR, Skare S, Ashburner J. 2003. How to correct susceptibility distortions in spin-echo echo-planar images: application to diffusion tensor imaging. Neuroimage. 20:870–888.

Arbabshirani MR, Plis S, Sui J, Calhoun VD. 2016. Single subject prediction of brain disorders in neuroimaging: Promises and pitfalls. Neuroimage.

Assaf Y, Alexander DC, Jones DK, Bizzi A, Behrens TEJ, Clark CA, Cohen Y, Dyrby TB, Huppi PS, Knoesche TR, Lebihan D, Parker GJM, Poupon C, Anaby D, Anwander A, Bar L, Barazany D, Blumenfeld-Katzir T, De-Santis S, Duclap D, Figini M, Fischi E, Guevara P, Hubbard P, Hofstetter S, Jbabdi S, Kunz N, Lazeyras F, Lebois A, Liptrot MG, Lundell H, Mangin J-F, Dominguez DM, Morozov D, Schreiber J, Seunarine K, Nava S, Riffert T, Sasson E, Schmitt B, Shemesh N, Sotiropoulos SN, Tavor I, Zhang HG, Zhou F-L. 2013. The CONNECT project: Combining macro- and micro-structure. Neuroimage. 80:273–282.

Assaf Y, Pasternak O. 2008. Diffusion tensor imaging (DTI)-based white matter mapping in brain research: a review. J Mol Neurosci. 34:51–61.

Basser PJ, Mattiello J, LeBihan D. 1994. MR diffusion tensor spectroscopy and imaging. Biophys J. 66:259–267.

Bassett DS, Bullmore ET. 2009. Human brain networks in health and disease. Curr Opin Neurol. 22:340–347.

Bloy L, Ingalhalikar M, Eavani H, Roberts TPL, Schultz RT, Verma R. 2011. HARDI based pattern classifiers for the identification of white matter pathologies. In: MICCAI. p. 234–241.

Bock DD, Lee W-CA, Kerlin AM, Andermann ML, Hood G, Wetzel AW, Yurgenson S, Soucy ER, Kim HS, Reid RC. 2011. Network anatomy and in vivo physiology of visual cortical neurons. Nature. 471:177–182.

Bria A, Iannello G. 2012. TeraStitcher - a tool for fast automatic 3D-stitching of teravoxel-sized microscopy images. BMC Bioinformatics. 13:316.

Bullmore E, Sporns O. 2009. Complex brain networks: graph theoretical analysis of structural and functional systems. Nat Rev Neurosci. 10:186–198.

Cahill L. 2006. Why sex matters for neuroscience. Nat Rev Neurosci. 7:477–484.

Cai X, Nie F, Huang H, Kamangar F. 2011. Heterogeneous image feature integration via multi-modal spectral clustering. In: CVPR. IEEE. p. 1977–1984.

Calamante F, Tournier J-D, Kurniawan ND, Yang Z, Gyengesi E, Galloway GJ, Reutens DC, Connelly A. 2012. Super-resolution track-density imaging studies of mouse brain: comparison to histology. Neuroimage. 59:286–296.

Cardona A, Saalfeld S, Schindelin J, Arganda-Carreras I, Preibisch S, Longair M, Tomancak P, Hartenstein V, Douglas RJ. 2012. TrakEM2 software for neural circuit reconstruction. PLoS One. 7:e38011.

Chang C-C, Lin C-J. 2011. LIBSVM: A library for support vector machines. ACM Trans Intell Syst Technol. 2:1–27.

Chen C-H, Gutierrez ED, Thompson W, Panizzon MS, Jernigan TL, Eyler LT, Fennema-Notestine C, Jak AJ, Neale MC, Franz CE, Lyons MJ, Grant MD, Fischl B, Seidman LJ, Tsuang MT, Kremen WS, Dale AM. 2012. Hierarchical genetic organization of human cortical surface area. Science. 335:1634–1636.

Chen H, Cai X, Zhu D, Nie F, Liu T, Huang H. 2012. Group-wise consistent parcellation of gyri via adaptive multi-view spectral clustering of fiber shapes. MICCAI, LNCS. 7511:271–279.

Chen H, Iraji A, Jiang X, Lv J, Kou Z, Liu T. 2015. Longitudinal Analysis of Brain Recovery After Mild Traumatic Brain Injury Based on Group-wise Consistent Brain Network Clusters. MICCAI, LNCS. 9350:194–201.

Chen H, Li K, Zhu D, Guo L, Jiang X, Liu T. 2014. Group-wise optimization and individualized prediction of structural connectomes. In: ISBI. IEEE. p. 742–745.

Chen H, Li K, Zhu D, Jiang X, Yuan Y, Lv P, Zhang T, Guo L, Shen D, Liu T. 2013. Inferring group-wise consistent multimodal brain networks via multi-view spectral clustering. IEEE Trans Med Imaging. 32:1576–1586.

Chen H, Li K, Zhu D, Liu T. 2013. Identifying consistent brain networks via maximizing predictability of functional connectome from structural connectome. In: ISBI. IEEE. p. 978–981.

Chen H, Liu T, Zhao Y, Zhang T, Li Y, Li M, Zhang H, Kuang H, Guo L, Tsien JZ, Liu T. 2015. Optimization of large-scale mouse brain connectome via joint evaluation of DTI and neuron tracing data. Neuroimage. 115:202–213.

Chen H, Xiao H, Liu T, Peng H. 2015. SmartTracing: self-learning-based Neuron reconstruction. Brain Informatics. 2:135–144.

Chen H, Zhang T, Guo L, Li K, Yu X, Li L, Hu XX, Han J, Liu T. 2013. Coevolution of gyral folding and structural connection patterns in primate brains. Cereb Cortex. 23:1208–1217.

Chen H, Zhang T, Liu T. 2013. Identifying group-wise consistent white matter landmarks via novel fiber shape descriptor. MICCAI, LNCS. 8149:66–73.

Chen ZJ, He Y, Rosa-Neto P, Germann J, Evans AC. 2008. Revealing modular architecture of human brain structural networks by using cortical thickness from MRI. Cereb cortex. 18:2374–2381.

Choe AS, Stepniewska I, Colvin DC, Ding Z, Anderson AW. 2012. Validation of diffusion tensor MRI in the central nervous system using light microscopy: quantitative comparison of fiber properties. NMR Biomed. 25:900–908.

Chung K, Wallace J, Kim S-Y, Kalyanasundaram S, Andalman AS, Davidson TJ, Mirzabekov JJ, Zalocusky KA, Mattis J, Denisin AK, Pak S, Bernstein H, Ramakrishnan C, Grosenick L, Gradinaru V, Deisseroth K. 2013. Structural and molecular interrogation of intact biological systems. Nature. 497:332–337.

Clarkson MJ, Malone IB, Modat M, Leung KK, Ryan N, Alexander DC, Fox NC, Ourselin S. 2010. A framework for using diffusion weighted imaging to improve cortical parcellation. In: MICCAI. p. 534–541.

Côté M-A, Girard G, Boré A, Garyfallidis E, Houde J-C, Descoteaux M. 2013. Tractometer: towards validation of tractography pipelines. Med Image Anal. 17:844–857.

Damoiseaux JS, Rombouts SARB, Barkhof F, Scheltens P, Stam CJ, Smith SM, Beckmann CF. 2006. Consistent resting-state networks across healthy subjects. Proc Natl Acad Sci U S A. 103:13848–13853.

Dauguet J, Peled S, Berezovskii V, Delzescaux T, Warfield SK, Born R, Westin C-F. 2007. Comparison of fiber tracts derived from in-vivo DTI tractography with 3D histological neural tract tracer reconstruction on a macaque brain. Neuroimage. 37:530–538.

Deacon TW. 1990. Fallacies of progression in theories of brain-size evolution. Int J Primatol. 11:193–236.

De Luca M, Beckmann CF, De Stefano N, Matthews PM, Smith SM. 2006. fMRI resting state networks define distinct modes of long-distance interactions in the human brain. Neuroimage. 29:1359–1367.

DeFelipe J. 2010. From the connectome to the synaptome: an epic love story. Science. 330:1198–1201.

Dercksen VJ, Hege H-C, Oberlaender M. 2014. The Filament Editor: an interactive software environment for visualization, proof-editing and analysis of 3D neuron morphology. Neuroinformatics. 12:325–339.

Derrfuss J, Mar RA. 2009. Lost in localization: the need for a universal coordinate database. Neuroimage. 48:1–7.

Ding C, Peng H. 2005. Minimum redundancy feature selection from microarray gene expression data. J Bioinform Comput Biol. 3:185–205.

Donohue DE, Ascoli GA. 2011. Automated reconstruction of neuronal morphology: an overview. Brain Res Rev. 67:94–102.

Duchenne O, Bach F, Kweon I-S, Ponce J. 2011. A Tensor-Based Algorithm for High-Order Graph Matching. IEEE Trans Pattern Anal Mach Intell. 33:2383–2395.

Dyrby TB, Søgaard L V, Parker GJ, Alexander DC, Lind NM, Baaré WFC, Hay-Schmidt A, Eriksen N, Pakkenberg B, Paulson OB, Jelsing J. 2007. Validation of in vitro probabilistic tractography. Neuroimage. 37:1267–1277.

Eierud C, Craddock RC, Fletcher S, Aulakh M, King-Casas B, Kuehl D, LaConte SM. 2014. Neuroimaging after mild traumatic brain injury: Review and meta-analysis. NeuroImage Clin. 4:283–294.

Fillard P, Descoteaux M, Goh A, Gouttard S, Jeurissen B, Malcolm J, Ramirez-Manzanares A, Reisert M, Sakaie K, Tensaouti F, Yo T, Mangin J-F, Poupon C. 2011. Quantitative evaluation of 10 tractography algorithms on a realistic diffusion MR phantom. Neuroimage. 56:220–234.

Friston KJ. 2009. Modalities, modes, and models in functional neuroimaging. Science. 326:399–403.

Gala R, Chapeton J, Jitesh J, Bhavsar C, Stepanyants A. 2014. Active learning of neuron morphology for accurate automated tracing of neurites. Front Neuroanat. 8:37.

Gao Y, Choe AS, Stepniewska I, Li X, Avison MJ, Anderson AW. 2013. Validation of DTI tractography-based measures of primary motor area connectivity in the squirrel monkey brain. PLoS One. 8:e75065.

Gönen M, Alpaydın E. 2011. Multiple Kernel Learning Algorithms. J Mach Learn Res. 12:2211–2268.

Gorski KM, Hivon E, Banday AJ, Wandelt BD, Hansen FK, Reinecke M, Bartelmann M. 2005. HEALPix: A Framework for High-Resolution Discretization and Fast Analysis of Data Distributed on the Sphere. Astrophys J. 622:759–771.

Greicius MD, Krasnow B, Reiss AL, Menon V. 2003. Functional connectivity in the resting brain: a network analysis of the default mode hypothesis. Proc Natl Acad Sci U S A. 100:253–258.

Hagmann P, Cammoun L, Gigandet X, Meuli R, Honey CJ, Wedeen VJ, Sporns O. 2008. Mapping the structural core of human cerebral cortex. PLoS Biol. 6:e159.

Hama H, Kurokawa H, Kawano H, Ando R, Shimogori T, Noda H, Fukami K, Sakaue-Sawano A, Miyawaki A. 2011. Scale: a chemical approach for fluorescence imaging and reconstruction of transparent mouse brain. Nat Neurosci. 14:1481–1488.

Hansen B, Flint JJ, Heon-Lee C, Fey M, Vincent F, King MA, Vestergaard-Poulsen P, Blackband SJ. 2011. Diffusion tensor microscopy in human nervous tissue with quantitative

correlation based on direct histological comparison. Neuroimage. 57:1458–1465.

He Y, Chen ZJ, Evans AC. 2007. Small-world anatomical networks in the human brain revealed by cortical thickness from MRI. Cereb cortex. 17:2407–2419.

Hellier P, Barillot C, Corouge I, Gibaud B, Le Goualher G, Collins DL, Evans A, Malandain G, Ayache N, Christensen GE, Johnson HJ. 2003. Retrospective evaluation of intersubject brain registration. IEEE Trans Med Imaging. 22:1120–1130.

Helmstaedter M, Briggman KL, Denk W. 2011. High-accuracy neurite reconstruction for high-throughput neuroanatomy. Nat Neurosci. 14:1081–1088.

Helmstaedter M, Mitra PP. 2012. Computational methods and challenges for large-scale circuit mapping. Curr Opin Neurobiol. 22:162–169.

Henderson A. 2007. The ParaView guide : A Parallel visualization application.

Herkenham M. 1978. The connections of the nucleus reuniens thalami: evidence for a direct thalamo-hippocampal pathway in the rat. J Comp Neurol. 177:589–610.

Hess CP, Mukherjee P, Han ET, Xu D, Vigneron DB. 2006. Q-ball reconstruction of multimodal fiber orientations using the spherical harmonic basis. Magn Reson Med. 56:104–117.

Hevner RF, Haydar TF. 2012. The (Not Necessarily) Convoluted Role of Basal Radial Glia in Cortical Neurogenesis. Cereb Cortex. 22:465–468.

Hogrebe L, Paiva ARC, Jurrus E, Christensen C, Bridge M, Korenberg JR, Tasdizen T. 2011. Trace driven registration of neuron confocal microscopy stacks. In: 2011 IEEE International Symposium on Biomedical Imaging: From Nano to Macro. IEEE. p. 1345–1348.

Honey CJ, Sporns O, Cammoun L, Gigandet X, Thiran JP, Meuli R, Hagmann P. 2009. Predicting human resting-state functional connectivity from structural connectivity. Proc Natl Acad Sci U S A. 106:2035–2040.

Hu X, Guo L, Zhang T, Li G, Nie J, Jiang X, Zhang D, Liu T. 2010. Joint analysis of fiber shape and cortical folding patterns. In: 2010 IEEE International Symposium on Biomedical Imaging: From Nano to Macro. IEEE. p. 1165–1168.

Huttenlocher DP, Klanderman GA, Rucklidge WJ. 1993. Comparing images using the Hausdorff distance. IEEE Trans Pattern Anal Mach Intell. 15:850–863.

Iraji A, Benson RR, Welch RD, O'Neil BJ, Woodard JL, Ayaz SI, Kulek A, Mika V, Medado P, Soltanian-Zadeh H, Liu T, Haacke EM, Kou Z. 2015. Resting State Functional Connectivity in Mild Traumatic Brain Injury at the Acute Stage: Independent Component and Seed-Based Analyses. J Neurotrauma.

Iraji A, Chen H, Wiseman N, Welch RD, O'Neil BJ, Haacke EM, Liu T, Kou Z. 2016. Compensation through Functional Hyperconnectivity: A Longitudinal Connectome Assessment

of Mild Traumatic Brain Injury. Neural Plast.

Iturria-Medina Y, Canales-Rodríguez EJ, Melie-García L, Valdés-Hernández PA, Martínez-Montes E, Alemán-Gómez Y, Sánchez-Bornot JM. 2007. Characterizing brain anatomical connections using diffusion weighted MRI and graph theory. Neuroimage. 36:645–660.

Iturria-Medina Y, Sotero RC, Canales-Rodríguez EJ, Alemán-Gómez Y, Melie-García L. 2008. Studying the human brain anatomical network via diffusion-weighted MRI and Graph Theory. Neuroimage. 40:1064–1076.

Jbabdi S, Johansen-Berg H. 2011. Tractography: where do we go from here? Brain Connect. 1:169–183.

Jbabdi S, Lehman JF, Haber SN, Behrens TE. 2013. Human and monkey ventral prefrontal fibers use the same organizational principles to reach their targets: tracing versus tractography. J Neurosci. 33:3190–3201.

Jenkinson M, Beckmann CF, Behrens TE, Woolrich MW, Smith SM. 2012. FSL. Neuroimage. 62:782–790.

Jenkinson M, Smith S. 2001. A global optimisation method for robust affine registration of brain images. Med Image Anal. 5:143–156.

Jiang H, van Zijl PCM, Kim J, Pearlson GD, Mori S. 2006. DtiStudio: resource program for diffusion tensor computation and fiber bundle tracking. Comput Methods Programs Biomed. 81:106–116.

Jiang T. 2013. Brainnetome: a new -ome to understand the brain and its disorders. Neuroimage. 80:263–272.

Jiang T. 2014. Brainnetome and related projects. Sci China Life Sci. 57:462–466.

Kaiser M, Görner M, Hilgetag CC. 2007. Criticality of spreading dynamics in hierarchical cluster networks without inhibition. New J Phys. 9:110–110.

Kötter R. 2007. Anatomical Concepts of Brain Connectivity. In: Handbook of Brain Connectivity. Springer Berlin Heidelberg. p. 149–167.

Krubitzer L. 2009. In Search of a Unifying Theory of Complex Brain Evolution. Ann N Y Acad Sci. 1156:44–67.

Krzywinski M, Schein J, Birol İ. 2009. Circos: an information aesthetic for comparative genomics. Genome Res. 19:1639–1645.

Kumar A, III HD. 2011. A Co-training Approach for Multi-view Spectral Clustering. In: ICML.

Lee P-C, Chuang C-C, Chiang A-S, Ching Y-T. 2012. High-throughput computer method for 3D neuronal structure reconstruction from the image stack of the Drosophila brain and its

applications. PLoS Comput Biol. 8:e1002658.

Leergaard TB, White NS, de Crespigny A, Bolstad I, D'Arceuil H, Bjaalie JG, Dale AM. 2010. Quantitative histological validation of diffusion MRI fiber orientation distributions in the rat brain. PLoS One. 5:e8595.

Li G, Guo L, Nie J, Liu T. 2009. Automatic cortical sulcal parcellation based on surface principal direction flow field tracking. Neuroimage. 46:923–937.

Li K, Guo L, Li G, Nie J, Faraco C, Cui G, Zhao Q, Miller LS, Liu T. 2010. Gyral folding pattern analysis via surface profiling. Neuroimage. 52:1202–1214.

Li K, Zhu D, Guo L, Li Z, Lynch ME, Coles C, Hu X, Liu T. 2013. Connectomics signatures of prenatal cocaine exposure affected adolescent brains. Hum Brain Mapp. 34:2494–2510.

Li L, Hu X, Preuss TM, Glasser MF, Damen FW, Qiu Y, Rilling J. 2013. Mapping putative hubs in human, chimpanzee and rhesus macaque connectomes via diffusion tractography. Neuroimage. 80:462–474.

Li X, Chen H, Zhang T, Yu X, Jiang X, Li K, Li L, Razavi MJ, Wang X, Hu X, Han J, Guo L, Hu X, Liu T. n.d. Evolutionarily-Preserved and Species-Specific Gyral Folding Patterns across Primate Brains. Cereb cortex.

Lichtman JW, Sanes JR. 2008. Ome sweet ome: what can the genome tell us about the connectome? Curr Opin Neurobiol. 18:346–353.

Liu C, Li W, Wu B, Jiang Y, Johnson GA. 2012. 3D fiber tractography with susceptibility tensor imaging. Neuroimage. 59:1290–1298.

Liu F, Suk H, Wee C, Chen H, Shen D. 2013. High-order graph matching based feature selection for Alzheimer's disease identification. Med Image Comput ….

Liu T. 2011. A few thoughts on brain ROIs. Brain Imaging Behav. 5:189–202.

Liu T, Li H, Wong K, Tarokh A, Guo L, Wong STC. 2007. Brain tissue segmentation based on DTI data. Neuroimage. 38:114–123.

Liu T, Nie J, Tarokh A, Guo L, Wong STC. 2008. Reconstruction of central cortical surface from brain MRI images: method and application. Neuroimage. 40:991–1002.

Logothetis NK. 2008. What we can do and what we cannot do with fMRI. Nature. 453:869–878.

Luxburg U. 2007. A tutorial on spectral clustering. Stat Comput. 17:395–416.

Luzzati F, Fasolo A, Peretto P. 2011. Combining confocal laser scanning microscopy with serial section reconstruction in the study of adult neurogenesis. Front Neurosci. 5:70.

Lv J, Jiang X, Li X, Zhu D, Chen H, Zhang T, Zhang S, Hu X, Han J, Huang H, Zhang J, Guo L, Liu T. 2015. Sparse representation of whole-brain fMRI signals for identification of functional

networks. Med Image Anal. 20:112–134.

Lv J, Jiang X, Li X, Zhu D, Zhang S, Zhao S, Chen H, Zhang T, Hu X, Han J, Ye J, Guo L, Liu T. 2015. Holistic atlases of functional networks and interactions reveal reciprocal organizational architecture of cortical function. IEEE Trans Biomed Eng. 62:1120–1131.

Ma L, Lu Z, Shang L, Li H. 2015. Multimodal Convolutional Neural Networks for Matching Image and Sentence. In: Proceedings of the IEEE International Conference on Computer Vision. p. 2623–2631.

Mallat SG. 1989. A theory for multiresolution signal decomposition: the wavelet representation. IEEE Trans Pattern Anal Mach Intell. 11:674–693.

Mao J, Xu W, Yang Y, Wang J, Yuille AL. 2014. Explain Images with Multimodal Recurrent Neural Networks.

McCrea M, Iverson GL, McAllister TW, Hammeke TA, Powell MR, Barr WB, Kelly JP. 2009. An integrated review of recovery after mild traumatic brain injury (MTBI): implications for clinical management. Clin Neuropsychol. 23:1368–1390.

Meijering E. 2010. Neuron tracing in perspective. Cytometry A. 77:693–704.

Meskaldji DE, Fischi-Gomez E, Griffa A, Hagmann P, Morgenthaler S, Thiran J-P. 2013. Comparing connectomes across subjects and populations at different scales. Neuroimage. 80:416–425.

Moldrich RX, Pannek K, Hoch R, Rubenstein JL, Kurniawan ND, Richards LJ. 2010. Comparative mouse brain tractography of diffusion magnetic resonance imaging. Neuroimage. 51:1027–1036.

Mori S, Crain BJ, Chacko VP, Van Zijl PCM. 1999. Three-dimensional tracking of axonal projections in the brain by magnetic resonance imaging. Ann Neurol. 45:265–269.

Mori S, Oishi K, Jiang H, Jiang L, Li X, Akhter K, Hua K, Faria A V, Mahmood A, Woods R, Toga AW, Pike GB, Neto PR, Evans A, Zhang J, Huang H, Miller MI, van Zijl P, Mazziotta J. 2008. Stereotaxic white matter atlas based on diffusion tensor imaging in an ICBM template. Neuroimage. 40:570–582.

Mori S, Zhang J. 2006. Principles of Diffusion Tensor Imaging and Its Applications to Basic Neuroscience Research. Neuron. 51:527–539.

Müller-Linow M, Hilgetag CC, Hütt M-T. 2008. Organization of excitable dynamics in hierarchical biological networks. PLoS Comput Biol. 4:e1000190.

Muraki S. 1993. Volume data and wavelet transforms. IEEE Comput Graph Appl. 13:50–56.

Narayanaswamy A, Wang Y, Roysam B. 2011. 3-D image pre-processing algorithms for improved automated tracing of neuronal arbors. Neuroinformatics. 9:219–231.

Ngiam J, Khosla A, Kim M. 2011. Multimodal deep learning. … Mach Learn (….

Nie J, Guo L, Li K, Wang Y, Chen G, Li L, Chen H, Deng F, Jiang X, Zhang T, Huang L, Faraco C, Zhang D, Guo C, Yap P-T, Hu XX, Li G, Lv J, Yuan Y, Zhu D, Han J, Sabatinelli D, Zhao Q, Miller LS, Xu B, Shen P, Platt S, Shen D, Liu T. 2012. Axonal Fiber Terminations Concentrate on Gyri. Cereb Cortex. 22:2831–2839.

NIH. 2014. BRAIN 2025: A Scientific Vision - Brain Research through Advancing Innovative Neurotechnologies (BRAIN) Working Group Report to the Advisory Committee to the Director, NIH.

O'Donnell LJ, Westin C-F, Golby AJ. 2009. Tract-based morphometry for white matter group analysis. Neuroimage. 45:832–844.

Oberlaender M, Bruno RM, Sakmann B, Broser PJ. 2007. Transmitted light brightfield mosaic microscopy for three-dimensional tracing of single neuron morphology. J Biomed Opt. 12:64029.

Oh SW, Harris JA, Ng L, Winslow B, Cain N, Mihalas S, Wang Q, Lau C, Kuan L, Henry AM, Mortrud MT, Ouellette B, Nguyen TN, Sorensen SA, Slaughterbeck CR, Wakeman W, Li Y, Feng D, Ho A, Nicholas E, Hirokawa KE, Bohn P, Joines KM, Peng H, Hawrylycz MJ, Phillips JW, Hohmann JG, Wohnoutka P, Gerfen CR, Koch C, Bernard A, Dang C, Jones AR, Zeng H. 2014. A mesoscale connectome of the mouse brain. Nature. 508:207–214.

Parekh R, Ascoli GA. 2013. Neuronal morphology goes digital: a research hub for cellular and system neuroscience. Neuron. 77:1017–1038.

Passingham RE, Stephan KE, Kötter R. 2002. The anatomical basis of functional localization in the cortex. Nat Rev Neurosci. 3:606–616.

Peng H, Bria A, Zhou Z, Iannello G, Long F. 2014. Extensible visualization and analysis for multidimensional images using Vaa3D. Nat Protoc. 9:193–208.

Peng H, Hawrylycz M, Roskams J, Hill S, Spruston N, Meijering E, Ascoli GA. 2015. BigNeuron: Large-Scale 3D Neuron Reconstruction from Optical Microscopy Images. Neuron.

Peng H, Long F, Ding C. 2005. Feature selection based on mutual information: criteria of max-dependency, max-relevance, and min-redundancy. IEEE Trans Pattern Anal Mach Intell. 27:1226–1238.

Peng H, Long F, Myers G. 2011. Automatic 3D neuron tracing using all-path pruning. Bioinformatics. 27:i239-47.

Peng H, Meijering E, Ascoli GA. 2015. From DIADEM to BigNeuron. Neuroinformatics. 13:259–260.

Peng H, Ruan Z, Atasoy D, Sternson S. 2010. Automatic reconstruction of 3D neuron structures using a graph-augmented deformable model. Bioinformatics. 26:i38-46.

Peng H, Ruan Z, Long F, Simpson JH, Myers EW. 2010. V3D enables real-time 3D visualization and quantitative analysis of large-scale biological image data sets. Nat Biotechnol. 28:348–353.

Petersen SE, Sporns O. 2015. Brain Networks and Cognitive Architectures. Neuron. 88:207–219.

Preibisch S, Saalfeld S, Tomancak P. 2009. Globally optimal stitching of tiled 3D microscopic image acquisitions. Bioinformatics. 25:1463–1465.

Ragan T, Kadiri LR, Venkataraju KU, Bahlmann K, Sutin J, Taranda J, Arganda-Carreras I, Kim Y, Seung HS, Osten P. 2012. Serial two-photon tomography for automated ex vivo mouse brain imaging. Nat Methods. 9:255–258.

Rakic P. 1988. Specification of cerebral cortical areas. Science (80-). 241:170–176.

Rakic P. 2009. Evolution of the neocortex: a perspective from developmental biology. Nat Rev Neurosci. 10:724–735.

Rand WM. 1971. Objective Criteria for the Evaluation of Clustering Methods. J Am Stat Assoc. 66:846–850.

Rilling JK, Glasser MF, Preuss TM, Ma X, Zhao T, Hu X, Behrens TEJ. 2008. The evolution of the arcuate fasciculus revealed with comparative DTI. Nat Neurosci. 11:426–428.

Rilling JK, Insel TR. 1999. The primate neocortex in comparative perspective using magnetic resonance imaging. J Hum Evol. 37:191–223.

Rilling JK, Seligman RA. 2002. A quantitative morphometric comparative analysis of the primate temporal lobe. J Hum Evol. 42:505–533.

Rogers J, Kochunov P, Zilles K, Shelledy W, Lancaster J, Thompson P, Duggirala R, Blangero J, Fox PT, Glahn DC. 2010. On the genetic architecture of cortical folding and brain volume in primates. Neuroimage. 53:1103–1108.

Salvador R, Suckling J, Coleman MR, Pickard JD, Menon D, Bullmore E. 2005. Neurophysiological architecture of functional magnetic resonance images of human brain. Cereb cortex. 15:1332–1342.

Schoenemann PT. 2006. Evolution of the Size and Functional Areas of the Human Brain. Annu Rev Anthropol. 35:379–406.

Seehaus AK, Roebroeck A, Chiry O, Kim D-S, Ronen I, Bratzke H, Goebel R, Galuske RAW. 2013. Histological validation of DW-MRI tractography in human postmortem tissue. Cereb Cortex. 23:442–450.

Shen D, Wong W, Ip HHS. 1999. Affine-invariant image retrieval by correspondence matching of shapes. Image Vis Comput. 17:489–499.

Shi J, Malik J. 2000. Normalized cuts and image segmentation. IEEE Trans Pattern Anal Mach

Intell. 22:888–905.

Shipley MT, Adamek GD. 1984. the connections of the mouse olfactory bulb: A study using orthograde and retrograde transport of wheat germ agglutinin conjugated to horseradish peroxidase. Brain Res Bull. 12:669–688.

Sohn K, Shang W, Lee H. 2014. Improved Multimodal Deep Learning with Variation of Information. In: Advances in Neural Information Processing Systems. p. 2141–2149.

Song HF, Kennedy H, Wang X-J. 2014. Spatial embedding of structural similarity in the cerebral cortex. Proc Natl Acad Sci. 111:16580–16585.

Sorg C, Riedl V, Mühlau M, Calhoun VD, Eichele T, Läer L, Drzezga A, Förstl H, Kurz A, Zimmer C, Wohlschläger AM. 2007. Selective changes of resting-state networks in individuals at risk for Alzheimer's disease. Proc Natl Acad Sci U S A. 104:18760–18765.

Sotiropoulos SN, Jbabdi S, Xu J, Andersson JL, Moeller S, Auerbach EJ, Glasser MF, Hernandez M, Sapiro G, Jenkinson M, Feinberg DA, Yacoub E, Lenglet C, Van Essen DC, Ugurbil K, Behrens TEJ. 2013. Advances in diffusion MRI acquisition and processing in the Human Connectome Project. Neuroimage. 80:125–143.

Sporns O. 2011. The human connectome: a complex network. Ann N Y Acad Sci. 1224:109–125.

Sporns O, Tononi G, Kötter R. 2005. The human connectome: A structural description of the human brain. PLoS Comput Biol. 1:e42.

Sporns O, Zwi JD. 2004. The small world of the cerebral cortex. Neuroinformatics. 2:145–162.

Srivastava N, Salakhutdinov RR. 2012. Multimodal Learning with Deep Boltzmann Machines. In: Advances in Neural Information Processing Systems. p. 2222–2230.

Suk H-I, Lee S-W, Shen D. 2014. Hierarchical feature representation and multimodal fusion with deep learning for AD/MCI diagnosis. Neuroimage. 101:569–582.

Supekar K, Musen M, Menon V. 2009. Development of large-scale functional brain networks in children. PLoS Biol. 7:e1000157.

Thomas C, Ye FQ, Irfanoglu MO, Modi P, Saleem KS, Leopold DA, Pierpaoli C. 2014. Anatomical accuracy of brain connections derived from diffusion MRI tractography is inherently limited. Proc Natl Acad Sci. 111:16574–16579.

Toussaint N, Souplet J, Fillard P. 2007. MedINRIA: Medical image navigation and research tool by INRIA. MICCAI. 1–8.

Tsien JZ, Li M, Osan R, Chen G, Lin L, Wang PL, Frey S, Frey J, Zhu D, Liu T, Zhao F, Kuang H. 2013. On initial Brain Activity Mapping of episodic and semantic memory code in the hippocampus. Neurobiol Learn Mem. 105:200–210.

Tuch DS. 2004. Q-ball imaging. Magn Reson Med. 52:1358–1372.

Tuch DS, Reese TG, Wiegell MR, Makris N, Belliveau JW, Wedeen VJ. 2002. High angular resolution diffusion imaging reveals intravoxel white matter fiber heterogeneity. Magn Reson Med. 48:577–582.

Tyszka JM, Kennedy DP, Adolphs R, Paul LK. 2011. Intact Bilateral Resting-State Networks in the Absence of the Corpus Callosum. J Neurosci. 31:15154–15162.

van den Heuvel M, Mandl R, Hulshoff Pol H. 2008. Normalized cut group clustering of resting-state FMRI data. PLoS One. 3:e2001.

Van Essen DC. 2013. Cartography and connectomes. Neuron. 80:775–790.

Van Essen DC, Ugurbil K, Auerbach E, Barch D, Behrens TEJ, Bucholz R, Chang A, Chen L, Corbetta M, Curtiss SW, Della Penna S, Feinberg D, Glasser MF, Harel N, Heath AC, Larson-Prior L, Marcus D, Michalareas G, Moeller S, Oostenveld R, Petersen SE, Prior F, Schlaggar BL, Smith SM, Snyder AZ, Xu J, Yacoub E. 2012. The Human Connectome Project: a data acquisition perspective. Neuroimage. 62:2222–2231.

Vincent JL, Patel GH, Fox MD, Snyder AZ, Baker JT, Van Essen DC, Zempel JM, Snyder LH, Corbetta M, Raichle ME. 2007. Intrinsic functional architecture in the anaesthetized monkey brain. Nature. 447:83–86.

Wang H, Nie F, Huang H, Ding C. 2013. Heterogeneous Visual Features Fusion via Sparse Multimodal Machine. In: Proceedings of the IEEE Conference on Computer Vision and Pattern Recognition. p. 3097–3102.

Wang Y, Narayanaswamy A, Tsai C-L, Roysam B. 2011. A broadly applicable 3-D neuron tracing method based on open-curve snake. Neuroinformatics. 9:193–217.

Watts DJ, Strogatz SH. 1998. Collective dynamics of "small-world" networks. Nature. 393:440–442.

Weber B, Tranfield EM, Höög JL, Baum D, Antony C, Hyman T, Verbavatz J-M, Prohaska S. 2014. Automated stitching of microtubule centerlines across serial electron tomograms. PLoS One. 9:e113222.

Wedeen VJ, Hagmann P, Tseng W-YI, Reese TG, Weisskoff RM. 2005. Mapping complex tissue architecture with diffusion spectrum magnetic resonance imaging. Magn Reson Med. 54:1377–1386.

Wedeen VJ, Wang RP, Schmahmann JD, Benner T, Tseng WYI, Dai G, Pandya DN, Hagmann P, D'Arceuil H, de Crespigny AJ. 2008. Diffusion spectrum magnetic resonance imaging (DSI) tractography of crossing fibers. Neuroimage. 41:1267–1277.

Witten IH, Frank E. 2005. Data Mining: Practical Machine Learning Tools and Techniques. Morgan Kaufmann.

Woods RP, Fears SC, Jorgensen MJ, Fairbanks LA, Toga AW, Freimer NB. 2011. A web-based brain atlas of the vervet monkey, Chlorocebus aethiops. Neuroimage. 54:1872–1880.

Wu J, He Y, Yang Z, Guo C, Luo Q, Zhou W, Chen S, Li A, Xiong B, Jiang T, Gong H. 2014. 3D BrainCV: simultaneous visualization and analysis of cells and capillaries in a whole mouse brain with one-micron voxel resolution. Neuroimage. 87:199–208.

Wu P, Hoi SCH, Xia H, Zhao P, Wang D, Miao C. 2013. Online multimodal deep similarity learning with application to image retrieval. In: Proceedings of the 21st ACM international conference on Multimedia - MM '13. New York, New York, USA: ACM Press. p. 153–162.

Xiao H, Peng H. 2013. APP2: automatic tracing of 3D neuron morphology based on hierarchical pruning of a gray-weighted image distance-tree. Bioinformatics. 29:1448–1454.

Xiong Y, Lee AC, Suter DM, Lee GU. 2009. Topography and Nanomechanics of Live Neuronal Growth Cones Analyzed by Atomic Force Microscopy. Biophys J. 96:5060–5072.

Xu J, Sun S-W, Naismith RT, Snyder AZ, Cross AH, Song S-K. 2008. Assessing optic nerve pathology with diffusion MRI: from mouse to human. NMR Biomed. 21:928–940.

Yan C, Gong G, Wang J, Wang D, Liu D, Zhu C, Chen ZJ, Evans A, Zang Y, He Y. 2011. Sex- and brain size-related small-world structural cortical networks in young adults: a DTI tractography study. Cereb cortex. 21:449–458.

Yang J, Gonzalez-Bellido PT, Peng H. 2013. A distance-field based automatic neuron tracing method. BMC Bioinformatics. 14:93.

Yap P-T, Wu G, Zhu H, Lin W, Shen D. 2009. TIMER: tensor image morphing for elastic registration. Neuroimage. 47:549–563.

Yixuan Y, Xi J, Dajiang Z, Hanbo C, Kaiming L, Peili L, Xiang Y, Xiaojin L, Shu Z, Tuo Z, Xintao H, Junwei H, Lei G, Tianming L. 2012. Meta-analysis of Functional Roles of DICCCOLs. Neuroinformatics.

Yuan Y, Chen H, Lu J, Zhang T, Liu T. 2015. Distance Networks for Morphological Profiling and Characterization of DICCCOL Landmarks. MICCAI, LNCS. 9350:380–387.

Zalesky A, Fornito A, Harding IH, Cocchi L, Yücel M, Pantelis C, Bullmore ET. 2010. Whole-brain anatomical networks: does the choice of nodes matter? Neuroimage. 50:970–983.

Zhang D, Guo L, Zhu D, Li K, Li L, Chen H, Zhao Q, Hu X, Liu T. 2013. Diffusion tensor imaging reveals evolution of primate brain architectures. Brain Struct Funct. 218:1429–1450.

Zhang D, Wang Y, Zhou L, Yuan H, Shen D. 2011. Multimodal classification of Alzheimer's disease and mild cognitive impairment. Neuroimage. 55:856–867.

Zhang H, Schneider T, Wheeler-Kingshott CA, Alexander DC. 2012. NODDI: practical in vivo neurite orientation dispersion and density imaging of the human brain. Neuroimage. 61:1000–

1016.

Zhang J, van Zijl PCM, Mori S. 2002. Three-dimensional diffusion tensor magnetic resonance microimaging of adult mouse brain and hippocampus. Neuroimage. 15:892–901.

Zhang T, Chen H, Guo L, Li K, Li L, Zhang S, Shen D, Hu X, Liu T. 2014. Characterization of U-shape Streamline Fibers: Methods and Applications. Med Image Anal.

Zhang T, Guo L, Li K, Jing C, Yin Y, Zhu D, Cui G, Li L, Liu T. 2012. Predicting functional cortical ROIs via DTI-derived fiber shape models. Cereb Cortex. 22:854–864.

Zhang Z, Huang H, Shen D. 2014. Integrative analysis of multi-dimensional imaging genomics data for Alzheimer's disease prediction. Front Aging Neurosci. 6:260.

Zhao Y, Chen H, Li Y, Lv J, Jiang X, Ge F, Zhang T, Zhang S, Ge B, Lyu C, Zhao S, Han J, Guo L, Liu T. 2016. Connectome-scale group-wise consistent resting-state network analysis in autism spectrum disorder. NeuroImage Clin. 12:23–33.

Zhou C, Zemanová L, Zamora G, Hilgetag C, Kurths J. 2006. Hierarchical Organization Unveiled by Functional Connectivity in Complex Brain Networks. Phys Rev Lett. 97.

Zhou J, Peng H. 2007. Automatic recognition and annotation of gene expression patterns of fly embryos. Bioinformatics. 23:589–596.

Zhou Z, Sorensen S, Peng H. 2015. Neuron crawler: an automatic tracing algorithm for very large neuron images. In: ISBI. p. in press.

Zhou Z, Sorensen S, Zeng H, Hawrylycz M, Peng H. 2014. Adaptive Image Enhancement for Tracing 3D Morphologies of Neurons and Brain Vasculatures. Neuroinformatics.

Zhu D, Li K, Faraco CC, Deng F, Zhang D, Guo L, Miller LS, Liu T. 2012. Optimization of functional brain ROIs via maximization of consistency of structural connectivity profiles. Neuroimage. 59:1382–1393.

Zhu D, Li K, Guo L, Jiang X, Zhang T, Zhang D, Chen H, Deng F, Faraco C, Jin C, Wee C-Y, Yuan Y, Lv P, Yin Y, Hu XX, Duan L, Hu XX, Han J, Wang L, Shen D, Miller LS, Li L, Liu T. 2013. DICCCOL: dense individualized and common connectivity-based cortical landmarks. Cereb Cortex. 23:786–800.

Zhu D, Li K, Terry DP, Puente AN, Wang L, Shen D, Miller LS, Liu T. 2013. Connectome-scale assessments of structural and functional connectivity in MCI. Hum Brain Mapp.

Zhu D, Zhang D, Faraco C, Li K, Deng F, Chen H, Jiang X, Guo L, Miller LS, Liu T. 2011. Discovering dense and consistent landmarks in the brain. In: IPMI. p. 97–110.

Zilles K, Armstrong E, Schleicher A, Kretschmann H-J. 1988. The human pattern of gyrification in the cerebral cortex. Anat Embryol (Berl). 179:173–179.